Fluctuation statistics and non-renewal behavior in nanoscale quantum transport

Samuel Rudge

B.Sc. Honours (Physics)

Thesis submitted
to the
College of Science and Engineering
at

James Cook University

in partial fulfillment of the requirements
for the degree of

Doctor of Philosophy (Physical Sciences)

April 2020

ħ electronics

Daniel Kosov's research group

James Cook University

Primary advisor:
A/Prof. Daniel Kosov
Secondary advisor:
Prof. Ronald White

Declaration of originality

I declare that this thesis is my own work and has not been submitted in any form for another degree or diploma at any university or other institute of tertiary education. Every reasonable effort has been made to gain permission and acknowledge the owners of copyright material. I would be pleased to hear from any copyright owner who has been omitted or incorrectly acknowledged.

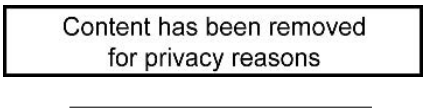

Samuel Rudge

27 April 2020

Evil is whatever distracts.
FRANZ KAFKA (1883-1924)

Dedicated to my family.

Acknowledgments

Of the many people who have helped me throughout my PhD, my greatest thanks go to my supervisor, A/Prof. Daniel Kosov. Without your surprising presence at a small regional university in northern Australia I would never have found entry into this fascinating field of physics, and I am eternally grateful for your gentle yet persistent flow of ideas, advice, and instruction. Many thanks also go to Prof. Ronald White, my secondary advisor, and the Chair of my Candidature Committee, A/Prof. Shaun Belward.

To my co-conspirators in $\hbar$-electronics, Julian, Vincent, Riley, and Thomas: thank you for years of interesting talks, deep discussion, and shared pain over failed trivia nights. Julian in particular I would like to thank for many fruitful discussions about both my research and his.

To all members of the College, thank you for providing me with employment and teaching opportunities throughout my PhD; the College is always an enjoyable place to work and this is because of your approach to teaching and the relationships you foster. To A/Prof. Yvette Everingham, the same thanks go to you, but I am additionally grateful for the personal interest you took in my professional development and our friendship.

To my family, my parents Ross and Julie, my sister Madeleine, and my partner Samantha: thank you for Friday night dinners, weekend coffee, and all the love and belief anyone could ever need. Mum and Dad, my education is a testament to the value you placed upon learning and the commitment you showed to the family. Madeleine, for my entire life you have been the leader and friend every little brother needs, influencing my identity with your extreme honesty and critical worldview. To Samantha, my partner, competitor, best friend, and namesake, you have been transformative to my entire life. Without your presence I would not live where I live, nor been where I have, nor be who I am. To Samantha's family too, thank you for accepting me into the fold.

To my friends, both close to home and far away, thank you for great times with board games, bars, and escape rooms. Your friendship, while sometimes remote, is always present and always appreciated. To Wanderers, of whom there are too many members to name, thank you for being what a club should be: a place of constant welcome and enjoyment. I may be a mediocre cricketer, but at least I play for a great club.

There are others who deserve my thanks, of course, and those that I have not mentioned by name. To you all I am grateful.

Statement of contribution of others

Beyond the personal contributions I have listed in the acknowledgements, there are also a series of contributions that have been made in direct addition to the thesis, which I gratefully detail in this section.

Financial support

The Australian Government provided support via the Research Training Program scheme. This took the form of a complete tuition fee waiver and also a stipend for general living costs, which supported me throughout the majority of my postgraduate study.

James Cook University provided support in the form of financial assistance to purchase necessary research materials and attend conferences.

Intellectual support

Since much of the thesis is drawn from papers, both published and in-preparation, it is imperative that I acknowledge the contribution of A./Prof Daniel Kosov of James Cook University, my supervisor, who was co-author on all publications. He provided large editorial input, and was also the driving force behind the project; many of the ideas for new research pathways, theory, and explanations of results originate from his contribution.

Daniel was also instrumental in constructing the thesis from these various publications, providing editorial assistance and comments on structure for the document as a whole.

Abstract

Molecular electronics is a field of physics concerned with designing and building electronic components made out of molecules. By necessity, it sits at the intersection of semiconductor technology, quantum physics, statistical mechanics, and chemistry. As demand for miniaturization grows and fabrication techniques improve, it is expected that these molecular devices and other nanotechnologies will feature heavily in the new wave of electronics. Beyond these technological applications, transport through nanoscale systems also offers an unparalleled glimpse into systems of a highly quantum nature, and the chance to answer fundamental physical questions over a wide range of sciences. The physical differences between nanoscale and macroscopic conductors are best exemplified by the presence of electronic fluctuations, which universally occur in the former yet rarely occur in the latter.

Fluctuations arise in nanoscale systems from various sources: the unavoidable probabilistic nature of quantum transport, discrete charge carriers coupled with low currents, and stochastic changes in intra-system dynamics. A complete description of nanoscale transport, therefore, requires a complete description of nanoscale current fluctuations, which is the primary concern of this thesis. Early measurements in such systems yielded little information on fluctuations, but as experimental techniques have improved over the last two decades, time-dependent current measurements have become available; these have been accompanied by a plethora of theoretical literature. In this thesis, three prominent fluctuation tools, the full counting statistics, the waiting time distribution, and the first-passage time distribution, are reviewed and applied to several different transport scenarios using Markovian master equations. Although they are only defined in the weak-coupling limit, master equations apply to a wide range of transport scenarios and are an apt choice for calculating fluctuation statistics.

The waiting time distribution and first-passage time distribution are relatively recent additions to the theoretical toolbox of nanoscale quantum transport. As opposed to the full counting statistics, they offer information on short timescales. This is usually framed within the context of renewal theory and correlations between successive waiting or first-passage times. Time-correlations in particular provide interesting information on transport behavior, and they form the main focus of the investigation. Before applying these tools to nanoscale transport scenarios, however, the thesis first presents a review collating the current information on fluctuation statistics from master equations, making some novel remarks on relationships between the waiting time and first-passage time distributions.

The first transport scenario is cotunneling through an Anderson impurity. First, it is shown that for an Anderson impurity deep in the Coulomb blockade, there is a non-zero probability for two electrons to cotunnel to the drain with zero waiting time in between, and that, at high voltages, cotunneling processes slightly modify the non-renewal behavior. In the intermediate voltage regime, previous theory has shown that inelastic cotunneling processes induce telegraphic switching and super-Poissonian noise; unfortunately, this regime has always been inaccessible to waiting times as they are unapplicable to bidirectional transitions. With the recent first-passage time development, which applies to all voltage regimes, it is demonstrated that correlations between successive first-passage times occur when the noise is super-Poissonian, although they are small and unexpectedly negative.

For sequential transport through the Holstein model, it is found that vibrational effects like the Franck-Condon blockade appear in the waiting time distribution just as they do in the current and noise. Again, the first-passage time distribution proves superior to the waiting time distribution, as the electron-phonon interaction produces bidirectional transitions even outside of the low bias regime. Additionally, while previous work has demonstrated that correlations between successive waiting times occur when certain phonon transitions open a shortcut channel, the first-passage time statistics are shown to provide a much better explanation of the non-renewal behavior. The first-passage time distribution is also applied to the Holstein model at zero bias but a non-zero temperature gradient.

Many molecular junctions display stochastic telegraphic switching between two distinct current values, which is an important fluctuation source in nanoscale quantum transport. We include telegraphic switching in a general master equation by introducing a switching rate, ν, between two distinct transport scenarios, considering three specific cases. In the first, stochastic transitions between an Anderson impurity with and without an applied magnetic field, B, are modeled. The other two scenarios couple the electronic level to a single vibrational mode via the Holstein model, stochastically switching between two vibrational conformations, with different electron-phonon couplings, λ, and vibrational frequencies, ω. Finally, a molecule attaching to and detaching from an electrode is modeled by switching between two different molecule-electrode coupling strengths, γ. For all three cases, including the telegraph process in the master equation induces relatively strong positive correlations between successive first-passage times, with Pearson correlation coefficient $p \approx 0.5$. These correlations only appear, however, when there is telegraphic switching between two significantly different transport scenarios and when $\nu \ll \gamma$.

The final transport scenario is that of a triangular triple quantum dot under various regimes of electron occupancy. Triangular triple quantum dots are well-known to produce interesting quantum effects, like coherent population blocking, known as the "dark" state, and Aharonov-Bohm interference. Indeed, coherent oscillations are immediately present in the waiting time

distribution, which are found to correlate with the occupancy of relative dots in the configuration. Dephasing via coupling to macroscopic leads is also present at long times. There are correlations between successive waiting times in the triple quantum dot, but they are relatively small, the largest being $|p| \approx 0.2$. The correlations also weakly depend on both the penetrating magnetic flux, ϕ, and strongly depend on parameters that govern the level of destructive interference in coherent population blocking.

Research output

Publications

[1] *Fluctuating-time and full counting statistics for quantum transport in a system with internal telegraphic noise*,
S.L. Rudge and D.S. Kosov, Phys. Rev. B **100**, 235430 (2019)

[2] *Counting quantum jumps: A summary and comparison of fixed-time and fluctuating-time statistics in electron transport* - invited review in the special issue "Dynamics of Open Quantum Systems",
S.L. Rudge and D.S. Kosov, J. Chem. Phys. **151**, 034107 (2019)

[3] *Non-renewal statistics in quantum transport from the perspective of first-passage and waiting time distributions*,
S.L. Rudge and D.S. Kosov, Phys. Rev. B, **99**, 115426 (2019)

[4] *Distribution of waiting times between electron cotunneling events*,
S.L. Rudge and D.S. Kosov, Phys. Rev. B, **98**, 245402 (2018)

[5] *Distribution of residence times as a marker to distinguish different pathways for quantum transport*,
S.L. Rudge and D.S. Kosov, Phys. Rev. E, **94**, 042134 (2016)

[6] *Distribution of tunnelling times for quantum electron transport*,
S.L. Rudge and D.S. Kosov, J. Chem. Phys. **144**, 124105 (2016)

Conference posters

[1] Poster title: *Non-renewal statistics for quantum electron transport*
Frontiers of Quantum and Mesoscopic Thermodynamics
Prague, Czech Republic, 2019

Structure and style

Before turning to the body of the thesis, it will help the reader to understand its structure in relation to the publications on which it is based. Rather than a series of papers presented without alteration and placed back-to-back, I have attempted to tie all work together into one coherent whole. In this section I outline the contribution each publication made to each chapter, as well as some choices of style. In referring to specific publications, I follow the order in the "Research output" section.

Since the Abstract and Chapter 1 were written to tie this specific thesis together, I have drawn neither from any particular publication. Likewise, Chapter 2, being a review on the well-established theoretical master equation method, is not based on any particular published manuscripts. Rather, the subsection on the rate equation and n-resolved master equation is based upon an amalgamation of many similar sections that appear in Pub.[1]-Pub.[4].

Chapter 3, in contrast, is cannibalized almost completely from the review paper in Pub.[2]. In the published version, all fluctuation statistics are demonstrated for the example of transport through the Holstein model: analytic results from the restriction equilibrated phonons, and numeric results from the unequilibrated case. As this is an introductory chapter, I have removed all numeric results and placed the pertinent ones in Chapter 5, which details results for the Holstein model. I have kept the analytic results as they are useful pedagogically, but I have reformulated the notation to that of transport through a single resonant level.

Chapter 4 has been constructed from the entirety of Pub.[4] as well as part of Pub.[3]. Pub.[4] was written first to investigate waiting times for cotunneling through an Anderson impurity, but later the first-passage time approach was developed and suited this transport scenario better. The resulting first-passage time paper, Pub.[3], contained results for sequential tunneling through the Holstein model and cotunneling through an Anderson impurity. Rather than presenting these two publications separately, I thought it more logical to separate the results into the two different models. In combining these two publications, I have removed redundant theory, written a new introduction, and reformatted results; the end product contains the same results, theory, and analysis, but is, in places, stylistically different to both publications.

The remainder of Pub.[3] forms Chapter 5, with numerical results from Pub.[2] included as well. Again, in reformatting these two publications, the results, theory, and analysis, alongside large swathes of text, remain the same.

Chapter 6 is almost identical to Pub.[1], except that the n-resolved master equation and fluctuation statistics theory has been removed. Chapter 7 is not based on, nor has any parts from, any paper, although it is likely it will form the basis for a publication after the thesis is submitted. Pub.[5] and Pub.[6] do not directly form any chapter in the thesis. They nonetheless contributed to the research project and are appropriately cited throughout.

Although I have provided this section as a reference to the whole thesis, I will also detail which were the relevant publications at the start of each chapter. All figures that have been taken from already published work will be identifiable by the publisher's copyright attached to them, and I note that I have obtained permission from the publishers of Pub.[1]-Pub.[6] to reprint my own work.

Finally, I note that all publications have appeared in American journals and, as such, have Americanized spellings throughout them. Since the thesis is largely based on pre-published work, I have chosen to keep this format and extended it to all other components of the manuscript. Furthermore, it is common in these journals for authors to speak in the first person "we" or "I"; since I wrote all articles alongside a co-author, I have kept this style as well.

Contents

List of Figures

List of Tables

Introduction

1.1 Background context

When first introduced, the idea of replacing components in electric circuits with single molecules was completely radical. The experimental breakthroughs required to realize these so-called "molecular electronics" were so vast that the first technical proposal of such a device, a molecular rectifier designed by Aviram and Ratner [1], remained entirely theoretical for years. As time passed and revolutionary techniques were developed, however, the idea gained momentum among mainstream science [2]. Researchers were excited by the dual prospects of observing fundamental physics found nowhere but the nanoscale, and also the potential technological application of these molecular-scale devices to a long-standing problem in microelectronics.

Early semiconductor development was marked by rapid advancements and miniaturization to the point that, in 1965, Roger Moore, then CEO of Intel, predicted that the number of transistors on an integrated circuit would double every year [3]. His revised estimate in 1975 of a doubling every two years has remained remarkably accurate, and it is only in the last 10 years that transistor miniaturization has failed to satisfy Moore's law, as it is famously known. This recent slowing is due in part to technological limitations, for example IBM's recent 5nm chip requires an entirely new chip architecture to work [4], but also to fundamental size constraints and quantum effects. To keep up with the demand for greater computing power, therefore, requires novel methods that either satisfy Moore's law or provide a completely new and more efficient approach.

One potential avenue is quantum computing, in which the classical bit is replaced with a quantum bit or "qubit", a superposition of the standard 0 and 1 states: $|\psi\rangle = a|0\rangle + b|1\rangle$, with $|a|^2 + |b|^2 = 1$ [5]. By manipulating the qubit via quantum logic gates, one can solve certain problems that are too difficult for classical computers; for example, Shor's algorithm uses quantum computing to calculate factors of large integers, a key part of modern encryption [6]. Results like this have lent quantum computing an air of excitement that has bled even into the public consciousness; although it appears that, while superior in solving certain problems, it

performs no better than classical computing at everyday tasks.

Molecular electronics, on the other hand, seeks to tackle the miniaturization aspect. Not only are single molecules, being on the order of $1 - 10$nm, naturally the smallest possible building block for electronic components, they also have several other potential advantages, such as chemical variability, faster transistor signals, and advanced assembly [7–9]. Now, more than 40 years after Aviram and Ratner's molecular rectifier, there has been sufficient experimental and theoretical progress to facilitate a large and ever-growing field concerned with designing, building, and manipulating molecular scale devices.

In most experiments, and in our theoretical treatments, the general paradigm is that of a molecule or small number of molecules sandwiched between two macroscopic metal electrodes; see the schematic in Fig.(1.1). Throughout the history of molecular electronics, there have been many ingenious methods of creating these junctions, but we will outline only the two most popular approaches. In scanning tunneling microscopy (STM) [10], a fine metal tip is brought near a metal-substrate-molecule setup to to form an atomic contact and measure the molecule's conductance [11] as in Fig.(1.2a). A mechanically controllable break-junction (MCBJ) [12], on the other hand, is formed by wire notching [13] or electron lithography [14]. A piezo-drive then applies force to break the junction, into which a molecule is deposited, like in Fig.(1.2b).

Because electrodes need to be prepared extremely cleanly, they are usually made out of inert metals like gold or silver, which then makes depositing the molecule of choice on the electrode a difficult task. To overcome this secondary problem, thiol anchor groups, $-SH$, can be added to the molecule, as the thiol-gold bond is chemically stable [15]. Although there are other anchor-electrode combinations, such as $-NC$ and Pt, they all have in common a stable chemical bond and high conductance through the anchor group [16].

Apart from the anchor groups required to form the metal-molecule-metal bonds, there are few restrictions on molecules in the junctions, and they are generally chosen for their specific functionality. Asymmetric pyrimidine [17], cyclophane [18] and ferrocenyl [19] molecules, for example, have produced the highly sought-after rectification behavior required for molecular diodes, while light-controlled conductance switching [20–22] and optical memory [22] have been demonstrated using diarylethene derivatives. Other results include measurements on DNA molecules [23], molecular switches [24], observance of negative differential resistance [25], quantum refrigerators [26], and applications to spintronics [27].

When considering that we have mentioned only a few of the many experimental techniques and applications of molecular electronics, it is evident that the field holds much promise. Despite its more extensive experimental history [28] when compared to contemporary alternatives like quantum computing, however, molecular electronics is still far away from being a viable alternative to traditional semiconductors. On the experimental side, molecular

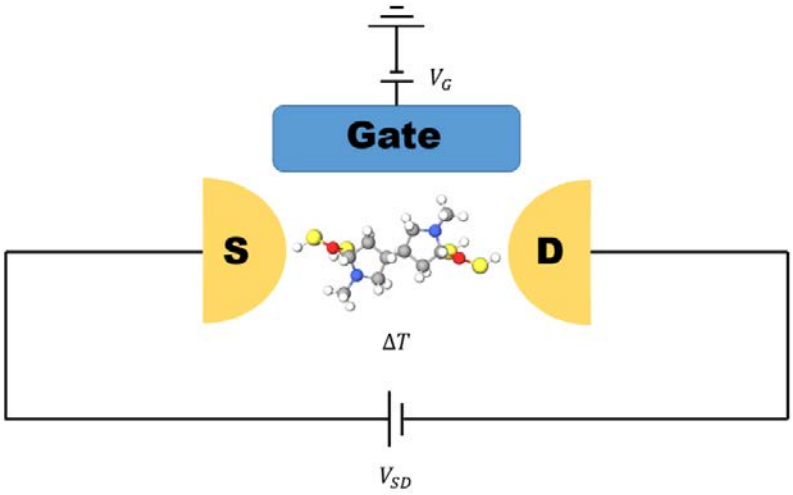

Figure 1.1: Schematic of a molecular junction, in which a molecule is attached to two metal electrodes: the source and drain. Applying a voltage difference, V_{SD}, or a thermal gradient, ΔT, drives the system out of equilibrium and causes electrons to flow across the molecular junction. Most experimental setups also include a gate voltage, V_g, to tune the system energies, although in all calculations we absorb V_g into the energy levels.

junctions are vulnerable to local heating, which makes them notoriously unstable at room temperature [29]. Furthermore, although individual molecular junctions can now be reliably synthesized and experimented upon, combining multitudes of molecular devices together into a single integrated circuit requires nanoscale control far beyond that available from current technology. Even if molecular devices do not supersede the current generation of microelectronics, the field is still critical to answering deep physical questions, and posing new ones. Probing transport phenomena on ever-decreasing size scales has historically been a goldmine of new physics and technology, and there is nothing to suggest that molecular electronics is any different.

Symptomatic of this duality between technology and fundamental physics is the central theme of the thesis: fluctuations. In nanoscale devices, electron tunneling events occur at random time intervals, due in part to thermal fluctuations in the macroscopic electrodes and also to the inherently stochastic nature of quantum transport. Any time-dependent observable, for example the current $\hat{I}(t)$, should therefore not be viewed as a constant, but rather a stochastic, dynamical variable fluctuating around an average [30, 31]. Because electronic components require reliable, steady currents and signals, from one point of view fluctuations can be viewed as an impediment to the performance of molecular devices. Simultaneously, though, the current fluctuations are largely determined by a molecule's underlying dynamics and can thus be used to characterize interesting nanoscale phenomena. Considering their integral role in nanoscale transport, therefore, it is imperative to have a rigorous theoretical and experimental framework in which to analyze them.

It is not surprising, then, that as various experimental nanotechnologies like molecular elec-

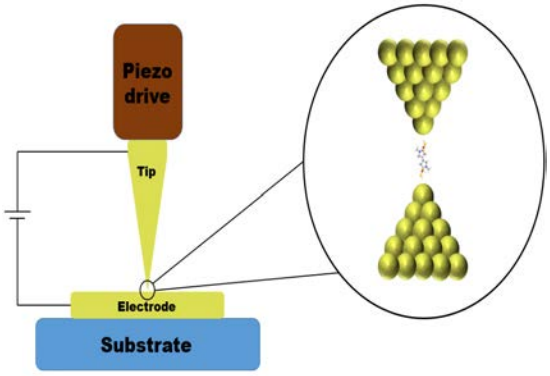

(a) Schematic of a scanning tunneling microscope setup. The STM tip width is usually 100 – 200nm [8].

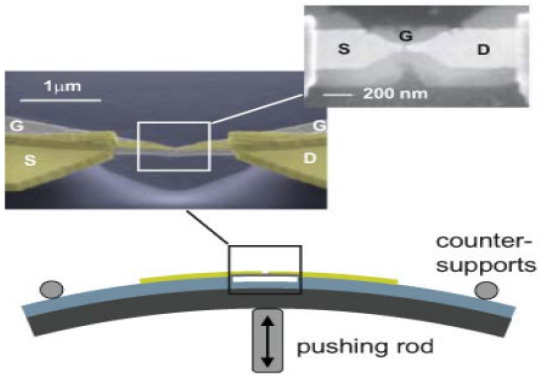

(b) Schematic of a mechanically controlled break-junction. Adapted with permission from Ref.[32], © 2010 Institute of Physics.

tronics have grown so too has complementary research into fluctuation behavior. There are now well-established experimental methods for measuring current fluctuations, and a large theoretical toolbox to accompany [33]. In Section 1.2, therefore, we will first outline the experimental background of current fluctuation measurements in nanoscale devices before stating the exact motivation, purpose, and scope of the thesis.

At this point, the reader may have noticed that we have transitioned from discussing only "molecular" devices to referring to the more inclusive "nanoscale" devices, a shift that reflects a major theoretical limitation for molecular electronics. To calculate the electronic spectra of actual molecular orbitals would require us to use a method such as density functional theory (DFT), in which the many-body problem of orbital electrons reduces to a series of single electron wavefunctions solved for an effective potential [34]. DFT has produced many outstanding results crucial to chemistry, biology, and physics, but it is also numerically intensive, sometimes inaccurate, and it omits electron-electron interactions and molecular vibrations [34]. More importantly, there is also no framework for calculating fluctuation behavior from DFT, and so it is unsuitable for our investigation.

In contrast to molecular junctions, other nanoscale devices are well-described by models that are constructed from a set of underlying physical principles. In addition, these nanostructures have Hamiltonians that submit to more accessible methods, like master equations and non-equilibrium Green's functions, for which there are established approaches in obtaining information about the fluctuation behavior. Out of these alternative nanostructures, we are particularly interested in lateral quantum dots, which are formed by three-dimensional quantum confinement [35].

To construct a lateral quantum dot, which we will now refer to as just a quantum dot, a two-dimensional electron gas (2DEG) is first grown between two semicondcutor sheets; a common example has the 2DEG at the the interface of GaAs and AlGaAs layers in a GaAs/AlGaAs heterostructure. Electrons are confined in the z dimension, but have high mobility within the plane of the 2DEG. Then, metallic gates are deposited on top of the heterostructure and a

negative voltage is applied, forming barriers within the 2DEG. By arranging the gates into an appropriate geometry, such as in Fig.(1.3a), a small number of electrons are spatially confined in the remaining two dimensions within a region of the 2DEG and so forming the quantum dot [36].

As Fig.(1.3a) shows, the gates are arrayed, and a voltage applied, so as to form a source-dot-drain setup analogous to that in Fig.(1.1). Because the electrons within the dot are spatially confined, they can be treated with the three-dimensional particle in a box model. The resulting quantized energy levels are reminiscent of atomic spectra, albeit on a different scale; consequently, they are often referred to as "artificial atoms" [35]. Additionally, while occupying the dot, electrons may experience electron-electron interactions or coupling to vibrational modes: two phenomena common in molecular junctions. These properties make quantum dots, and derivative nanostructures like double or triple quantum dots, excellent proxies for actual molecular junctions. In our investigation, therefore, we will use various dot Hamiltonians as conceptual models for molecular orbitals.

1.2 Fluctuation measurements

Early experimental measurements in nanoscale transport focused on the stationary average electric current $\langle I \rangle$ and, as techniques improved, the zero-frequency noise $\mathcal{S}(0)$. While $\langle I \rangle$ is perhaps the single most important observable in nanoscale devices, it offers no information on fluctuation behavior. The noise, meanwhile, clearly does incorporate fluctuations about the mean:

$$\mathcal{S}(\omega) = \int_{-\infty}^{\infty} dt\, e^{i\omega t} \left\langle \left[\delta\hat{I}(t), \delta\hat{I}(0)\right]_+ \right\rangle, \tag{1.1}$$

where $\delta\hat{I}(t) = \hat{I}(t) - \langle I \rangle$.

Electric current in nanoscale conductors exhibits two fundamental noise types: thermal or Johnson-Nyquist noise [37, 38], from the random motion of electrons at non-zero temperatures, and shot noise, from the stochastic nature of electron transport through a barrier [30]. Shot noise has historically been treated with the Schottky formula [39], which assumes that electron tunnelings are independent and can be modeled as a Poisson process. In nanoscale transport, however, this assumption is often violated and the noise becomes super-Poissonian [40–48] or sub-Poissonian [49, 50].

These limited experiments were eventually superseded by a powerful new experimental technique: time-resolved single-electron detection. In this method, a quantum point contact (QPC) is defined in the same 2DEG as the quantum dot, see Fig.(1.3a). The QPC confines electrons in the lateral direction, producing conductance quantization [51] that depends on the effective electric field in which it sits. Its proximity to the quantum dot ensures capacitive coupling be-

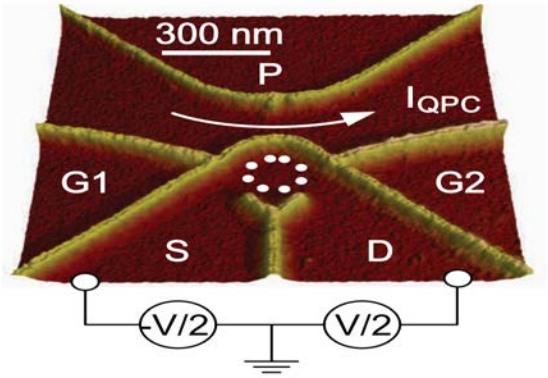

(a) Lateral quantum dot formed by a 2DEG grown within a GaAs/AlGaAs via appropriate gate geometry. Adapted with permission from Ref.[52], © 2009 Elsevier.

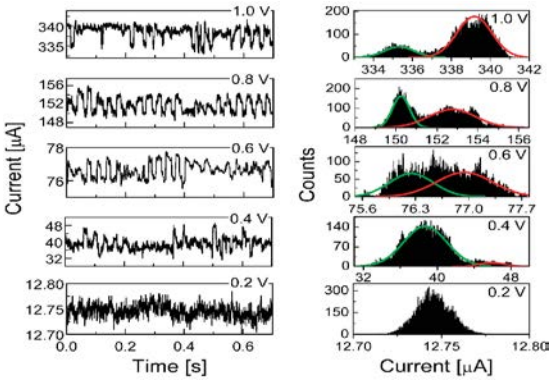

(b) Example of a time-dependent current measurement, with accompanying current distribution. Adapted with permission from Ref.[53], © 2010 American Chemical Society.

tween the two, which manifests when individual tunneling events in the quantum dot change the charging energy by a discrete amount. The conductance of the QPC, therefore, acts as a charge detector for the quantum dot. If the electrode-system couplings are tuned to below the QPC bandwidth, furthermore, then the QPC can detect tunneling events in real-time, as in Fig.(1.3b) [52, 53].

The resulting time-dependent current traces, such as in Fig.(1.3b), contain much more information about current fluctuations than before. For example, defining a time-interval, Δt, and measuring the number of detections in each interval produces a probability distribution of current, also shown in Fig.(1.3b). The average current is the first cumulant of such a distribution and, as shown in Chapter 3, the zero-frequency noise is the second [31]. There are many instances where the first two cumulants provide an unsatisfactory description of the transport though; one example is a non-Gaussian current distribution, which is not fully described by its average and variance alone [54–56]. In these cases, time-resolved single-electron detection gives us access to all higher-order current cumulants as well, $\langle\langle \hat{I}(t)^k \rangle\rangle$: the full counting statistics (FCS).

Initial real-time single-electron detection experiments were performed by Lu *et al.* [57] and Fujisawa *et al.* [58], while the FCS of a quantum dot was first measured by Bomze *et al.* [56] and Gustavsson *et al.* [59]. Using real-time single-electron detection, Gustvasson *et al.* were also able to detect single photon absorption from a QPC via the shot noise of a nearby double quantum dot [60]. Other groups extended the methodology to include bidirectional transitions by including a double quantum dot in the detection process [61], and demonstrated that bimodal current distributions are possible [62]. Single-electron detection was also used to measure electron-electron interference in a double quantum dot [52, 63, 64], the FCS of superconducting junctions [65], the FCS in the transient regime [66], non-Gaussian fluctuations [67], and finite-frequency FCS [68]. Sukhorukov *et al.* [69] analyzed the effect that single-electron detection has on transport, showing that the FCS is altered by the back-action of the QPC on

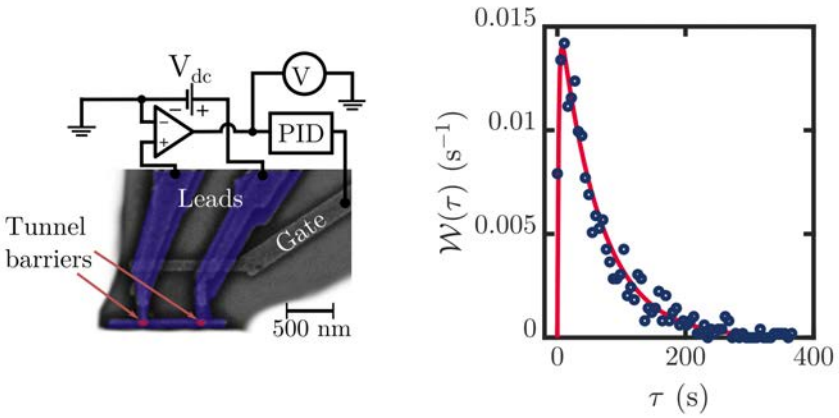

Figure 1.4: Scanning electron micrograph (left) of a Josephson-junction-based charge detector, used to experimentally construct the WTD of a two-level fluctuator (right). Adapted with permission from Ref.[72], © 2019 American Physical Society.

the QD. Even before single-electron detection, Reulet *et al.* [55] related measurements of the skewness of voltage fluctuations to the skewness of current fluctuations.

Although most experiments have operated at ultra-low temperatures, usually in the mK range, recently a group has managed to use the optical blinking of a nearby semiconductor nanocrystal to make room temperature measurements on a carbon nanotube [70]. A similar method, using resonance fluorescence, has analyzed spin dynamics in a quantum dot [71]. Unfortunately, single-electron counting methods are still restricted to extremely low tunneling rates, in the order of 1kHz, which translate to currents in the order of 0.1fA.

The FCS have been a remarkably successful tool in describing current fluctuations, and in Chapter 3 we outline a more detailed history of their use. In the last 15 years, however, a complementary statistical tool has been introduced to nanoscale quantum transport: the waiting time distribution (WTD). In this approach, rather than measuring the number of tunneling events in a time interval, the time *between* each tunneling event is measured instead; information that is also available from the same time-dependent current measurements in Fig.(1.3b). Since their introduction, one of the central questions surrounding the WTD has been whether its cumulants can be derived from the FCS or whether they are distinct quantities and thus contain new information: a valid question considering that they are generated from the same experimental data.

This question has in large part been answered by renewal theory, which demonstrated that the cumulants of the WTD exactly reproduce the zero-frequency FCS if successive waiting times are uncorrelated [73, 74]. In the case where successive waiting times *are* correlated, then the WTD contains information about short-time physics that is unavailable from the FCS alone. Because tools like the WTD are so new to nanoscale transport, there are many nanoscale systems for which it has not been applied. In this thesis, therefore, the main goal is to investigate time correlations in a variety of transport scenarios, discerning interesting dynamics that we

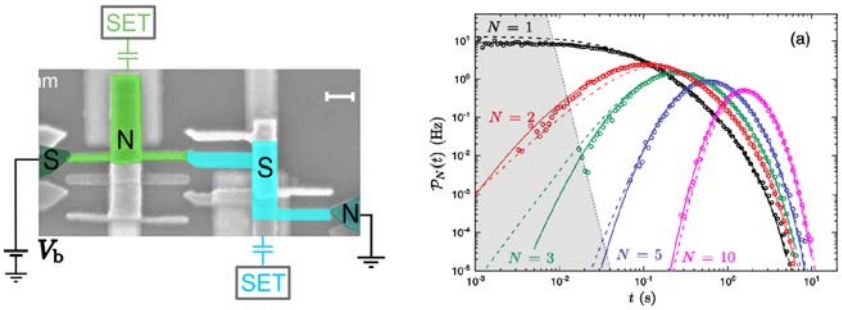

Figure 1.5: Scanning electron micrograph (left) of a double quantum dot comprised of one normal and one superconducting island, coupled to two single-electron transistors from which the FPTD (right) is obtained. Adapted with permission from Ref.[77], © 2019 American Physical Society.

cannot see elsewhere. In doing so, we will also use a more general statistical tool than the WTD: the first-passage time distribution (FPTD), which is applicable for bidirectional transport when the WTD is not. The FPTD is an extremely recent addition to nanoscale transport, and many of our FPTD results are the first for such systems.

Because they are recent introductions to nanoscale quantum transport, the experimental history of the WTD and the FPTD is much shorter than that for the FCS. Jenei *et al.*, for example, used a superconducting charge detector, made from two Josephson junctions and shown in Fig.(1.4), to construct the WTD of a two-level fluctuator [72]. Singh *et al.*, meanwhile, used a series of superconducting and normal components to measure the FPTD of a double quantum dot, shown in Fig.(1.5). Other groups have recently measured the effect of a magnetic field on the WTD of a quantum dot constructed from phosphorous atoms [75], and the WTD in the Pauli-spin blockade regime of a double quantum dot [76]. Fluctuating-time statistics theory, in comparison, is extremely well-developed.

To calculate the WTD and FPTD, we rely exclusively on the quantum master equation approach. Although comparable methods, like non-equilibrium Green's functions or scattering theory, can be used to obtain fluctuation statistics, master equations have a neat and simple formalism that is applicable to a wide variety of systems. The drawback is that master equations rely on assuming the baths are Markovian, and their simplified version, rate equations, rely on eliminating quantum coherence: two important correlation sources in nanoscale systems. As a result, we investigate transport scenarios that either remove one of these assumptions, like cotunneling or fully coherent transport in a triple quantum dot, include electron-phonon interactions, or have some additional effect, like telegraphic switching.

In Section 1.3, we outline both the model describing the general electrode-molecule-electrode configuration in Fig.(1.1), and the specific conceptual model of the nanoscale device used throughout the thesis. This includes both the Hamiltonians and the pertinent assumptions applying to each part of the system.

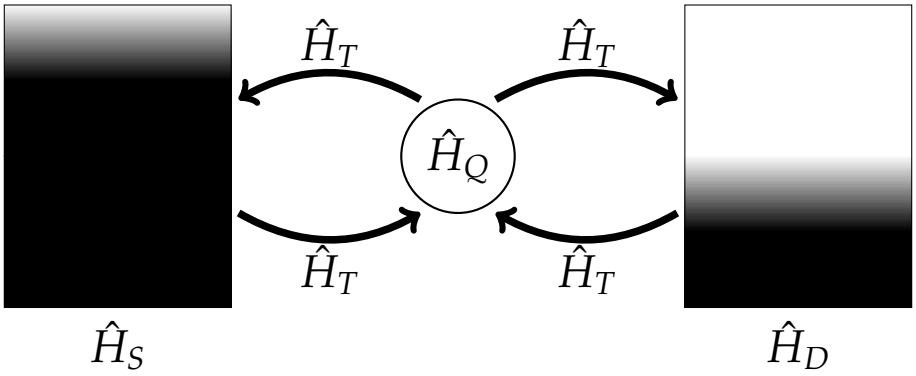

Figure 1.6: Hamiltonian breakdown in the molecular junction configuration. The quantum system is coupled to two macroscopic metal electrodes, with tunneling between. The electrode shading indicates state occupancy: solid black is fully occupied; grey is partially occupied; and white is unoccupied.

1.3 Model

The general model in Fig.(1.1) consists of a quantum subsystem coupled to two macroscopic metal electrodes: the source (S) and drain (D). We will find it useful to treat the Hamiltonian as being made of three distinct parts, which are shown in Fig.(1.1). The source and drain are described by $\hat{H}_S$ and $\hat{H}_D$, respectively; the nanoscale quantum system is described by $\hat{H}_Q$; and the system-electrode interaction is $\hat{H}_T$. The total Hamiltonian, written in second quantization, is

$$\hat{H} = \hat{H}_Q + \hat{H}_S + \hat{H}_D + \hat{H}_T. \tag{1.2}$$

The electrodes are modeled as a sea of non-interacting electrons,

$$\hat{H}_S + \hat{H}_D = \sum_{\alpha=S,D} \sum_{\mathbf{k}_\alpha} \varepsilon_{\mathbf{k}_\alpha} \hat{a}^\dagger_{\mathbf{k}_\alpha} \hat{a}_{\mathbf{k}_\alpha}, \tag{1.3}$$

and the interaction Hamiltonian describes tunneling of electrons between the two,

$$\hat{H}_T = \sum_{\alpha=S,D} \sum_{q,\mathbf{k}_\alpha} t_{\mathbf{k}_\alpha,q} (\hat{a}^\dagger_{\mathbf{k}_\alpha} \hat{a}_q + \hat{a}^\dagger_q \hat{a}_{\mathbf{k}_\alpha}). \tag{1.4}$$

The operators $\hat{a}^\dagger_{\mathbf{k}_\alpha}$ and $\hat{a}_{\mathbf{k}_\alpha}$ create and annihilate an electron in state $\mathbf{k}$ in electrode α with energy $\varepsilon_{\mathbf{k}_\alpha}$. Likewise, $\hat{a}^\dagger_q$ and $\hat{a}_q$ are the creation and annihilation operators for the quantum subsystem. Finally, $t_{\mathbf{k}_\alpha,q}$ is the tunneling matrix element between system state q and state $\mathbf{k}$ in electrode α.

The source and drain are held at their respective chemical potentials, μ_α, and temperatures,

T_α. Due to their macroscopic size and connection to a closed electronic circuit, we can safely treat them as heat baths and particle reservoirs; adding or removing an electron does not affect the underlying dynamics of either electrode and they are well-described as grand canonical ensembles held at local equilibrium. The occupancy of state $\mathbf{k}$ in electrode α, for example, follows the Fermi-Dirac distribution $n_F(\varepsilon_{\mathbf{k}_\alpha} - \mu_\alpha)$:

$$n_F(\varepsilon_{\mathbf{k}_\alpha} - \mu_\alpha) = \frac{1}{e^{(\varepsilon_{\mathbf{k}_\alpha} - \mu_\alpha)/k_B T_\alpha} + 1}. \tag{1.5}$$

We cannot treat the total system with standard thermodynamics, however, because we always consider a non-zero bias voltage, $V_{SD} = \mu_S - \mu_D$, or temperature gradient, $\Delta T = T_S - T_D$, so that the junction experiences non-equilibrium dynamics. We exclusively define the source and drain potentials as symmetric around the Fermi energy of the junction, E_F: $\mu_S = E_F + \frac{V_{SD}}{2}$ and $\mu_D = E_F - \frac{V_{SD}}{2}$. In all calculations we set $E_F = 0$. This construction ensures that electrons are induced to flow from the source, across the quantum subsystem, to the drain. In this, and subsequent discussions, we will use a "B" subscript, representing the total bath, to denote the source and drain collectively.

1.3.1 Anderson-Holstein model

All results in the thesis are calculated for systems that are based on the Anderson-Holstein model, shown in Fig.(1.7), a non-trivial conceptual model that includes vibrations and electron-electron interactions. For the model to be valid, transport must occur through a single spin-degenerate or spin-split level coupled to a single harmonic vibrational mode:

$$\hat{H} = \sum_\sigma \varepsilon_\sigma \hat{a}_\sigma^\dagger \hat{a}_\sigma + U\hat{n}_\uparrow \hat{n}_\downarrow + \lambda(\hat{b}^\dagger + \hat{b})(\hat{n}_\uparrow + \hat{n}_\downarrow) + \hbar\omega(\hat{b}^\dagger \hat{b} + 1/2). \tag{1.6}$$

The fermionic operators, $\hat{a}_\sigma^\dagger$ and $\hat{a}_\sigma$, create and annihilate an electron with spin $\sigma \in \{\uparrow, \downarrow\}$ and energy ε_σ, respectively, while U is the Coulomb repulsion when two electrons occupy the level. The spin-dependent particle number operator is $\hat{n}_\sigma = \hat{a}_\sigma^\dagger \hat{a}_\sigma$. Likewise, the bosonic operators, $\hat{b}^\dagger$ and $\hat{b}$, create and annihilate vibrational phonons with frequency ω. These electronic and vibrational degrees of freedom interact via the middle term, which models the effect of charging and discharging on molecular vibrations. When there are zero electrons in the system, the harmonic potential contained in the last term remains unchanged. For one or two electron occupancy, however, $\sum_\sigma n_\sigma \neq 0$ and the translation operator $\hat{b}^\dagger + \hat{b}$ spatially shifts the potential. The electron-phonon interaction strength, λ, is then interpreted as the size of this shift.

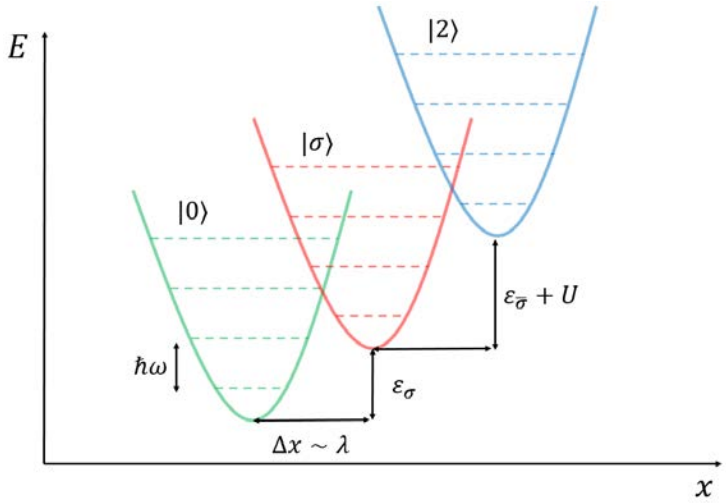

Figure 1.7: Schematic of the Anderson-Holstein model. The orbital may be occupied by an electron of either spin, or two electrons of opposite spin. If spin-degenerate, then $\varepsilon_\uparrow = \varepsilon_\downarrow$, but if a magnetic field B is applied the levels become spin-split: $\varepsilon_\uparrow \neq \varepsilon_\downarrow$. Double occupancy is accompanied by a Coulomb repulsion U. The orbital is coupled to a harmonic vibrational mode at frequency ω, where the electron-phonon coupling strength is λ.

1.4 Outline

The thesis chapters are organized as follows. In **Chapter 2**, we introduce the master equation as a method for describing transport in nanoscale quantum systems. This includes an introduction to the Schrödinger, Heisenberg, and interaction pictures of quantum mechanics, as well as why it is necessary to use the density matrix rather than a wavefunction representation. From there we derive the Redfield master equation under the Born-Markov approximation and keeping only the first non-zero term of the perturbation. We also discuss the simplification under the secular approximation, where off-diagonal elements of the density matrix are ignored and the transport can be described by a rate equation instead. To calculate transition rates in the rate equation, we derive Fermi's generalized golden rule for many-body systems, introducing sequential tunneling and cotunneling as well. Finally in this chapter, we present the master equation in super-operator form, unfolding the density matrix into a probability vector and defining the Liouvillian. We then make the transition to an n-resolved master equation, which is necessary to calculate all fluctuation statistics.

Chapter 3 is the last introductory chapter, containing a review of each fluctuation statistic we work with: the FCS, the WTD, and the FPTD. For all three, we briefly sketch the history, theoretical outline, and an analytic demonstration for the trivial single resonant level system. Our review contains a novel derivation connecting two separate WTD definitions, as well as a discussion on why the WTD fails for bidirectional transport. This chapter also contains a discussion on renewal theory, laying out an exact definition of the renewal assumption for both the WTD and FPTD. We introduce the Pearson coefficient as a way of measuring the correlation between successive waiting or first-passage times, and provide a derivation of the

exact relationship between the FCS and waiting time or first-passage time cumulants, when the renewal assumption is satisfied.

In **Chapter 4**, we investigate fluctuations for cotunneling through an Anderson impurity, where all vibrations are neglected. Previous research [46] has shown that inelastic cotunneling processes produce telegraphic switching in an Anderson impurity, and thus super-Poissonian noise. We address this scenario from the perspective of the WTD and FPTD. We show that, since elastic cotunneling processes do not enter the standard master equation, it is necessary to use the WTD as defined from the n-resolved master equation. This in turn means that the particular regime of interest is blocked to waiting time analysis, as it contains bidirectional transitions; we instead apply the FPTD, demonstrating its usefulness. As expected, we find that the super-Poissonian noise is accompanied by correlations in successive first-passage times, but the correlations are unexpectedly negative and quite small.

Chapter 5, on the other hand, neglects electron-electron interactions and investigates vibrational effects via sequential tunneling through the Holstein model. In the WTD, we demonstrate well-known features of vibrationally assisted transport, like the Franck-Condon blockade for large λ. It has previously been shown [78] that there are correlations between successive waiting in a particular voltage regime and for strong λ; we demonstrate that bidirectional transport exists in this regime and the WTD is not accurate. Using the FPTD, we find similar correlations and an exact agreement with renewal theory in the first-passage time cumulants and the FCS. We also analyze the Holstein model in the presence of a temperature gradient as opposed to a voltage bias: a topical research path given recent experiment [79].

To investigate telegraphic switching further, in **Chapter 6** we define a general master equation for a telegraphic switching process and apply it to three different transport scenarios. Unlike previous approaches [80, 81], we add no stochastic element to the master equation but rather a switching rate, ν, between appropriate elements of the density matrix. Using the FPTD, we investigate transport in an Anderson impurity, where a magnetic field B is switched on and off. We find that when the magnetic field pushes one of the levels just outside the bias window, telegraphic switching causes strong positive correlations between successive first-passage times. The correlation strength depends on ν, which must be much smaller than the electrode-system transition rate, γ, for correlations to be present. We also apply the method to model a system undergoing conformational change, first by a single level switching between two different harmonic vibrational modes and then by switching between two different electronic levels as well. In both cases, the interplay of Franck-Condon physics and telegraphic switching produces distinct positive correlations at multiple voltages. Finally, we constructed a crude model of a nanoscale system randomly attaching to and detaching from one of the electrodes; a common occurrence in molecular junctions. Intuitively, current is much lower when the system is detached, and there were strong positive correlations for this scenario as well.

As opposed to the other transport scenarios, in which we use the secular rate equation, **Chapter 7** requires the fully coherent master equation, as we apply the WTD to a triangular triple quantum dot. Triple quantum dots are interesting systems that display Aharonov-Bohm interference, where electrons interfere with themselves over different paths through the dots, and coherent population trapping, which can cause a "dark state" and block current. We model each dot as an Anderson impurity, and consider three regimes in which one, two, or three electrons may occupy the triple quantum dot. We find that coherent oscillations appear in the WTD that relate directly to the occupation of each dot in the configuration. We also demonstrate that in the two and three electron occupancy regimes there are small negative correlations between successive waiting times, which are modulated by the constructive or destructive interference from population trapping, and Aharonov-Bohm interference.

Chapter 8 contains a summary of the thesis, as well as a brief outline of future work. We finish with the **References** and then an **Appendix**, containing all necessary derivations that are too long for the main text.

Throughout the thesis, we work in natural units, so that $\hbar = e = m_e = 1$. From this point on, we also do not include the $\hat{}$ notation to represent operators; they will be evident from context.

Master equations

2.1 Motivation

In order to analyze current fluctuations in a molecular junction, we first need to be able to reliably describe the dynamics of such systems. It is our goal in this chapter, therefore, to introduce the master equation as a method for describing nanoscale quantum systems. The master equation is a remarkably powerful method for describing the dynamics of many-particle systems as it describes a wide variety of physical phenomena, including treating strongly correlated systems [82], and with it we will be able to calculate all fluctuation statistics of interest.

We will start this chapter not with the master equation itself, but rather an introduction to three important pictures of quantum mechanics. Once formulated, we will then outline why a typical wavefunction approach will fail in this system, and why the density matrix is required; this will include a discussion on the use of the density matrix, its properties, and operator averages. We then derive a general Redfield master equation describing the time-evolution of the density matrix for a general quantum subsystem between two electrodes. Following from this rigorous approach, which includes the populations and coherences, we will also outline Fermi's golden rule: a method that calculates transition rates between populations only, thus creating the less descriptive rate equation. Finally, we will derive the n-resolved master equation, which transforms the master and rate equation into a form suitable for generating fluctuation statistics.

2.2 Pictures of quantum mechanics

Our overriding goal for the configuration in Fig.(1.1) is to calculate averages for operators that exist in the nanoscale quantum subsystem only: $O(t) = O_Q(t) \otimes I_S \otimes I_D$, where the subscript Q denotes the nanoscale quantum subsystem and $I_\alpha = \sum_{\mathbf{k}_\alpha} |\mathbf{k}_\alpha\rangle\langle\mathbf{k}_\alpha|$ are the identity operators for each electrode. To do so, we will need a method for obtaining the state of the quantum subsystem at any time.

A natural starting point is the time-dependent wavefunction, $|\Psi(t)\rangle$, which describes the state of a general quantum system and evolves according to the Schrödinger equation [83]:

$$i\frac{\partial}{\partial t}|\Psi(t)\rangle = H(t)\,|\Psi(t)\rangle. \tag{2.1}$$

For a time-independent Hamiltonian, H, the Schrödinger equation has the solution

$$|\Psi(t)\rangle = e^{-iH(t-t_0)}|\Psi(t_0)\rangle. \tag{2.2}$$

With the wavefunction in hand, we can calculate quantum averages of any time-dependent observable $O(t)$,

$$\langle O(t)\rangle = \langle\Psi(t)|O(t)|\Psi(t)\rangle \tag{2.3}$$

$$= \langle\Psi(t_0)|e^{iH(t-t_0)}O(t)e^{-iH(t-t_0)}|\Psi(t_0)\rangle; \tag{2.4}$$

this formulation is the Schrödinger picture of quantum mechanics. The Heisenberg picture [84], in contrast, moves all time-dependence onto the operators,

$$O_H(t) = e^{iH(t-t_0)}O(t)e^{-iH(t-t_0)}, \tag{2.5}$$

while the wavefunction $|\Psi(t_0)\rangle$ remains stationary in time. Since both formulations yield the same result, both are equivalent pictures of quantum mechanics.

In general, however, the Hamiltonian is *not* time-independent; the trivial solution in Eq.(2.2) no longer applies and we cannot use the Schrödinger or Heisenberg pictures. We expect, instead, that the general solution will follow

$$|\Psi(t)\rangle = U(t,t_0)\,|\Psi(t_0)\rangle, \tag{2.6}$$

where $U(t,t_0)$ is a unitary operator that evolves the wavefunction from an initial time t_0 to some later time t, satisfying $U(t_0,t_0) = 1$.

One of the simplest ways to include time-dependence into the Hamiltonian, and one that includes the model we consider throughout the project, is via a time-dependent interaction:

$$H(t) = H_0 + H_T(t). \tag{2.7}$$

Here, the total Hamiltonian is deconstructed into a time-independent part, H_0, with known eigenvalues and eigenvectors satisfying $H_0|m_0\rangle = E_{m_0}|m_0\rangle$, and a time-dependent interaction $H_T(t)$.

For such Hamiltonians, the interaction picture [84] is an especially useful framework. Both

the wavefunction and the operators are now time-dependent:

$$|\Psi_I(t)\rangle = e^{iH_0(t)}|\Psi(t)\rangle \tag{2.8}$$

$$O_I(t) = e^{iH_0(t-t_0)}O(t)e^{-iH_0(t-t_0)}, \tag{2.9}$$

where the "I" subscript denotes the interaction picture. Differentiating Eq.(2.8), as shown in Appendix A, yields the time-evolution equation in the interaction picture,

$$i\frac{\partial}{\partial t}|\Psi_I(t)\rangle = H_{T,I}(t)|\Psi_I(t)\rangle, \tag{2.10}$$

implying that the wavefunction in the interaction picture has a solution analogous to Eq.(2.6):

$$\Psi_I(t)\rangle = S_I(t,t_0)|\Psi_I(t_0)\rangle. \tag{2.11}$$

Like $U(t,t_0)$, the unitary operator $S_I(t,t_0)$ evolves the wavefunction, now in the interaction picture, from $t_0 \to t$. Inserting Eq.(2.11) into Eq.(2.12) yields a differential equation for the time-evolution operator in the interaction picture

$$i\frac{\partial}{\partial t}S_I(t,t_0) = H_{T,I}(t)S_I(t,t_0), \tag{2.12}$$

which is solved according to the initial condition $S_I(t_0,t_0) = 1$. The equivalent integral equation is

$$S_I(t,t_0) = 1 + (-i)\int_{t_0}^{t} dt_1 H_{T,I}(t_1) + (-i)^2\int_{t_0}^{t} dt_1 H_{T,I}(t_1)\int_{t_0}^{t_1} dt_2 H_{T,I}(t_2) + \dots . \tag{2.13}$$

We cannot easily simplify this integral because interactions at different times do not commute: $[H_{T,I}(t_1), H_{T,I}(t_2)] \neq 0$. Instead, we can ease the notation via the introduction of the time-ordering operator $\tilde{T}$. If, for example, $t_1 > t_2$, then $\tilde{T}\left[H_{T,I}(t_1)H_{T,I}(t_2)\right] = H_{T,I}(t_1)H_{T,I}(t_2)$ and, conversely, if $t_1 < t_2$, then $\tilde{T}\left[H_{T,I}(t_1)H_{T,I}(t_2)\right] = H_{T,I}(t_2)H_{T,I}(t_1)$. After adjusting for overcounting from the time-ordering operator, the solution of the wavefunction in the interaction picture is

$$S_I(t,t_0) = \sum_{n=0}^{\infty}\frac{(-i)^n}{n!}\int_{t_0}^{t} dt_1 \dots \int_{t_0}^{t} dt_n\, \tilde{T}\left[H_{T,I}(t_1),\dots,H_{T,I}(t_n)\right] \tag{2.14}$$

$$= \tilde{T}\left[e^{-i\int_{t_0}^{t} dt_1\, H_{T,I}(t_1)}\right]. \tag{2.15}$$

The overall solution to the Schrödinger equation is now

$$|\Psi(t)\rangle = e^{-iH_0t}S_I(t,t_0)e^{iH_0t_0}|\Psi(t_0)\rangle, \tag{2.16}$$

so that the total time-evolution operator is $U(t,t_0) = e^{-iH_0t}S_I(t,t_0)e^{iH_0t_0}$.

The interaction picture is quite useful for us, because the molecular junction configuration we use easily fits into it. The time-independent part consists of the electrodes and quantum subsystem,

$$H_0 = H_S + H_D + H_Q, \tag{2.17}$$

which are initially uncoupled until the interaction H_T is turned on at $t = t_0$:

$$\left.\begin{aligned} H_T(t) = 0 \quad t < t_0 \\ H_T(t) = H_T \quad t \geq t_0 \end{aligned}\right\}.$$

Although we now have a formalism for finding the time-dependent solution to the Schrödinger equation in the interaction picture, and we have seen that the total Hamiltonian fits into this picture, we cannot use the wavefunction description for two key reasons. First, consider a total system containing two subsystems a and b; the total Hilbert space is a tensor product of the two sub-Hamiltonians, $H = H_a \otimes H_b$. The wavefunction describing the total system is, therefore, an entangled state $|\Psi(t)\rangle = |\Psi(\vec{\boldsymbol{a}}, \vec{\boldsymbol{b}}, t)\rangle$. Unfortunately, this implies we cannot obtain a reduced wavefunction *just* for subsystem a or b, unless the two subsystems are unentangled so that $|\Psi(t)\rangle = |\Psi_a(t)\rangle \otimes |\Psi_b(t)\rangle$. Since our configuration consists of a nanostructure coupled to two electrodes, we consequently cannot obtain the wavefunction for the quantum subsystem alone. Without this wavefunction, furthermore, we cannot calculate observable averages in the quantum subsystem: the main objective of this section.

The electrodes are also the source of the second problem. Since they are macroscopic and treated thermodynamically, the electrodes introduce a classical uncertainty into the system, reflecting our lack of knowledge about the exact state. The total wavefunction, as a result, is not a pure quantum state, described by $|\Psi(t)\rangle$, but rather can be in any number of pure states, $|\Psi_k(t)\rangle$, each with classical probability p_k: a mixed state. To resolve both of these issues, we turn to the density matrix.

2.3 The density matrix

The density matrix is

$$\rho(t) = \sum_k p_k \, |\Psi_k(t)\rangle\langle\Psi_k(t)|, \tag{2.18}$$

which defines a mixed state as an ensemble of pure quantum states $|\Psi_k(t)\rangle$, each weighted by probability p_k. Written in an appropriate orthonormal basis, the diagonal components, ρ_{ii}, reflect the probability for each population to be occupied, while off-diagonal components, $\rho_{ij} = \langle\Psi_i(t)|\rho|\Psi_j(t)\rangle$ where $i \neq j$, are coherences between these populations. The density

matrix has several nice properties; alongside being a Hermitian operator, it is normalized so that $\mathrm{Tr}[\rho(t)] = 1$. Since it incorporates mixed states, the density matrix can also accommodate the classical uncertainty in the baths, and so does not fall prey to the second failure of the wavefunction we highlighted at the end of the previous section.

To obtain the time-evolution of the density matrix, we differentiate Eq.(2.18) and apply the Schrödinger equation:

$$i\frac{d\rho}{dt} = [H(t), \rho(t)], \tag{2.19}$$

which is the famous Liouville-von Neumann equation [85]. Using the unitary time-evolution operator $U(t, t_0)$, the general solution of Eq.(2.19) is

$$\rho(t) = \sum_k p_k \, U(t, t_0)|\Psi_k(t_0)\rangle\langle\Psi_k(t_0)|U^\dagger(t, t_0). \tag{2.20}$$

Immediate among the benefits of using the density matrix is its efficient definition of quantum averages. Using a suitable orthonormal basis, $\{|i\rangle\}$, the trace operator is $\mathrm{Tr}[O(t)] = \sum_i \langle i|O(t)|i\rangle$ and

$$\begin{aligned}
\mathrm{Tr}[\rho(t)O(t)] &= \sum_{ik} p_k \langle i|\Psi_k(t)\rangle\langle\Psi_k(t)|O(t)|i\rangle \\
&= \sum_{ik} p_k \delta_{ik} \langle\Psi_k(t)|O(t)|i\rangle \\
&= \sum_k p_k \langle\Psi_k(t)|O(t)|\Psi_k(t)\rangle \\
&= \langle O(t)\rangle.
\end{aligned} \tag{2.21}$$

Eq.(2.21) shows that, unlike the wavefunction, the density matrix naturally calculates observable averages over a statistical ensemble. Furthermore, by tracing out the bath degrees of freedom, we can also generate a reduced density matrix $\rho_Q(t)$ for the quantum subsystem only, $\rho_Q(t) = \mathrm{Tr}_B[\rho_T(t)]$, which resolves the first key failure of the wavefunction approach. We can now calculate averages for operators in the quantum system subspace only:

$$\langle O_Q(t)\rangle = \mathrm{Tr}_Q[\rho_Q(t)O_Q(t)], \tag{2.22}$$

where the trace is over an appropriate quantum subsystem basis .

From this point our goal is to calculate the reduced density matrix for the quantum system, which of course means we need to solve the Liouville-von Neumann equation of motion. We note that from here we will refer to three distinct density matrices: the density matrix of the total system-electrode configuration ρ_T, the reduced density matrix of the baths ρ_B, and the reduced density matrix of the quantum subsystem ρ.

In the following subsections, we will re-derive the Redfield master equation [86] and Fermi's golden rule [87]: two famous and oft-used approaches in condensed matter physics. Although the results are not novel, this section serves as a reference point for the notation we use throughout the rest of the project.

2.4 The master equation

In deriving the Redfield master equation, we will generally follow the approach of Breuer [88]. By writing the Liouville-von Neumann equation for $\rho_T(t)$,

$$i\frac{d\rho_T}{dt} = [H(t), \rho_T(t)], \tag{2.23}$$

and then tracing out the bath degrees of freedom, we obtain a time-evolution equation for the reduced system density matrix:

$$i\frac{d\rho}{dt} = \mathrm{Tr}_B\left([H(t), \rho(t)]\right). \tag{2.24}$$

Before proceeding, however, we will move to the interaction picture and reformat Eq.(2.23). Since the interaction switches on at $t = 0$, before this point the quantum subsystem is uncoupled from the source and the drain and Eq.(2.24) is solved according to the initial condition

$$\rho_T(0) = \rho(0) \otimes \rho_S \otimes \rho_D. \tag{2.25}$$

In the interaction picture, the differential form of the Liouville-von Neumann equation is

$$i\frac{d\rho_I}{dt} = \mathrm{Tr}_B\left([H_{T,I}(t), \rho_{T,I}(t)]\right), \tag{2.26}$$

while its equivalent integral equation is

$$\rho_I(t) = \rho_I(0) - i\int_0^t dt_1\, \mathrm{Tr}_B\left[H_{T,I}(t_1), \left(\rho_{T,I}(0) - i\int_0^{t_1} dt_2\, [H_{T,I}(t_2), \rho_{T,I}(t_2)]\right)\right], \tag{2.27}$$

where here and onwards we choose $t_0 = 0$. Crucially, we have only applied the expansion twice, implying that there are some constraints on $H_{T,I}(t)$, which we will discuss under the Born approximation. In actuality, the recursion in Eq.(2.27) can be continued infinitely, similarly to Eq.(2.16). Next, we differentiate and apply relative time $\tau = t - t_2$:

$$\dot{\rho}_I(t) = -\int_0^t d\tau\, \mathrm{Tr}_B\left[H_{T,I}(t), [H_{T,I}(t-\tau)\rho_{T,I}(t-\tau)]\right], \tag{2.28}$$

also using the fact that our interaction Hamiltonian H_T does not have any diagonal components so that $\mathrm{Tr}_B\left[H_{T,I}(t), \rho_{T,I}(0)\right] = 0$.

At this point, we need to assume that the coupling between the quantum subsystem and the electrodes is weak: the Born approximation. Considering the macroscopic size of the baths, this means that they remain unaffected by transport through the quantum subsystem and can be treated as if they are in local equilibrium. The electrode density matrices, therefore, evolve independently of the quantum subsystem and we can write $\rho_{T,I}(t) \approx \rho_I(t) \otimes \rho_S \otimes \rho_D$. The Born approximation also provides justification for cutting off the expansion in Eq.(2.27); if $H_{T,I}(t)$ is weak then it can be treated as a perturbation and we can end the expansion after the first non-zero term.

For brevity, we are also going to rewrite the interaction Hamiltonian as

$$\begin{aligned} H_T &= \sum_{\alpha=S,D} \sum_{q,\mathbf{k}_\alpha} t_{\mathbf{k}_\alpha,q}(a^\dagger_{\mathbf{k}_\alpha} a_q + a^\dagger_q a_{\mathbf{k}_\alpha}) \\ &= \sum_q a^\dagger_q d - a_q d^\dagger, \end{aligned} \tag{2.29}$$

where we have introduced the bath operators

$$\begin{aligned} d^\dagger &= \sum_\alpha d^\dagger_\alpha && \text{and} && d &= \sum_\alpha d_\alpha \\ &= \sum_\alpha \sum_{\mathbf{k}_\alpha} t_{\mathbf{k}_\alpha} a^\dagger_{\mathbf{k}_\alpha} && && &= \sum_\alpha \sum_{\mathbf{k}_\alpha} t_{\mathbf{k}_\alpha} a_{\mathbf{k}_\alpha}, \end{aligned} \tag{2.30}$$

and included a negative in the second term because fermionic operators anti-commute. With these changes, and writing $\rho_I(t) \otimes \rho_S \otimes \rho_D = \rho_I(t)\rho_B$ for notational ease, Eq.(2.28) becomes

$$\begin{aligned} \dot\rho_I(t) = -\int_0^t d\tau \sum_{qq'} \mathrm{Tr}_B \Big[& a^\dagger_{q,I}(t) d_I(t) - a_{q,I}(t) d^\dagger_I(t), \\ & \Big[a^\dagger_{q',I}(t-\tau) d_I(t-\tau) - a_{q',I}(t-\tau) d^\dagger_I(t-\tau), \rho_I(t-\tau)\rho_B \Big] \Big]. \end{aligned} \tag{2.31}$$

We are faced now with a long expansion; it is helped, however, by noticing that any terms containing two bath annihilation operators dd or two bath creation operators $d^\dagger d^\dagger$ will disappear under the bath trace, since fermions obey the Pauli exclusion principle:

$$\begin{aligned} \dot\rho_I(t) = \int_0^t d\tau \sum_{qq'} \mathrm{Tr}_B \Big(& a^\dagger_{q,I}(t) d_I(t) a_{q',I}(t-\tau) d^\dagger_I(t-\tau) \rho_I(t-\tau)\rho_B \\ & + a_{q,I}(t) d^\dagger_I(t) a^\dagger_{q',I}(t-\tau) d_I(t-\tau) \rho_I(t-\tau)\rho_B - a^\dagger_{q,I}(t) d_I(t) \rho_I(t-\tau)\rho_B a_{q',I}(t-\tau) d^\dagger_I(t-\tau) \\ & - a_{q,I}(t) d^\dagger_I(t) \rho_I(t-\tau)\rho_B a^\dagger_{q',I}(t-\tau) d_I(t-\tau) - a^\dagger_{q',I}(t-\tau) d_I(t-\tau) \rho_I(t-\tau)\rho_B a_{q,I}(t) d^\dagger_I(t) \\ & - a_{q',I}(t-\tau) d^\dagger_I(t-\tau) \rho_I(t-\tau)\rho_B a^\dagger_{q,I}(t) d_I(t) + \rho_I(t-\tau)\rho_B a^\dagger_{q',I}(t-\tau) d_I(t-\tau) a_{q,I}(t) d^\dagger_I(t) \\ & + \rho_I(t-\tau)\rho_B a_{q',I}(t-\tau) d^\dagger_I(t-\tau) a^\dagger_{q,I}(t) d_I(t) \Big). \end{aligned} \tag{2.32}$$

If we switch the positions of system and bath operators in each term, again adding a negative from fermionic anti-commutation, then all bath operators will be together and we can apply

the trace, which we express as bath-correlation functions:

$$\begin{aligned} G^{>}(\tau) &= \mathrm{Tr}_B\left(\rho_B d_I(t) d_I^\dagger(t-\tau)\right) & G^{<}(\tau) &= \mathrm{Tr}_B\left(\rho_B d_I^\dagger(t) d_I(t-\tau)\right) \\ G^{>}(-\tau) &= \mathrm{Tr}_B\left(d_I^\dagger(t)\rho_B d_I(t-\tau)\right) & G^{<}(-\tau) &= \mathrm{Tr}_B\left(d_I(t)\rho_B d_I^\dagger(t-\tau)\right) \\ &= \mathrm{Tr}_B\left(\rho_B d_I(t-\tau) d_I^\dagger(t)\right) & &= \mathrm{Tr}_B\left(\rho_B d_I^\dagger(t-\tau) d_I(t)\right) \\ &= \mathrm{Tr}_B\left(\rho_B d_I(t) d_I^\dagger(t+\tau)\right) & &= \mathrm{Tr}_B\left(\rho_B d_I^\dagger(t) d_I(t+\tau)\right). \end{aligned} \tag{2.33}$$

The last four terms of Eq.(2.32) are clearly the hermitian conjugate of the first four, and the total master equation is

$$\begin{aligned} \dot\rho_I(t) = -\sum_{qq'}\int_0^t d\tau\, \mathrm{Tr}_B\Big(&G^{>}(\tau) a_{q,I}^\dagger(t) a_{q',I}(t-\tau)\rho_I(t-\tau) + G^{<}(\tau) a_{q,I}(t) a_{q',I}^\dagger(t-\tau)\rho_I(t-\tau) \\ &- G^{<}(-\tau) a_{q,I}^\dagger(t)\rho_I(t-\tau) a_{q',I}(t-\tau) - G^{>}(-\tau) a_{q,I}(t)\rho_I(t-\tau) a_{q',I}^\dagger(t-\tau) + \text{h.c.}\Big). \end{aligned} \tag{2.34}$$

We come now to the second key assumption: that the baths are Markovian. We first assume that correlations in the baths decay rapidly after some correlation time τ_c, so that $G^{<,>}(\tau) \to 0$ for $\tau > \tau_c$. If the characteristic time of the system t is much greater than τ_c, then the baths are effectively memoryless; the density matrix of the system will not change much in time τ, $\rho_I(t-\tau) \approx \rho_I(t)$, and the upper limit of integration in Eq.(2.34) can be considered infinite:

$$\begin{aligned} \dot\rho_I(t) = -\sum_{qq'}\int_0^\infty d\tau\, \Big(&G^{>}(\tau) a_{q,I}^\dagger(t) a_{q',I}(t-\tau)\rho_I(t) + G^{<}(\tau) a_{q,I}(t) a_{q',I}^\dagger(t-\tau)\rho_I(t) \\ &- G^{<}(-\tau) a_{q,I}^\dagger(t)\rho_I(t) a_{q',I}(t-\tau) - G^{>}(-\tau) a_{q,I}(t)\rho_I(t) a_{q',I}^\dagger(t-\tau) + \text{h.c.}\Big). \end{aligned} \tag{2.35}$$

Proceeding from here, we need to explicitly apply the interaction picture. Using the time-derivative of a general operator in the interaction picture, defined in Appendix A, the master equation becomes

$$\begin{aligned} i\dot\rho(t) = [H_Q, \rho(t)] - i\sum_{qq'}\int_0^\infty d\tau\, \Big(&G^{>}(\tau) a_q^\dagger e^{-iH_Q\tau} a_{q'} e^{iH_Q\tau}\rho(t) + G^{<}(-\tau) a_q e^{iH_Q\tau} a_{q'}^\dagger e^{iH_Q\tau}\rho(t) \\ &- G^{<}(\tau) a_q^\dagger \rho(t) e^{-iH_Q\tau} a_{q'} e^{iH_Q\tau} - G^{>}(-\tau) a_q \rho(t) e^{-iH_Q\tau} a_{q'}^\dagger e^{iH_Q\tau} + \text{h.c.}\Big) \end{aligned} \tag{2.36}$$

To simplify further from Eq.(2.36), we need to evaluate the bath-correlation functions, which is shown explicitly in Appendix B.1. In short, they can be expressed in terms of lesser $\Sigma^{<}(\tau)$

and greater $\Sigma^{>}(\tau)$ self-energies, also defined in Appendix B.1:

$$i\dot{\rho}(t) = [H_Q, \rho(t)] + \sum_q \int_0^\infty d\tau \Big(\Sigma^{>}(\tau) a_q^\dagger e^{-iH_Q\tau} a_{q'} e^{iH_Q\tau} \rho(t) - \Sigma^{<}(-\tau) a_q e^{iH_Q\tau} a_{q'}^\dagger e^{iH_Q\tau} \rho(t) + \Sigma^{<}(\tau) a_q^\dagger \rho(t) e^{-iH_Q\tau} a_{q'} e^{iH_Q\tau} - \Sigma^{>}(-\tau) a_q \rho(t) e^{-iH_Q\tau} a_{q'}^\dagger e^{iH_Q\tau} - \text{h.c.} \Big). \tag{2.37}$$

Eq.(2.37) is a general master equation for the density matrix of the quantum subsystem $\rho(t)$. It contains a part detailing the coherent time-evolution due to the Hamiltonian of the quantum subsystem, $[H_Q, \rho(t)]$, and a part detailing the time-evolution due to dissipative interactions with the electrodes. In practice, we will calculate the time-evolution of each element, written in the basis of eigenstates of H_Q: $\rho_{mn} = \langle m|\rho|n\rangle$. Applying these basis vectors, and also inserting the identity operator of the quantum subsystem, we get

$$\begin{aligned} i\dot{\rho}_{mn} = (E_m - E_n)\rho_{mn} + \sum_{qq'} \sum_{kl} \int_0^\infty d\tau \Big(& \Sigma^{>}(\tau) \langle m|a_q^\dagger|k\rangle \langle k|e^{-iH_Q\tau} a_{q'} e^{iH_Q\tau}|l\rangle \rho_{ln} \\ & - \Sigma^{<}(-\tau) \langle m|a_q|k\rangle \langle k|e^{-iH_Q\tau} a_{q'}^\dagger e^{iH_Q\tau}|l\rangle \rho_{ln} + \Sigma^{<}(\tau) \langle m|a_q^\dagger|k\rangle \rho_{kl} \langle l|e^{-iH_Q\tau} a_{q'} e^{iH_Q\tau}|n\rangle \\ & - \Sigma^{>}(-\tau) \langle m|a_q|k\rangle \rho_{kl} \langle l|e^{-iH_Q\tau} a_{q'}^\dagger e^{iH_Q\tau}|n\rangle - (m \leftrightarrow n)^* \Big). \end{aligned} \tag{2.38}$$

The final step is to introduce the energy separation between eigenstates, $\omega_{mn} = E_m - E_n$, and perform the time-integral:

$$\begin{aligned} i\dot{\rho_{mn}} = \omega_{mn}\rho_{mn} + \sum_q \sum_{kl} \Big(& \Sigma^{>}(\omega_{lk}) \langle m|a_q^\dagger|k\rangle \langle k|a_q|l\rangle \rho_{ln} + \Sigma^{<}(\omega_{kl})^* \langle m|a_q|k\rangle \langle k|a_{q'}^\dagger|l\rangle \rho_{ln} \\ & + \Sigma^{<}(\omega_{nl}) \langle m|a_q^\dagger|k\rangle \rho_{kl} \langle l|a_q|n\rangle + \Sigma^{>}(\omega_{ln})^* \langle m|a_q|k\rangle \rho_{kl} \langle l|a_{q'}^\dagger|n\rangle - (m \leftrightarrow n)^* \Big). \end{aligned} \tag{2.39}$$

Note that, in doing so, we have made the rotating wave approximation and removed all those terms for which $q \neq q'$.

We have provided an explicit calculation of the frequency-dependent self-energies in Appendix B.2. As a short summary, the lesser and greater self-energies of electrode α are

$$\Sigma_\alpha^{<}(\omega) = \Delta_\alpha^{<}(\omega) + \frac{i}{2}\gamma^\alpha(\omega) n_F(\omega - \mu_\alpha) \tag{2.40}$$

$$\Sigma_\alpha^{>}(\omega) = -\Delta_\alpha^{>}(\omega) - \frac{i}{2}\gamma^\alpha(\omega)[1 - n_F(\omega - \mu_\alpha)], \tag{2.41}$$

with real components given by the Lamb shift,

$$\Delta_\alpha^{<}(\omega) = \lim_{\eta \to 0^+} \sum_{\mathbf{k}_\alpha} \frac{|t_{\mathbf{k}_\alpha, q}|^2 (\varepsilon_{\mathbf{k}_\alpha} - \omega) n_F(\omega - \mu_\alpha)}{(\omega - \varepsilon_{\mathbf{k}_\alpha})^2 + \eta^2} \tag{2.42}$$

$$\Delta_\alpha^{>}(\omega) = \lim_{\eta \to 0^+} \sum_{\mathbf{k}_\alpha} \frac{|t_{\mathbf{k}_\alpha, q}|^2 (\varepsilon_{\mathbf{k}_\alpha} - \omega)[1 - n_F(\omega - \mu_\alpha)]}{(\omega - \varepsilon_{\mathbf{k}_\alpha})^2 + \eta^2}, \tag{2.43}$$

and imaginary components given by the electrode-system coupling strength,

$$\gamma^{\alpha}(\omega) = 2\pi|t_{\omega}|^2\rho_{\alpha}(\omega). \tag{2.44}$$

The Lamb shift is so-called because it renormalizes the energies of the isolated quantum subsystem due to interaction with the electrodes [88]. The imaginary component, meanwhile, broadens these energy levels. At all points throughout the project, we apply the wide-band limit and assume that, within the conduction band of electrode α, the density of states $\rho_{\alpha}(\omega)$ and therefore the tunnel coupling $t_{\mathbf{k}_{\alpha},q}$ is constant: $\gamma^{\alpha}(\omega) = \gamma^{\alpha}$.

We now have all the tools required to generate the master equation of a general quantum system weakly coupled to two macroscopic metal electrodes.

2.5 The rate equation

Although the Redfield equation rigorously describes the time-evolution of a molecular junction, in many cases it is necessary to simplify the full master equation by ignoring all coherence terms in the density matrix, which lie off the diagonal: $\rho_{mn} = 0$ for $m \neq n$. In this case, we are left with the probabilities for the system to be in any of the molecular eigenstates. To highlight this point, from here we will use notation that expresses the diagonal components as probabilities: $\rho_{nn}(t) = P_n(t)$. After removing the coherences, the remaining components of the master equation, Γ_{nm}, are physically interpreted as the transition rate from pure state $|m\rangle$ to pure state $|n\rangle$. The master equation is now better labeled as a *rate* equation [89–92], with each diagonal element following the 1$^{\text{st}}$-order differential equation:

$$\dot{P}_n(t) = \sum_m \Gamma_{nm}P_m(t) - \Gamma_{mn}P_n(t). \tag{2.45}$$

Although, in principle, we could use the full Redfield master equation and merely cut out the off-diagonal terms, there is a simpler method for deriving transition rates between eigenstates of quantum many-body systems: the T-matrix approach and Fermi's golden rule.

2.5.1 Fermi's golden rule

In this subsection, we will briefly summarize the method outlined by Bruus and Flensberg [84], Timm [93], and Merzbacher [94]. First, the Hamiltonian is reformulated in the interaction picture as

$$H(t) = H_S + H_D + H_Q + H_T e^{\eta t}, \tag{2.46}$$

where again we have a time-independent part $H_0 = H_S + H_D + H_Q$ and a perturbation $H_T(t) = H_T e^{\eta t}$. The time factor $e^{\eta t}$ ensures that the perturbation is turned on adiabatically at

some point in the distant past by assuming that $\eta \to 0^+$ and $t_0 \to -\infty$. It is important that the turning on time, which is of order $\mathcal{O}(\eta^{-1})$, is much shorter than the separation between turning the perturbation on and the time t we are interested in: $t - t_0 \gg \eta^{-1}$. The limit $t_0 \to -\infty$ must therefore be taken *before* $\eta \to 0^+$.

Our goal now is to calculate the transition rate Γ_{fi} from an initial state $|i\rangle$ to a final $|f\rangle$ state, where $|i\rangle$ and $|f\rangle$ are eigenstates of the unperturbed Hamiltonian. Given that the system started in state $|i\rangle$ at time t_0, the probability $P_f(t)$ that at time t it is in state $|f\rangle$ is the square of the magnitude of the overlap between $|f\rangle$ and the time-evolved initial state $|i(t)\rangle$. From Eq.(2.16), we have

$$|i(t)\rangle = e^{-iH_0 t} S_I(t, t_0) e^{iH_0 t_0} |i(t_0)\rangle, \tag{2.47}$$

which to 1st-order in H_T is

$$|i(t)\rangle = e^{-iH_0 t} \left[1 - i \int_{t_0}^{t} dt_1 e^{iH_0 t_1} H_T e^{\eta t_1} e^{-iH_0 t_1}\right] e^{iH_0 t_0} |i(t_0)\rangle. \tag{2.48}$$

After applying $\langle f|$ and taking the appropriate limits, the overlap is

$$\begin{aligned}
\langle f|i(t)\rangle &= \lim_{\eta\to 0^+} \lim_{t_0 \to -\infty} \langle f| e^{-iH_0 t} \left[1 - i \int_{t_0}^{t} dt_1 e^{iH_0 t_1} H_T e^{\eta t_1} e^{-iH_0 t_1}\right] e^{iH_0 t_0} |i(t_0)\rangle \\
&= -i \lim_{\eta\to 0^+} \lim_{t_0 \to -\infty} \langle f| \int_{t_0}^{t} dt_1 \left[e^{iH_0 t_1} H_T e^{\eta t_1} e^{-iH_0 t_1}\right] |i\rangle e^{-iE_f t} e^{iE_i t_0} \\
&= -i \lim_{\eta\to 0^+} \lim_{t_0 \to -\infty} e^{-iE_f t} e^{iE_i t_0} \langle f|H_T|i\rangle \int_{t_0}^{t} dt_1 \left[e^{iE_f t_1} e^{\eta t_1} e^{-iE_i t_1}\right] \\
&= -i \lim_{\eta\to 0^+} \lim_{t_0 \to -\infty} e^{-iE_f t} e^{iE_i t_0} \langle f|H_T|i\rangle \frac{1}{-i\left(E_i + i\eta - E_f\right)} \left[e^{-i(E_i + i\eta - E_f)t} - e^{-i(E_i + i\eta - E_f)t_0}\right].
\end{aligned} \tag{2.49}$$

The limit $t_0 \to -\infty$ eliminates the exponential term in the brackets, but does not affect the oscillatory prefactor:

$$\langle f|i(t)\rangle = -\langle f|H_T|i\rangle \lim_{\eta\to 0^+} \lim_{t_0 \to -\infty} \frac{e^{-iE_i(t-t_0)} e^{\eta t}}{\left(E_f - E_i - i\eta\right)}. \tag{2.50}$$

Consequently, the probability $P_f(t)$ is

$$P_f(t) = |\langle f|i(t)|^2 \tag{2.51}$$

$$= |\langle f|H_T|i\rangle|^2 \lim_{\eta\to 0^+} \frac{e^{2\eta t}}{(E_f - E_i)^2 + \eta^2}. \tag{2.52}$$

Taking the time-derivative of Eq.(2.52), we get the transition rate

$$\begin{aligned}\Gamma_{if} &= \frac{d}{dt}|\langle f|i(t)|^2 \\ &= 2|\langle f|H_T|i\rangle|^2 \lim_{\eta\to 0^+} \frac{\eta e^{2\eta t}}{(E_f - E_i)^2 + \eta^2} \\ &= 2\pi|\langle f|H_T|i\rangle|^2 \delta(E_f - E_i),\end{aligned} \tag{2.53}$$

using the definition of the delta function highlighted in Eq.(B.11). The transition rate in Eq.(2.53) is known as Fermi's golden rule. While useful, it neglects all contributions from higher-order interaction terms.

Going to 2nd-order in the transition rates requires a different form for the time-dependent perturbation $H_T(t) = H_T g(t)$. In the 1st-order approach, the exponential term $e^{\eta t}$ was introduced to ensure that the perturbation turned on adiabatically at some time in the distant past. For 2nd-order processes there can be multiple scatterings from the perturbation and, in order to again separate the turning on time and the interaction time, we must choose the functional form $g(t) = (1 + \exp[-\eta(t - t_0)])^{-1}$.

Combining these changes with Eq.(2.16), we find that the 2nd-order contribution to the overlap is

$$\langle f|i(t)\rangle = -\lim_{\eta\to 0^+}\lim_{t_0\to-\infty}\langle f|\int_{t_0}^{t} dt_1 H_{T,I}(t_1)g(t_1)\int_{t_0}^{t_1} dt_2 H_{T,I}(t_2)g(t_2)|i\rangle e^{-iE_f t}e^{iE_i t_0}. \tag{2.54}$$

If the perturbation is turned on between $[t_0, t_2]$, then it must also be on in $[t_1, t]$, as $t_1 > t_2$. Therefore, $g(t_1)$ may be replaced with unity and, since there is only one interaction to now turn on, $g(t_2)$ can be replaced with $e^{\eta t_2}$:

$$\begin{aligned}\langle f|i(t)\rangle &= -\lim_{\eta\to 0^+}\lim_{t_0\to-\infty}\langle f|\int_{t_0}^{t} dt_1 \int_{t_0}^{t_1} t_2 H_{T,I}(t_1)H_{T,I}(t_2)e^{\eta t_2}|i\rangle e^{-iE_f t}e^{iE_i t_0} \\ &= -\lim_{\eta\to 0^+}\lim_{t_0\to-\infty} e^{-iE_f t}e^{iE_i t_0}\left[\langle f|\int_{t_0}^{t} dt_1 \int_{t_0}^{t_1} dt_2\, e^{iH_0 t_1}H_T e^{-iH_0(t_1-t_2)}H_T e^{-i(H_0+i\eta)t_2}|i\rangle\right] \\ &= -\lim_{\eta\to 0^+}\lim_{t_0\to-\infty} e^{-iE_f t}e^{iE_i t_0}\left[\langle f|\int_{t_0}^{t} dt_1\, e^{iE_f t_1}H_T e^{-iH_0 t_1}\int_{t_0}^{t_1} dt_2\, e^{-i(E_i - H_0 + i\eta)t_2}H_T|i\rangle\right]\end{aligned} \tag{2.55}$$

At this point, all we have done is written the perturbation H_T explicitly in the interaction picture and collected appropriate terms under the integrals. Next, we evaluate the second integral and note that, as in Eq.(2.49), under the limit $t_0 \to -\infty$ the $e^{\eta t_0}$ term disappears:

$$\langle f|i(t)\rangle = -\lim_{\eta\to 0^+}\lim_{t_0\to-\infty} e^{-iE_f t}e^{iE_i t_0}\langle f|\int_{t_0}^{t} dt_1 e^{iE_f t_1}H_T e^{-iH_0 t_1}\frac{1}{-i(E_i - H_0 + i\eta)}e^{-i(E_i - H_0 + i\eta)t_1}H_T|i\rangle. \tag{2.56}$$

Since H_0 commutes with itself, we can bring Eq.(2.56) into a suitable form to evaluate the

remaining integral,

$$\begin{aligned}\langle f|i(t)\rangle &= -i\lim_{\eta\to 0^+}\lim_{t_0\to-\infty} e^{-iE_f t}e^{iE_i t_0}\langle f|\int_{t_0}^{t} dt_1 H_T \frac{1}{(E_i - H_0 + i\eta)} e^{-i(E_i-E_f+i\eta)t_1} H_T|i\rangle \\ &= \lim_{\eta\to 0^+}\lim_{t_0\to-\infty} \frac{e^{-iE_i(t-t_0)}e^{\eta t}}{(E_i - E_f + i\eta)}\langle f|H_T\frac{1}{E_i - H_0 + i\eta}H_T|i\rangle, \end{aligned} \tag{2.57}$$

and the square of the overlap is

$$P_F(t) = \lim_{\eta\to 0}\frac{e^{2\eta t}}{(E_i - E_f)^2 + \eta^2}\left|\langle f|H_T\frac{1}{E_i - H_0 + i\eta}H_T|i\rangle\right|^2. \tag{2.58}$$

Finally, the time-derivative yields the 2$^{\text{nd}}$-order contribution to the transition rate:

$$\Gamma_{fi} = 2\lim_{\eta\to 0^+}\frac{\eta e^{2\eta t}}{(E_i - E_f)^2 + \eta^2}\left|\langle f|H_T\frac{1}{E_i - H_0 + i\eta}H_T|i\rangle\right|^2 \tag{2.59}$$

$$= 2\pi\lim_{\eta\to 0^+}\left|\langle f|H_T\frac{1}{E_i - H_0 + i\eta}H_T|i\rangle\right|^2\delta(E_i - E_f). \tag{2.60}$$

This technique can be extended up to all higher-order contributions from $S_I(t,t_0)$, which is known as Fermi's generalized golden rule:

$$\Gamma_{fi} = 2\pi\lim_{\eta\to 0^+}|\langle f|T|i\rangle|^2\,\delta(E_i - E_f), \tag{2.61}$$

where the T-matrix is

$$T = H_T + H_T\frac{1}{E_i - H_0 + i\eta}H_T + H_T\frac{1}{E_i - H_0 + i\eta}H_T\frac{1}{E_i - H_0 + i\eta}H_T + \dots. \tag{2.62}$$

The leading term in Eq.(2.62) yields *sequential tunneling* transport; the resulting transition rates are 1$^{\text{st}}$-order in γ and 2$^{\text{nd}}$-order in H_T. These terms are what we would get if we only included diagonal components from the master equation in Eq.(2.39), as one of the key components in deriving the Redfield master equation was the linear truncation in Eq.(2.27). Since sequential tunnelings involve only one scattering off the perturbation, they involve only one transition between either electrode and the quantum subsystem; they are essentially classical processes.

If we include the next-to-leading-order T-matrix contribution, we would add in a layer of *co-tunneling* processes; these transition rates are 2$^{\text{nd}}$-order in γ and 4$^{\text{th}}$-order in H_T. Cotunneling involves two scatterings off the perturbation, so an electron may transition from one electrode to the quantum subsystem and then out to the other electrode within the same process: this is a purely quantum phenomenon. As we will see in Chapter 4, going to 2$^{\text{nd}}$-order in Fermi's golden rule is non-trivial, but unfolding the full rigorous master equation one step further [95] is so difficult that it is rarely used.

2.5.2 Fermi's golden rule for many-body systems

Although we were motivated to understand Fermi's golden rule because the total Hamiltonian of the molecular junction so neatly splits into the definition of the interaction picture, the transition rate defined by Eq.(2.61) is completely general for any Hamiltonian with some time-independent part and a time-dependent interaction. The goal for this subsection, then, is to bring Eq.(2.61) into a form that more reflects the nature of our electrode-system-electrode configuration.

In the many-body configuration of the full Fock space, the initial and final states are tensor products of eigenstates of H_Q and eigenstates of H_S and H_D: $|i\rangle = |m\rangle \otimes |i_S\rangle \otimes |i_D\rangle = |m\rangle |i_S\rangle |i_D\rangle$ and$|f\rangle = |n\rangle \otimes |f_S\rangle \otimes |f_D\rangle = |n\rangle |f_S\rangle |f_D\rangle$, with eigenenergies $E_i = E_m + \varepsilon_{i_s} + \varepsilon_{i_d}$ and $E_f = E_n + \varepsilon_{f_s} + \varepsilon_{f_d}$, respectively. There are, as a result, multiple initial and final states that correspond to a particular eigenstate of H_Q; they must be summed over and the initial states weighted with a thermal distribution function $W^S_{i_m} W^D_{i_m}$:

$$\Gamma_{nm} = 2\pi \lim_{\eta \to 0^+} \sum_{\alpha} \sum_{f_\alpha, i_\alpha} |\langle f_D|\langle f_S|\langle n|T|m\rangle|i_S\rangle|i_D\rangle|^2 W^S_{i_m} W^D_{i_m} \delta(E_m - E_n + \varepsilon_{i_S} - \varepsilon_{f_S} + \varepsilon_{i_D} - \varepsilon_{f_D}), \tag{2.63}$$

where the T-matrix is now

$$T = H_T + H_T \frac{1}{E_i - H_0 + i\eta} H_T + H_T \frac{1}{E_i - H_0 + i\eta} H_T \frac{1}{E_i - H_0 + i\eta} H_T + \dots . \tag{2.64}$$

In calculating Fermi's golden rule, we have implicitly applied the Born-Markov approximation. The thermal distribution functions $W^\alpha_{i_m}$ are inserted with no dependence on the state of the quantum subsystem, which is equivalent to assuming the Born assumption: $\rho_T = \rho \otimes \rho_B$. Additionally, since we are considering the probability that the system is in state f at time t, given that it was in state i at time t_0, we have implicitly assumed that P_m does not change in the interval, which was a key part of the Markovian assumption: $\rho(t - t_0) \approx \rho(t)$.

2.6 Superoperator form

In practice, we will not actually work with $\rho(t)$ as an $N \times N$ density *matrix*; instead we will unfold it to a vector $\mathbf{P}(t)$ of length N^2. This is merely a way of writing a two-dimensional array in a computationally accessible manner. This vector will always take the form

$$\mathbf{P}(t) = [\underbrace{P_1(t), \dots, P_n(t), \dots, P_N(t)}_{\text{Populations}} \Big| \underbrace{\rho_{12}(t), \dots, \rho_{mn}(t), \dots, \rho_{N,N-1}(t)}_{\text{Coherences}}]^T, \tag{2.65}$$

where the indices simply refer to the different eigenstates of H_Q. For the rate equation we will evidently keep only the first N terms, the population probabilities, while the coherences will be included for the full master equation. The unfolding in Eq.(2.65) also transforms the definition of the trace:

$$\mathrm{Tr}\,(\rho) = (\mathbf{I}, \mathbf{P})\,, \tag{2.66}$$

where the round brackets denote an inner product and $\mathbf{I} = [1, 1, \ldots, 1, 0, 0, \ldots, 0]$ is a row vector in which the first N elements are unity and the last $N(N-1)$ elements are zero.

Since each element of the density matrix obeys a 1^{st}-order differential equation, the unfolding in Eq.(2.65) also allows us to collect all dynamics into one "superoperator" $\mathbf{L}$: the Liouvillian. Both the master and rate equation, then, have the general form

$$\dot{\mathbf{P}}(t) = \mathbf{L}\mathbf{P}(t), \tag{2.67}$$

where $\mathbf{L}$ is time-independent under the Markovian assumption. We assume that Eq.(2.67) has a unique stationary solution, steady state $\bar{\mathbf{P}}$, which is a null vector satisfying $\mathbf{L}\bar{\mathbf{P}} = 0$. In general, Eq.(2.67) has the solution

$$\mathbf{P}(t) = e^{\mathbf{L}t}\mathbf{P}(0), \tag{2.68}$$

where $\mathbf{P}(0)$ is the state of the initial system at $t = 0$. We always start measurement in the stationary state, so $\mathbf{P}(0) = \bar{\mathbf{P}}$.

If we are able to obtain the Liouvillian $\mathbf{L}$ and apply the solution in Eq.(2.68), then we can, in principle, calculate any time-dependent quantum averages of any observable: for example, the electric current $\langle I \rangle$. In connecting the dynamics to the fluctuation statistics, however, it is much more natural to use the n-resolved master equation instead.

2.6.1 n-resolved master equation

As opposed to Eq.(2.67), which we refer to as the *standard* master equation to avoid confusion, the n-resolved master equation resolves the transport upon the total number of particles n transferred to the drain in the interval $[0, t]$ [96]:

$$\dot{\mathbf{P}}(n, t) = \sum_{n'} \mathbf{L}(n - n')\mathbf{P}(n, t). \tag{2.69}$$

For populations, $[\mathbf{P}(n, t)]_k$ is the probability that the system is in state k at time t and n total particles have been transferred to the drain in the time $[0, t]$. The total number of transferred

particles,

$$n = n_F - n_B, \tag{2.70}$$

is simply the difference between the number of forward and backward transitions. In the literature, it is sometimes referred to as the jump number, a term that we readily adopt [97]. We consider processes that, at most, add or remove one particle from the drain, so $n - n' = 0, \pm 1$.

Eq.(2.69), consequently, can be written using quantum jump operators that move particles forward to the drain, $\mathbf{J}_F$, or backwards from the drain, $\mathbf{J}_B$, alongside an operator containing the remaining dynamics, $\mathbf{L}_0 = \mathbf{L} - \mathbf{J}_F - \mathbf{J}_B$:

$$\dot{\mathbf{P}}(n,t) = \mathbf{L}_0\mathbf{P}(n,t) + \mathbf{J}_F\mathbf{P}(n-1,t) + \mathbf{J}_B\mathbf{P}(n+1,t). \tag{2.71}$$

Note that the $\mathbf{J}_F$ and $\mathbf{J}_B$ are technically superoperators, but the term quantum jump operators is ubiquitous in the literature and we regularly use it throughout the thesis. In Fourier space, and using the relation $\sum_{n=-\infty}^{\infty} e^{in\chi}\mathbf{P}(n \mp 1, t) \rightarrow \sum_{m=-\infty}^{\infty} e^{i(m\pm1)\chi}\mathbf{P}(m,t)$, Eq.(2.71) becomes

$$\dot{\mathbf{P}}(\chi,t) = \mathbf{L}(\chi)\mathbf{P}(\chi,t), \text{ where} \tag{2.72}$$

$$\mathbf{L}(\chi) = \mathbf{L}_0 + \mathbf{J}_F e^{i\chi} + \mathbf{J}_B e^{-i\chi}. \tag{2.73}$$

The infinite set of coupled differential equations has now become a workable problem via the introduction of a counting field χ [98, 99], where the χ-dependent Liouvillian originates from the Fourier transform of $\mathbf{P}(n,t)$:

$$\mathbf{P}(\chi,t) = \sum_{n=-\infty}^{\infty} e^{in\chi}\mathbf{P}(n,t), \tag{2.74}$$

$$\mathbf{P}(n,t) = \frac{1}{2\pi}\int_0^{2\pi} d\chi e^{-in\chi}\mathbf{P}(\chi,t). \tag{2.75}$$

The initial condition of Eq.(2.72) is $\mathbf{P}(\chi,0) = \bar{\mathbf{P}}$, since at time $t = 0$ the open system has already reached the stationary state, and it has the general solution

$$\mathbf{P}(\chi,t) = e^{\mathbf{L}(\chi)t}\bar{\mathbf{P}}. \tag{2.76}$$

2.6.2 Constructing the n-resolved master equation

In order to obtain the n-resolved master equation, we must be able to identify the forward and backward jump operators from the total Liouvillian $\mathbf{L}$. In the rate equation [100], this is trivial because all rates describe easily understood physical processes. We can simply identify those

transitions between eigenstates of H_Q that must be accompanied by a transition to or from the drain, and they will comprise our jump operators. To demonstrate, consider the rate equation of a single resonant level (SRL), which may be empty $|0\rangle$ or occupied by a single electron $|1\rangle$. Being such a simple system, the probability vector can be constructed from physical intuition:

$$\frac{d}{dt}\begin{bmatrix} P_0(t) \\ P_1(t) \end{bmatrix} = \begin{bmatrix} -(\Gamma_{10}^S + \Gamma_{10}^D) & \Gamma_{01}^S + \Gamma_{01}^D \\ \Gamma_{10}^S + \Gamma_{10}^D & -(\Gamma_{01}^S + \Gamma_{01}^D) \end{bmatrix} \begin{bmatrix} P_0(t) \\ P_1(t) \end{bmatrix}. \tag{2.77}$$

The SRL is a good demonstrative model, as it can be solved exactly. The stationary state, for example, is

$$\bar{\mathbf{P}} = \frac{1}{\Gamma_{10} + \Gamma_{01}} \begin{bmatrix} \Gamma_{01} \\ \Gamma_{10} \end{bmatrix}. \tag{2.78}$$

This case is also an example of a *single-reset* open quantum system: a system where every tunneling to the drain leaves the molecule empty. For single-reset systems $\left(\mathbf{J}_F\right)^k \mathbf{P} = 0$ and $\left(\mathbf{J}_B\right)^k \mathbf{P} = 0$ for any vector $\mathbf{P}$ when $k > 1$. In comparison, in a *multiple-reset* system, after a tunneling to the drain the molecule may be occupied by a non-zero number of electrons. Multiple-reset systems are often difficult to handle analytically due to larger matrix sizes and system complexity.

Examining Eq.(2.77), the jump operator that moves an electron from the system to the drain is clearly

$$\mathbf{J}_F = \begin{bmatrix} 0 & \Gamma_{01}^D \\ 0 & 0 \end{bmatrix}, \tag{2.79}$$

since applying this operator to the probability vector to an occupied system, $\mathbf{P} = [0, 1]^T$, empties it via an interaction with the drain, which must mean an electron has been transferred into the drain. Similar reasoning leads us to the backward jump operator:

$$\mathbf{J}_B = \begin{bmatrix} 0 & 0 \\ \Gamma_{10}^D & 0 \end{bmatrix}. \tag{2.80}$$

With the jump operators now defined, we can easily write the χ-dependent Liouvillian:

$$\mathbf{L}(\chi) = \begin{bmatrix} -(\Gamma_{10}^S + \Gamma_{10}^D) & \Gamma_{01}^S + \Gamma_{01}^D e^{i\chi} \\ \Gamma_{10}^S + \Gamma_{10}^D e^{-i\chi} & -(\Gamma_{01}^S + \Gamma_{01}^D) \end{bmatrix}. \tag{2.81}$$

For the full master equation, however, the jump operator may contain parts not just from the transition rates between eigenstates of H_Q, but also from the less intuitive elements corresponding to the coherences. In this case, it is not clear from phenomenological considerations only which elements should contribute to the jump operators. Fortunately, as outlined by Li

et al. [101], we can resolve the master equation upon n by partitioning the bath into a number of subspaces $B^{(n)}$ [102, 103]. The total bath space is then the tensor product of all of these subspaces,

$$B = \lim_{K\to\infty} B^{(-K)} \otimes \ldots \otimes B^{(-n)} \otimes \ldots \otimes B^{(-1)} \otimes B^{(0)} \otimes B^{(1)} \otimes \ldots \otimes B^{(-n)} \otimes \ldots \otimes B^{(K)}, \tag{2.82}$$

and we will now trace over B_n to obtain the density matrix conditioned upon n electrons being detected in the drain by time t:

$$\rho^{(n)}(t) = \mathrm{Tr}_{B^{(n)}}\left[\rho_T(t)\right]. \tag{2.83}$$

Again, we want to the time-evolution of this n-resolved density matrix; so now the master equation in Eq.(2.28) is

$$\dot{\rho}_I^{(n)}(t) = -\int_0^t d\tau\, \mathrm{Tr}_{B^{(n)}}\left[H_{T,I}(t), [H_{T,I}(t-\tau)\rho_{T,I}(t-\tau)]\right]. \tag{2.84}$$

Instead of the Born approximation, we assume that the density matrix follows the ansatz

$$\rho_T(t) \simeq \sum_{n=-\infty}^{\infty} \rho^{(n)}(t) \otimes \rho_{B^{(n)}}. \tag{2.85}$$

We will also write the interaction Hamiltonian as we did in Eq.(2.29) and again ignore the dd and $d^\dagger d^\dagger$ terms in the expansion:

$$\begin{aligned}
\dot{\rho}_I^{(n')}(t) = \int_0^t d\tau \sum_{qq'}\sum_{n'} \mathrm{Tr}_{B^{(n)}} \Big(& a^\dagger_{q,I}(t) d_I(t) a_{q',I}(t-\tau) d^\dagger_I(t-\tau) \rho_I^{(n')}(t-\tau) \rho_{B^{(n')}} \\
& + a_{q,I}(t) d^\dagger_I(t) a^\dagger_{q',I}(t-\tau) d_I(t-\tau) \rho_I^{(n')}(t-\tau) \rho_{B^{(n')}} \\
& - a^\dagger_{q,I}(t) d_I(t) \rho_I^{(n')}(t-\tau) \rho_{B^{(n')}} a_{q',I}(t-\tau) d^\dagger_I(t-\tau) \\
& - a_{q,I}(t) d^\dagger_I(t) \rho_I^{(n')}(t-\tau) \rho_{B^{(n')}} a^\dagger_{q',I}(t-\tau) d_I(t-\tau) \\
& - a^\dagger_{q',I}(t-\tau) d_I(t-\tau) \rho_I^{(n')}(t-\tau) \rho_{B^{(n')}} a_{q,I}(t) d^\dagger_I(t) \\
& - a_{q',I}(t-\tau) d^\dagger_I(t-\tau) \rho_I^{(n')}(t-\tau) \rho_{B^{(n')}} a^\dagger_{q,I}(t) d_I(t) \\
& + \rho_I^{(n')}(t-\tau) \rho_{B^{(n')}} a^\dagger_{q',I}(t-\tau) d_I(t-\tau) a_{q,I}(t) d^\dagger_I(t) \\
& + \rho_I^{(n')}(t-\tau) \rho_{B^{(n')}} a_{q',I}(t-\tau) d^\dagger_I(t-\tau) a^\dagger_{q,I}(t) d_I(t) \Big)
\end{aligned} \tag{2.86}$$

Let us categorize the terms in Eq.(2.86) into two different types. In the first,

$$\begin{aligned}
(1) \qquad & \sum_{n'} \mathrm{Tr}_{B^{(n)}}\left(d^\dagger d \rho^{(n')} \rho_{B^{(n')}}\right), \quad \sum_{n'} \mathrm{Tr}_{B^{(n)}}\left(d d^\dagger \rho^{(n')} \rho_{B^{(n')}}\right), \\
& \sum_{n'} \mathrm{Tr}_{B^{(n)}}\left(\rho^{(n')} \rho_{B^{(n')}} d^\dagger d\right), \quad \sum_{n'} \mathrm{Tr}_{B^{(n)}}\left(\rho^{(n')} \rho_{B^{(n')}} d d^\dagger\right),
\end{aligned}$$

we can easily replace the trace $\mathrm{Tr}_{B^{(n)}} \to \mathrm{Tr}_B$, as all the $B^{(n)}$ subspaces are orthogonal:

$$\sum_{n'} \mathrm{Tr}_{B^{(n)}} \left(d^\dagger d \rho^{(n)} \rho_{B^{(n)}} \right) = \mathrm{Tr}_B \left(d^\dagger d \rho^{(n')} \rho_{B^{(n')}} \right), \quad \sum_{n'} \mathrm{Tr}_{B^{(n)}} \left(d d^\dagger \rho^{(n')} \rho_{B^{(n')}} \right) = \mathrm{Tr}_B \left(d d^\dagger \rho^{(n)} \rho_{B^{(n)}} \right),$$

$$\sum_{n'} \mathrm{Tr}_{B^{(n)}} \left(\rho^{(n')} \rho_{B^{(n')}} d^\dagger d \right) = \mathrm{Tr}_B \left(\rho^{(n)} \rho_{B^{(n)}} d^\dagger d \right), \quad \sum_{n'} \mathrm{Tr}_{B^{(n)}} \left(\rho^{(n')} \rho_{B^{(n')}} d d^\dagger \right) = \mathrm{Tr}_B \left(\rho^{(n)} \rho_{B^{(n)}} d d^\dagger \right).$$

The second type, however, will yield different results for source and drain operators:

$$(2) \qquad \begin{aligned} &\sum_{n'} \mathrm{Tr}_{B^{(n)}} \left(d_S^\dagger \rho^{(n')} \rho_{B^{(n')}} d_S \right), \quad \sum_{n'} \mathrm{Tr}_{B^{(n)}} \left(d_D^\dagger \rho^{(n')} \rho_{B^{(n')}} d_D \right), \\ &\sum_{n'} \mathrm{Tr}_{B^{(n)}} \left(d_S \rho^{(n')} \rho_{B^{(n')}} d_S^\dagger \right), \quad \sum_{n'} \mathrm{Tr}_{B^{(n)}} \left(d_D \rho^{(n')} \rho_{B^{(n')}} d_D^\dagger \right). \end{aligned}$$

For those terms with $d_S^\dagger$ and d_S, we can replace $\mathrm{Tr}_{B^{(n)}} \to \mathrm{Tr}_B$ as before, because source operators will not move between subspaces of different n. The drain operators, in contrast, produce two different cases:

$$\begin{aligned} \sum_{n'} \mathrm{Tr}_{B^{(n)}} \left(d_D^\dagger \rho^{(n')} \rho_{B^{(n')}} d_D \right) &= \mathrm{Tr}_{B^{(n)}} \left(d_D^\dagger \rho^{(n-1)} \rho_{B^{(n-1)}} d_D \right) = \mathrm{Tr}_B \left(d_D^\dagger \rho^{(n-1)} \rho_{B^{(n-1)}} d_D \right) \\ \sum_{n'} \mathrm{Tr}_{B^{(n)}} \left(d_D \rho^{(n')} \rho_{B^{(n')}} d_D^\dagger \right) &= \mathrm{Tr}_{B^{(n)}} \left(d_D \rho^{(n+1)} \rho_{B^{(n+1)}} d_D^\dagger \right) = \mathrm{Tr}_B \left(d_D \rho^{(n+1)} \rho_{B^{(n+1)}} d_D^\dagger \right). \end{aligned} \tag{2.87}$$

We can now see exactly where the $n+1, n-1,$ and n contributions enter the master equation. Because the baths are macroscopic and connected to a closed circuit, after the "state selection" they relax quickly to local equilibrium and we can replace $\rho_{B^{(n)}}, \rho_{B^{(n\pm1)}} \to \rho_B$. With these adjustments, applying the Markovian assumption, and expanding the interaction picture operators, the master equation is

$$\begin{aligned} \dot{\rho}^{(n)}(t) = \left[H_Q, \rho^{(n)}(t) \right] - i \sum_{qq'} \int_0^\infty d\tau \Big(\sum_\alpha \Big[& G_\alpha^>(\tau) a_q^\dagger e^{-iH_Q\tau} a_{q'} e^{iH_Q\tau} \rho^{(n)} + G_\alpha^<(\tau) a_q e^{-iH_Q\tau} a_{q'}^\dagger e^{iH_Q\tau} \rho^{(n)} \Big] \\ - \Big[& G_S^>(\tau) e^{-iH_Q\tau} a_{q'} e^{iH_Q\tau} \rho^{(n)} a_q^\dagger + G_S^<(\tau) e^{-iH_Q\tau} a_{q'}^\dagger e^{iH_Q\tau} \rho^{(n)} a_q + \\ & G_D^>(\tau) e^{-iH_Q\tau} a_{q'} e^{iH_Q\tau} \rho^{(n-1)} a_q^\dagger + G_D^<(\tau) e^{-iH_Q\tau} a_{q'}^\dagger e^{iH_Q\tau} \rho^{(n+1)} a_q \Big] + \text{h.c.} \Big). \end{aligned} \tag{2.88}$$

The final step is to evaluate the bath-correlation functions in terms of self-energies and write the master equation in the basis of eigenstates of H_Q; doing so, we get an analogous n-resolved master equation to Eq.(2.39)

$$\begin{aligned} i\dot{\rho}_{mn}^{(n)} = \omega_{mn} \rho_{mn}^{(n)} + \sum_{qq'} \sum_{kl} \Big(\sum_\alpha & \Big[\Sigma_\alpha^>(\omega_{lk}) \langle m | a_q^\dagger | k \rangle \langle k | a_{q'} | l \rangle \rho_{ln}^{(n)} + \Sigma_\alpha^<(\omega_{kl})^* \langle m | a_q | k \rangle \langle k | a_{q'}^\dagger | l \rangle \rho_{ln}^{(n)} \Big] \\ & + \Sigma_S^<(\omega_{nl}) \langle m | a_q^\dagger | k \rangle \rho_{kl}^{(n)} \langle l | a_{q'} | n \rangle + \Sigma_S^>(\omega_{ln})^* \langle m | a_q | k \rangle \rho_{kl}^{(n)} \langle l | a_{q'}^\dagger | n \rangle \\ & \Sigma_D^<(\omega_{nl}) \langle m | a_q^\dagger | k \rangle \rho_{kl}^{(n+1)} \langle l | a_{q'} | n \rangle + \Sigma_D^>(\omega_{ln})^* \langle m | a_q | k \rangle \rho_{kl}^{(n-1)} \langle l | a_{q'}^\dagger | n \rangle - (m \leftrightarrow n)^* \Big). \end{aligned} \tag{2.89}$$

Eq.(2.89) can, of course, be written in χ-space by performing a Fourier transform.

2.7 Summary

In this chapter we have detailed the various master equation approaches to nanoscale quantum transport: the Redfield master equation and the rate equation. Furthermore, we have outlined how to obtain the n-resolved version of each. As we will see in the next chapter, the n-resolved master equation will prove to be an easy point from which to generate fluctuation statistics.

Fluctuation statistics

This chapter contains material that has been previously published in the following journal article:

Counting quantum jumps: A summary and comparison of fixed-time and fluctuating-time statistics in electron transport - invited review in the special issue "Dynamics of Open Quantum Systems", S.L. Rudge and D.S. Kosov, J. Chem. Phys. **151**, 034107 (2019)

3.1 Motivation

The purpose of this chapter is to connect the master and rate equations derived in Chapter 2 to the relevant current fluctuation statistics. It will serve as a pedagogical introduction to fluctuation statistics through molecular junctions. These can be split into two broad categories: fixed-time statistics and fluctuating-time statistics.

To distinguish between them, we will first discuss the difference between quantum events and quantum jumps, two notions we use extensively throughout the chapter. In the context of quantum transport, the quantum event is the tunneling of an electron between the molecule and specific electrode, while the quantum jump is the associated transition between two molecular states accompanying the electron tunneling. Consider an approach in which the number of quantum events $n(t)$ is measured in the time interval $[0, t]$. Given the stochastic nature of quantum transport, repeat measurements over the same time interval will see $n(t)$ fluctuate about its mean, with probability distribution $P(n(t))$. Alternatively, we could repeatedly measure the time τ it takes for the number of measured quantum jumps to reach n and construct a probability density distribution $P(\tau(n))$, as we demonstrate in Fig.(3.1) and is experimentally demonstrated in Fig.(1.3b). The first quantity, $n(t)$, is an example of a *fixed-time* statistic, while $\tau(n)$ is an example of a *fluctuating-time* statistic [97, 104, 105].

Throughout the chapter, we will use the case of a single resonant level as a demonstrative example, since the matrices are all 2×2 and we can analytically derive all fluctuation statistics. The rate equation for a SRL, alongside the jump operators and stationary solution, can all be found in Eq.(2.77)-Eq.(2.81).

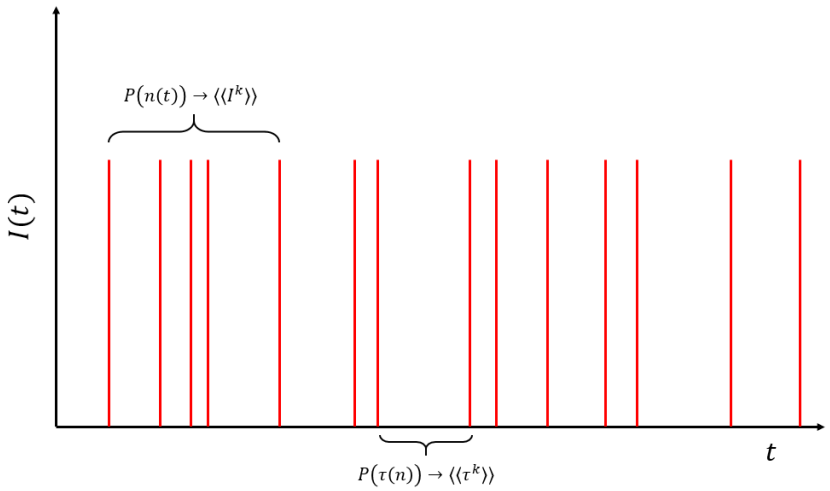

Figure 3.1: Schematic of time-dependent current measurements, like those from Fig.(1.3b).

3.2 Fixed-time statistics

In Chapter 1, we discussed the experimental history of the higher-order current cumulants, more commonly known as the full counting statistics. Similarly to early conductance experiments, theoretical calculations of the FCS initially faced great difficulty because quantum mechanical current operators at different times, $I(t)$ and $I(t')$, do not commute. For the first and second cumulants the problem is not so great; we are able to compute the average current and the noise spectrum directly, see Eq.(1.1), but directly calculating higher-order cumulants is a non-trivial task.

This time-ordering problem was first solved by Levitov and Lesovik [106] in a scattering theory framework via the explicit inclusion of a measuring device in the theoretical setup, which has since been extended to a general quantum mechanical variable [107] and applied to various transport scenarios [108, 109]. Non-equilibrium Green's functions have proved indispensable in calculating transient FCS for both electron [110] and electron energy [111] current, as well as the FCS of junctions with electron-phonon [112–115] and electron-electron [116] interactions; although for strong interactions quantum master equations are generally used.

Master equations have been used to calculate the FCS in various systems [31], such as multi-level quantum dots [40], systems with cotunneling effects [47, 95, 117, 118], systems with strong electron-phonon interactions [119], and systems experiencing the Coulomb blockade [98]. Furthermore, master equations have been used to calculate the FCS of non-Markovian transport. Such work has shown, for example, that non-Markovian behavior enters the higher-order cumulants via cotunneling effects [120], and is also present in the FCS of a dissipative double quantum dot [121, 122]. The FCS are also closely related to fluctuation theorems: those relations that describe fluctuations in far-from-equilibrium quantum systems [123].

In the Markovian master equation framework, current cumulants are expressed in terms of cu-

mulants of the distribution of total transferred charge, $P(n,t)$. The first and second cumulants, for example, are just the average $\langle n(t)\rangle$ and the variance $\langle\langle n(t)^2\rangle\rangle = \langle (n(t) - \langle n(t)\rangle)^2\rangle$.

Assuming that $P(n,t)$ has an exponential asymptotic behavior [74, 124],

$$\lim_{t\to\infty} P(n,t) \approx \exp\left[-t\phi(\frac{n}{t})\right], \tag{3.1}$$

then as $t \to \infty$ the cumulants of transferred charge grow linearly according to the asymptotic growth rates $\langle\langle I^k\rangle\rangle$:

$$\langle\langle n(t)^k\rangle\rangle \approx \langle\langle I^k\rangle\rangle t. \tag{3.2}$$

The approximation in Eq.(3.1) implies that $P(n,t)$ satisfies a large deviation principle [124], where $\phi(\frac{n}{t})$ is the rate function of a large deviation process. In essence, measurements of n in the time interval $[0,t]$ will focus around the average $\langle n(t)\rangle = \min_n \{\phi(\frac{n}{t})\}$ and large deviations away from this value are exponentially suppressed. The large deviation principle is satisfied for a wide variety of physical systems, including the ones we consider here, and it forms the basis of the connections between the fluctuation statistics we present. It should be noted, however, that not all transport scenarios display the scaling in Eq.(3.2); Karzig and von Oppen, for example, have shown that the current cumulants in a chain of quantum dots do not scale linearly in time while undergoing a phase transition [125].

From Eq.(3.2), the current cumulants are related to the charge cumulants via

$$\lim_{t\to\infty}\langle\langle I(t)^k\rangle\rangle = e^k\frac{d}{dt}\langle\langle n(t)^k\rangle\rangle \tag{3.3}$$

$$\approx \langle\langle I^k\rangle\rangle, \tag{3.4}$$

since we set $e = 1$. This is the reason we chose $\langle\langle I^k\rangle\rangle$ as notation for the asymptotic growth rates in Eq.(3.2). Clearly, the long-time limit is crucial to a relationship between current cumulants and cumulants of transferred charge. As we will see, it is also a necessary limit from the point of view of master equation theory. Restricting cumulants to the long-time limit, however, also restricts us to analyzing their zero-frequency power spectrum, ignoring short-time physics. We will demonstrate how this manifests by comparing the noise, as defined in Eq.(1.1), and the second cumulant of $P(n,t)$ [107].

Direct differentiation of the second cumulant gives

$$\frac{d}{dt}\langle\langle n(t)^2\rangle\rangle = \left\langle\left[n(t), \frac{d}{dt}n(t)\right]_+\right\rangle - 2\langle n(t)\rangle\langle\frac{d}{dt}n(t)\rangle. \tag{3.5}$$

By noting that

$$n(t) = \int_0^t dt_1 \hat{I}(t_1), \tag{3.6}$$

we then get

$$\frac{d}{dt}\langle\langle n(t)^2\rangle\rangle = \int_0^t dt_1 \left\langle [\delta I(t_1), \delta I(t)]_+ \right\rangle, \tag{3.7}$$

which already bears similarity to Eq.(1.1). Changing the integration variable from t_1 to relative time $\tau = t_1 - t$ gives

$$\frac{d}{dt}\langle\langle n(t)^2\rangle\rangle = \int_{-t}^0 d\tau \left\langle [\delta I(t+\tau), \delta I(t)]_+ \right\rangle. \tag{3.8}$$

In the limit $t \to \infty$, the measurement time t is greater than the characteristic current-current correlation time τ and we can replace the integration limits to get the MacDonald formula [126]:

$$\frac{d}{dt}\langle\langle n(t)^2\rangle\rangle = \frac{1}{2}\int_{-\infty}^{\infty} d\tau \left\langle [\delta I(t+\tau), \delta I(t)]_+ \right\rangle. \tag{3.9}$$

In the stationary state, Eq.(3.9) depends only on the time delay τ and, comparing with Eq.(1.1), therefore reduces to half the zero-frequency noise power

$$\lim_{t\to\infty} \frac{d}{dt}\langle\langle n(t)^2\rangle\rangle \approx \langle\langle I^2\rangle\rangle \tag{3.10}$$

$$= \frac{1}{2}\mathcal{S}(0); \tag{3.11}$$

so we see that the long-time limit necessarily restricts cumulants to the zero-frequency power regime, where they potentially miss important short-time physics. Counting statistics at finite times, or rather finite frequencies, remain an active theoretical [127–134] and experimental [68] research area; non-Poissonian behavior of higher-order cumulants, for example, has been shown to depend on frequency [135]. Time-dependent current cumulants are also able to identify short-time correlations between electrons [136, 137]; in fact it has been proposed that higher-order factorial cumulants can be used as a detection technique for electron-electron interactions [138–140]. Despite this interesting progress, in all calculations throughout the thesis we restrict our analysis to the zero-frequency current cumulants, as they are numerically easier to compute but still provide valuable transport information.

Scaling the zero-frequency noise by the average current, for example, yields a quantity known

as the Fano factor:

$$F = \frac{\mathcal{S}(0)}{2\langle I\rangle} \tag{3.12}$$

$$= \frac{\langle\langle n^{(2)}\rangle\rangle}{\langle n\rangle}. \tag{3.13}$$

Since the variance and mean of a Poisson process are equal, we can use the Fano factor to characterize current distributions as either sub-Poissonian ($F < 1$), Poissonian ($F = 1$), or super-Poissonian ($F > 1$), and consequently identify the transport effects causing this behavior. Indeed, super-Poissonian noise is caused by a host of physical effects, such as the dynamical channel blockade [40, 41], asymmetric couplings [42], avalanching electrons [43], telegraphic switching [44–47], and negative differential resistance [48].

3.2.1 Practical calculations

In the introduction to this section, we saw that the long-time limit FCS are recast in terms of the distribution of transferred charge $P(n,t)$. Fortunately, in the framework of master equations, there is an easy path to calculating cumulants of this distribution [98]. First, $P(n,t)$ is related to the density matrix via the trace:

$$P(n,t) = (\mathbf{I}, \mathbf{P}(n,t))\,. \tag{3.14}$$

From Eq.(2.74), we can see that

$$(\mathbf{I}, \mathbf{P}(\chi,t)) = \sum_{n=0}^{\infty} e^{in\chi} P(n,t). \tag{3.15}$$

If we take successive derivatives of Eq.(3.15) with respect to χ and set $\chi = 0$, the right-hand side will produce the moments of transferred charge and therefore the current:

$$\langle I^k\rangle = \frac{d}{dt}(-i)^k \frac{\partial^k}{\partial\chi^k} (\mathbf{I}, \mathbf{P}(\chi,t))\Big|_{\chi=0} \tag{3.16}$$

$$= \frac{d}{dt}(-i)^k \frac{\partial^k}{\partial\chi^k} \left(\mathbf{I}, e^{\mathbf{L}(\chi)t}\bar{\mathbf{P}}\right)\Big|_{\chi=0}, \tag{3.17}$$

using Eq.(2.76) and assuming all measurements are performed in the stationary state. The moment generating function of $P(n,t)$ is therefore $M(\chi,t) = \left(\mathbf{I}, e^{\mathbf{L}(\chi)t}\bar{\mathbf{P}}\right)$; taking its natural logarithm we find the cumulant generating function $K(\chi,t)$:

$$K(\chi,t) = \ln\left(\mathbf{I}, e^{\mathbf{L}(\chi)t}\bar{\mathbf{P}}\right). \tag{3.18}$$

Eq.(3.18) is, in general, too difficult to evaluate exactly. Bagrets and Nazarov [98, 107], making the same assumption about the asymptotic behavior of $P(n,t)$ as in Eq.(3.1), have shown that as $t \to \infty$ the cumulant generating function can be approximated as

$$\lim_{t\to\infty} K(\chi,t) = t\Lambda_{\max}, \tag{3.19}$$

where $\Lambda_{\max}$ is the eigenvalue of $M(\chi,t)$ with the largest real part. Although this is a great simplification, analytic calculations of $\Lambda_{\max}$ can be difficult for systems with a large Liouvillian. The common approach then is to expand $\Lambda_{\max}(\chi)$ in χ using Rayleigh-Schrödinger perturbation theory [121, 122, 141].

Cumulants of the current distribution are now

$$\langle\langle I^k \rangle\rangle = \frac{d}{dt}(-i)^k \frac{\partial^k}{\partial \chi^k} t\Lambda_{\max}\Big|_{\chi=0} \tag{3.20}$$

$$= (-i)^k \frac{\partial^k}{\partial \chi^k}\Lambda_{\max}\Big|_{\chi=0}. \tag{3.21}$$

3.2.2 FCS of a SRL

For a SRL, we can calculate the FCS analytically. Considering the χ-dependent Liouvillian defined by Eq.(2.81), which we write again as

$$\mathbf{L}(\chi) = \begin{bmatrix} -\Gamma_{10} & \Gamma_{01}(\chi) \\ \Gamma_{10}(\chi) & -\Gamma_{01} \end{bmatrix}, \tag{3.22}$$

where $\Gamma_{10}(\chi) = \Gamma^S_{01} + \Gamma^D_{01}e^{i\chi}$ and $\Gamma^S_{10} + \Gamma^D_{10}e^{-i\chi}$; the eigenvalue with the largest real part is

$$t\Lambda_{\max}(\chi) = \frac{t}{2}\left[-(\Gamma_{01}+\Gamma_{10}) + \sqrt{(\Gamma_{01}+\Gamma_{10})^2 - 4[\Gamma_{01}\Gamma_{10} - \Gamma_{10}(\chi)\Gamma_{01}(\chi)]}\right]. \tag{3.23}$$

Treating $t\Lambda_{\max}(\chi)$ as the cumulant generating function and using Eq.(3.21), the average current is

$$\langle I \rangle = (-i)\frac{\partial}{\partial\chi}\Lambda_{\max}(\chi)\Big|_{\chi=0} \tag{3.24}$$

$$= \frac{\Gamma^S_{10}\Gamma^D_{01} - \Gamma^S_{01}\Gamma^D_{10}}{\Gamma_{10}+\Gamma_{01}}; \tag{3.25}$$

the variance is

$$\langle\langle I^2\rangle\rangle = (-i)^2 \frac{\partial^2}{\partial\chi^2}\Lambda_{\max}(\chi)\bigg|_{\chi=0} \tag{3.26}$$

$$= \frac{1}{(\Gamma_{01}+\Gamma_{10})^3}\left[(\Gamma^S_{01}\Gamma^D_{10}+\Gamma^S_{10}\Gamma^D_{01})(\Gamma_{01}+\Gamma_{10})^2 - 2(\Gamma^S_{10}\Gamma^D_{01}-\Gamma^S_{01}\Gamma^D_{10})^2\right]; \tag{3.27}$$

and the Fano factor is

$$F = \frac{(\Gamma^S_{01}\Gamma^D_{10}+\Gamma^S_{10}\Gamma^D_{01})(\Gamma_{01}+\Gamma_{10})^2 - 2(\Gamma^S_{10}\Gamma^D_{01}-\Gamma^S_{01}\Gamma^D_{10})^2}{(\Gamma^S_{10}\Gamma^D_{01}-\Gamma^S_{01}\Gamma^D_{10})(\Gamma_{01}+\Gamma_{10})^2}. \tag{3.28}$$

3.3 Fluctuating-time statistics

Fluctuating-time statistics provide an alternative view of the transport. Consider the time-series of current spikes in Fig.(3.1). Rather than recording the number of electrons detected in the drain in a certain interval, we could instead record the time between successive tunnelings to the drain. Repeated measurements could then be used to generate the WTD, $w(t_a, t_b)$: the conditional probability density that, given an electron tunneling event occured at time t_a, the next electron tunneling event to the drain occurs at time t_b [142]. This measurement scheme does not have to be restricted to electron tunneling events; we could measure a WTD in a similar manner for any situation where physical events occur at specific but random points in time. Indeed, waiting times have a broad history in multiple disciplines, such as queueing theory in mathematics [143], reaction kinetics in chemistry [144], and quantum optics in physics [145–149]. They are, however, a relatively recent addition to nanoscale transport; the first formalism was outlined by Brandes in 2008 [150].

Since their introduction, waiting times have been calculated for a wide variety of nanoscale transport scenarios. Scattering theory, for example, has been used to calculate waiting times in superconducting junctions [151–153], periodically driven transport [73, 154], and coherent conductors [155–157]. As with the FCS, waiting times in the transient regime are generally calculated via the non-equilibrium Green's functions method [110, 158, 159], which has been used to analyze the role of spin [110, 160] and molecular vibrations [161] in electron transport.

Alongside these two methods, substantial research has followed Brandes' original formalism and calculated waiting times from quantum master equations. Walldorf *et al.* [162] and Rajabi *et al.* [163], for example, have both used master equations to explore the relationship between waiting times and Cooper pair emission in superconducting junctions, while Potanina and Flindt [164] have investigated periodically driven electron transport. Waiting times have also been calculated for double-quantum dots [44, 45, 150, 165], quantum dot spin-valves [166], and non-Markovian transport [167]. Further work in the master equation framework has shown that waiting times can identify transport through HOMO and LUMO levels in a single

resonant level [168], analyze electron-electron interactions in the sequential [44, 150, 169] and cotunneling [170] regimes, and analyze electron-phonon interactions [78, 171–173].

Unlike the FCS, waiting times are not restricted to the long-time limit and so provide insight into interesting physics on short timescales. Phenomena such as inelastic interactions [78, 170], quantum coherence [154, 155], fermionic statistics [44, 157], spin-polarised leads [45], and superconducting junctions [151, 152] have all been shown to produce temporal correlations observable from the WTD.

Experimentally, however, waiting times do have several drawbacks. Since measurements rely on single-electron detection, as with the FCS, all currents must be small: in the order of 1kHz. Furthermore, if we analyze purely quantum processes in the transport, such as cotunneling, then direct measurement via a QPC is impossible as it will destroy any coherence [47]. An interesting experimental approach, in which the WTD is extracted directly from low-order current correlations via theoretical post-processing using continuous matrix product state tomography, has recently been proposed and could possibly overcome this limitation [174]. The experimental setup of real-time single electron detection is also restricted to large bias voltages, so that the current is unidirectional. We will see that this limit also applies in theoretical calculations as well; we are restricted to calculating the WTD for successive tunnelings to and from the drain separately. Considering that bidirectional transitions play an important role outside of the large bias limit and in many physical systems [61], it is imperative to have a fluctuating-time statistic capable of incorporating them. From a theoretical perspective, we could work with bidirectional transitions if there was a fluctuation statistic for the time between the *total* number of forward and backward tunnelings.

Recently, it has been demonstrated that the first-passage time is such a statistic. In the context of nanoscale electron transport, we define the FPTD, $F(n|t_0, t_0+\tau)$, as the probability density that, given an initial tunneling event to the drain at time t_0, the next time the jump number reaches n is after a time delay τ. Since n is the difference between the sum of forward and backward transitions, it naturally incorporates bidirectional transport. Indeed, since its introduction, the FPTD has been applied to a number of scenarios where bidirectional transport is unavoidable [97, 175, 176].

First-passage times, in the form that we will use, were initially developed to describe fluctuations of entropic variables in the stationary state of Markovian systems [97, 177–181]; they have since been used to theoretically and experimentally verify fluctuation relations [77]. We note, also, that Ridley *et al.* have recently calculated FPTDs using the inchworm quantum Monte Carlo method and found queuing effects arising from the Coulomb repulsion [116]. The notation we use in this chapter and beyond was first outlined by Saito and Dhar [181], with significant contributions from Ptaszynski [97].

In this section we will first outline general relationships between time statistics for fluctuating

variables, before detailing methods for calculating the WTD and FPTD from Markovian master equations. We will conclude with an example using transport through a SRL, and a discussion on renewal theory.

3.3.1 Outline

We first define several important probability distributions associated with individual electron tunneling events and establish various useful relations between these distributions. We will closely follow van Kampen's discussion of stochastic time distributions [142]:

$F(t_a, t_b)$ – the probability *density* that, given that the recording starts at time t_a, the first electron tunneling event is detected at time t_b. Therefore, $F(t_a, t_b)dt_b$ is the probability to first detect an electron at time interval $(t_b, t_b + dt_b)$ if the recording of the events starts at t_a; and

$\Pi(t_a, t_b)$ – the probability that no electron detection occurs in the interval (t_a, t_b), which has recently been named the idle-time probability [156, 157].

These two probability distributions are connected by the self-evident integral relation

$$\int_{t_a}^{t_b} dt\ F(t_a, t) = 1 - \Pi(t_a, t_b). \tag{3.29}$$

Differentiating this relation with respect to t_b and t_a gives, respectively,

$$F(t_a, t_b) = -\frac{\partial}{\partial t_b}\Pi(t_a, t_b) \tag{3.30}$$

$$= \frac{\partial}{\partial t_a}\Pi(t_a, t_b). \tag{3.31}$$

There are three more important probability distributions:

$p(t)$ – the probability density to detect an electron at time t, which, based on physical reasoning, satisfies $p(t_a) = F(t_a, t_a)$. An electron tunneling event occuring in the interval $[t, t + dt]$ has associated probability $p(t)dt$;

$p(t_a, t_b)$ – the *joint* probability density to detect an electron at time t_a and to next detect an electron at time t_b. The joint probability for an electron tunneling event to occur in $[t_a, t_a + dt_a]$ and the next electron tunneling event to occur in $[t_b, t_b + dt_b]$ is then $p(t_a, t_b)dt_a dt_b$; and

$w(t_a, t_b)$ – the *conditional* probability density that, given an electron tunneling occurred at time t_a, the next electron tunneling event occured at t_b: the WTD. The expression $w(t_a, t_b)dt_b$ is thus the conditional probability that, given an electron tunneling occurred at time t_a, the

next electron tunneling event occured in the time interval $[t_b, t_b + dt_b]$.

Using the standard relation between joint and conditional probabilities,

$$p(t_a, t_b)dt_a dt_b = p(t_a)dt_a\, w(t_a, t_b)dt_b, \tag{3.32}$$

we get a simple expression for the WTD in terms of the joint probability density:

$$p(t_a, t_b) = p(t_a)\, w(t_a, t_b) \tag{3.33}$$

$$w(t_a, t_b) = \frac{p(t_a, t_b)}{p(t_a)}. \tag{3.34}$$

Based on these definitions, the probability density for an electron tunneling to occur at t_b, irrespective of any prior tunnelings before measurement started at t_a, is also

$$\int_{-\infty}^{t_a} dt\, p(t, t_b) = F(t_a, t_b). \tag{3.35}$$

Differentiating with respect to t_a we get

$$p(t_a, t_b) = \frac{\partial}{\partial t_a} F(t_a, t_b). \tag{3.36}$$

Hence, we have the following relations between the WTD and idle-time probability

$$w(t_a, t_b) = -\frac{1}{p(t_a)} \frac{\partial^2}{\partial t_a \partial t_b} \Pi(t_a, t_b), \text{ and} \tag{3.37}$$

$$w(t_a, t_b) = \frac{1}{p(t_a)} \frac{\partial^2}{\partial t_a^2} \Pi(t_a, t_b). \tag{3.38}$$

As in the previous section we perform all calculations in the stationary non-equilibrium state, where all two-time distributions now depend only on the relative time $\tau = t_b - t_a$. Using $\frac{\partial}{\partial \tau} = \frac{\partial}{\partial t_b} = -\frac{\partial}{\partial t_a}$ we get

$$w(\tau) = \frac{1}{p} \frac{\partial^2}{\partial \tau^2} \Pi(\tau), \tag{3.39}$$

with p now also computed from the idle time probability:

$$p = -\frac{\partial}{\partial \tau} \Pi(\tau)\Big|_{\tau=0}. \tag{3.40}$$

It is important to note that, since p is just the rate at which the $\Pi(\tau)$ changes in time, which in the unidirectional limit is equivalent to $\frac{1}{\langle \tau \rangle}$. Indeed, in the literature Eq.(3.39) is often written as

$$w(\tau) = \langle \tau \rangle \frac{\partial^2}{\partial \tau^2} \Pi(\tau). \tag{3.41}$$

3.3.2 Waiting time distribution

For a generic quantum system described by the Markovian master equation in Eq.(2.67), we can intuitively generate the distribution of waiting times between successive electron tunneling events. For simplicity, let us assume that we are examining the waiting time τ between two electron tunneling events of the same type, described by jump operator $\mathbf{J}$. The conditional probability density that, given that tunneling event of type $\mathbf{J}$ occurs at some time in the stationary state, the next tunneling event of type $\mathbf{J}$ will occur after a delay τ is

$$w(\tau) = \frac{\left(\mathbf{I}, \mathbf{J}e^{\mathbf{L}_0\tau}\mathbf{J}\bar{\mathbf{P}}\right)}{\left(\mathbf{I}, \mathbf{J}\bar{\mathbf{P}}\right)}, \tag{3.42}$$

where $\mathbf{L}_0 = \mathbf{L} - \mathbf{J}$ is the Liouvillian with $\mathbf{J}$ removed.

Let us physically examine the top line of Eq.(3.42). The system starts in the stationary state $\bar{\mathbf{P}}$ and undergoes quantum jump $\mathbf{J}$, after which it evolves for a time according to $\mathbf{L}_0$, during which no jump of type $\mathbf{J}$ takes place, until another quantum jump $\mathbf{J}$ occurs after a time τ. Summing the resulting probability vector, which is equivalent to computing the inner product with vector $\mathbf{I}$, thus gives the joint probability for two successive quantum jumps of type $\mathbf{J}$ to occur in the stationary state at times separated by a delay τ. The bottom line is just the probability for quantum jump $\mathbf{J}$ to occur at any time during the stationary state; so that, together, the top and bottom lines of Eq.(3.42) denote the conditional probability that, given an initial quantum jump of type $\mathbf{J}$ in the stationary state, the next quantum jump of type $\mathbf{J}$ will occur after a waiting time τ. Eq.(3.42) is Brandes' original definition [150].

Since we aim to relate time statistics to current statistics, we will focus on $w_F(\tau)$, the distribution of waiting times between tunnelings from the molecule to the drain, which are contained in the forward current operator $\mathbf{J}_F$, and $w_B(\tau)$, the distribution of waiting times between tunnelings from the drain to the molecule, which are contained in the backward current operator $\mathbf{J}_B$. Note that, from here onwards, if we have omitted the subscript, we are referring to $w_F(\tau)$.

If we assume that the transport is unidirectional, such that $\mathbf{L}(\chi) = \mathbf{L}_0 + \mathbf{J}_F e^{i\chi}$, then we can derive an equivalent expression for the WTD from the n-resolved master equation and the idle-time probability, since in this limit

$$\Pi(t) = P(0, t). \tag{3.43}$$

Again, this follows from physical intuition; $\Pi(\tau)$ is the probability that at time τ no tunneling event has occurred, which for unidirectional transport is $P(0, t)$ since $n \geq 0$. The probability

$P(0,t)$ is obtained from the cumulant generating function, defined in Eq.(3.18):

$$M(\chi,t) = e^{K(\chi,t)} \tag{3.44}$$

$$= \sum_{n=0}^{\infty} e^{in\chi} P(n,t) \tag{3.45}$$

$$= P(0,t) + \sum_{n=1}^{\infty} e^{in\chi} P(n,t), \tag{3.46}$$

where all the terms in the summation for which $n < 0$ are excluded since the transport is unidirectional. All the terms inside the summation disappear in the limit $\chi \to i\infty$, so that [167, 182]

$$P(0,t) = \lim_{\chi \to i\infty} M(\chi,t). \tag{3.47}$$

which, combined with Eq.(3.18), yields

$$\Pi(\tau) = \lim_{\chi \to i\infty} \left(\mathbf{I}, e^{\mathbf{L}(\chi)t} \bar{\mathbf{P}} \right). \tag{3.48}$$

This immediately shows the necessity of excluding all terms for which $n < 0$; if included each would be accompanied by a factor of $e^{-i\chi}$, which would diverge in the limit $\chi \to i\infty$.

From here, we proceed using Eq.(3.39) alongside the definition of $\Pi(\tau)$ in Eq.(3.48):

$$w_F(\tau) = -\lim_{\chi \to i\infty} \frac{(\mathbf{I}, \mathbf{L}(\chi) e^{\mathbf{L}(\chi)\tau} \mathbf{L}(\chi) \bar{\mathbf{P}})}{(\mathbf{I}, \mathbf{L}(\chi) \bar{\mathbf{P}})}. \tag{3.49}$$

$$= -\lim_{\chi \to i\infty} \frac{(\mathbf{I}, (\mathbf{L}_0 + \mathbf{J}_F e^{i\chi}) e^{(\mathbf{L}_0 + \mathbf{J}_F e^{i\chi})\tau} (\mathbf{L}_0 + \mathbf{J}_F e^{i\chi}) \bar{\mathbf{P}})}{(\mathbf{I}, (\mathbf{L}_0 + \mathbf{J}_F e^{i\chi}) \bar{\mathbf{P}})} \tag{3.50}$$

$$= -\frac{(\mathbf{I}, \mathbf{L}_0 e^{\mathbf{L}_0 \tau} \mathbf{L}_0 \bar{\mathbf{P}})}{(\mathbf{I}, \mathbf{L}_0 \bar{\mathbf{P}})}. \tag{3.51}$$

At this point we use the splitting $\mathbf{L}_0 = \mathbf{L}(0) - \mathbf{J}_F$, the definition of the stationary state $\mathbf{L}(0)\bar{\mathbf{P}} = 0$, along with the easily verifiable relation between any Liouvillian $\mathbf{L}(0)$ and any vector $\mathbf{A}$ that $(\mathbf{I}, \mathbf{L}(0)\mathbf{A}) = 0$, to obtain

$$w_F(\tau) = \frac{(\mathbf{I}, \mathbf{J}_F e^{\mathbf{L}_0 \tau} \mathbf{J}_F \bar{\mathbf{P}})}{(\mathbf{I}, \mathbf{J}_F \bar{\mathbf{P}})}. \tag{3.52}$$

Eq.(3.52) is the same definition as that provided in Eq.(3.42). The important distinction, however, is that while Eq.(3.42) can include bidirectional transitions in $\mathbf{L}_0$, from the very start of deriving Eq.(3.52) we are forced to assume that the transport is unidirectional. We may of course use the same approach to derive a similar expression for $w_B(\tau)$ from the idle-time probability in the limit $\chi \to -i\infty$, but the assumption would then be that the transport is unidirectional in the $n \leq 0$ direction.

To resolve this backward tunneling divergence catastrophe, we might intuitively return to Eq.(3.15) and Eq.(3.18) and write the moment generating function as

$$M(\chi,t) = P(0,t) + \sum_{n=1}^{\infty} e^{in\chi} P(n,t) + \sum_{n=-1}^{-\infty} e^{in\chi} P(n,t). \tag{3.53}$$

Integrating both sides from $0 \to 2\pi$ will thus eliminate all terms for which $n > 0$ and $n < 0$:

$$P(0,t) = \int_0^{2\pi} d\chi\, M(\chi,t). \tag{3.54}$$

This method is still flawed, because for bidirectional transport $P(0,t) \neq \Pi(t)$. To see this, consider the physical definition of the idle-time probability $\Pi(\tau)$: the probability that *no* tunneling event occurs in the interval $[0,\tau]$. $P(0,t)$ is the probability that the jump number at time t is 0: that is, the probability that the sum of forward and backward transitions is zero. This does not preclude a tunneling event from occurring; indeed, there may have been any number of forward tunneling events in $[0,t]$, as long as there were also exactly the same number of backward tunneling events.

At this point it is natural to question the need for a WTD derived from the n-resolved master equation, as it is applicable to unidirecitonal transport only and we obtain the same results from the definition in Eq.(3.42). In some cases, however, the n-resolved master equation must be used to include all transitions that change the jump number n. Elastic cotunneling events, for example, do not change the state of the quantum system, and so do not appear in the standard master equation, but contribute to the total current in the drain and must be included in $\mathbf{J}_F$ and $\mathbf{J}_B$. When we calculate waiting times including elastic cotunneling events, then, we must first define $\mathbf{L}(\chi)$ from the corresponding n-resolved master equation and then define $\mathbf{L}_0 = \mathbf{L}(0) - \mathbf{J}_F$ from it [170, 175]. In fact, since waiting times calculated from Markovian master equations have largely been restricted to the infinite bias voltage regime, many authors define the WTD using the n-resolved approach [150, 167].

Most waiting time analysis will be done via the cumulants, in particular the average waiting time $\langle\langle\tau\rangle\rangle = \langle\tau\rangle$ and the variance $\langle\langle\tau^2\rangle\rangle = \langle\tau^2\rangle - \langle\tau\rangle^2$. The Laplace transform of the WTD,

$$\tilde{w}(z) = \int_0^{\infty} d\tau\, e^{z\tau} w(\tau) \tag{3.55}$$

$$= \frac{\left(\mathbf{I}, \mathbf{J}\left[z - \mathbf{L}_0\right]^{-1} \mathbf{J}\bar{\mathbf{P}}\right)}{(\mathbf{I}, \mathbf{J}\bar{\mathbf{P}})}, \tag{3.56}$$

conveniently defines a cumulant generating function:

$$\langle\langle\tau^k\rangle\rangle = (-1)^k \frac{d^k}{dz^k} \ln \tilde{w}(z)\bigg|_{z=0}. \tag{3.57}$$

Scaling the second waiting time cumulant by the first yields a quantity known as the randomness parameter:

$$R = \frac{\langle\langle \tau^2 \rangle\rangle}{\langle \tau \rangle^2}, \tag{3.58}$$

which is commonly compared with the Fano factor.

We now have a comprehensive framework in which to calculate WTDs from Markovian master equations. Several problems remain, however. For those transport scenarios that do require an n-resolved master equation, how do we move beyond the unidirectional transport limit? Furthermore, we will see later that even if we are able to calculate $w_F(\tau)$ and $w_B(\tau)$ for bidirectional transport, it is not clear how to use them to obtain the total current distribution: one of the key interests in fluctuation analysis being the relations between fixed-time and fluctuating-time statistics. To resolve, we need a fluctuating-time distribution for the jump number n, which inherently includes both forward and backward transitions. Unfortunately, the idle-time probability offers no solution here either; instead, we need a method to evaluate when the jump number *first* reaches n.

3.3.3 First-passage time distribution

The quantity we seek is the FPTD, $F(n|t_0, t_0+\tau)$: the probability density that the time delay until the jump number first reaches n is τ, given that measurement started at t_0. Again, because we work in the stationary state, the starting time can be taken as $t = 0$, and $F(n|t_0, t_0 + \tau) = F(n|\tau)$. Since n is the sum of forward and backward transitions, the FPTD is naturally bidirectional. It is calculated from the n-resolved master equation: a relationship that was first outlined by Saito and Dhar [181] and Ptaszynski [97], whose work we closely follow in the derivations below.

Considering the master equation context of our approach, it is natural to treat $F(n|t)$ as a trace over a first-passage time vector $(\mathbf{I}, \mathbf{F}(n|t))$, where each element $[\mathbf{F}(n|\tau)]_l$ is the probability density that the jump number reaches n for the first time at τ and that the system is in state l at this time. We next need to relate $\mathbf{F}(n|\tau)$ to the probability vector $\mathbf{P}(n,t)$, which means that the jump number n cannot experience an overall change in the interval $[\tau, t+\tau]$. We therefore define $\mathbf{T}(0|t-\tau)$ as the matrix of conditional probability densities that, given at time given at time τ the jump number reaches n for the first time, the jump number does not change overall in the time interval $[\tau, t]$. $\mathbf{P}(n,t)$ is then the product of this conditional probability and the initial first-passage time probability, integrated over all possible first-passage times:

$$\mathbf{P}(n,t) = \int_0^t d\tau\, \mathbf{T}(0|t-\tau)\mathbf{F}(n|\tau). \tag{3.59}$$

In general, the element $[\mathbf{T}(n-n'|t-t')]_{kl}$ is the conditional probability that, given the system is initially in state l and the jump number is n' at time t', at time t it will be in state k and the jump number will be n. Evidently $\mathbf{T}(n|t)$ defines a transition matrix moving the system from some arbitrary state at time $t=0$ to $\mathbf{P}(n,t)$:

$$\mathbf{P}(n,t) = \mathbf{T}(n|t)\mathbf{P}(0). \tag{3.60}$$

Equating Eq.(3.59) and Eq.(3.60) relates the first-passage time to the transition matrix:

$$\mathbf{T}(n|t)\mathbf{P}(0) = \int_0^t d\tau\, \mathbf{T}(0|t-\tau)\mathbf{F}(n|\tau). \tag{3.61}$$

Since Eq.(3.59) is a convolution, from here it is easier to work in Laplace space:

$$\tilde{\mathbf{T}}(n|z)\mathbf{P}(0) = \tilde{\mathbf{T}}(0|z)\tilde{\mathbf{F}}(n|z). \tag{3.62}$$

Rearranging Eq.(3.62) yields the first-passage time distribution in Laplace space:

$$\tilde{F}(n|z) = \left(\mathbf{I}, \tilde{\mathbf{T}}(0|z)^{-1}\tilde{\mathbf{T}}(n|z)\mathbf{P}(0)\right). \tag{3.63}$$

All that remains now is to calculate $\mathbf{T}(n|t)$, which is obtained by comparing Eq.(3.60) with the inverse Fourier transform of Eq.(2.72):

$$\mathbf{T}(n|t) = \frac{1}{2\pi}\int_0^{2\pi} d\chi e^{-in\chi} e^{\mathbf{L}(\chi)t}, \text{ and} \tag{3.64}$$

$$\tilde{\mathbf{T}}(n|z) = \frac{1}{2\pi}\int_0^{2\pi} d\chi e^{-in\chi} \left[z - \mathbf{L}(\chi)\right]^{-1}. \tag{3.65}$$

Evaluating the contour integral in Eq.(3.65) must in general be done numerically, although it can be done analytically for a single resonant level [97, 181].

The final step is to choose $\mathbf{P}(0)$ so that the FPTD relates directly to the WTD and FCS. For $n>0$, $\mathbf{P}(0)$ must intuitively be the normalized probability vector after a forward jump in the stationary state:

$$\mathbf{P}(0) = \frac{\mathbf{J}_F\bar{\mathbf{P}}}{(\mathbf{I}, \mathbf{J}_F\bar{\mathbf{P}})}. \tag{3.66}$$

Similarly, the initial vector for $n<0$ is

$$\mathbf{P}(0) = \frac{\mathbf{J}_B\bar{\mathbf{P}}}{(\mathbf{I}, \mathbf{J}_B\bar{\mathbf{P}})}. \tag{3.67}$$

With this definition, $F(n|\tau)$ is the probability density that the jump number first reaches n

at time τ, given measurement started after an initial tunneling to the drain at $t = 0$ in the stationary state, and $\tilde{F}(n|z)$ is its Laplace transform:

$$\tilde{F}(n|z) = \frac{\left(\mathbf{I}, \tilde{\mathbf{T}}(0|z)^{-1}\tilde{\mathbf{T}}(n|z)\mathbf{J}_F\bar{\mathbf{P}}\right)}{\left(\mathbf{I}, \mathbf{J}_F\bar{\mathbf{P}}\right)}. \tag{3.68}$$

The inverse Laplace transform yields an explicit equation for $F(n|\tau)$,

$$F(n|\tau) = \frac{1}{2\pi i}\lim_{R\to\infty}\int_{c-iR}^{c+iR} dz\, e^{z\tau}\frac{\left(\mathbf{I}, \tilde{\mathbf{T}}(0|z)^{-1}\tilde{\mathbf{T}}(n|z)\mathbf{J}_F\bar{\mathbf{P}}\right)}{\left(\mathbf{I}, \mathbf{J}_F\bar{\mathbf{P}}\right)}; \tag{3.69}$$

however, $\tilde{F}(n,z)$ is a convenient form for calculating cumulants of the FPTD:

$$\langle\langle \tau_n^k \rangle\rangle^* = (-1)^k \lim_{z\to 0^+}\left[\frac{d^k}{dz^k}\ln\tilde{F}(n|z)\right]. \tag{3.70}$$

Here, the notation $\langle\langle \tau_n^k \rangle\rangle^*$ translates to the kth cumulant of $F(n|\tau)$ and the limit $z \to 0^+$ is necessary since $\mathbf{L}(\chi)$ is singular for $\chi = \{0, 2\pi\}$ [97]. The * notation is chosen to distinguish between cumulants of the WTD and cumulants of the FPTD.

As with the WTD and FCS, we focus on the first $\langle\tau_n\rangle^*$ and second $\langle\langle\tau_n^2\rangle\rangle^*$ cumulants, and their combination into the first-passage time randomness parameter:

$$R_n^* = \frac{\langle\langle\tau_n^2\rangle\rangle^*}{\left(\langle\tau_n\rangle^*\right)^2}. \tag{3.71}$$

3.3.4 Fluctuating-time statistics of a SRL

For the simple case of a SRL, the forward and backward tunneling WTDs are

$$w_F(\tau) = \frac{\Gamma_{10}\Gamma_{01}^D}{A}e^{-\frac{\tau}{2}(\Gamma_{01}+\Gamma_{10})}\left[e^{\frac{\tau}{2}A} - e^{-\frac{\tau}{2}A}\right] \qquad \text{and} \tag{3.72}$$

$$w_B(\tau) = \frac{\Gamma_{01}\Gamma_{10}^D}{B}e^{-\frac{\tau}{2}(\Gamma_{01}+\Gamma_{10})}\left[e^{\frac{\tau}{2}B} - e^{-\frac{\tau}{2}B}\right], \tag{3.73}$$

where

$$A = \sqrt{(\Gamma_{01}-\Gamma_{10})^2 + 4\Gamma_{10}\Gamma_{01}^S} \qquad \text{and} \tag{3.74}$$

$$B = \sqrt{(\Gamma_{01}-\Gamma_{10})^2 + 4\Gamma_{01}\Gamma_{10}^S}. \tag{3.75}$$

Their Laplace transforms are

$$\tilde{w}_F(z) = \frac{\Gamma_{10}\Gamma_{01}^D}{z^2 + (\Gamma_{01} + \Gamma_{10})z + \Gamma_{01}\Gamma_{01}^D} \qquad \text{and} \tag{3.76}$$

$$\tilde{w}_B(z) = \frac{\Gamma_{10}\Gamma_{01}^D}{z^2 + (\Gamma_{01} + \Gamma_{10})z + \Gamma_{01}\Gamma_{10}^D}. \tag{3.77}$$

From Eq.(3.57) the first and second cumulants are

$$\langle\tau\rangle_F = \frac{\Gamma_{01} + \Gamma_{10}}{\Gamma_{10}\Gamma_{01}^D} \tag{3.78}$$

$$\langle\tau\rangle_B = \frac{\Gamma_{01} + \Gamma_{10}}{\Gamma_{01}\Gamma_{10}^D} \tag{3.79}$$

and

$$\langle\langle\tau^2\rangle\rangle_F = \frac{(\Gamma_{01})^2 + \Gamma_{10}(\Gamma_{10} + 2\Gamma_{01}^S)}{(\Gamma_{10}\Gamma_{01}^D)^2} \tag{3.80}$$

$$\langle\langle\tau^2\rangle\rangle_B = \frac{(\Gamma_{10})^2 + \Gamma_{01}(\Gamma_{01} + 2\Gamma_{10}^S)}{(\Gamma_{01}\Gamma_{10}^D)^2}, \tag{3.81}$$

respectively.

For a full derivation of the first-passage time statistics of a SRL, see Ref.[97]. We focus only on the case when $n > 0$, for which the FPTD is

$$\tilde{F}(n|z) = \frac{[\tilde{\mathbf{T}}(n|z)]_{11}}{[\tilde{\mathbf{T}}(0|z)]_{11}}, \tag{3.82}$$

where the simplification arises from the structure of $\mathbf{J}_F$. Using Eq.(3.65), the element $[\tilde{\mathbf{T}}(n|z)]_{11}$ is

$$[\tilde{\mathbf{T}}(n|z)]_{11} = \frac{1}{2\pi}\int_0^{2\pi} d\chi e^{-in\chi}\left[[z - \mathbf{L}(\chi)]^{-1}\right]_{11} \tag{3.83}$$

$$= \frac{z + \Gamma_{01}}{2\pi}\int_0^{2\pi} \frac{d\chi}{e^{in\chi}} \frac{1}{\det[z - \mathbf{L}(\chi)]}. \tag{3.84}$$

The determinant of $[z - \mathbf{L}(\chi)]$ defines an equation in χ with only $e^{i\chi}$, $e^{-i\chi}$, and e^0 terms. It can thus be written as

$$[\tilde{\mathbf{T}}(n|z)]_{11} = \frac{z + \Gamma_{01}}{2\pi}\int_0^{2\pi} \frac{d\chi}{e^{i(n-1)\chi}} \frac{1}{[e^{i\chi} - \lambda_+(z)]\,[e^{i\chi} - \lambda_-(z)]}. \tag{3.85}$$

The quantities $\lambda_+(z)$ and $\lambda_-(z)$ are the upper and lower roots of $\det[z - \mathbf{L}(\chi)]$, respectively, and are known to satisfy $\lambda_+(z) > 1$ and $\lambda_-(z) < 1$ [97]. Eq.(3.85) can then be solved directly using residue theory, as only one pole lies within the contour, or more easily as the $(n-1)^{\text{th}}$

term in the Laurent series expansion of $\left(\left[e^{i\chi}-\lambda_+(z)\right]\left[e^{i\chi}-\lambda_-(z)\right]\right)^{-1}$:

$$[\tilde{\mathbf{T}}(n|z)]_{11}=\frac{(z+\Gamma_{01})\lambda_+(z)}{\lambda_-(z)-\lambda_+(z)}. \tag{3.86}$$

From Eq.(3.82) the first-passage time distribution is then

$$\tilde{F}(n|z)=[\lambda_+(z)]^n \tag{3.87}$$

$$=[\tilde{F}(1|z)]^n. \tag{3.88}$$

All that remains is to evaluate $\lambda_+(z)$:

$$\lambda_+(z)=\frac{-b(z)}{2\Gamma^S_{10}\Gamma^D_{01}}+\frac{\sqrt{b(z)^2-4\Gamma^S_{10}\Gamma^S_{01}\Gamma^D_{10}\Gamma^D_{01}}}{2\Gamma^S_{10}\Gamma^D_{01}}, \tag{3.89}$$

where

$$b(z)=(z+\Gamma_{01})(z+\Gamma_{10})-\left(\Gamma^S_{01}\Gamma^S_{10}+\Gamma^D_{01}\Gamma^D_{10}\right). \tag{3.90}$$

Eq.(3.88) demonstrates that for a SRL the FPTD can be factored and the cumulants are therefore linearly related:

$$\langle\langle\tau^k_n\rangle\rangle^*=(-1)^k\lim_{z\to0^+}\left[\frac{d^k}{dz^k}\ln\tilde{F}(1|z)^n\right]\Big|_{z\to0} \tag{3.91}$$

$$=n\langle\langle\tau^k_1\rangle\rangle^*. \tag{3.92}$$

The first and second cumulants of $F(1|\tau)$ are

$$\langle\tau_1\rangle^*=\frac{\Gamma_{01}+\Gamma_{10}}{\Gamma^S_{10}\Gamma^D_{01}-\Gamma^S_{01}\Gamma^D_{10}} \tag{3.93}$$

and

$$\langle\langle\tau^2_1\rangle\rangle^*=\frac{(\Gamma^S_{01}\Gamma^D_{10}+\Gamma^S_{10}\Gamma^D_{01})(\Gamma_{01}+\Gamma_{10})^2-2(\Gamma^S_{10}\Gamma^D_{01}-\Gamma^S_{01}\Gamma^D_{10})}{(\Gamma^S_{10}\Gamma^D_{01}-\Gamma^S_{01}\Gamma^D_{10})^3}, \tag{3.94}$$

respectively. Their combination, the FPTD randomness parameter, is

$$R^*=\frac{(\Gamma^S_{01}\Gamma^D_{10}+\Gamma^S_{10}\Gamma^D_{01})(\Gamma_{01}+\Gamma_{10})^2-2(\Gamma^S_{10}\Gamma^D_{01}-\Gamma^S_{01}\Gamma^D_{10})^2}{(\Gamma^S_{10}\Gamma^D_{01}-\Gamma^S_{01}\Gamma^D_{10})(\Gamma_{01}+\Gamma_{10})^2}. \tag{3.95}$$

3.3.5 Renewal theory

Eq.(3.88) presents an interesting possibility for how multi-time distributions could be related to one another. It is, in fact, an example of a branch of analysis called renewal theory, which is based on the titular renewal assumption. For first-passage times, the factorization in Eq.(3.88) is one expression of the renewal assumption. It can be written alternatively as

$$F(n|\tau_n; n'|\tau_{n'}) = F(n|\tau_n)\, F(n'-n|\tau_{n'}-\tau_n), \tag{3.96}$$

where $F(n|\tau_n; n'|\tau_{n'})$ is the joint conditional probability density that the jump number first reaches n at time τ_n and first reaches n' at time $\tau_{n'}$ [97]. We can write the renewal assumption similarly for waiting times:

$$w_2(\tau, \tau') = w(\tau)w(\tau'), \tag{3.97}$$

where $w_2(\tau, \tau')$ is the joint conditional probability density that, given an initial tunneling, the system waits time τ until the next tunneling and then waits another time τ' for the tunneling after that. The renewal assumption therefore implies that successive waiting times are independently and identically distributed and the system state is "renewed" after each waiting time. The same logic follows for first-passage times.

If the renewal assumption is violated, then successive waiting times are no longer independent, temporal correlations emerge in quantum dynamics, and we see non-renewal behavior. As we will observe, non-renewal dynamics can emerge even under the Markovian assumption, indicating that correlations between successive waiting times arise from the internal dynamics of the quantum system. Although in nanoscale electron transport non-renewal statistics are a relatively new research premise [44, 73, 74, 78, 97, 155, 175], they have a long history in chemical physics, where they were used to describe single-molecule processes in spectroscopy[147–149, 183] and kinetics [144, 184].

Correlations between successive waiting times τ and τ' are described by the Pearson correlation coefficient:

$$p = \frac{\langle \tau\tau' \rangle - \langle \tau \rangle^2}{\langle\langle \tau^2 \rangle\rangle}. \tag{3.98}$$

Here, $\langle \tau\tau' \rangle$ is the first moment of the second-order distribution $w_2(\tau, \tau')$; in order to obtain the Pearson correlation coefficient, we need moments of higher-order WTDs.

Just as we can define probability distributions for time delays between two tunneling events, so can we also define distributions for multiple time delays between a series of tunneling

events: the higher-order time distributions. Consider the second-order WTD [78],

$$w_2(\tau,\tau') = \frac{\left(\mathbf{I},\mathbf{J}e^{\mathbf{L}_0\tau'}\mathbf{J}e^{\mathbf{L}_0\tau}\mathbf{J}\bar{\mathbf{P}}\right)}{(\mathbf{I},\mathbf{J}\bar{\mathbf{P}})}. \tag{3.99}$$

The top line is the joint probability that the system starts in $\bar{\mathbf{P}}$ and undergoes quantum jump $\mathbf{J}$, after which it evolves according to $\mathbf{L}_0$, until another quantum jump of type $\mathbf{J}$ occurs after a time τ, and the system again evolves according to $\mathbf{L}_0$ until the final quantum jump of type $\mathbf{J}$ occurs after another waiting time τ'. As usual, the bottom line provides the probability for quantum jump $\mathbf{J}$ to occur at any time during the stationary state, so that $w_2(\tau,\tau')$ is the probability density that three quantum jumps of type $\mathbf{J}$ will be separated by successive waiting times τ and τ', conditioned upon the probability density of the initial jump.

The first moment $\langle\tau\tau'\rangle$ is easily obtained via a moment generating function:

$$\langle\tau\tau'\rangle = \frac{\partial}{\partial z}\frac{\partial}{\partial z'}\tilde{w}(z,z')\Big|_{z=z'=0} \tag{3.100}$$

$$= \frac{(\mathbf{I},\mathbf{J}\mathbf{L}_0^{-2}\mathbf{J}\mathbf{L}_0^{-2}\mathbf{J}\bar{\mathbf{P}})}{(\mathbf{I},\mathbf{J}\bar{\mathbf{P}})}, \tag{3.101}$$

where

$$\tilde{w}(z,z') = \int_0^\infty\int_0^\infty d\tau'\,d\tau\,e^{-(z\tau+z'\tau')}w(\tau,\tau'). \tag{3.102}$$

The Pearson correlation coefficient between two subsequent first-passage times, p^*, follows the same definition as Eq.(3.98). Unfortunately, the method presented in Eq.(3.68) does not easily transfer to $F(n|\tau;n'|\tau_{n'})$. Ptaszynski has shown, however, that we can obtain the Pearson correlation coefficient from FPTDs of higher n [97]. To demonstrate, consider the variance of $F(2|\tau)$, which is

$$\langle\langle\tau_2^2\rangle\rangle^* = \langle\tau_2^2\rangle^* - (\langle\tau_2\rangle^*)^2. \tag{3.103}$$

The average $\langle\ldots\rangle$ here implies an integral over all possible τ_2; so that the second term, for example, is

$$(\langle\tau_2\rangle^*)^2 = \left(\int_0^\infty d\tau_2\,\tau_2 F(2|\tau_2)\right)^2. \tag{3.104}$$

We are interested in the joint distribution $F(1|\tau_1;2|\tau_2)$, but we are *not* searching for correlations between τ_1 and τ_2; we expect that τ_2 will automatically be linearly correlated with τ_1, since $\tau_2 = \tau_1 + \tau_{1'}$. Rather, we are searching for the correlation between τ_1 and $\tau_{1'}$. With this in

mind, we write

$$F(1|\tau_1;2|\tau_2) = F(1|\tau 1;2|\tau_1+\tau_{1'}) \tag{3.105}$$

and

$$F(1|\tau_1) = \int_0^\infty d\tau_{1'}\, F(1|\tau_1;2|\tau_1+\tau_{1'}) \tag{3.106}$$

$$F(1|\tau_{1'}) = \int_0^\infty d\tau_1\, F(1|\tau_1;2|\tau_1+\tau_{1'}), \tag{3.107}$$

where $F(1|\tau_{1'})$ is the probability density that the jump number first increases from $+1$ to $+2$ after a time delay of $\tau_{1'}$. From here we use the probabilistically self-evident identity, defined for $k = \{1, 2, \ldots\}$, that

$$\langle \tau_2^k \rangle^* = \int_0^\infty \int_0^\infty d\tau_1\, d\tau_{1'}\, (\tau_1+\tau_{1'})^k\, F(1|\tau_1;2|\tau_1+\tau_{1'}), \tag{3.108}$$

and we obtain the relations

$$(\langle \tau_2 \rangle^*)^2 = (\langle \tau_1 \rangle^*)^2 + 2\langle \tau_1\tau_{1'} \rangle^* + \langle \tau_{1'} \rangle^* \tag{3.109}$$

$$= 2(\langle \tau_1 \rangle^*)^2 + 2\langle \tau_1\tau_{1'} \rangle^*, \text{ and} \tag{3.110}$$

$$\langle \tau_2^2 \rangle^* = \langle \tau_1^2 \rangle^* + 2\langle \tau_1\tau_{1'} \rangle^* + \langle \tau_{1'}^2 \rangle^* \tag{3.111}$$

$$= 2\langle \tau_1^2 \rangle^* + 2\langle \tau_1\tau_{1'} \rangle^*, \tag{3.112}$$

where the correlation function of two first-passage times is defined as

$$\langle \tau_1\tau_{1'} \rangle^* = \int_0^\infty \int_0^\infty d\tau_1 d\tau_{1'}\, (\tau_1\tau_{1'}) F(1|\tau_1;2|\tau_1+\tau_{1'}). \tag{3.113}$$

Using the above averages, the Pearson coefficient is

$$p^* = \frac{\langle \tau_1\tau_{1'} \rangle^* - \langle \tau_1 \rangle^* \langle \tau_{1'} \rangle^*}{\langle\langle \tau_1^2 \rangle\rangle^*} \tag{3.114}$$

$$= \frac{\langle\langle \tau_2^2 \rangle\rangle^*}{2\langle\langle \tau_1^2 \rangle\rangle^*} - 1. \tag{3.115}$$

We have seen that for a SRL the FPTD renewal assumption is satisfied, which means $F(1,2|\tau_1,\tau_2) = F(1|\tau_1)\, F(1|\tau_1)$, from Eq.(3.96). This simplifies much of Eq.(3.104) and we can easily show that, as a result, $\langle \tau_1\tau_{1'} \rangle^* = \langle \tau_1 \rangle^* \langle \tau_{1'} \rangle^*$. Evaluating the joint WTD in Eq.(3.99) for a SRL yields $\langle \tau\tau' \rangle = \langle \tau \rangle^2$ and clearly for both fluctuating-time distributions the Pearson correlation coefficient is $p = p^* = 0$.

3.4 Connections

From the previous sections, it is clear that there are a multitude of quantum statistics available, all describing the same transport scenario. An obvious question is whether all statistics provide complementary information, or whether, as is more interesting, there is information unique to each? We naturally expect that, if fixed-time statistics contained identical information to fluctuating-time statistics, we should be able to reproduce the current cumulants from cumulants of the WTD or FPTD.

For example, the total average current is intuitively related to the average waiting time of the forward and backward distributions via

$$\langle I\rangle_T = \langle I\rangle_F - \langle I\rangle_B \tag{3.116}$$

$$= \frac{1}{\langle\tau\rangle_F} - \frac{1}{\langle\tau\rangle_B}, \tag{3.117}$$

where $\langle I\rangle_F$ and $\langle I\rangle_B$ are the forward and backward currents, respectively. Here, we see a relationship between the first cumulant of the directional current distribution and the first cumulant of the directional WTD. Two questions arise; first, is Eq.(3.117) always true and if not under what conditions is it true? And secondly, do similar relations exist between all higher-order cumulants?

These queries are neatly encapsulated by renewal theory. We can show that there exists exact relations between the FCS and cumulants of the WTD when the renewal assumption, Eq.(3.97), is satisfied. Although Brandes initially demonstrated this for just a single-reset open quantum system [150], Budini [74] and Albert *et al.* [157] have shown that, under the renewal and unidirectional assumptions, the same one-to-one relations between WTD and FCS exist for multiple-reset systems. In the next section, we turn to the details of this derivation, following the works in Ref.[150], Ref.[74], and Ref.[73]. The calculations are performed in the forward tunneling direction, but all results are equivalent for backward tunneling as well.

We start with the moment generating function of the current distribution:

$$M(\chi,t) = \sum_{n=0} e^{in\chi}P(n,t), \tag{3.118}$$

where the sum is for $n \geq 0$ since the transport is unidirectional. For $n > 0$ the probability $P(n,t)$ can be written generally in terms of the WTD:

$$P(n,t) = \int_0^t \int_0^{t_{n-1}} \dots \int_0^{t_0} dt_{n-1}dt_{n-2}\dots dt_0\, w_n(t_0, t_1-t_0, \dots, t_{n-1}-t_{n-2}, t-t_{n-1})P(0,t_0). \tag{3.119}$$

In the stationary state the joint WTD does not depend on the initial time t_0. If the renewal

assumption is satisfied, furthermore, then the joint WTD also factorizes:

$$P(n,t) = \int_0^t \int_0^{t_{n-1}} \dots \int_0^{t_0} dt_{n-1} dt_{n-2} \dots dt_0 \, w(t-t_{n-1}) w(t_{n-1}-t_{n-2}) \dots w(t_1-t_0) P(0,t_0) \tag{3.120}$$

Recognizing that $P(1,t) = \int_0^t dt_0 w(t-t_0) P(0,t_0)$, and so on, $P(n,t)$ can now be written recursively as

$$P(n,t) = \int_0^t dt_{n-1} \, w(t-t_{n-1}) P(n-1,t_{n-1}). \tag{3.121}$$

Eq.(3.121) is now inserted into the moment generating function to obtain

$$M(\chi,t) = P(0,t) + \sum_{n=1}^{\infty} \int_0^t dt_{n-1} \, w(t-t_{n-1}) e^{in\chi} P(n-1,t_{n-1}) \tag{3.122}$$

$$= P(0,t) + e^{i\chi} \int_0^t dt_{n-1} \, w(t-t_{n-1}) M(\chi,t_{n-1}). \tag{3.123}$$

As usual with convolution integrals, it is easier to work in Laplace space:

$$\tilde{M}(\chi,z) = \tilde{P}(0,z) + e^{i\chi} \tilde{w}(z) \tilde{M}(\chi,z). \tag{3.124}$$

Rearranging gives us

$$\tilde{M}(\chi,z) = \frac{\tilde{P}(0,z)}{1 - e^{i\chi}\tilde{w}(z)}, \tag{3.125}$$

which in time-space is given by the inverse Laplace transform

$$M(\chi,t) = \frac{1}{2\pi i} \int_{c-i\infty}^{c+i\infty} \tilde{M}(\chi,z) = \sum_{z_k} \text{Res}\left(\tilde{M}(\chi,z), z_k\right). \tag{3.126}$$

Examining $\tilde{M}(\chi,z)$, we see that the poles are those values $\{z_k(\chi)\}$ that satisfy the equation

$$0 = 1 - w(z_k(\chi)) e^{i\chi}. \tag{3.127}$$

If this equation has one solution, corresponding to a simple pole $z_0(\chi)$, then the integral is easily evaluated:

$$M(\chi,t) = \lim_{z \to z_0(\chi)} (z - z_0(\chi)) \frac{\tilde{P}(0,z) e^{zt}}{1 - e^{i\chi}\tilde{w}(z)} \tag{3.128}$$

$$= \tilde{P}(0, z_0(\chi)) e^{z_0(\chi) t}. \tag{3.129}$$

We now write the moment generating function in terms of the cumulant generating function,

as in Eq.(3.44), and note that in the long-time limit, as $t \to \infty$, the cumulant generating function is given by Eq.(3.19), the large deviation principle:

$$\lim_{t\to\infty} M(\chi,t) = \lim_{t\to\infty} e^{K(\chi,t)} \tag{3.130}$$

$$\approx e^{\Lambda_{\max} t}. \tag{3.131}$$

Applying the long-time limit to Eq.(3.129) as well, we see that the exponential term dominates $\tilde{P}(0, z_0(\chi))$ and so in this limit $\Lambda_{\max} = z_0(\chi)$.

We now demonstrate that the same result also holds in the case when $\tilde{M}(\chi, z)$ poses multiple poles of any order. Suppose that $\tilde{M}(\chi, z)$ has M poles $z_0(\chi), \ldots, z_{M-1}(\chi)$, where $z_0(\chi)$ is the the dominant pole with the largest real part. For a pole of order m, the residue in Eq.(3.126) is

$$\frac{1}{(m-1)!}\frac{d^{m-1}}{dz^{m-1}}\left[(z - z_k(\chi))\tilde{M}(\chi,z)\right]\Big|_{z=z_k(\chi)} = \alpha_{z_k(\chi)}(t)e^{tz_k(\chi)}, \tag{3.132}$$

where $\alpha_{z_k(\chi)}(t)$, a polynomial of order $m-1$, comes from evaluating the successive $(m-1)$ derivatives at $z = z_k(\chi)$. The moment generating function is then given by Eq.(3.126), which is

$$M(\chi,t) = \sum_{k=0}^{M-1} \alpha_{z_k(\chi)}(t)e^{tz_k(\chi)} \tag{3.133}$$

$$= \alpha_{z_0(\chi)}(t)e^{tz_0(\chi)}\left[1 + \sum_{k=1}^{M-1} \alpha_{z_k(\chi)}(t)e^{tz_k(\chi)/z_0(\chi)}\right]. \tag{3.134}$$

In the long-time limit the exponential term $e^{tz_0(\chi)}$ dominates the expression, yielding

$$M(\chi,t) \approx e^{tz_0(\chi)} \tag{3.135}$$

Therefore, regardless of the nature of the poles, in the long-time limit we are left with a dominant solution of Eq.(3.127): $z_0(\chi) = \Lambda_{\max}(\chi)$.

With this information, we rewrite Eq.(3.127) in the long-time limit as

$$0 = i\chi + \ln \tilde{w}(z)\Big|_{z=\Lambda_{\max}(\chi)}. \tag{3.136}$$

We note that at $\chi = 0$, $\mathbf{L}(\chi) = \mathbf{L}$ and $\Lambda_{\max}(0) = 0$, since all other eigenvalues are negative due to the structure of the Liouvillian. Let us now take successive derivatives of Eq.(3.136) with respect to χ and then set $\chi = 0$, as we do when generating current cumulants in Eq.(3.21).

The first derivative yields

$$0 = -i\frac{\partial}{\partial\chi}\left[i\chi + \ln\tilde{w}(z)\right]\Big|_{z=\Lambda_{\max}(\chi);\chi=0} \tag{3.137}$$

$$= 1 - i\frac{\partial z}{\partial\chi}\frac{\partial \ln\tilde{w}}{\partial z}\Big|_{z=\Lambda_{\max}(\chi);\chi=0} \tag{3.138}$$

$$= 1 - i\frac{\partial\Lambda_{\max}}{\partial\chi}\Big|_{\chi=0}\frac{\partial \ln\tilde{w}}{\partial z}\Big|_{z=0}. \tag{3.139}$$

Comparing Eq.(3.139) with the definitions of the WTD cumulants and the FCS in Eq.(3.57) and Eq.(3.21), respectively, we see that it contains the first cumulants of both distributions:

$$0 = 1 - \langle\langle I\rangle\rangle\,\langle\langle\tau\rangle\rangle, \qquad \text{so that} \tag{3.140}$$

$$\langle\langle I\rangle\rangle = \frac{1}{\langle\langle\tau\rangle\rangle}, \tag{3.141}$$

which is the intuitive relationship outlined earlier in Eq.(3.117). Taking the second derivative we get

$$0 = (-i)^2\frac{\partial^2}{\partial\chi^2}\left[i\chi + \ln\tilde{w}(z)\right]\Big|_{z=\Lambda_{\max}(\chi);\chi=0} \tag{3.142}$$

$$0 = \frac{\partial}{\partial\chi}\left[\frac{\partial z}{\partial\chi}\frac{\partial \ln\tilde{w}}{\partial z}\right]\Big|_{z=\Lambda_{\max}(\chi);\chi=0} \tag{3.143}$$

$$0 = \frac{\partial^2\Lambda_{\max}}{\partial\chi^2}\Big|_{\chi=0}\frac{\partial \ln\tilde{w}}{\partial z}\Big|_{z=0} + \left(\frac{\partial\Lambda_{\max}}{\partial\chi}\right)^2\Big|_{\chi=0}\frac{\partial^2 \ln\tilde{w}}{\partial z^2}\Big|_{z=0}, \tag{3.144}$$

which, after comparison with the definitions of the second-order current and waiting time cumulants, reduces to

$$\frac{\langle\langle I^2\rangle\rangle}{\langle\langle I\rangle\rangle} = \frac{\langle\langle\tau^2\rangle\rangle}{\langle\langle\tau\rangle\rangle^2}. \tag{3.145}$$

The LHS of Eq.(3.145) is the Fano factor and the RHS is the randomness parameter. These quantities, therefore, provide a direct test of whether the transport is renewal; we can plot the Fano factor alongside the randomness parameter and identify non-renewal behavior where they deviate.

Continuing, we get all relationships between higher-order cumulants as well; the skewness, for example, is

$$\frac{\langle\langle I^3\rangle\rangle}{\langle\langle I\rangle\rangle} = 3\frac{\langle\langle\tau^2\rangle\rangle^2}{\langle\langle\tau\rangle\rangle^4} - \frac{\langle\langle\tau^3\rangle\rangle}{\langle\langle\tau\rangle\rangle^3}, \tag{3.146}$$

and so on.

This mapping between the two sets of statistics unfortunately does not hold for bidirectional transport. As a further disappointment, although we can define relations between the cumulants of the WTD and current distribution in either the forward or backward direction, we cannot combine them to reproduce the appropriate cumulants of the total current distribution $\langle\langle I^k\rangle\rangle_T$. The obvious exception is the physically evident relation for the average current in Eq.(3.117). Not only does it relate the first cumulant of the directional WTDs to the first cumulant of the total current distribution, but it has the additional property of being true regardless of whether the renewal assumption is satisfied. To see, we will consider the forward current $\langle I\rangle_F$, which is reconstructed from the WTD in the long-time limit as

$$\langle I\rangle = \lim_{N\to\infty} \frac{N}{\langle \tau_1 + \ldots + \tau_N\rangle_F}. \tag{3.147}$$

Now, the average waiting times can be simplified without using the renewal assumption:

$$\langle \tau_1 + \tau_2 + \ldots + \tau_N\rangle_F = \int_0^\infty d\tau_N \ldots \int_0^\infty d\tau_2 \int_0^\infty d\tau_1 \, (\tau_1 + \tau_2 + \ldots + \tau_N)\, w_F(\tau_1, \tau_2 \ldots, \tau_N). \tag{3.148}$$

$$= \sum_{k=1}^{N} \int_0^\infty d\tau_k \, \tau_k \, w_F(\tau_k) \tag{3.149}$$

$$= N\langle\tau\rangle_F. \tag{3.150}$$

Eq.(3.147) then reduces to

$$\langle I\rangle_F = \frac{1}{\langle\tau\rangle_F}, \tag{3.151}$$

The backward current can be similarly defined, and thus Eq.(3.117) is satisfied. We cannot do the same for higher-order cumulants, since for $k > 1$ we cannot write $\langle\langle I^k\rangle\rangle$ as an explicit reconstruction from the direction WTDs. In renewal theory, as a result, the WTD is evidently limited to unidirectional transport.

It has recently been shown, however, that when the renewal assumption is satisfied, similar relations exist between the FCS and cumulants of the FPTD, relations that hold even when the transport is bidirectional [97]. We will not reproduce the derivation here, but rather direct the reader to Ref.[97] for an explicit overview. In Eq.(3.92) we saw that for renewal transport all FPTD cumulants are linearly related, so the relations between current cumulants and FPTD

cumulants can all be expressed using $F(1|\tau)$:

$$\langle I\rangle_T = \frac{n}{\langle\tau_n\rangle^*} = \frac{1}{\langle\tau_1\rangle^*} \tag{3.152}$$

$$\frac{\langle\langle I^2\rangle\rangle_T}{\langle I\rangle_T} = n\frac{\langle\langle\tau_n^2\rangle\rangle^*}{(\langle\tau_n\rangle^*)^2} = \frac{\langle\langle\tau_1^2\rangle\rangle^*}{(\langle\tau_1\rangle^*)^2}, \tag{3.153}$$

which hold even when the transport is bidirectional. Examining the exact results in Eq.(3.95) and Eq.(3.28), we see that the Fano factor and FPTD randomness parameter do indeed match.

We might expect that, since Eq.(3.152) is analogous to Eq.(3.147), it also holds regardless of the renewal assumption. In this case, though, the average current is reconstructed from the FPTD as

$$\langle I\rangle_T = \lim_{N\to\infty}\frac{N}{\langle\tau_N\rangle^*}, \tag{3.154}$$

and this cannot be simplified since for non-renewal statistics $\langle\tau_N\rangle \neq N\langle\tau_1\rangle$ and in general $F(k|\tau) \neq F(1|\tau_1;\ldots;1|\tau_1^{(k)})$, unless the transport is unidirectional.

As we saw in Section (3.3.5), non-renewal transport is accompanied by temporal correlations in the first-passage and waiting times. This is an example of the unique information only available to the fluctuating-time distributions when the renewal assumption is violated.

3.5 Summary

Upon finishing this chapter and the preceding one, the reader should have all the tools necessary to calculate the FCS, the WTD, and the FPTD from the master or rate equations. In the remaining four chapters, we will use these three fluctuation statistics to describe various transport scenarios in nanoscale quantum systems.

The key benefit of using the fluctuating-time statistics compared to just the FCS is that they are able to characterize behavior on short timescales. Correlations between successive waiting or first-passage times are especially interesting because they indicate that the molecule is not "renewed" after each tunneling to the drain, and that some effect is felt between tunneling electrons. In the following chapters, we will see that correlations can arise from a variety of physical effects.

Cotunneling through an Anderson impurity

This chapter contains material that has been previously published in the following journal articles:

Non-renewal statistics in quantum transport from the perspective of first-passage and waiting time distributions, S.L. Rudge and D.S. Kosov, Phys. Rev. B, **99**, 115426 (2019)

Distribution of waiting times between electron cotunneling events, S.L. Rudge and D.S. Kosov, Phys. Rev. B, **98**, 245402 (2018)

4.1 Motivation

In Chapter 2, we discussed the difference between sequential tunneling, essentially classical processes arising from the leading term in a perturbative expansion around H_T, and cotunneling, purely quantum processes arising from the next-to-leading term. Previous work on cotunneling has shown that it can produce interesting fluctuation behavior, which has until now only been researched using the FCS. To our knowledge, all previous work on fluctuating-time statistics has only included only sequential tunneling when calculating the WTD or FPTD.

On the one hand, theorists have been well justified in ignoring cotunneling processes in fluctuating-time statistics as they are relatively difficult to calculate. From an experimental point of view, however, cotunneling is regularly present in molecular junctions; all that is needed is a strong enough system-electrode coupling so that the electron wavefunction can delocalize across the configuration. In this chapter, then, we propose to examine the effect that cotunneling processes have on the WTD and FPTD.

To focus this rather general goal, we will aim to supplement previous research, [46, 47, 185–188] demonstrating that super-Poissonian noise arises in an Anderson impurity from inelastic cotunneling processes, with complementary results for fluctuating-time statistics in the same

transport scenario. To this end, we will devote the introduction to a detailed review of cotunneling, alongside the specific motivation behind our investigation. Section 4.3 contains the Anderson model, the exact form for the sequential tunneling and cotunneling rates, and the associated rate equation. Our results are in Section 4.4. We find that this super-Poissonian noise is indeed accompanied by small negative correlations between successive first-passage times.

4.2 Introduction

To understand the mechanism of cotunneling, let us first describe sequential tunneling, following Fermi's golden rule in Eq.(2.63). To 1^{st}-order, each rate contains only one scattering upon H_T. A sequential tunneling transition thus involves a single electron tunneling from electrode α to the quantum system, or vice versa. Cotunneling, in contrast, involves two scatterings upon H_T separated by an intermediate "virtual" state with lifetime $\mathcal{O}(\eta^{-1})$. There are no limitations on the energy of this virtual state, and so there is a possibility that cotunneling occurs through energetically forbidden levels [8, 84, 189]. It is commonly thought that this is an example of the Heisenberg uncertainty principle, $\Delta t \Delta E \sim \hbar$. Energy conservation can be violated only if the electron spends a sufficiently short time in the virtual state; although we note that this notion has recently been challenged by Romito and Gefen [190].

The most common cotunneling process we are interested in is that of an electron tunneling from the source to the molecule and then from the molecule to the drain. The net result is that the charge occupation of the molecule remains the same and an extra electron is detected in the drain. Other examples include the reverse process from the drain to the source, or instead one that involves two tunnelings from the same electrode. Regardless of the net result, we can generally classify cotunneling processes into two categories. If the molecule is left in the same energetic state after the cotunneling as it was before, then it is an *elastic* cotunneling process, and if it is left in an excited or de-excited state, then it is an *inelastic* cotunneling process. An example of each is shown in Fig.(4.1a) and Fig.(4.1b).

Since cotunneling can occur through energetically forbidden levels, it actually becomes the dominant contribution to the current when all levels are outside the bias window and sequential tunneling is exponentially suppressed. Indeed, cotunneling was first detected experimentally by Geerligs *et al.* [191] as a leakage current in the Coulomb blockade regime. Their measurement was preceded by the theory of Averin and Odintsov, who predicted inelastic cotunneling in 1989 [192]; the modern combined inelastic and elastic theory was subsequently detailed simultaneously by Averin and Nazarov [193, 194].

Since then, the effect of cotunneling on quantum observables has been explored for a wide variety of transport scenarios. Similarly to the initial measurements made by Geerligs *et al.*,

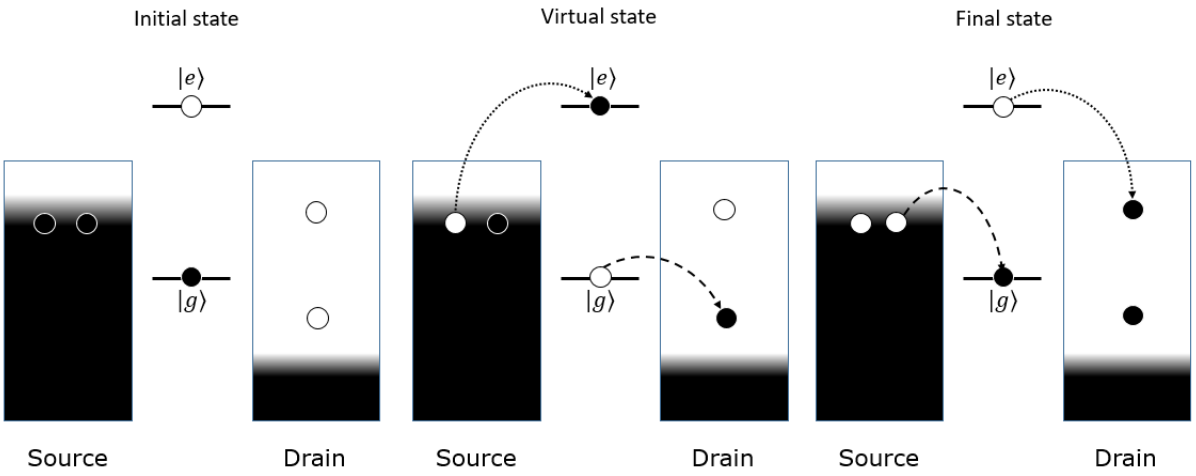

(a) Example schematic of two different elastic cotunneling processes: one through the ground state, $|g\rangle$, and one through the excited state $|e\rangle$. In the lower transition, denoted by a dash line, the ground state level is initially occupied. An electron then tunnels from this level to the drain, leaving the system in the virtual empty state $|0\rangle$, before another electron tunnels in from the source to again fill the ground state. By contrast, the top process, denoted by a dotted line, starts with the system initially empty. An electron then tunnels into $|e\rangle$ in the virtual state, before another electron tunnels out again from the excited state to the drain. In both processes, the net result is that the system has the same charge occupation number as it did before the cotunneling and it is also in the same energetic state, but an extra electron has been counted in the drain.

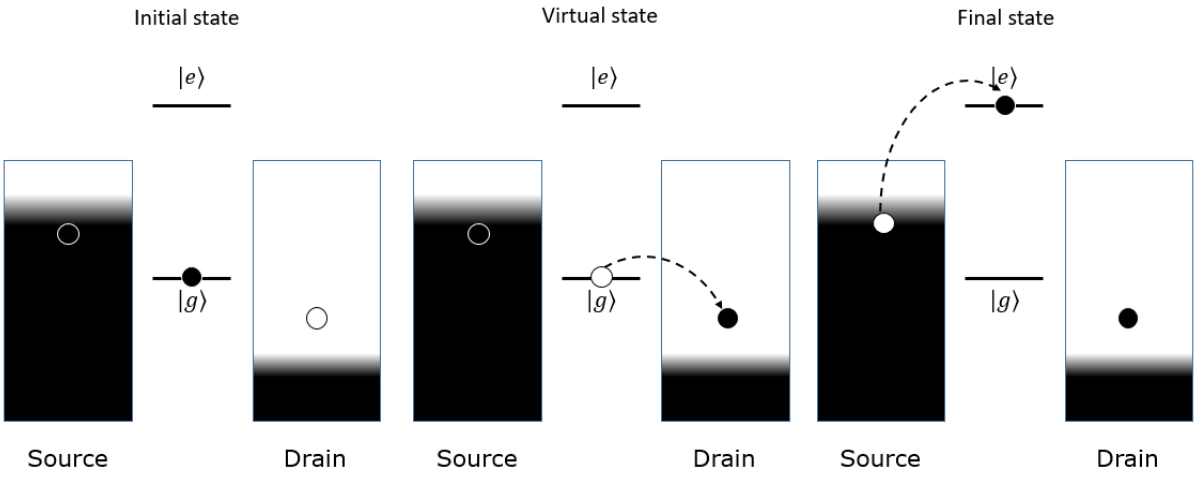

(b) Example schematic of an inelastic cotunneling process. Here, the system is initially occupied by an electron in the ground state. It tunnels out to leave the system empty in the virtual state, until finally another electron tunnels into the excited state. The net result, then, is that the charge occupation of the system is the same before and after the cotunneling, and an extra electron has been counted in the drain, but after the cotunneling the system is in an excited state as compared to before.

Franceschia *et al.* [195] observed leakage current in the Coulomb blockade regime due to inelastic and elastic cotunneling processes and were able to distinguish each. Koch and von Oppen have investigated cotunneling in the context of electron-phonon interactions, and their elegant formalism for regularizing analytic cotunneling rates forms the basis from which we derive all results in Appendix C.2 [173, 196]. Turek and Matveev [197], meanwhile, used cotunneling theory to explain the behavior of low-temperature thermopower in a single electron transistor. Other research has focused on heat conductance [198, 199], transport in double quantum dots [200, 201], molecular or nanoparticle arrays [202, 203], and inelastic cotunneling spectroscopy [204–207]; this last being one of the most useful potential applications.

Since cotunneling is a purely quantum effect, it has also attracted interest from the point of view of current fluctuations. Cotunneling has been shown to affect the shot noise in carbon nanotubes [208], of interacting levels with different molecule-electrode couplings [42], and in multi-level quantum dots in the resonant tunneling regime [209], where cotunneling appears as a small correction to the sequential current. Cotunneling effects on the FCS, additionally, have been reported for non-Markovian systems [120] and single-electron transistors [118]. Most interestingly, several groups [46, 47, 185] have reported that inelastic cotunneling processes can induce super-Poissonian shot noise in interacting systems: drastically different from the sub-Poissonian noise usually attributed to, say, a quantum dot experiencing sequential transitions under the Coulomb blockade. Experimental measurements on semiconductor quantum dots [186, 187] and carbon nanotubes [188] have also detected super-Poissonian shot noise due to inelastic cotunneling, which supports these theoretical predictions. To understand this interesting mechanism, we will use the plots in Fig.(4.2a) and Fig.(4.2b), which have been reprinted from Ref.[46] and Ref.[47], respectively.

At low voltages, $V_{SD}/2 < 0.5\text{meV}$, $\varepsilon_\downarrow$ is below the bias window and $\varepsilon_\uparrow$ is above it; the dominant transport pathway is elastic cotunneling through either level. This results in Poissonian transport and $F = 1$. Between $0.5\text{meV} \geq V_{SD}/2 \geq 1.5\text{meV}$, however, $\varepsilon_\uparrow$ is fully within the bias window while $\varepsilon_\downarrow$ is still below. Now there are two distinct tranport pathways: sequential tunneling through the spin-$\uparrow$ level and elastic cotunneling through the spin-$\downarrow$ level. These two pathways are connected by inelastic cotunneling processes that induce a spin-flip and switch between them, although there can also be relaxation from $\uparrow \rightarrow \downarrow$. The transport in this regime is thus best described as a telegraphic switching process, which is naturally accompanied by an increase in the noise, in this case up to $F \simeq 2$ at $V_{SD}/2 \simeq 1\text{meV}$. Since the transport is spending significant periods of time in each tunneling pathway, with telegraphic switching in-between, we might naturally expect that there will be positive correlations between successive waiting or first-passage times in this regime.

Before we can introduce the rate equation and subsequent results, however, there are some technical points that warrant discussion. First, since elastic cotunneling events do not change the state of the quantum system, they will not appear in the standard rate equation. Brandes'

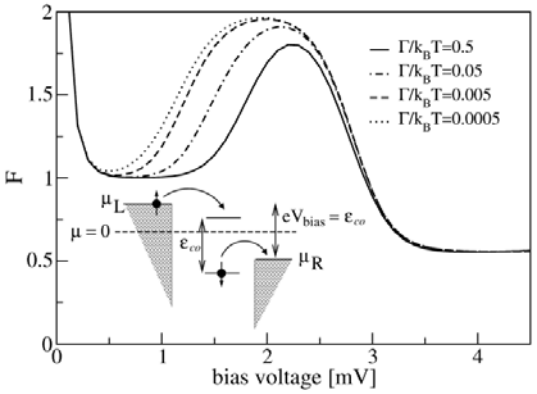

(a) Reprinted with permission from Ref.[46], © 2015 American Physical Society.

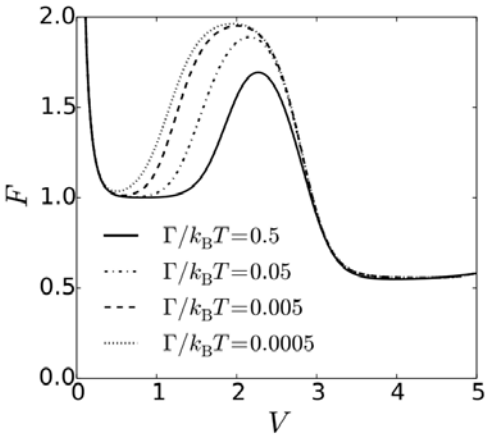

(b) Reprinted with permission from Ref.[47], © 2015 American Physical Society.

Figure 4.2: Plots of the Fano factor as a function of bias voltage for an Anderson impurity with cotunneling effects included. In both figures, the energies of the spin split electronic levels are $\varepsilon_\uparrow = 0.5$meV and $\varepsilon_\downarrow = -1.5$meV, the Coulomb repulsion is $U = 4$meV, the temperature is $T = 75\mu$eV, and the system-electrode coupling is $\gamma = 0.5T$. The Fano factor in (a) is calculated using a rigorous real-time diagrammatic method, while (b) is calculated using the less accurate rate equation approach.

definition of the WTD, consequently, fails to include elastic cotunneling processes. The n-resolved rate equation, on the other hand, *will* include elastic cotunneling processes, as they do change the jump number n. The WTD defined from the idle-time probability, therefore, does incorporate elastic cotunneling events and it is this definition that we must use.

Even defined from the n-resolved master equation, the WTD is still insufficient in the voltage regime that induces super-Poissonian noise; the spin-$\downarrow$ level is below the bias window and the transport is bidirectional. In this regime, therefore, we must use the FPTD instead. This begs the question of why, if the FPTD is equivalent to the WTD for unidirectional transport and can also be defined in the bidirectional case, we would still include the WTD at all? The answer is that, from a computational point of view, it is much easier to obtain the WTD cumulants than the FPTD cumulants, and we can also calculate the WTD in time-space; the numerical inverse Laplace transform of the FPTD being too difficult for the Anderson impurity.

As with any theory, the overarching goal is to see experimental verification. We envision great difficulty in this area, because any measurement of a cotunneling process will collapse the virtual state [64, 210]. Recently, however, Haack *et al.* [174] have proposed a possible method for experimentally reconstructing the WTD, including quantum processes, from low order charge correlation functions.

Finally, we need to discuss the appropriate limits under which we can apply the rate equation. Cotunneling has previously been explored via a comprehensive real-time diagrammatic method [46, 120, 211, 212]; however, the T-matrix approach is a suitable approximation for this more rigorous method when the dynamics does not exhibit non-Markovian phenomena

[47]. This occurs for large temperatures $T \gg \gamma$, a condition that we abide by with $\gamma = 0.5T$. An example of this contrast is provided by the two calculations of super-Poissonian shot noise from Thielmann *et al.*, who used the rigorous diagrammatic method, and Kaasbjerg *et al.*, who used the rate equation; for the chosen parameters there is not more than a 10% difference anywhere, which we can see in Fig.(4.2a) and Fig.(4.2b).

4.3 Anderson impurity model

If we take the conceptual model for a molecular orbital in Eq.(1.6) and assume that the molecule is completely rigid, then all vibrational terms disappear and we are left with the Hamiltonian for an Anderson impurity:

$$H_Q = \sum_\sigma \varepsilon_\sigma a_\sigma^\dagger a_\sigma + U n_\uparrow n_\downarrow. \tag{4.1}$$

First introduced to describe local magnetic impurities in metals [213], Eq.(4.1) has since found great use in molecular electronics theory, where U generally describes repulsive electron-electron interactions within the orbital.

The corresponding Fock space is spanned by four basis vectors; the molecule can either be empty, occupied by a single spin-$\uparrow$ electron, occupied by a single spin-$\downarrow$ electron, or occupied by a spin-$\uparrow$ and spin-$\downarrow$ electron. When considering only the pure states, the associated χ-dependent probability vector is

$$\mathbf{P}(\chi, t) = \left[P_0(\chi, t), P_\uparrow(\chi, t), P_\downarrow(\chi, t), P_2(\chi, t)\right]^T. \tag{4.2}$$

When coupled to two macroscopic particle baths as in the electrode-system-electrode configuration we consider, the corresponding interaction Hamiltonian is

$$H_T = \sum_\alpha \sum_{\mathbf{k}_\alpha, \sigma} t_{\mathbf{k}_\alpha, \sigma} \left(a_{\mathbf{k}_\alpha}^\dagger a_\sigma + a_\sigma^\dagger a_{\mathbf{k}_\alpha} \right). \tag{4.3}$$

Although other groups have previously derived the sequential and cotunneling rates we display in this section [47, 214], it is important, for the sake of self-completeness and as an introduction to our notation, that we lay out both the exact form of the rates and their derivation in Appendix C. The cotunneling rates especially have a complex and interesting regularization procedure.

The well-known sequential tunneling rates for an Anderson impurity, obtained from Fermi's

generalized golden rule in Eq.(2.63), are

$$\begin{aligned}
\Gamma_{\sigma 0} &= \textstyle\sum_\alpha \Gamma^\alpha_{\sigma 0} & & & \Gamma^\alpha_{\sigma 0} &= \gamma^\alpha n_F(\varepsilon_\sigma - \mu_\alpha) \\
\Gamma_{0\sigma} &= \textstyle\sum_\alpha \Gamma^\alpha_{0\sigma} & & \text{with individual} & \Gamma^\alpha_{0\sigma} &= \gamma^\alpha \left[1 - n_F(\varepsilon_\sigma - \mu_\alpha)\right] \\
\Gamma_{\sigma 2} &= \textstyle\sum_\alpha \Gamma^\alpha_{\sigma 2} & & \text{transition rates} & \Gamma^\alpha_{\sigma 2} &= \gamma^\alpha \left[1 - n_F(\varepsilon_\sigma + U - \mu_\alpha)\right] \\
\Gamma_{2\sigma} &= \textstyle\sum_\alpha \Gamma^\alpha_{2\sigma} & & & \Gamma^\alpha_{2\sigma} &= \gamma^\alpha n_F(\varepsilon_\sigma + U - \mu_\alpha),
\end{aligned}$$

where explicit calculations are shown in Appendix C.1. Here, $\Gamma_{0\sigma}$ is the transition rate from the orbital being occupied by a spin-σ electron to being empty; $\Gamma_{\sigma 2}$ is the transition rate from the orbital being occupied by two electrons of opposite spin to being occupied by a spin-σ electron; and $\Gamma_{\sigma 0}$ and $\Gamma_{2\sigma}$ are the rates of their respective reverse processes.

The cotunneling rates receive similar notation. The general cotunneling transition rate is $\Gamma^{\alpha\alpha'}_{m'm}$, which denotes the process that moves an electron from electrode α to electrode α', while the system changes from state m to state m'. For elastic cotunnelings, we get

$$\begin{aligned}
\Gamma^{(2)}_{00} &= \sum_{\alpha\neq\alpha'} \Gamma^{\alpha\alpha'}_{00} & \Gamma^{(2)}_{\uparrow\uparrow} &= \sum_{\alpha\neq\alpha'} \Gamma^{\alpha\alpha'}_{\uparrow\uparrow} \\
\Gamma^{(2)}_{\downarrow\downarrow} &= \sum_{\alpha\neq\alpha'} \Gamma^{\alpha\alpha'}_{\downarrow\downarrow} & \Gamma^{(2)}_{22} &= \sum_{\alpha\neq\alpha'} \Gamma^{\alpha\alpha'}_{22},
\end{aligned} \tag{4.4}$$

where we exclude those elastic transitions involving the same electrode, as they do not change the state of the system or the jump number n. The general form of the regularized elastic cotunneling rate for an Anderson impurity is

$$\begin{aligned}
\Gamma^{\alpha\alpha'}_{mm} = \gamma^\alpha\gamma^{\alpha'} n_B(\mu_{\alpha'} - \mu_\alpha) \Bigg[& \frac{\beta}{4\pi^2} \Im\Bigg\{ \psi^{(1)}\left(\frac{1}{2} + \frac{i\beta}{2\pi}(E_1 - \mu_\alpha)\right) - \psi^{(1)}\left(\frac{1}{2} + \frac{i\beta}{2\pi}(E_1 - \mu_{\alpha'})\right) \\
& + \psi^{(1)}\left(\frac{1}{2} + \frac{i\beta}{2\pi}(E_2 - \mu_\alpha)\right) - \psi^{(1)}\left(\frac{1}{2} + \frac{i\beta}{2\pi}(E_2 - \mu_{\alpha'})\right) \Bigg\} \\
& \pm \frac{1}{\pi(E_1 - E_2)} \Re\Bigg\{ \psi\left(\frac{1}{2} + \frac{i\beta}{2\pi}(E_2 - \mu_\alpha)\right) - \psi\left(\frac{1}{2} + \frac{i\beta}{2\pi}(E_1 - \mu_\alpha)\right) \\
& - \psi\left(\frac{1}{2} + \frac{i\beta}{2\pi}(E_2 - \mu_{\alpha'})\right) + \psi\left(\frac{1}{2} + \frac{i\beta}{2\pi}(E_1 - \mu_{\alpha'})\right) \Bigg\} \Bigg],
\end{aligned} \tag{4.5}$$

where we have introduced $\beta = \frac{1}{T}$, the digamma $\psi(x)$ and trigamma $\psi^{(1)}(x)$ functions, and the Bose-Einstein distribution $n_B(\mu_\alpha - \mu_{\alpha'})$:

$$n_B(\mu_\alpha - \mu_{\alpha'}) = \frac{1}{e^{(\mu_\alpha - \mu_\alpha)\beta} - 1}. \tag{4.6}$$

We note also that, in Eq.(4.5), the $\pm$ is negative only for $\Gamma^{\alpha\alpha'}_{\sigma\sigma}$ and the energies E_1 and E_2 refer to the two different pathways for each cotunneling process; the values of E_1 and E_2 for each

rate are given in Table C.1.

The possible inelastic cotunneling rates, on the other hand, take two forms:

$$\Gamma^{(2)}_{\bar{\sigma}\sigma} = \sum_{\alpha,\alpha'} \Gamma^{\alpha\alpha'}_{\bar{\sigma}\sigma} \qquad \text{and} \qquad \Gamma^{(2)}_{02} = \sum_{\alpha,\alpha'} \Gamma^{\alpha\alpha'}_{02}$$
$$\Gamma^{(2)}_{20} = \sum_{\alpha,\alpha'} \Gamma^{\alpha\alpha'}_{20}. \tag{4.7}$$

We will exclude those rates that transition between a system between being doubly-occupied and being empty, as they generally apply only in regimes with a negative U; systems where other effects, such as long-range lattice vibrations, actually cause an effective electron-electron attraction [214–217].

The exact formula for the remaining inelastic cotunneling rates is similar to that for the elastic rates:

$$\begin{aligned}\Gamma^{\alpha\alpha'}_{\bar{\sigma}\sigma} = \gamma^{\alpha}\gamma^{\alpha'} n_B(\mu_{\alpha'} - \mu_\alpha - \varepsilon_\sigma + \varepsilon_{\bar{\sigma}}) \Bigg[\frac{\beta}{4\pi^2} \Im \Bigg\{ & \psi^{(1)}\left(\frac{1}{2} + \frac{i\beta}{2\pi}(\varepsilon_{\bar{\sigma}} + U - \mu_\alpha)\right) \\ & - \psi^{(1)}\left(\frac{1}{2} + \frac{i\beta}{2\pi}(\varepsilon_\sigma + U - \mu_{\alpha'})\right) + \psi^{(1)}\left(\frac{1}{2} + \frac{i\beta}{2\pi}(\varepsilon_{\bar{\sigma}} - \mu_\alpha)\right) - \psi^{(1)}\left(\frac{1}{2} + \frac{i\beta}{2\pi}(\varepsilon_\sigma - \mu_{\alpha'})\right) \Bigg\} \\ & \pm \frac{1}{\pi U} \Re \Bigg\{ \psi\left(\frac{1}{2} + \frac{i\beta}{2\pi}(\varepsilon_{\bar{\sigma}} - \mu_\alpha)\right) - \psi\left(\frac{1}{2} + \frac{i\beta}{2\pi}(\varepsilon_{\bar{\sigma}} + U - \mu_\alpha)\right) - \psi\left(\frac{1}{2} + \frac{i\beta}{2\pi}(\varepsilon_\sigma - \mu_{\alpha'})\right) \\ & + \psi\left(\frac{1}{2} + \frac{i\beta}{2\pi}(\varepsilon_\sigma + U - \mu_{\alpha'})\right) \Bigg\} \Bigg]. \end{aligned} \tag{4.8}$$

4.3.1 Rate equation

With the rates in hand, we can construct the n-resolved master equation from ad hoc principles; after transforming to Fourier space, the χ-dependent Liouvillian is

$$\mathbf{L}(\chi) = \begin{bmatrix} -[\Gamma_{\uparrow 0} + \Gamma_{\downarrow 0}] \\ +\Gamma_{00}^{SD}(e^{i\chi} - 1) \\ +\Gamma_{00}^{DS}(e^{-i\chi} - 1) & \Gamma_{0\uparrow}^{S} + \Gamma_{0\uparrow}^{D} e^{i\chi} & \Gamma_{0\downarrow}^{S} + \Gamma_{0\downarrow}^{D} e^{i\chi} & 0 \\ \Gamma_{\uparrow 0}^{S} + \Gamma_{\uparrow 0}^{D} e^{-i\chi} & -[\Gamma_{0\uparrow} + \Gamma_{2\uparrow} + \Gamma_{\downarrow\uparrow}^{(2)}] \\ +\Gamma_{\uparrow\uparrow}^{SD}(e^{i\chi} - 1) \\ +\Gamma_{\uparrow\uparrow}^{DS}(e^{-i\chi} - 1) & \Gamma_{\uparrow\downarrow}^{SS} + \Gamma_{\uparrow\downarrow}^{SD} e^{i\chi} \\ +\Gamma_{\uparrow\downarrow}^{DD} + \Gamma_{\uparrow\downarrow}^{DS} e^{-i\chi} & \Gamma_{\uparrow 2}^{S} + \Gamma_{\uparrow 2}^{D} e^{i\chi} \\ \Gamma_{\downarrow 0}^{S} + \Gamma_{\downarrow 0}^{D} e^{-i\chi} & \Gamma_{\downarrow\uparrow}^{SS} + \Gamma_{\downarrow\uparrow}^{SD} e^{i\chi} \\ +\Gamma_{\downarrow\uparrow}^{DD} + \Gamma_{\downarrow\uparrow}^{DS} e^{-i\chi} & -[\Gamma_{0\downarrow} + \Gamma_{2\downarrow} + \Gamma_{\uparrow\downarrow}^{(2)}] \\ +\Gamma_{\downarrow\downarrow}^{SD}(e^{i\chi} - 1) \\ +\Gamma_{\downarrow\downarrow}^{DS}(e^{-i\chi} - 1) & \Gamma_{\downarrow 2}^{S} + \Gamma_{\downarrow 2}^{D} e^{i\chi} \\ 0 & \Gamma_{2\uparrow}^{S} & \Gamma_{2\downarrow}^{S} & -[\Gamma_{\uparrow 2} + \Gamma_{\downarrow 2}] \\ & & & +\Gamma_{22}^{SD}(e^{i\chi} - 1) \\ & & & +\Gamma_{22}^{DS}(e^{-i\chi} - 1) \end{bmatrix}, \tag{4.9}$$

and the jump operators are

$$\mathbf{J}_F = \begin{bmatrix} \Gamma_{00}^{SD} & \Gamma_{0\uparrow}^{D} & \Gamma_{0\downarrow}^{D} & 0 \\ 0 & \Gamma_{\uparrow\uparrow}^{SD} & \Gamma_{\uparrow\downarrow}^{SD} & \Gamma_{\uparrow 2}^{D} \\ 0 & \Gamma_{\downarrow\uparrow}^{SD} & \Gamma_{\downarrow\downarrow}^{SD} & \Gamma_{\downarrow 2}^{D} \\ 0 & 0 & 0 & \Gamma_{22}^{SD} \end{bmatrix} \quad \text{and} \quad \mathbf{J}_B = \begin{bmatrix} \Gamma_{00}^{DS} & 0 & 0 & 0 \\ \Gamma_{\uparrow 0}^{D} & \Gamma_{\uparrow\uparrow}^{DS} & \Gamma_{\uparrow\downarrow}^{DS} & 0 \\ \Gamma_{\downarrow 0}^{D} & \Gamma_{\downarrow\uparrow}^{DS} & \Gamma_{\downarrow\downarrow}^{DS} & 0 \\ 0 & \Gamma_{2\uparrow}^{D} & \Gamma_{2\uparrow}^{D} & \Gamma_{22}^{DS} \end{bmatrix}. \tag{4.10}$$

4.4 Results

We present the results of our cotunneling analysis in three distinct regimes: under Coulomb blockade where cotunneling dominates, at high bias when the transport is unidirectional and the WTD and FPTD are equivalent, and the interesting bidirectional regime in which telegraphic switching occurs.

At low bias, when neither $\varepsilon_\uparrow$ or $\varepsilon_\downarrow$ are in the bias window, we expect the sequential current to

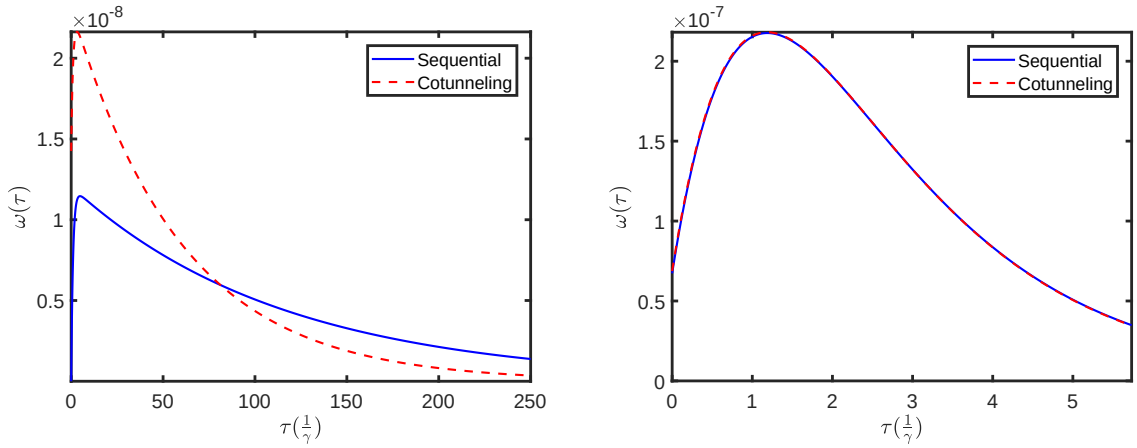

Figure 4.3: WTD calculated for only sequential tunneling and also with cotunneling processes added, for two different voltages; in (a) the level is in the Coulomb blockade regime and in (b) the level is in the resonant tunneling regime. The energies of the spin split electronic levels are $\varepsilon_\uparrow = 0.5$meV and $\varepsilon_\downarrow = 1.5$meV, the Coulomb repulsion is $U = 4$meV, T $= 75\mu$eV, and $\gamma = 0.5$T. Parameters for each plot are: (a) $\mu_S = -\mu_D = 0.25$meV, $\langle\tau\rangle_{seq} = 2.04$ns, and $\langle\tau\rangle_{co} = 1.06$ns; (b) $\mu_S = -\mu_D = 5$meV, $\langle\tau\rangle_{seq} = 46.81$ps, and $\langle\tau\rangle_{co} = 46.43$ps.

be negligible. In such a case, we also expect the corresponding average sequential waiting time $\langle\tau\rangle_{seq}$ to be large; that is, on average there is a long time delay between successive tunnelings to the drain. In contrast, cotunneling provides a quantum pathway for electrons to tunnel through the system that is not visible in the sequential physics. This is evident in Fig.(4.3a), where $\langle\tau\rangle_{co}$ is half $\langle\tau\rangle_{seq}$; whereas in the tunneling regime, shown in Fig.(4.3b), sequential processes dominate and $\langle\tau\rangle_{co}$ is comparable to $\langle\tau\rangle_{seq}$.

At high voltages, an Anderson impurity behaves as a multiple-reset system, since an electron tunneling to the drain can leave the system singly occupied and another tunneling can occur to the drain immediately; Fig.(4.3b) demonstrates this, as $w(0) \neq 0$ for both sequential tunneling and cotunneling. In comparison, at low voltages double occupancy is energetically denied and the sequential tunneling causes the impurity behaves as a single-reset system, $w_{seq}(0) = 0$, while adding cotunneling processes makes $w_{co}(0) \neq 0$.

Sequential tunneling through an Anderson impurity displays non-renewal behavior in the high voltage regime, which is seen in Fig.(4.5b). Here, due to the availability of the double occupancy state, successive waiting times are negatively correlated; a short waiting time is more likely to be followed by a long waiting time and vice versa. We note that the Coulomb repulsion is an order of magnitude greater than the electronic single-particle energies, so that if the system is doubly occupied it is likely for both electrons to subsequently tunnel out, which is a short waiting time, and then for the system to fill and empty again, which is a long waiting time. Thus, the non-renewal behavior does not arise from non-Markovian behavior, as we work under the Markovian assumption, but rather from the multiple tunneling processes contained in the drain jump operator [44]. Importantly, even though sequential processes

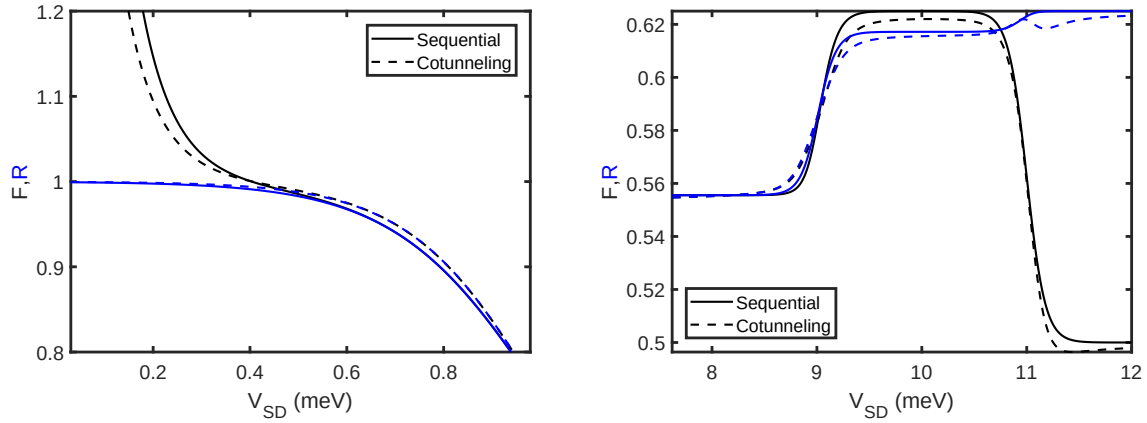

Figure 4.4: Exact Fano factor F and its prediction from waiting times under the renewal assumption R over a range of voltages in (a) the Coulomb blockade regime and (b) the tunneling regime. All parameters are the same as in Fig.(4.3a) and Fig.(4.3b).

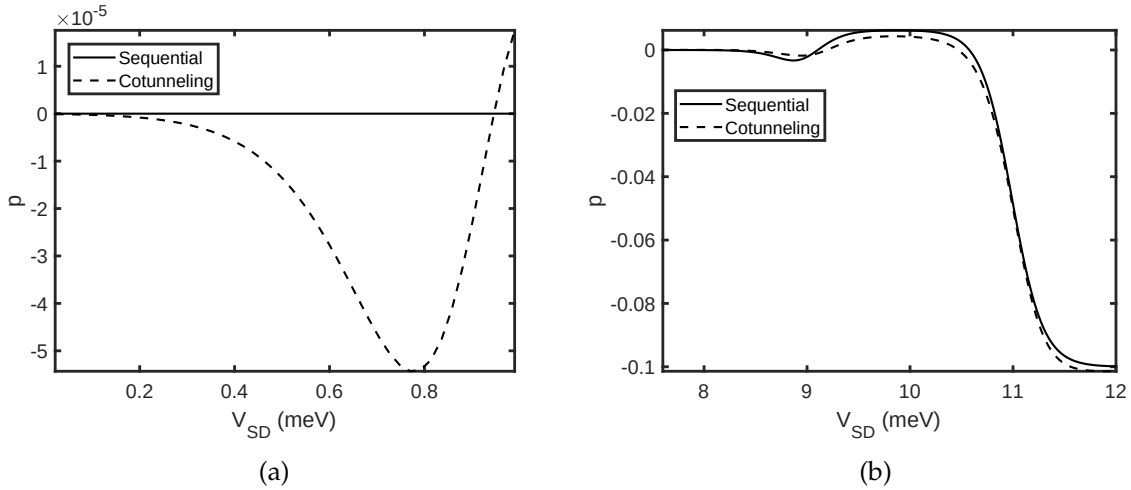

Figure 4.5: Pearson correlation coefficient as a function of voltage in (a) the Coulomb blockade regime and (b) the resonant tunneling regime. All parameters are the same as in Fig.(4.3a) and Fig.(4.3b).

dominate in this regime, cotunneling still has an effect on the non-renewal behavior, slightly increasing the strength of the negative correlation between successive waiting times.

In Fig.(4.4b), we can detect the presence of non-renewal behavior as well; F and R diverge at the same voltage that the sequential correlation coefficient becomes non-zero. Furthermore, when cotunneling processes are included, F and R diverge at a larger voltage, following the behavior of the cotunneling correlation coefficient.

Since multiple cotunneling rates appear in the drain jump operator, one might expect that non-renewal behavior could be observed even in the Coulomb blockade regime. Fig.(4.5a) shows that for small voltages the correlation is non-zero but still negligible. This is apparent in Fig.(4.4a); the presence of cotunneling changes the Fano factor and randomness parameter from their sequential values, but they still are not visibly different. We note that, for equal source and drain temperatures, at low bias the total current naturally disappears. The Fano factor, consequently, diverges in this limit. Even though F is different to R in this regime, the renewal assumption is still satisfied; the difference is due to the inability of the WTD to accommodate bidirectional transport.

Before discussing the telegraphic switching scenario we highlighted at the beginning of the chapter, we will draw attention to the fact that, so far, we have shown plots that are either deep in the Coulomb blockade regime or well in the resonant tunneling regime. This is because for certain voltage ranges between these two extremes the rate equation approach produces unphysically negative probability densities for small waiting times. To understand why, we will first detour to inspect the WTD of a SRL with cotunneling rates included:

$$w(\tau) = \frac{a - bz_-}{z_+ - z_-} e^{-z_-\tau} - \frac{a - bz_+}{z_+ - z_-} e^{-z_+\tau}, \tag{4.11}$$

where the coefficients of the linear function in the numerator are

$$\begin{aligned} a = &\Big((\Gamma^D \Gamma^S_{10})^2 + \Gamma^{(2)} [\Gamma^D + \Gamma^S_{10} + \Gamma^S_{01}] [(\Gamma^{(2)})^2 + 2\Gamma^D \Gamma^S_{10}] + \\ &(\Gamma^{(2)})^2 [(\Gamma^D)^2 + (\Gamma^S_{10} + \Gamma^S_{01})^2 + \Gamma^D (2\Gamma^S_{01} + 3\Gamma^S_{10})] \Big) / \left(\Gamma^D \Gamma^S_{10} + \Gamma^{(2)} (\Gamma^D + \Gamma^S_{10} + \Gamma^S_{01}) \right), \end{aligned} \tag{4.12}$$

$$b = \frac{\Gamma^{(2)} \left(2\Gamma^D \Gamma^S_{10} + \Gamma^{(2)} (\Gamma^D + \Gamma^S_{10} + \Gamma^S_{01}) \right)}{\Gamma^D \Gamma^S_{10} + \Gamma^{(2)} (\Gamma^D + \Gamma^S_{10} + \Gamma^S_{01})}. \tag{4.13}$$

These results can be easily derived from the rate equation for a SRL with cotunneling included, shown in Appendix C.54. The strange short time behavior of the WTD is evident from Eq.(4.11):

$$w(0) = \frac{\Gamma^{(2)} \left(2\Gamma^D \Gamma^S_{10} + \Gamma^{(2)} (\Gamma^D + \Gamma^S_{10} + \Gamma^S_{01}) \right)}{\Gamma^D \Gamma^S_{10} + \Gamma^{(2)} (\Gamma^D + \Gamma^S_{10} + \Gamma^S_{01})}. \tag{4.14}$$

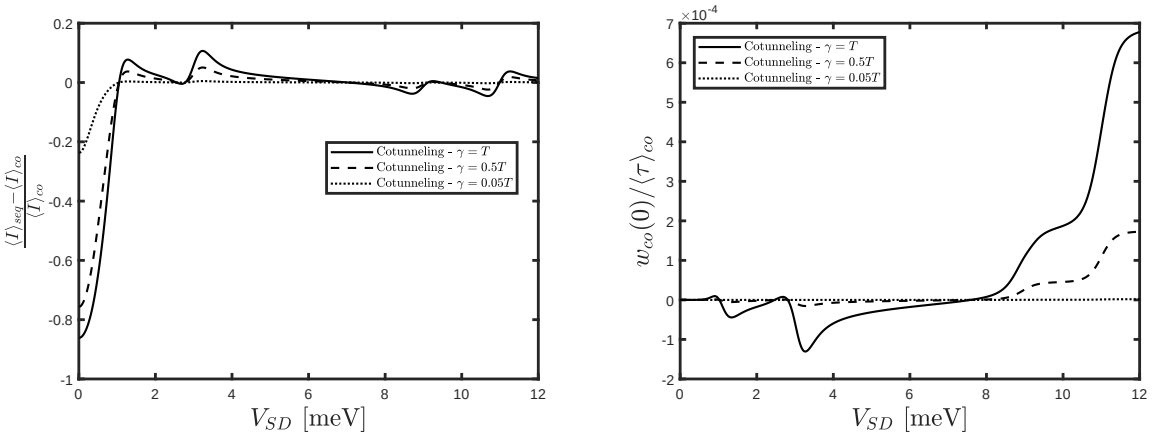

(a) (b)

Figure 4.6: (a) Relative difference between the average current with only sequential processes, and then with cotunneling processes included as well, as a function of bias voltage. (b) The value of the WTD, with cotunneling included, at $\tau = 0$, for the same range of parameters. All parameters are the same as in Fig.(4.5a) and Fig.(4.5b).

In certain regimes, cotunneling processes actually reduce the total current, which amounts to *negative* regularized cotunneling rates. From the point of view of the theory the total transition rate, $\Gamma_{00} = \frac{\gamma}{2} n_F(\varepsilon - \mu_S)(1 - n_F(\varepsilon - \mu_D)) + \Gamma^{(2)}$, is still positive, but $\Gamma^{(2)}$ can be negative [173, 196]. We can see from Eq.(4.14) that, in such a regime and for $\tau \lessapprox 10^3$fs, that the WTD of a SRL actually becomes negative.

For an Anderson impurity the situation is more complex. In Fig.(4.6a) we have plotted the difference between the sequential current and the current with cotunneling included, while in Fig.(4.6b), we have plotted the WTD, including cotunneling effects, at $\tau = 0$. When all levels are above the bias window, cotunneling current evidently dominates and the resulting distribution that in Fig.(4.3a). At intermediate voltages, it is evident that when cotunneling processes significantly diminish the total current, the WTD becomes negative for small τ. It is not yet clear how to resolve this interesting pathology; evidently there should be a well-defined WTD for all voltage ranges. One possibility is that this violation of the positivity requirement is an artifact of only going to 2^{nd}-order perturbation theory; Fig.(4.6a) and Fig.(4.6b) show that the effect vanishes as $\gamma \to 0$. This is perhaps an indication of when using the rate equation is appropriate and when non-Markovian effects need to be included.

Let us turn now to the interesting regime of telegraphic switching identified in Fig.(4.2a) and Fig.(4.2b). The Fano factor in Fig.(4.7a) is a reproduction of Fig.(3) from Ref.[46], with the first-passage randomness parameter included as well. Here, $U \gg V_{SD}$, so that transport through one σ level blocks transport through the other $\bar{\sigma}$ level. At small voltages and for sequential tunneling, Belzig has shown that the molecule goes through cycles of transferring $n - 1$ electrons quickly through the spin-$\uparrow$ level until it gets "stuck" in the spin-$\downarrow$ level. The cycle completes when the spin-$\downarrow$ level empties via thermal broadening of the drain occupation

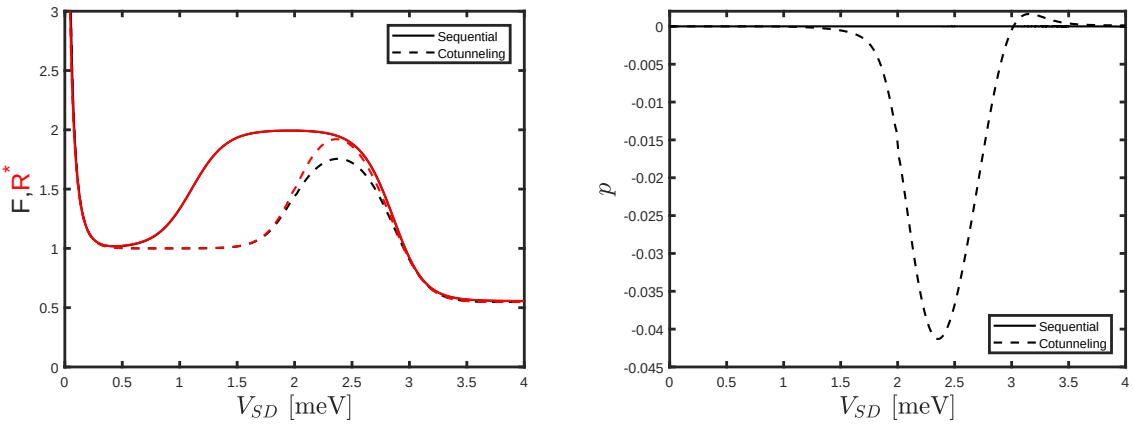

(a) (b)

Figure 4.7: (a) Fano factor and randomness parameter, and (b) the Pearson correlation coefficient, calculated from the FPTD only. The energies of the spin split electronic levels are $\varepsilon_\uparrow = 0.5$meV and $\varepsilon_\downarrow = -1.5$meV, the Coulomb repulsion is $U = 4$meV, $T = 75\mu$eV, and $\gamma = 0.5T$.

function [40]. The noise is therefore characteristic of a sum of Poissonian processes, each transferring n electrons and weighted by $(\frac{1}{2})^n$.

In contrast, when cotunneling processes are included, super-Poissonian noise arises from a different mechanism, which we discussed at the beginning of the chapter. Fig.(4.7a) successfully reproduces the super-Poissonian noise, and also shows that the transport is non-renewal since $F \neq R^*$. We expect, consequently, to see correlations between successive first-passage times in this voltage regime.

Positive correlations between successive waiting times are known to occur for systems undergoing telegraphic switching: for example, in systems with spin-polarized electrodes [44]. The current switches between two transport channels, each with a characteristic waiting time. When in the faster channel, waiting times between successive tunnelings are more likely to be shorter, and vice versa in the slower channel. Consequently, waiting times between successive tunnelings to the drain are positively correlated; one would expect that there would be similar positive correlations between the first-passage times. In Fig.(4.7b), however, we report intriguing negative correlations between successive first-passage times. That is, if the jump number reaches $+1$ after a short time-interval, it is more likely that the time until the jump number reaches $+2$ will be long.

The small size of the correlations can be explained by considering the various timescales involved. The rate of switching, $\Gamma^{(2)}_{\sigma\bar{\sigma}}$, is of the same order of magnitude as the elastic cotunneling current in one of the channels, $\Gamma^{(2)}_{mm}$. Furthermore, the rate of relaxation due to sequential processes will be the same order as current through the sequential channel. When taken together, it is clear that the system does not spend long enough in that channel for successive waiting times to be significantly correlated.

The transport picture might then appear more as "avalanche" tunneling; there are long periods with almost no detections in the drain, corresponding to transport through the elastic cotunneling channel, followed by a short period of many detections, corresponding to the transport through the sequential channel. In true avalanche tunneling, there are periods of *no* detections; this difference is likely what produces the small negative correlations.

4.5 Summary

In this chapter, we have included cotunneling processes into transport through an Anderson impurity, and calculated the resulting fluctuating-time statistics. We were particularly focused on a regime of super-Poissonian transport, where inelastic cotunneling processes induced telegraphic switching. We found that, while there is non-renewal behavior accompanying the super-Poissonian, the resulting correlations are small and negative, which we attribute the small correlation size to the relative similarity between tunneling rates and the switching rate. We also identified that the positivity condition of the WTD and FPTD is violated for certain voltage regimes, perhaps indicating the areas for which a rate equation approach is not suitable.

Sequential tunneling through the Holstein model

This chapter contains material that has been previously published in the following journal articles:

Non-renewal statistics in quantum transport from the perspective of first-passage and waiting time distributions, S.L. Rudge and D.S. Kosov, Phys. Rev. B, **99**, 115426 (2019)

Counting quantum jumps: A summary and comparison of fixed-time and fluctuating-time statistics in electron transport - invited review in the special issue "Dynamics of Open Quantum Systems", S.L. Rudge and D.S. Kosov, J. Chem. Phys. **151**, 034107 (2019)

5.1 Motivation

In this chapter we will turn away from cotunneling and electron-electron interactions and instead focus on a different effect that is generally unavoidable in nanoscale transport: molecular vibrations [218, 219]. In doing so, we will approach from the polaron perspective; each molecular surface potential is treated as harmonic and each electron occupying the orbital experiences a "cloud" of vibrations, which is modeled as an electron-phonon interaction. Nuclear motion is an unavoidable consequence of electron transport in molecular junctions, and so vibrations are a necessary component of any transport description, including fluctuating-time statistics. More than that, however, is the interesting physics that arises *because* of vibrational effects.

The Franck-Condon blockade is one such example of interesting physics in the Holstein model; destructive interference between vibrational states suppresses the current at small voltages, producing avalanche tunneling and large Fano factors [43, 220]. Recent work in has shown that this avalanche tunneling is not accompanied by correlations between successive waiting times but, in a similar voltage regime, elastic phonon transitions open a shortcut channel through the junction, producing positive waiting time correlations [78]. These results

were calculated at small V_{SD}, however, where phonon transitions make the transport bidirectional. Since Ref.[78] focuses solely on waiting times, we are motivated to investigate this same transport scenario with the FPTD and compare the results.

Another regime where we expect a strong contribution from backtunneling processes is that of zero voltage, $V_{SD} = 0$, and a non-zero temperature gradient, $\Delta T \neq 0$ [221]. This is a particularly topical avenue of research as recent experimental work by Lumbroso *et al.* [79] has generated fundamental electronic noise, akin to electronic shot noise, generated entirely by temperature differences across the junction. Our other goal for this chapter, then, is to investigate the fluctuating-time statistics for this so-called delta-T noise.

5.2 Holstein model

Unlike Chapter 4, where we assumed the molecule was completely rigid, we now assume the molecule undergoes vibrations described by an electron-phonon coupling and that the electron-electron interaction is large: $U \to \infty$. In effect, double occupation of the molecular orbital is now energetically forbidden and it behaves as a single level coupled to a harmonic vibrational mode. In this limit, the Hamiltonian in Eq.(1.6) becomes just the Holstein model [222]:

$$H_Q = \varepsilon_0 a^\dagger a + \lambda(b^\dagger + b)a^\dagger a + \omega\left(b^\dagger b + 1/2\right). \tag{5.1}$$

It is convenient, at this point, to diagonalize the Holstein Hamiltonian with the canonical Lang-Firsov [223] transformation, which we demonstrate in Appendix D.1. To diagonalize, the Lang-Firsov transformation uses the molecular eigenstates, $|nq\rangle$, which mean that the system is described by two quantum numbers, where $n = \{0, 1\}$ is the electron occupation number and $q = \{0, 1, ..., +\infty\}$ is the vibrational quanta occupation number. The associated eigenenergy is $E_{nq} = \varepsilon n + \omega q$ and the diagonalized Hamiltonian is

$$\tilde{H}_Q = \varepsilon \tilde{a}^\dagger \tilde{a} + \omega \tilde{b}^\dagger \tilde{b}, \tag{5.2}$$

with $\varepsilon = \varepsilon_0 - \frac{\lambda^2}{\omega}$ and new fermionic $\tilde{a}^\dagger\tilde{a}$ and bosonic $\tilde{b}^\dagger\tilde{b}$ operators obtained from the original operators via the canonical transformation. Note that in Eq.(5.2), we have ignored the $\frac{\omega}{2}$ component of the Hamiltonian, as all uses of $\tilde{H}_Q$ involve differences between eigenenergies, so this term will always cancel.

5.2.1 Rate equation

Considering the possible pure states $|nq\rangle$, we write the Fourier transformed probability vector as

$$\mathbf{P}(\chi,t) = \Big[P_{00}(\chi,t), P_{10}(\chi,t), P_{01}(\chi,t), P_{11}(\chi,t), \ldots, P_{1(N-1)}(\chi,t), P_{0N}(\chi,t), P_{1N}(\chi,t)\Big]^T, \quad (5.3)$$

and note that there are two rates we need to consider: those that transition the system from being occupied by 1 electron and q phonons to being occupied by 0 electrons and q' phonons, $\Gamma_{0q';1q} = \sum_\alpha \Gamma^\alpha_{0q';1q}$, and those that transition the system from being occupied by 0 electrons and q phonons to being occupied by 1 electron and q' phonons, $\Gamma_{1q';0q} = \sum_\alpha \Gamma^\alpha_{1q';0q}$. With these possible rates, the master equation is [224]

$$\dot{P}_{0q}(\chi,t) = \sum_{q'} \left(\Gamma^S_{0q;1q'} + \Gamma^D_{0q;1q'} e^{i\chi}\right) P_{1q'}(\chi,t) - \sum_{\alpha q'} \Gamma^\alpha_{1q';0q} P_{0q}(\chi,t), \quad (5.4)$$

$$\dot{P}_{1q}(\chi,t) = \sum_{q'} \left(\Gamma^S_{1q;0q'} + \Gamma^D_{1q;0q'} e^{-i\chi}\right) P_{0q'}(\chi,t) - \sum_{\alpha q'} \Gamma^\alpha_{0q';1q} P_{1q}(\chi,t). \quad (5.5)$$

Evidently, there can be any number of interacting vibrations and $\mathbf{P}(\chi,t)$ is a vector of infinite length. In practice, however, we only include a finite number of vibrations, N, in the transport calculations, so that $\mathbf{P}(\chi,t)$ and $\mathbf{I}$ are vectors of length $2(N+1)$. Likewise, the Liouvillian and two jump operators are $2(N+1)\times 2(N+1)$ matrices. $\mathbf{J}_F$ and $\mathbf{J}_B$ are explicitly written in Appendix D.2.2. N is chosen to be a number greater than the maximum number of phonons allowed by V_{SD}.

The rates are calculated explicitly in Appendix D.2 and summarized below:

$$\Gamma^\alpha_{1q';0q} = \gamma \left|\mathbf{X}_{q'q}\right|^2 n_F(\varepsilon + \omega(q'-q) - \mu_\alpha) \text{ and} \quad (5.6)$$

$$\Gamma^\alpha_{0q';1q} = \gamma \left|\mathbf{X}_{q'q}\right|^2 \left[1 - n_F(\varepsilon + \omega(q'-q) - \mu_\alpha)\right], \quad (5.7)$$

where the Franck-Condon matrix elements, see Appendix D.2.1, are

$$X_{qq'} = \langle q|e^{-\lambda(b^\dagger - b)}|q'\rangle. \quad (5.8)$$

Up to this point we have made no assumptions on the phonon distribution of the molecular orbital. If we assume that the phonons are interacting with an external bath at temperature T_V, then they will be forced to relax to equilibrium immediately after a tunneling process. In this case, the phonons will assume a Boltzmann distribution and the probabilities are defined by the ansatz

$$P_{nq}(\chi,t) = P_n(\chi,t)\frac{e^{-q\omega/T_V}}{1-e^{-\omega/T_V}}. \quad (5.9)$$

The rate equation is now effectively that of a SRL, with Liouvillian

$$\mathbf{L}_0 = \begin{bmatrix} -T_{10} & T_{01}^S \\ T_{10}^S & -T_{01} \end{bmatrix} \qquad \text{and jump operators} \qquad \mathbf{J}_F = \begin{bmatrix} 0 & T_{01}^D \\ 0 & 0 \end{bmatrix}, \quad \mathbf{J}_B = \begin{bmatrix} 0 & 0 \\ T_{10}^D & 0 \end{bmatrix},$$

where the total transition rates are $T_{kl} = \sum_\alpha T_{kl}^\alpha$ and the individual transition rates are

$$T_{kl}^\alpha = \sum_{qq'} \Gamma_{kq;lq'}^\alpha \frac{e^{-q\omega/T_V}}{1 - e^{-\omega/T_V}}. \tag{5.10}$$

We will refer to this case as that of equilibrated phonons, and the other case, in which there is no assumption about the relaxation time, as unequilibrated phonons. They are well-known to produce drastically different FCS, and we will see that the fluctuating-time statistics are no different.

5.3 Results

5.3.1 Finite bias voltage

In Fig.(5.1a)-Fig.(5.1d), we have plotted the WTD as a function of both V_{SD} and τ. The WTDs alone display many of the interesting features characteristic of phonon-assisted transport, and we will focus our initial discussion on them.

Immediately noticeable are the steps occurring when the voltage reaches multiples of 2ω: $V_{SD}/2 = q\omega$. At these voltages, high- or low-energy electrons may interact with q vibrational quanta and either lose or gain the exact energy required to resonantly tunnel through the $\varepsilon = 0$ level, effectively opening another conduction channel [8, 43, 224]. These conductance steps are accompanied by step-like increases in $\langle I \rangle$, and also step-like decreases in $\langle \tau \rangle_F$: the average waiting time between forward tunnelings to the drain. We can see this, as well as a decrease in the mode of $w_F(\tau)$, from Fig.(5.1a) and Fig.(5.1c); the WTD peak moves closer to $\tau = 0$ at each voltage step.

Of course, we would expect that, if forward transitions are preferred, then $\langle \tau \rangle_B$ would correspondingly increase as we reach each conductance step. In Fig.(5.1b), which has a moderate electron-phonon coupling of $\lambda = 1$, this is indeed the case; as each conduction channel opens, the peak of $w_B(\tau)$ shifts to higher τ. Before this step, however, $w_B(\tau)$ has local peaks at exactly $V_{SD}/2 = q\omega$; when μ_D is in resonance with one of the quasi-energy levels, $\varepsilon - q\omega$, an effective backtunneling channel is opened. The conductance peaks disappear as V_{SD} increase; the electron does not spend enough time in the molecule to interact with high-energy phonons.

When the interaction is much stronger, as it is in Fig.(5.1d) where $\lambda = 4$, spatial separation

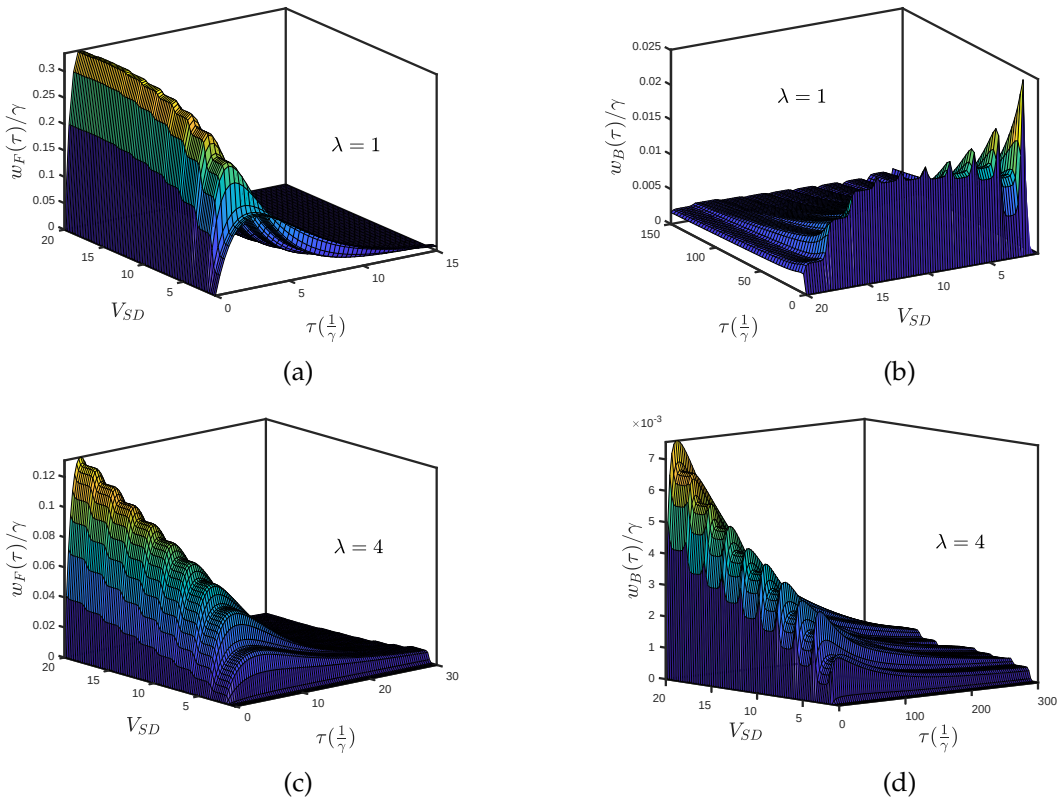

Figure 5.1: Contour plots of the WTD as a function of voltage and time, for transport through the Holstein model for unequilibrated phonons and for different λ. In (a) and (c) $w_F(\tau)$ is plotted for $\lambda = 1$ and $\lambda = 4$, respectively. Likewise, in (b) and (d) $w_B(\tau)$ is plotted for $\lambda = 1$ and $\lambda = 4$, respectively. The WTD is calculated using Eq.(3.42) and the respective choices of jump operator: $\mathbf{J}_F$ and $\mathbf{J}_B$. The vibrationally adjusted energy level is $\varepsilon = 0$, the vibrational frequency is $\omega = 1$, $T = 0.05$, and $\gamma_\alpha = \frac{\gamma}{2} = 0.01$. The source and drain chemical potentials are shifted symmetrically about zero: $\mu_S = -\mu_D = V_{SD}/2$. We scale all energy parameters in terms of ω, or $\hbar\omega/e$ outside of natural units.

between surface potentials of different electron occupancy forces highly inelastic phonon transitions to be preferred. For a visual representation, see Fig.(D.1). These inelastic transitions allow low energy electrons from the drain to interact with enough unequilibrated phonons to enter the resonant level; $\langle\tau\rangle_B$ actually decreases as V_{SD} increases, although the conductance peaks are still present. The effect disappears completely for equilibrated phonons.

While $w_B(\tau)$ in both Fig.(5.1b) and Fig.(5.1d) displays qualitatively interesting behavior, the waiting times between backward tunnelings are still an order of magnitude bigger than the waiting times between forward tunnelings; the resulting current will be an order of magnitude smaller. Despite this difference, backtunneling processes evidently contribute to transport for unequilibrated phonons, and we cannot simply ignore them for the remaining fluctuating-time results. Indeed, it would be more instructive to display the FPTD for the same parameters, but it is too numerically difficult to obtain in the time domain.

In Fig.(5.2a) and Fig.(5.2b), however, we have displayed $\tilde{F}(1|z)$ for equilibrated and unequilibrated phonons. These plots alone demonstrates the complexity difference between the two regimes. In these two plots, the chemical potentials are $\mu_S = -\mu_D = 4.5$. At this voltage, backscattering effects are suppressed because μ_D is off-resonance with the vibrationally shifted energy levels, and $\tilde{F}(1|z)$ will resemble $\tilde{w}_F(z)$. For equilibrated phonons, the definition in Eq.(3.76) indicates that the FPTD behavior will be determined by two poles at

$$z = -(T_{10} + T_{01}) \pm \sqrt{(T_{10} + T_{01})^2 - 4T_{10}T_{01}^D}; \tag{5.11}$$

however, for the parameters chosen, $T_{01} \approx T_{01}^D$ and the transport is dominated by one pole at approximately $-(T_{10} + T_{01})$. The FPTD for unequilibrated phonons is by contrast much more complicated, with multiple poles and additional side peaks. While interesting, plots of the FPTD and WTD themselves do not provide any information on the non-renewal behavior, for which we must turn to cumulant analysis.

Fig.(5.3a) and Fig.(5.3b) display well-known current phenomena; see, for example, Ref.[224] and Ref.[141]. To draw connections with fluctuating-time statistics, we have superimposed plots of the total current reconstructed from the WTD, outlined in Eq.(3.117), and from the FPTD, outlined in Eq.(3.152). In these plots we can see many of the same features as we saw in the WTDs; for example, the current steps when $V_{SD}/2 = q\omega$. Also visible is the Franck-Condon blockade; in the strong electron-phonon coupling regime, such as in Fig.(5.2b) where $\lambda = 4$, the Franck-Condon matrix elements, $|\mathbf{X}_{qq'}|$, are minimized for small $|q - q'|$. Since for low voltages elastic and near-elastic transitions involving small numbers of vibrational quanta dominate the transport, $\langle I\rangle$ is suppressed until $V_{SD}/2 \approx 2.5$.

The Franck-Condon blockade is evidently stronger for equilibrated phonons than unequilibrated, as the high energy transitions needed to overcome the blockade are more likely when the phonons are out-of-equilibrium. For a moderate electron-phonon coupling $\lambda \sim 1$, shown

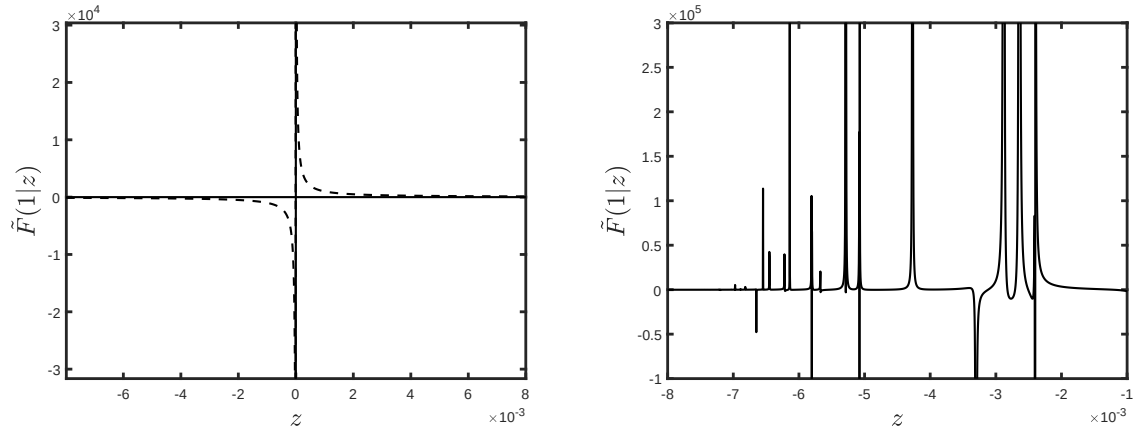

(a) (b)

Figure 5.2: The FPTD in Laplace space for transport through the Holstein model, where (a) the phonons are in equilibrium and (b) the phonons are out-of-equilibrium. All parameters and units are the same as in Fig.(5.1a)-Fig.(5.1d).

in Fig.(5.3a), the blockade disappears and forcing the phonons to equilibrium actually increases the current; transport is dominated by elastic or small $|q - q'|$ transitions, which are more populated in equilibrium [43].

Koch and von Oppen also noticed that, when under the Franck-Condon blockade, the transport displayed avalanche tunneling: long periods of no tunneling events followed by short bursts of many tunneling events. This widens the current distribution and so increases the Fano factor orders of magnitude above the Poissonian value [43], as we can see in Fig.(5.4a) and Fig.(5.4b). This is also visible in the WTDs; for $\lambda = 1$, the WTD has a much narrower peak at much smaller voltages than for $\lambda = 4$.

From these plots of the first and second cumulants, we are also now able to identify regimes of non-renewal behavior. In Fig.(5.3a), the total electronic current is exactly reproduced by the WTD and FPTD for both equilibrated and unequilibrated phonons; the blue, red, and black dashed and solid lines coincide. As shown in Chapter 3, $\frac{1}{\langle\tau\rangle_F} - \frac{1}{\langle\tau\rangle_B}$ always correctly predicts the current. The FPTD prediction, however, is an indicator of renewal behavior; we conclude that, for $\lambda = 1$, the transport is renewal at all voltages. Fig.(5.4a) supports this notion, as R^* exactly matches F at all voltages. Noticeably, though, this is the first instance in which the WTD fails; for $V_{SD}/2 < 0.25$, R and F diverge, because the WTD cannot accommodate the bidirectional transitions occurring at such small voltages.

In Fig.(5.3b), the total electronic current is exactly reproduced by the WTD for both equilibrated and unequilibrated phonons, as expected, but the FPTD prediction diverges slightly when $V_{SD}/2 > 5$ for unequilibrated phonons, indicating non-renewal transport in this regime. Comparing $\langle I\rangle$ and $\frac{1}{\langle\tau\rangle^*}$ can be deceiving, because, as Fig.(5.4b) shows, the transport is actually non-renewal for $V_{SD/2} > 0.5$. Indeed, it is for voltages between $0 < V_{SD}/2 < 2$ that Ref.[78] found strong positive correlations, for which there is no indication from the current

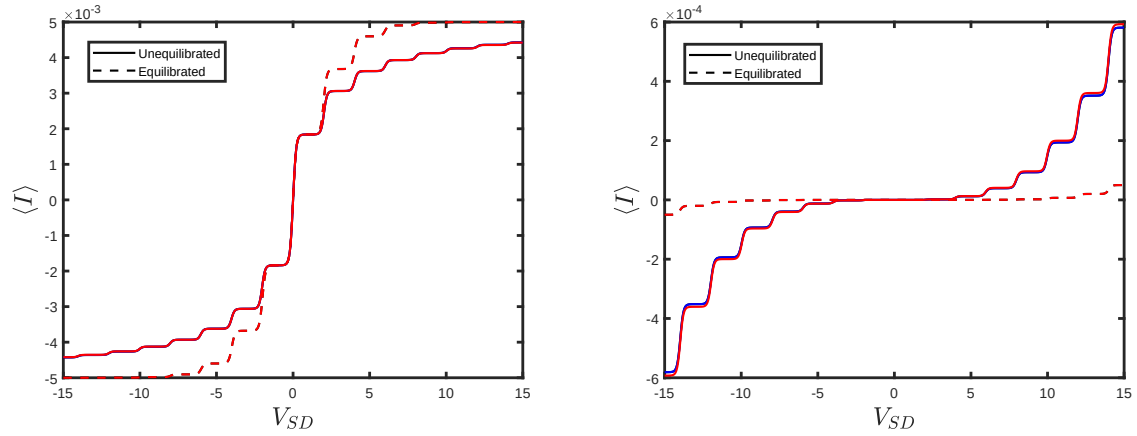

(a) (b)

Figure 5.3: Exact current for equilibrium and non-equilibrium phonons, (black) compared to the respective predictions from the FPTD $\frac{1}{\langle\tau_1\rangle^*}$ (red) and WTD $\frac{1}{\langle\tau\rangle_F} - \frac{1}{\langle\tau\rangle_B}$ (blue). The electron-phonon interaction is (a) $\lambda = 1$ and (b) $\lambda = 4$. For $V_{SD} < 0$, the FPTD current is $-\frac{1}{\langle\tau_{(-1)}\rangle^*}$ and for $V_{SD} > 0$ it is $\frac{1}{\langle\tau_1\rangle^*}$. All other parameters are the same as in Fig.(5.1a)-Fig.(5.1d). The current is scaled in terms of ω, or $e\omega$ outside of natural units.

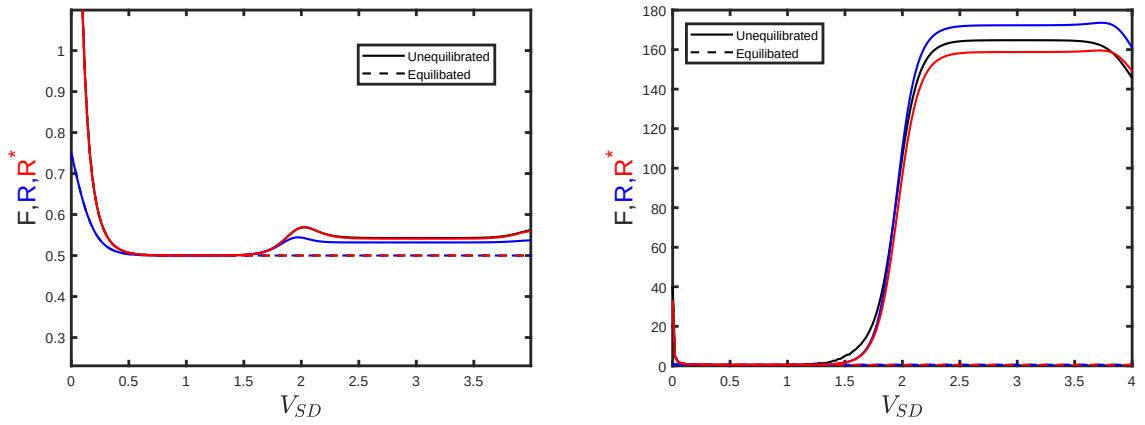

(a) (b)

Figure 5.4: The WTD randomness parameter, R, and the FPTD randomness parameter, R^*, compared to the Fano factor, F, for (a) $\lambda = 1$ and (b) $\lambda = 4$. Note that R is calculated from $w_F(\tau)$ only. All parameters and units are the same as in Fig.(5.1a)-Fig.(5.1d).

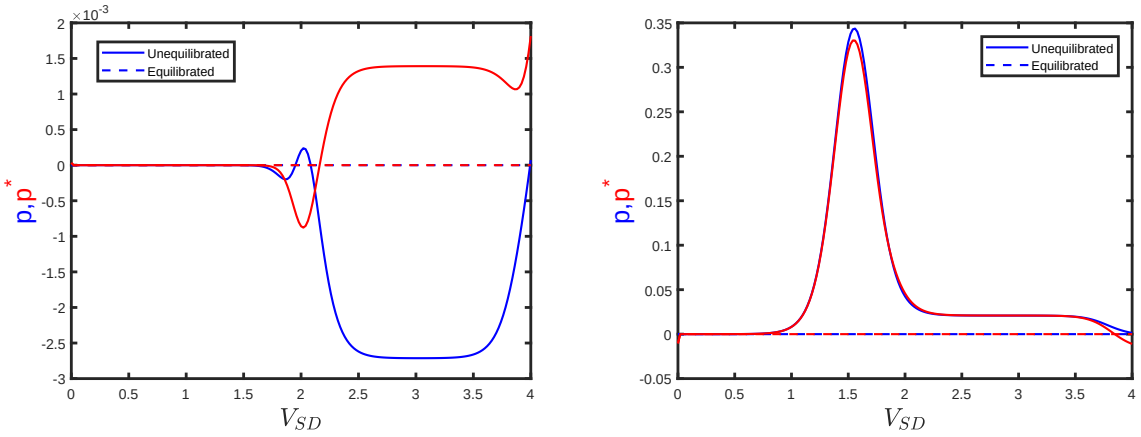

(a) (b)

Figure 5.5: The Pearson correlation coefficient for equilibrated and unequilibrated phonons, calculated from the WTD and the FPTD, for (a) $\lambda = 1$ and (b) $\lambda = 4$. All parameters and units are the same as in Fig.(5.1a)-Fig.(5.1d).

plot alone; the second cumulants and above are thus a better method for identifying non-renewal behavior.

Fig.(5.5b) is a reproduction from Ref.[78], except now the Pearson correlation coefficient between successive first-passage times has been added. The two distributions yield similar results; p and p^* have a peak value of ~ 0.3 at $V_{SD}/2 \approx 0.75$. In this voltage regime, if the first waiting time, τ, is small, then the $q = 3$ phonon state is highly occupied. The corresponding elastic Franck-Condon matrix element, $|\mathbf{X}_{33}|$, is much larger than smaller elastic transitions, and so it is probable that the next transition is through this elastic "shortcut", resulting in the second waiting time, τ', also being short [78]. Evidently, the effect lasts long enough to exist between successive first-passage times as well; although the peak of p^* is smaller. Backtunneling events ensure that the first-passage time must be greater than the waiting time, $\tau^* \geq \tau$, and so correlations between successive first-passage times must be smaller.

The Fano factor and randomness parameters in Fig.(5.4b) also identify non-renewal behavior. In the 0.5meV $< V_{SD} <$ 1eV voltage range, F and R^* differ: correctly predicting the correlations in Fig.(5.5b). In comparison, R actually equals F at $V_{SD} \approx 1.9$eV, while at the same voltage the waiting time Pearson coefficient is still non-zero $p \approx 0.05$. The correlations disappear when the phonons are forced to relax to equilibrium immediately, as the excited phonon state providing the elastic shortcut channel is no longer occupied. This is visible in Fig.(5.5a) as $p, p^* \sim 10^{-3}$, and Fig.(5.4a), where $F = R^*$ for all voltages.

5.3.2 Vibrations with a finite temperature gradient

At finite temperatures, and when the electrode Fermi energies are approximately in resonance with $\varepsilon + \omega q$, the bidirectional transport is dominated by thermal noise. A recent experimental

paper has shown, however, that electronic noise distinct from the thermal noise can be generated from a temperature gradient ΔT in the absence of a bias voltage, which they label delta-T noise [79]. We finish this chapter by exploring the effect a temperature gradient has on the first-passage times for sequential tunneling through the Holstein model.

Since the transport in this scenario is described by a standard master equation, the exact current matches the prediction from the WTD, which is shown in Fig.(5.6a); all black and blue lines coincide. The FPTD current prediction, on the other hand, differs from $\langle I \rangle$ at low ΔT, implying non-renewal behavior in this regime. Otherwise, the red FPTD lines coincide with all blue and black lines. Interestingly, the equilibrium current is larger than the non-equilibrium current, which is understood by examining $|\mathbf{X}_{qq'}|$ and the phonon occupation probabilities. When $\lambda = 1$ and $\omega = 1$ the Franck-Condon factor is largest for elastic $q = 0$ transitions. These transitions are more accessible to phonons in equilibrium, as the $q = 0$ state has a larger relative occupation probability for equilibrium phonons than non-equilibrium phonons:

$$\frac{P^{eq}_{q=0}}{P^{eq}_{q=1}} > \frac{P^{ne}_{0;q=0} + P^{ne}_{1;q=0}}{P^{ne}_{0;q=1} + P^{ne}_{1;q=1}}. \tag{5.12}$$

We note that for large ΔT the total current is the same order as that induced by a voltage bias in Fig.(5.3a) and Fig.(5.3b).

In Fig.(5.6b), F diverges as $\Delta T \to 0$, which is expected since the total current vanishes and thermal processes dominate in this regime. At larger ΔT the noise no longer diverges but is still super-Poissonian, and distinct from the shot noise generated by a voltage bias. We attribute this to the relatively large temperatures; even the smallest drain temperature we consider is large enough to cause backtunnelings from the drain, hence the super-Poissonian partition noise normally associated with a voltage bias.

It is evident that $R^* \neq F$ at small ΔT, implying that the transport is non-renewal in this temperature range. Despite this non-renewal behavior, we have chosen not to display the Pearson correlations; they are non-zero but small. At larger ΔT the transport is renewal as $F = R^*$, while again $R \neq F$ because the transport is bidirectional.

5.4 Summary

In this chapter, we analyzed the Holstein model at finite bias voltage, in which correlations between successive first-passage times are smaller than correlations between successive waiting times when backtunneling events are present. We also considered transport through the Holstein model at zero bias voltage and a finite temperature gradient. The temperature gradient induces a current, but also significant bidirectional transitions. The forward waiting time

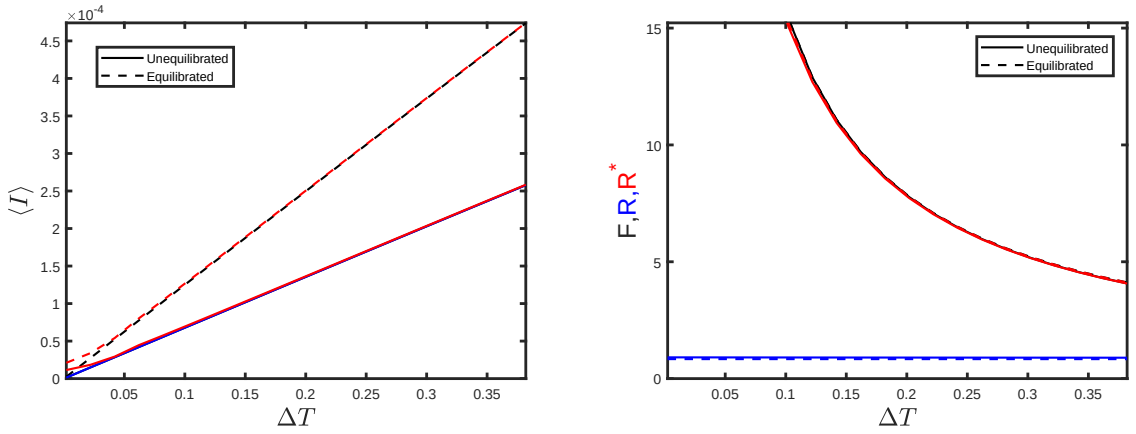

(a) (b)

Figure 5.6: Current (a) and Fano factor (b) predicted from the WTD in (blue) and FPTD (red) and compared to the exact results (black) for equilibrium and nonequilibrium vibrations, as a function of the temperature gradient ΔT. The vibrationally adjusted energy level is $\varepsilon = 1$, the vibrational frequency is $\omega = 1$, the electron-phonon coupling strength is $\lambda = 1$, the voltage is $V_{SD} = 0$, $\gamma^{\alpha} = \frac{\gamma}{2} = 0.01$. The average temperature across the molecule is $\bar{T} = \frac{T_S + T_D}{2} = 0.75$ and the electrode temperatures are symmetric around $\bar{T}$: $T_S = \bar{T} + \Delta T/2$ and $T_D = \bar{T} - \Delta T/2$. The equilibrium phonons are kept at a vibrational temperature of $T_V = \bar{T}$.

randomness parameter was consequently incapable of accurately predicting the Fano factor in renewal regimes, as opposed to the first-passage time randomness parameter.

Telegraphic switching

This chapter contains material that has been previously published in the following journal article:

Fluctuating-time and full counting statistics for quantum transport in a system with internal telegraphic noise, S.L. Rudge and D.S. Kosov, Phys. Rev. B **100**, 235430 (2019)

6.1 Motivation

In Chapter 4, we investigated a switching process produced by inelastic cotunneling and found that, because the switching rate was proportional to the tunneling rate, the resulting correlations were essentially negligible. This is not the only tunneling scenario in which such switching is observed, however. Molecular junctions regularly undergo random changes in intra-system dynamics [31] that cause the electric current to stochastically move between two different values: commonly referred to as telegraphic switching or a telegraph process. Telegraph noise is distinct from thermal and shot noise, often producing super-Poissonian effects, as we saw in Chapter 4. Our goal in this chapter, then, is to investigate the fluctuating-time statistics of a telegraphic switching process for three transport scenarios.

In the first, we stochastically switch a magnetic field B on and off an Anderson impurity, so that the electronic energy level switches between being spin-split and spin-degenerate. Next, we model two different molecular conformations via coupling of an electronic level to two different vibrational modes. Finally, we mimic a contact forming and breaking the molecule-electrode bonds at random points in time. Previous fluctuation research using Markovian rate equations has struggled to find significant correlations between successive electron tunnelings [97, 170, 175], since the T-matrix approach [93] neglects quantum coherent effects and the Markovian baths are memory-less. In contrast, we find that, with the inclusion of telegraphic switching in the dynamics, there are significant correlations present in all scenarios.

Section 6.1.1 is devoted to a review of relevant telegraphic switching literature. Section 6.2 outlines our general model as well as the three specific scenarios we consider, relying on

transition rates from previous chapters, and Section 6.3 contains the results.

6.1.1 Introduction

Telegraphic switching is a common experimental phenomenon, which is visible in scenarios containing two or more distinct states with different parameters governing the transport. Telegraph noise, which is distinct from $1/f$ noise, has been measured in systems with localized electron states [225, 226] and charge traps [53, 227, 228], as well as bistable molecular conformations [229–235], controllable bistability using a single-electron box near a single-electron transistor [236], and from the forming and breaking of metal-molecule bonds [15]. Using a quantum point contact as a charge detector, Fricke *et al.* have also measured bimodal counting statistics in a quantum dot arising from telegraphic switching [62].

If one of the switching states blocks the current, then the transport will display avalanche tunneling properties, as we have already discussed in Chapter 5. Lau *et al.* have even reported experimental measurements of avalanche tunneling in a single-molecule graphene-fullerene transistor, and successfully modeled their results using a two-state stochastic process [237]. This system, in particular, is indicative of an important transport scenario we consider in this chapter: telegraphic switching arising from molecular vibrations. We show that temporal correlations arise in this scenario, and are thus potentially crucial for understanding such experimental results.

Despite these many interesting experiments, there remains a dearth of theoretical literature on telegraph noise in nanoscale quantum transport. Although not a quantum system, Jordan and Sukhorukov studied a classical bistable system with a stochastic path integral formalism [238]. In the 1990s, Galperin *et al.* studied the average transparency [239] and low-frequency noise [240] through double barriers with dynamic defects. After a long gap of 20 years, theoretical quantum telegraphic switching research has resumed; Entin-Wohlman *et al.* [241], for example, used Green's functions to study quantum heat transport via a fluctuating electronic level, proposed as a model for an applied stochastic electric field. Gurvitz *et al.* [81] also used a fluctuating electronic level, but instead analyzed steady-state and transient dynamics. Kosov [80] has also recently investigated telegraph noise in a junction with electron-phonon interactions by adding a stochastic component to the quantum master equation.

The common theme among these treatments of the telegraph noise are time-dependent stochastic additions, $\zeta(t)$, whether they be to the electronic level, $\varepsilon + U\zeta(t)$, or to the master equation itself: $\dot{\mathbf{P}}(t) = \mathbf{L}\mathbf{P}(t) + \zeta(t)\mathbf{A}\mathbf{P}(t)$. Instead, we use a general Markovian master equation with two distinct sets of states, associated with transport scenario a and transport scenario b, connected only by a constant switching rate ν. All rates are time-independent and the master equation can be solved via normal methods.

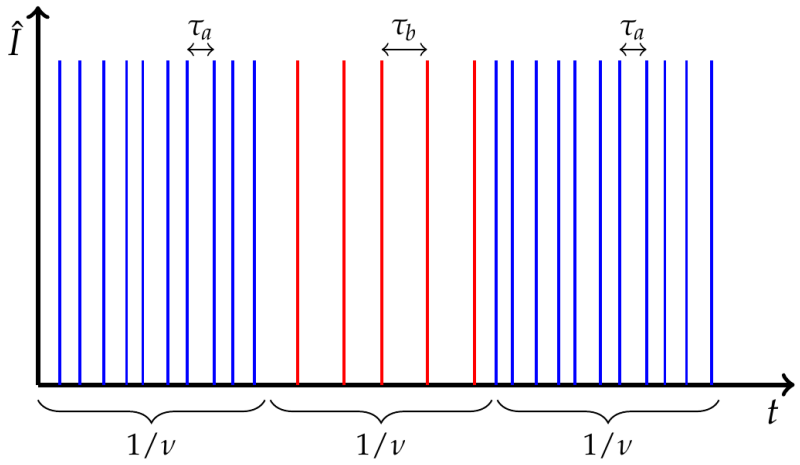

Figure 6.1: Schematic of a time-series of current spikes in a system telegraphically switching, at rate ν, between two characteristic first-passage times τ_a and τ_b. To exaggerate the effects we have reduced the stochasticity of time-intervals *within* each configuration. Each current spike represents the total current increasing by $+1$ since the last measurement.

6.2 Telegraphic switching model

Since we switch between two transport scenarios, we unfortunately cannot write a single Hamiltonian to describe the system dynamics. Rather, we will write the Hamiltonian for each scenario and then construct the master equation from ad hoc principles. The master equation for a general quantum system undergoing telegraphic switching between two scenarios a and b is

$$\frac{d}{dt}\begin{bmatrix} \mathbf{P}_a(\chi,t) \\ \mathbf{P}_b(\chi,t) \end{bmatrix} = \begin{bmatrix} \mathbf{L}_a(\chi) - \boldsymbol{\nu} & \boldsymbol{\nu} \\ \boldsymbol{\nu} & \mathbf{L}_b(\chi) - \boldsymbol{\nu} \end{bmatrix} \begin{bmatrix} \mathbf{P}_a(\chi,t) \\ \mathbf{P}_b(\chi,t) \end{bmatrix}. \tag{6.1}$$

From here, we will use the notation $\varphi \in [a,b]$ when referring to either of the two different transport scenarios, and $\bar{\varphi}$ when referring to the opposite scenario. Each $\mathbf{L}_\varphi(\chi)$ thus refers to the χ-dependent Liouvillian of the φ scenario without telegraphic switching. The matrix $\boldsymbol{\nu}$ contains the telegraphic switching rates, which are the same for each φ. They must be subtracted from $\mathbf{L}_\varphi(\chi)$ to conserve probability. Finally, the vector $\mathbf{P}(\chi,t) = [\mathbf{P}_a(\chi,t), \mathbf{P}_b(\chi,t)]^T$ is comprised of the probability distributions for the two scenarios. The transport scenarios we consider will all follow the dynamics in Eq.(6.1). The jump operators are similarly defined:

$$\mathbf{J}_F = \begin{bmatrix} \mathbf{J}_F^a & 0 \\ 0 & \mathbf{J}_F^b \end{bmatrix}, \qquad \mathbf{J}_B = \begin{bmatrix} \mathbf{J}_B^a & 0 \\ 0 & \mathbf{J}_B^b \end{bmatrix}. \tag{6.2}$$

6.2.1 Anderson impurity

Our first scenario uses the familiar Anderson impurity model. We model switching between scenarios a and b: a molecular orbital without an applied magnetic field and a molecular orbital with an applied magnetic field B, respectively. In the absence of a magnetic field, and barring further fine splitting, spin-$\uparrow$ and spin-$\downarrow$ electrons require the same charging energy to enter the molecule: $\varepsilon^a_\uparrow = \varepsilon^a_\downarrow = \varepsilon_0$. Once the magnetic field is applied, however, the spin-split energies are $\varepsilon^b_\downarrow = \varepsilon_0 + B/2$ and $\varepsilon^b_\uparrow = \varepsilon_0 - B/2$.

We combine these two scenarios in the probability vector

$$\mathbf{P}(\chi,t) = [P^a_0(\chi,t), P^a_\uparrow(\chi,t), P^a_\downarrow(\chi,t), P^a_2(\chi,t), P^b_0(\chi,t), P^b_\uparrow(\chi,t), P^b_\downarrow(\chi,t), P^b_2(\chi,t)]^T. \tag{6.3}$$

For sequential tunneling only, and under the Born-Markov approximation [224], the χ-dependent Liouvillian of scenario φ is

$$\mathbf{L}_\varphi(\chi) = \begin{bmatrix} -(\Gamma^\varphi_{\uparrow 0} + \Gamma^\varphi_{\downarrow 0}) & \Gamma^\varphi_{0\uparrow}(\chi) & \Gamma^\varphi_{0\downarrow}(\chi) & 0 \\ \Gamma^\varphi_{\uparrow 0}(\chi) & -(\Gamma^\varphi_{0\uparrow} + \Gamma^\varphi_{2\uparrow}) & 0 & \Gamma^\varphi_{\uparrow 2}(\chi) \\ \Gamma^\varphi_{\downarrow 0}(\chi) & 0 & -(\Gamma^\varphi_{0\downarrow} + \Gamma^\varphi_{2\downarrow}) & \Gamma^\varphi_{\downarrow 2}(\chi) \\ 0 & \Gamma^\varphi_{2\uparrow}(\chi) & \Gamma^\varphi_{2\downarrow}(\chi) & -(\Gamma^\varphi_{\uparrow 2} + \Gamma^\varphi_{\downarrow 2}) \end{bmatrix}, \tag{6.4}$$

and the jump operators are

$$\mathbf{J}^\varphi_F = \begin{bmatrix} 0 & \Gamma^{D,\varphi}_{0\uparrow} & \Gamma^{D,\varphi}_{0\downarrow} & 0 \\ 0 & 0 & 0 & \Gamma^{D,\varphi}_{\uparrow 2} \\ 0 & 0 & 0 & \Gamma^{D,\varphi}_{\downarrow 2} \\ 0 & 0 & 0 & 0 \end{bmatrix} \quad \text{and} \quad \mathbf{J}^\varphi_B = \begin{bmatrix} 0 & 0 & 0 & 0 \\ \Gamma^{D,\varphi}_{\uparrow 0} & 0 & 0 & 0 \\ \Gamma^{D,\varphi}_{\downarrow 0} & 0 & 0 & 0 \\ 0 & \Gamma^{D,\varphi}_{2\uparrow} & \Gamma^{D,\varphi}_{2\downarrow} & 0 \end{bmatrix}. \tag{6.5}$$

The total χ-dependent rates contain a source and drain component:

$$\Gamma^\varphi_{lk} = \Gamma^{S,\varphi}_{lk} + \Gamma^{D,\varphi}_{lk} e^{\pm i\chi}, \tag{6.6}$$

where the $\pm$ is positive if the fermionic occupation decreases from state k to state l, and

negative if the fermionic occupation increases. Explicitly now, the spin-dependent rates are

$$\Gamma^{\alpha,\varphi}_{\sigma 0} = \gamma^{\alpha,\varphi}\, n_F(\varepsilon^{\varphi}_{\sigma} - \mu_\alpha), \tag{6.7}$$

$$\Gamma^{\alpha,\varphi}_{0\sigma} = \gamma^{\alpha,\varphi}\, \left[1 - n_F(\varepsilon^{\varphi}_{\sigma} - \mu_\alpha)\right], \tag{6.8}$$

$$\Gamma^{\alpha,\varphi}_{\sigma 2} = \gamma^{\alpha,\varphi}\, \left[1 - n_F(\varepsilon^{\varphi}_{\sigma} + U - \mu_\alpha)\right], \qquad \text{and} \tag{6.9}$$

$$\Gamma^{\alpha,\varphi}_{2\sigma} = \gamma^{\alpha,\varphi}\, n_F(\varepsilon^{\varphi}_{\sigma} + U - \mu_\alpha). \tag{6.10}$$

6.2.2 Holstein model

We also consider a molecule changing conformations, and thus changing its vibrational interactions. Conformation φ is assumed to be a single molecular orbital ε^{φ}_0 interacting with a vibrational mode ω_φ, which we will again model via the Holstein Hamiltonian.

Since the system switches between two configurations, there will be two sets of parameters: $\{\varepsilon^a_0, \lambda_a, \omega_a\}$ and $\{\varepsilon^b_0, \lambda_b, \omega_b\}$. We therefore seek a master equation for the probability that at time t the system is occupied by m electrons and q phonons while in configuration φ, which is denoted $P^{\varphi}_{mq}(t)$:

$$\dot{P}^{\varphi}_{0q}(t) = \nu_0 \left(P^{\bar{\varphi}}_{0q}(t) - P^{\varphi}_{0q}(t)\right) + \sum_{\alpha q'} \Gamma^{\alpha,\varphi}_{0q,1q'} P^{\varphi}_{1q'}(t) - \Gamma^{\alpha,\varphi}_{1q',0q} P^{\varphi}_{0q}(t), \tag{6.11}$$

$$\dot{P}^{\varphi}_{1q}(t) = \nu_1 \left(P^{\bar{\varphi}}_{1q}(t) - P^{\varphi}_{1q}(t)\right) + \sum_{\alpha q'} \Gamma^{\alpha,\varphi}_{1q,0q'} P^{\varphi}_{0q'}(t) - \Gamma^{\alpha,\varphi}_{0q',1q} P^{\varphi}_{1q}(t), \tag{6.12}$$

The molecule switches between the two vibrational modes with rate ν_0, when the system is electronically empty, and rate ν_1, when the system is singly occupied. Transitions within the configurations obey the usual rules;

$$\Gamma^{\alpha,\varphi}_{0q',1q} = \gamma^{\alpha,\varphi} |\mathbf{X}^{\varphi}_{q'q}|^2 \left[1 - n_F(\varepsilon_\varphi - \omega_\varphi(q' - q) - \mu_\alpha)\right] \tag{6.13}$$

is the transition rate from state $|1q\rangle_\varphi$ to state $|0q'\rangle_\varphi$, via tunneling to electrode α, and

$$\Gamma^{\alpha,\varphi}_{1q',0q} = \gamma^{\alpha,\varphi} |\mathbf{X}^{\varphi}_{q'q}|^2 n_F\left(\varepsilon_\varphi + \omega_\varphi(q' - q) - \mu_\alpha\right) \tag{6.14}$$

is the transition rate between $|0q\rangle_\varphi$ and $|1q'\rangle_\varphi$.

The Fourier transformed n-resolved probability vector is

$$\mathbf{P}(\chi, t) = \left[P^a_{00}(\chi,t), P^a_{10}(\chi,t), \ldots, P^a_{0N}(\chi,t), P^a_{1N}(\chi,t), P^b_{00}(\chi,t), P^b_{10}(\chi,t), \ldots, P^b_{0N}(\chi,t), P^b_{1N}(\chi,t)\right], \tag{6.15}$$

where N is chosen such that $N\omega_\varphi \gg V_{SD}, \gamma^\varphi, T$. $\mathbf{P}(\chi, t)$ therefore has length $4(N+1)$ and its

components $\mathbf{P}^{\varphi}(\chi,t)$ follow the master equation:

$$\dot{P}^{\varphi}_{0q}(\chi,t) = \nu_0\left(P^{\bar{\varphi}}_{0q}(\chi,t) - P^{\varphi}_{0q}(\chi,t)\right) + \sum_{q'}\left(\Gamma^{S,\varphi}_{0q;1q'} + \Gamma^{D,\varphi}_{0q;1q'}e^{i\chi}\right)P^{\varphi}_{1q'}(\chi,t) - \sum_{\alpha q'}\Gamma^{\alpha,\varphi}_{1q';0q}P^{\varphi}_{0q}(\chi,t), \tag{6.16}$$

$$\dot{P}^{\varphi}_{1q}(\chi,t) = \nu_1\left(P^{\bar{\varphi}}_{1q}(\chi,t) - P^{\varphi}_{1q}(\chi,t)\right) + \sum_{q'}\left(\Gamma^{S,\varphi}_{1q;0q'} + \Gamma^{D,\varphi}_{1q;0q'}e^{-i\chi}\right)P^{\varphi}_{0q'}(\chi,t) - \sum_{\alpha q'}\Gamma^{\alpha,\varphi}_{0q';1q}P^{\varphi}_{1q}(\chi,t). \tag{6.17}$$

From here the χ-dependent master equation can easily be split into the quantum jump operators, which are constructed according to Eq.(6.2). The individual $\mathbf{J}^{\varphi}_F$ and $\mathbf{J}^{\varphi}_B$ are also easily defined, as in Appendix D.2.2.

For equilibrated phonons, we can again use the ansatz

$$P^{\varphi}_{nq}(\chi,t) = P^{\varphi}_{n}(\chi,t)\frac{e^{-q\omega_\varphi/T_V}}{1-e^{-\omega_\varphi/T_V}}. \tag{6.18}$$

to obtain effective transition rates:

$$T^{\varphi}_{lk} = \sum_{\alpha} T^{\alpha,\varphi}_{lk} \tag{6.19}$$

$$= \sum_{\alpha,qq'}\Gamma^{\alpha,\varphi}_{lq;kq'}\frac{e^{-q\omega_\varphi/T_V}}{1-e^{-\omega_\varphi/T_V}}, \tag{6.20}$$

which define the corresponding master equation,

$$\mathbf{L}(\chi) = \begin{bmatrix} -(T^{a}_{10}+\nu_0) & T^{S,a}_{01} + T^{D,a}_{01}e^{i\chi} & \nu_0 & 0 \\ T^{S,a}_{10} + T^{D,a}_{10}e^{-i\chi} & -(T^{a}_{01}+\nu_1) & 0 & \nu_1 \\ \nu_0 & 0 & -(T^{b}_{10}+\nu_0) & T^{S,b}_{01} + T^{D,b}_{01}e^{i\chi} \\ 0 & \nu_1 & T^{S,b}_{10} + T^{D,b}_{10}e^{-i\chi} & -(T^{b}_{01}+\nu_1) \end{bmatrix}, \tag{6.21}$$

and jump operators:

$$\mathbf{J}_F = \begin{bmatrix} 0 & T^{D,a}_{01} & 0 & 0 \\ 0 & 0 & 0 & 0 \\ 0 & 0 & 0 & T^{D,b}_{01} \\ 0 & 0 & 0 & 0 \end{bmatrix} \text{ and } \mathbf{J}_B = \begin{bmatrix} 0 & 0 & 0 & 0 \\ T^{D,a}_{10} & 0 & 0 & 0 \\ 0 & 0 & 0 & 0 \\ 0 & 0 & T^{D,b}_{10} & 0 \end{bmatrix}. \tag{6.22}$$

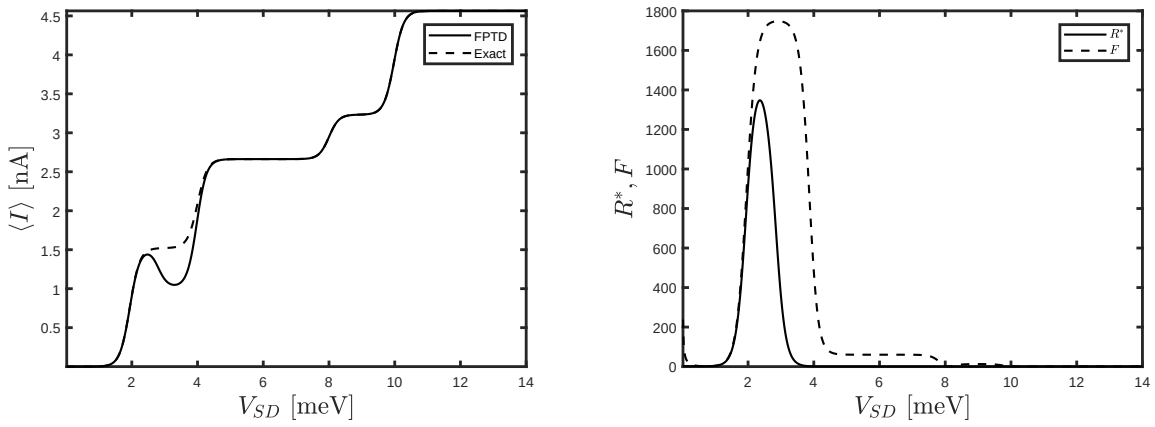

(a) (b)

Figure 6.2: Comparison of the first (a) and second (b) cumulants of the FCS and the FPTD as a function of V_{SD}. The spin-degenerate energy level is $\varepsilon_0 = 1$meV, the magnetic field is $B/2 = 3$meV, the Coulomb repulsion is $U = 1$meV, the S-D temperature is $T = 75\mu$eV, and $\gamma^{\alpha,\varphi} = \frac{\gamma}{2} = \frac{T}{4}$. All telegraphic switching rates are equal: $\nu_k = \nu = 10^{-4}\gamma$, where $k \in \{0, \uparrow, \downarrow, 2\}$.

6.3 Results

We will start this section with a discussion on the fluctuation behavior expected from telegraph noise. Regardless of the underpinning Hamiltonians, all scenarios we analyze follow a simple premise. The nanoscale quantum system H_m randomly switches between two configurations with two distinct sets of transport parameters. We expect, therefore, that each transport configuration has a characteristic current $\langle I_a \rangle$ and $\langle I_b \rangle$ and an associated characteristic first-passage time $\langle \tau_a \rangle^*$ and $\langle \tau_b \rangle^*$.

If the transport parameters are set such that these characteristic first-passage times are appreciably different, and the switching rate between configurations is small enough that the transport tends to get "stuck" in each for a long amount of time, then the dynamics will be quantitatively similar to Fig.(6.1). In it, there are relatively long periods where the first-passage times are clustered around $\langle \tau_a \rangle^*$ and then relatively long periods where the first-passage times are clustered around $\langle \tau_b \rangle^*$. That is, if a first-passage time close to $\langle \tau_a \rangle^*$ is recorded, then the next first-passage time is likely to be close to $\langle \tau_a \rangle^*$ as well, and likewise for $\langle \tau_b \rangle^*$. The transport should thus be characterized by positive correlations between successive first-passage times.

We note that all results comparing the Fano factor and the randomness parameter refer to $R^* = R_1^*$, the randomness parameter of $F(1|\tau)$.

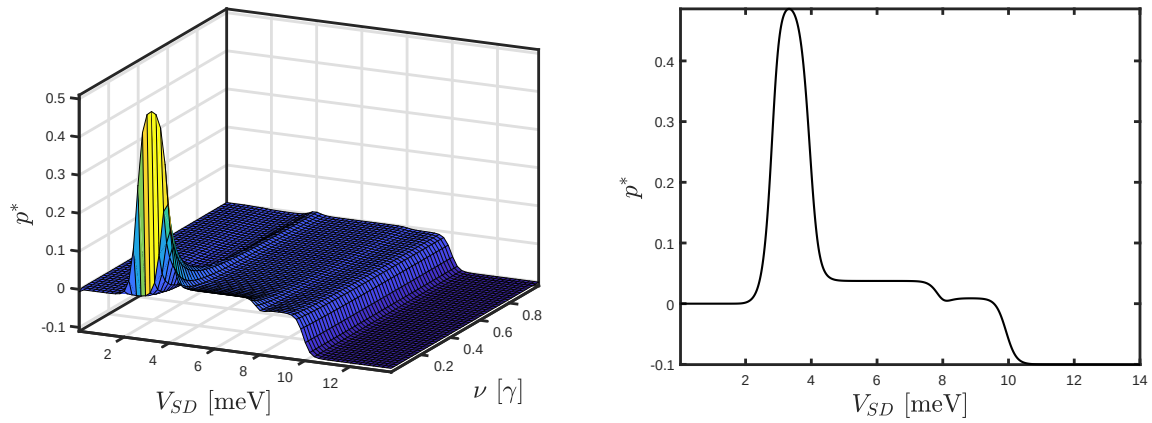

(a) (b)

Figure 6.3: Pearson correlation coefficient as a function of (a) V_{SD} and ν, and (b) as a slice at $\nu = 10^{-4}\gamma$. All other parameters are the same as in Fig.(6.2a) and Fig.(6.2b).

6.3.1 Magnetic switching: Anderson model

The current plot in Fig.(6.2a) displays the $I - V$ characteristics we expect from an Anderson impurity undergoing telegraphic switching. The current undergoes steplike increases as V_{SD} approaches each energy level: ε_0, $\varepsilon_0 \pm B/2$, and $\varepsilon_T = \varepsilon_\uparrow + \varepsilon_\downarrow + U$. The step at $V_{SD}/2 = 1$meV is larger as it corresponds to the $\varepsilon^a_\uparrow$ and $\varepsilon^a_\downarrow$ levels simultaneously opening, while the step at $V_{SD}/2 = 5$meV corresponds to the double level ε_T opening for both scenarios. The FPTD largely mimics this behavior except for a region between $1\text{meV} \leq V_{SD}/2 \leq 2\text{meV}$: a regime of non-renewal behavior.

The Fano factor and randomness parameter diverge to an even greater degree over the same voltage, reinforcing that this is non-renewal behavior. In fact, Fig.(6.2b) shows that F and R^* differ at all voltages except $V_{SD}/2 < 1$meV, while this feature is difficult to see from the current alone. Fig.(6.3b) confirms the non-renewal behavior as $p^* \approx 0.5$ peaks between $1\text{meV} \leq V_{SD}/2 \leq 2\text{meV}$; as expected, there are relatively strong positive correlations accompanying telegraphic switching. What remains now is to analyze *why* the characteristic first-passage times of scenario a and b are so different in this regime. We note that, since $F, R^* \to +\infty$ as $V_{SD} \to 0$, we plot all results starting just outside this region.

The degenerate ε^a_σ level is fully open at $V_{SD}/2 = 1$meV, but all levels for the b scenario remain closed. As $V_{SD}/2$ increases from $1 - 2$meV, the $\varepsilon^b_\uparrow$ begins to open due to thermal effects in the baths. Because it is not fully open, though, the current (first-passage time) through $\varepsilon^b_\uparrow$ in this voltage regime is much smaller (greater) than that through ε^a_σ.

In Fig.(6.3a), we have also plotted the Pearson correlation coefficient as a function of V_{SD} and ν. In it, we see that, as ν increases, the correlations present for $1\text{meV} \leq V_{SD}/2 \leq 2\text{meV}$ decrease, until they are close to zero when $\nu = \gamma$. Physically, if $\nu = \gamma$, then the molecule

switches between configurations at the same rate at which electrons enter and leave, so that the system does not spend long enough in either configuration for significant correlations between successive first-passage times. Also noticeable is that the correlation peak shifts closer to $V_{SD}/2 = 2\text{meV}$, since at larger ν the system does not spend long enough in the b configuration to record many tunnelings, and thus correlations, at lower voltages.

Apart from identifying non-renewal behavior, the second cumulants reveal telegraphic switching behavior in the magnitude of their peaks, which are $\mathcal{O}(10^3)$. This is unusual for Markovian quantum systems, in which transport is usually close to Poissonian and $F, R^* \propto 1$. Such F and R^* arise from the large differences between the characteristic first-passage times $\langle\tau_a\rangle^*$ and $\langle\tau_b\rangle^*$. As the voltage increases and telegraphic switching influences the transport less, these effects accordingly disappear from the F, R^* and p^*.

As $V_{SD}/2$ approaches 4meV, the $\varepsilon^b_\downarrow$ begins to open and there is little difference between scenario a and b. Between $2\text{meV} < V_{SD} < 4\text{meV}$ the noise is thus better described by the Fano factor under the Coulomb blockade, $F = \left((\gamma^S)^2 + 4(\gamma^D)^2\right) / \left(\gamma^S + 2\gamma^D\right)^2$, which for symmetric coupling reduces to $F = 5/9$ [98]. Indeed, at $V_{SD}/2 = 4\text{meV}$ the Fano factor comes close to this value, although it is not visible in Fig.(6.2b). At higher voltages, when $V_{SD}/2 > 5\text{meV}$ all energy levels are open and the system is effectively non-interacting; the corresponding noise is the well-known result $F = \left((\gamma^S)^2 + (\gamma^D)^2\right) / \left(\gamma^S + \gamma^D\right)^2$ [49, 50]. Since we use symmetric couplings, the Fano factor reduces to $F = 0.5$, which is the exact value in Fig.(6.2b). In this regime the Pearson coefficient is $p^* \approx -0.1$: the standard result for a single Anderson impurity in the high-bias limit.

6.3.2 Vibrational switching: Holstein model

In Fig.(6.4a)-Fig.(6.4c), we have assumed that a single level, ε_0, telegraphically switches between two different vibrational coupling configurations. The energy ε_0 is chosen as the polaron shift for configuration b, $\frac{\lambda_b^2}{\omega_b}$, so that $\varepsilon_a = 7$ and $\varepsilon_b = 0$. We note that, for all calculations from the Holstein model, we have chosen to scale all energy parameters in terms of ω_a, or $\hbar\omega_a/e$ outside of natural units, and $\langle I\rangle$ is also scaled in terms of ω_a, or e/ω_a.

The polaron-shifted energy of configuration a is large enough that, at low voltages, many phonon interactions are required for electrons to tunnel through the molecule. For $\lambda_a = 1$, however, only small $|q - q'|$ transitions have non-negligible Franck-Condon matrix elements, and so the contribution to the current remains zero until $V_{SD}/2 \to 7$, when ε_a begins to open for elastic $q = 0$ transitions.

The Franck-Condon blockade [43] is present at low voltages for configuration b, since $\lambda_b = 4$ and $\omega_b = 2$; hence the small current steps $V_{SD}/2 = 2q$. The current due to unequilibrated phonons is initially larger than that due to equilibrated phonons, because at low voltages the

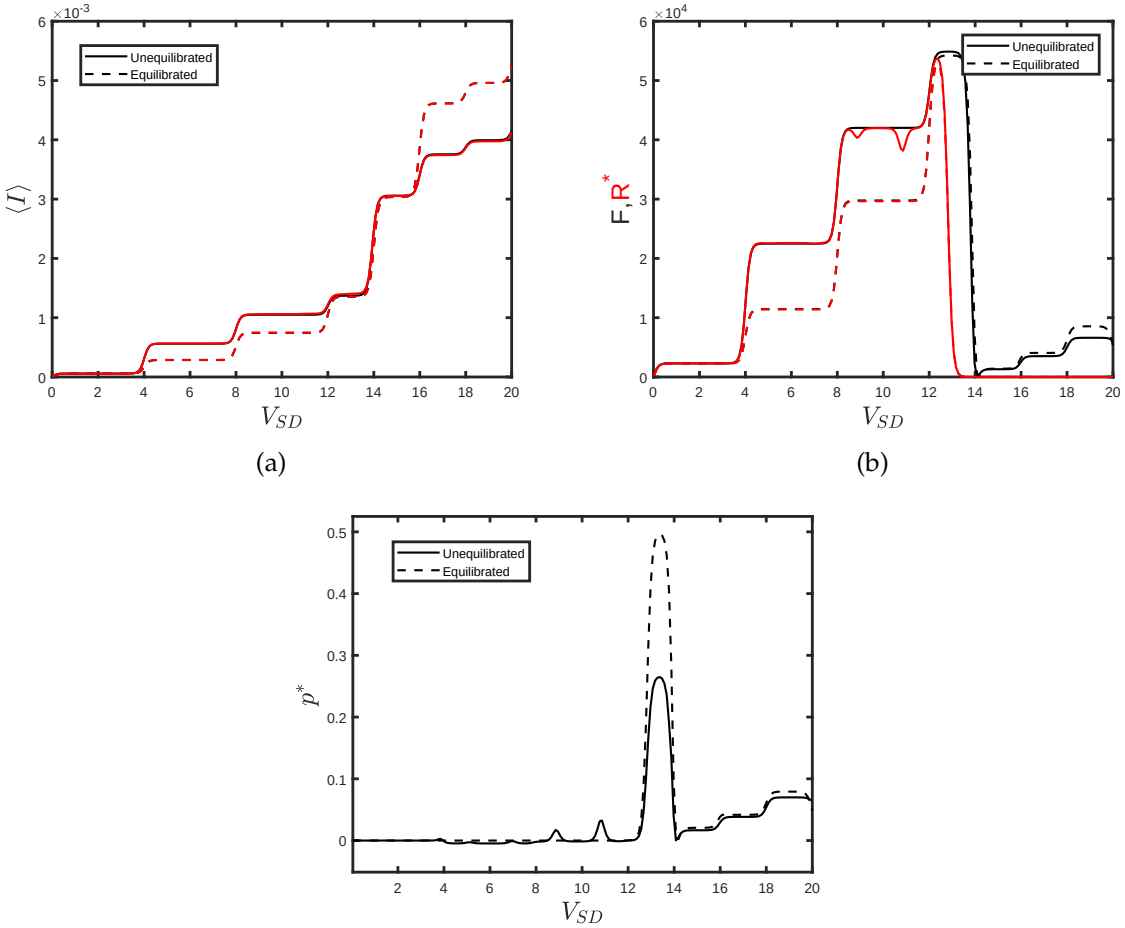

Figure 6.4: Comparison of the first (a) and second (b) cumulants of the FCS and the FPTD, as well as (c) the Pearson correlation coefficient, as a function of V_{SD} and for both equilibrated and unequilibrated vibrations. The polaron shifted energy levels are $\varepsilon_a = \frac{\lambda_b^2}{\omega_b} - \frac{\lambda_a^2}{\omega_a}$ and $\varepsilon_b = 0$; the phonon frequencies are $\omega_a = 1$ and $\omega_b = 2$; and the electron-phonon couplings are $\lambda_a = 1$ and $\lambda_b = 4$. The temperature of both the source and the drain, as well as the effective phonon temperature, is $T = T_V = 0.05$, from which we again define $\gamma = 0.5T$. The molecule-electrode couplings are $\gamma^{\alpha,\varphi} = \frac{\gamma}{2}$ and the telegraphic switching rates are $\nu_0 = \nu_1 = 10^{-6}\gamma$.

high $|q - q'|$ transitions required to overcome the blockade are more likely when phonons are out of equilibrium. When the voltage window contains both energy levels, in contrast, the equilibrated phonons provide a larger current, since low $|q - q'|$ transitions dominate through the ε_a level and transitions to the $q = 0$ state are required for transport through the ε_b level.

Fig.(6.4a), while illuminating, does not visually display any non-renewal behavior. Numerical differences between $\langle I \rangle$ and $\frac{1}{\langle \tau_1 \rangle}$ may be present, but they are not easily visible to the naked eye. In Fig.(6.4b) and Fig.(6.4c), however, we can easily determine the renewal behavior. When $V_{SD}/2 < 2$, $F = R$ and the transport is clearly renewal, which we can also see in Fig.(6.4c), since in this voltage range $p^* = 0$. This result seems counter-intuitive: the two conformations have different characteristic currents, so why does telegraphic switching not produce positive correlations?

The transport is renewal in this regime because the current through configuration a is negligible; telegraphic switching just places large time gaps of no tunneling between periods of tunneling through configuration b, and so producing avalanche tunneling instead. As we have already seen, in avalanche tunnleing the mean of the first-passage time distribution is much larger than the mode, and is accompanied by large Fano factors and randomness parameters $F, R^* \sim 10^4$, but negligible correlations between successive first-passage times [43].

The most noticeable non-renewal behavior is the correlation peak $p^* \approx 0.5$ at $V_{SD}/2 \approx 6.5$: when the ε_a level begins to open for elastic $q = 0$ transitions, which for $\lambda_a = 1$ are the dominant current contribution. At this point, the current from configuration a is non-negligible and telegraphic switching correlations appear. These are larger for equilibrated phonons for two reasons. First, when phonons are in equilibrium the elastic $q = 0$ transition is maximized, and second, when phonons are unequilibrated, the Franck-Condon blockade is minimized. There are also two similar, but much smaller, correlation spikes at $V_{SD}/2 \approx 4.5$ and $V_{SD}/2 \approx 5.5$ corresponding to $q = 1$ and $q = 2$ transitions beginning to open. As expected, these non-renewal regimes are accompanied by a discrepancy between F and R^*.

In Fig.(6.5a)-Fig.(6.5c) we exclude the polaron shift by setting $\varepsilon_a = \varepsilon_b = 0$, which implies that the two molecular configurations correspond to two different orbitals separately coupled to two vibrational modes. We also keep identical electron-phonon couplings, so that telegraphic switching phenomena arises solely from the difference between $\omega_a = 1$ and $\omega_b = 2$.

At all V_{SD} in Fig.(6.5a), we can clearly see double steps in the $I - V$ characteristics. As with the Fig.(6.4a), there are small steps at $V_{SD}/2 = (2q + 1)$, corresponding to phonon interactions in configuration a only, and larger steps at $V_{SD}/2 = 2q$, corresponding to phonon interactions in both configurations. The Franck-Condon blockade is present at low voltages for configuration a, since $\lambda_a = 3$ and $\omega_a = 1$. However, current is not suppressed through configuration b, as the magnitude of the blockade effect depends on the ratio $\frac{\lambda}{\omega}$.

Although, again, we cannot see any difference between $\langle I \rangle$ and $\frac{1}{\langle \tau \rangle^*}$, at all voltages $F \gg$

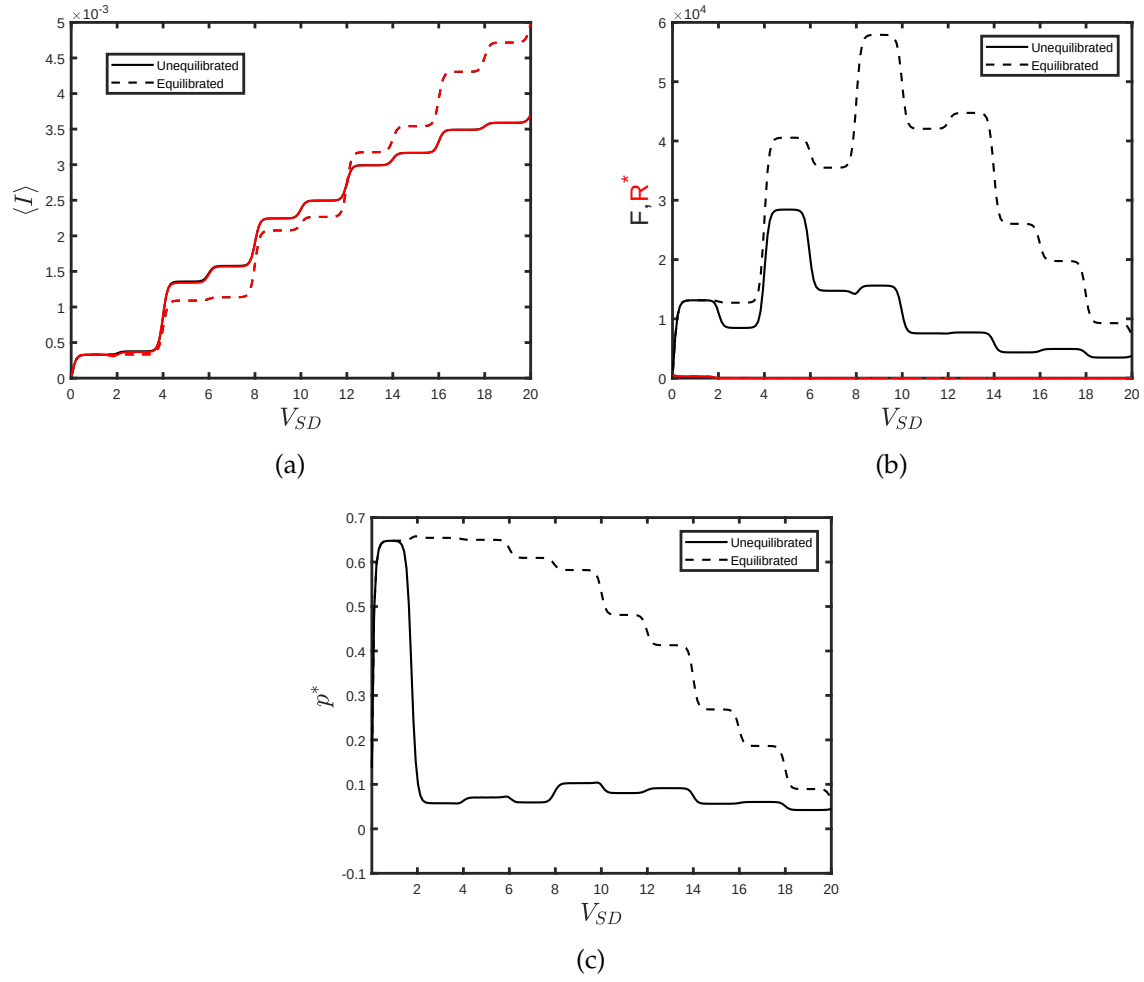

Figure 6.5: Comparison of the first (a) and second (b) cumulants of the FCS and the FPTD, as well as (c) the Pearson correlation coefficient, as a function of V_{SD} and for both equilibrated and unequilibrated vibrations. The polaron shifted energy levels are $\varepsilon_a = \varepsilon_b = 0$; the phonon frequencies are $\omega_a = 1$ and $\omega_b = 2$; and the electron-phonon couplings are $\lambda_a = \lambda_b = 3$.

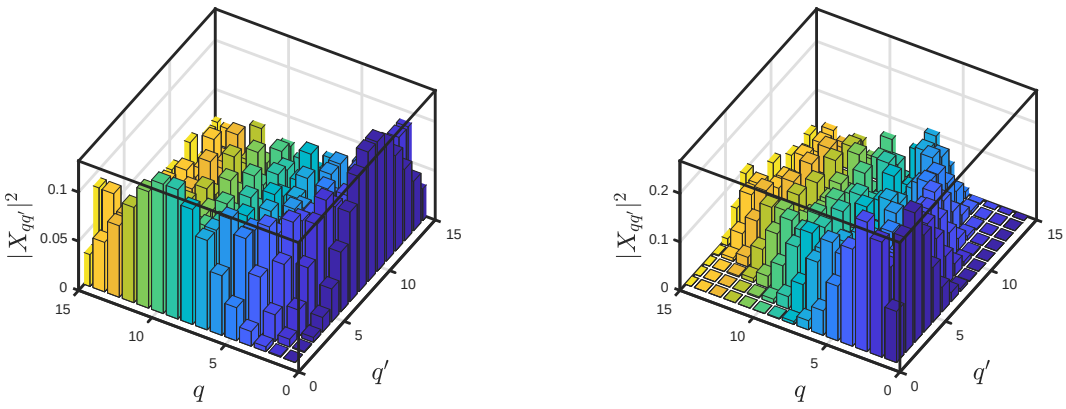

(a) (b)

Figure 6.6: The Franck-Condon matrix elements over a range of q and q', for two different sets of parameters: (a) $\frac{\lambda_a}{\omega_a} = 3$ and (b) $\frac{\lambda_b}{\omega_b} = \frac{3}{2}$.

R^*, indicating non-renewal behavior. Fig.(6.5c) corroborates this, as the Pearson correlation coefficient peaks at 0.65 between $0 < V_{SD}/2 < 1$ and never fully decays to zero. We can understand the peak in terms of the Franck-Condon blockade.

The matrix elements $|\mathbf{X}_{qq'}|^2$ in Fig.(6.6a), where $\frac{\lambda_a}{\omega_a} = 3$, are suppressed for low $|q - q'|$ and especially for $q = q' = 0$. In contrast, the matrix element $|\mathbf{X}_{00}|^2$, where $\frac{\lambda_b}{\omega_b} = \frac{3}{2}$ in Fig.(6.6b) is non-zero. The elastic $q = 0$ transition, therefore, is available to configuration b in the voltage range $0 < V_{SD}/2 < 1$, but not to configuration a. Since this is the only transition available in this voltage range, there is current through configuration b and no current through configuration a: hence the large correlations between successive first-passage times. Because the Franck-Condon blockade affects equilibrated phonons more than unequilibrated phonons, the correlations for equilibrated phonons last into higher voltages than for unequilibrated, which decay to $p \approx 0.1$ immediately outside of $0 < V_{SD}/2 < 1$.

6.3.3 Noise on the interface: Holstein model

Our last scenario concerns a fluctuating molecular-electrode coupling. Defining a scaling constant $\gamma = 0.5T$, we fix the molecule-source coupling at $\gamma_\varphi^S = \gamma/2$, and vary the molecule-drain coupling between configuration a, $\gamma_a^D = \gamma/2$, and configuration b, $\gamma_b^D = 0.01\gamma$. In this manner, we are able to model, albeit crudely, the molecule attaching to and detaching from the drain electrode.

The current associated with this process, shown in Fig.(6.7a), does not display double-step behavior, as $\omega_a = \omega_b$ and $\lambda_a = \lambda_b$. Fig.(6.7b) and Fig.(6.7c) show that the transport dynamics are non-renewal; $F \gg R^*$ and $p^* \neq 0$, for all non-zero voltages.

The correlation for unequilibrated phonons peaks at $p^* \approx 0.3$ between $0 \leq V_{SD}/2 \leq 1$ before

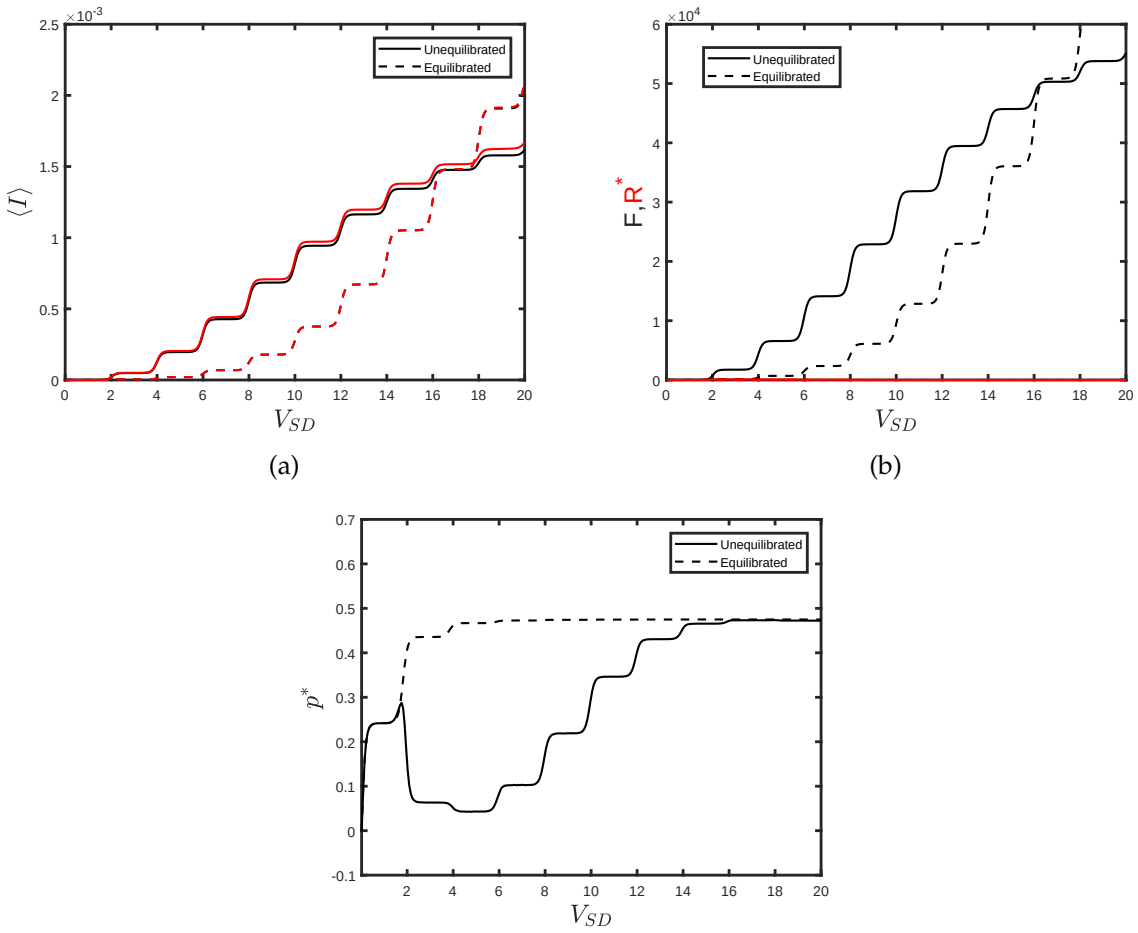

Figure 6.7: Comparison of the first (a) and second (b) cumulants of the FCS and the FPTD, as well as (c) the Pearson correlation coefficient, as a function of V_{SD} and for both equilibrated and unequilibrated vibrations. The only difference between configuration a and b are the molecule-lead couplings. We first define a constant $\gamma = 0.5T$, and then $\gamma^{S,\varphi} = \gamma^{D,a} = \gamma/2$, and $\gamma^{D,b} = 0.01\gamma$. Else, they share the same parameters: $\varepsilon_\varphi = 0$, $\lambda_\varphi = 3$, $\omega_\varphi = 1$, $T = 0.05$, $T_V = 0.05$, $\nu_0 = \nu_1 = \nu = 10^{-6}\gamma$.

decaying to near zero and then stepping up to a maximum of $p^* \approx 0.5$ at higher voltages. Since $\frac{\lambda_\varphi}{\omega_\varphi} = 3$, the Franck-Condon blockade is in effect at low voltages. We surmise, then, that the weak γ_b^D is unable to overcome the blockade and the two currents $\langle I_a \rangle$ and $\langle I_b \rangle$ are different enough so as to see correlations. Between $1 < V_{SD}/2 < 4$, however, configuration a overcomes the blockade but $\langle I_b \rangle$ is still negligible. The difference between configuration a and b is large enough that avalanche tunneling, not telegraphic switching, is the result. At higher voltages still, $\langle I_b \rangle$ is now non-negligible, so telegraphically switching between the two currents $\langle I_a \rangle$ and $\langle I_b \rangle$ produces correlations. Correlations arising from equilibrated phonons, in contrast, are stable around $p^* \approx 0.6$ over the same voltage regime, since the Franck-Condon blockade is stronger than the difference between $\langle I_a \rangle$ and $\langle I_b \rangle$.

6.4 Summary

The major result from this chapter is that strong positive correlations exist for transport scenarios involving telegraphic switching. To see these correlations, however, the switching rate, ν, must be much smaller than the rate of molecule-electrode tunneling, γ, and the two transport scenarios must have significantly different characteristic currents and first-passage times, $\langle I_a \rangle, \langle \tau_a \rangle^*$ and $\langle I_b \rangle, \langle \tau_b \rangle^*$. We demonstrated this for three scenarios: telegraphic switching between an Anderson impurity with and without an applied magnetic field, telegraphic switching between two vibrational conformations, and telegraphic switching between two different γ.

Triple quantum dot

7.1 Motivation

All systems in previous chapters have been treated in parameter regimes where the rate equation provides a suitable description of the transport. Upon reflection, it is somewhat surprising that these systems displayed any sort of non-renewal behavior at all, as we have removed major sources of correlations by ignoring coherences and using the Markovian assumption. All correlations, in fact, arose from including some form of extra dynamics, like cotunneling, electron-phonon interactions, or telegraphic switching. In this last chapter, however, we reintroduce the off-diagonal density matrix elements and analyze the fluctuating-time statistics of a system in which quantum coherences play an important role in the transport: the triple quantum dot (TQD).

Previous research has shown that quantum interference significantly affects current and noise in a TQD via Aharonov-Bohm oscillations or coherent population trapping [242]. We propose that interference effects will present in correlations between successive tunnelings, and thus between successive waiting times. Our analysis covers several regimes well-documented in the literature, for which we provide new results from the perspective of fluctuating-time statistics. Of all the possible TQD arrangements, we compute results for the ring geometries in Fig.(7.1a) and Fig.(7.1b). To include coherent effects, we use the full n-resolved master equation, as opposed to the rate equation approach of previous chapters. Because of the large Fock space for TQDs, we also restrict our analysis to the WTD. We find that interference effects do present in correlations between successive waiting times, although they are generally quite small. Also, similarly to Ref.[243], we find that coherences produce oscillations in the distribution of waiting times itself, which correlate to time-dependent dot occupancies.

Our analysis follows the previous chapters' format; Section 7.2 provides an outline and introduction of the system, discussing experimental measurements and previous theoretical work; Section 7.3 contains the Hamiltonian and full master equation necessary for our analysis; and Section 7.4 holds the results.

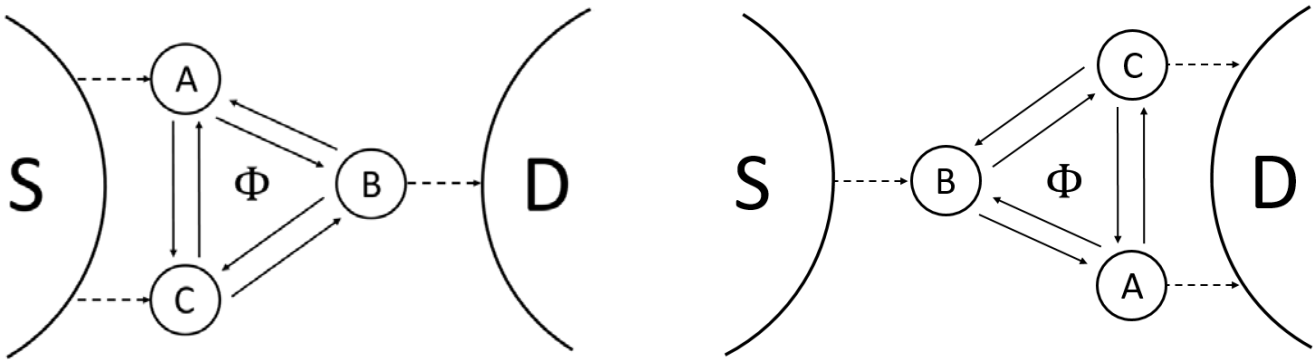

Figure 7.1: Schematics of the two triangular TQD geometries used in this chapter. In (a) dots A and C are coupled to the source, while dot B alone is coupled to the drain, and (b) contains the mirror configuration.

7.2 Introduction

Throughout all the transport scenarios we have so far considered, the common theme has been the Anderson-Holstein model. Although it more accurately describes simple nanostructures like quantum dots rather than molecules, the Anderson-Holstein model serves as good conceptual model for a molecular orbital as it contains effects typically found in molecular junctions. If we consider the Anderson-Holstein model to model one quantum dot, which are often referred to as "artifical atoms" due to their discrete energy spectrum, then coherently coupling multiple dots together will produce an analogous "artificial molecule"; the motivation for producing nanostructures like TQDs. This is not an easy experimental task, however, and it is only in the last 15 years that experimental techniques have become sophisticated enough to create TQDs; the initial challenge was to coherently couple just two quantum dots [244].

Synthesizing a double quantum dot (DQD) is a similar process to a single quantum dot, which we described in Chapter 1. As a reminder, metal gates are deposited onto a heterostructure, such as GaAs/AlGaAs, with a 2DEG about 100nm below the surface. The gates are arrayed so that applying a negative voltage and depleting electrons below the surface causes two QDs to form [245, 246]; see, for example, Fig.(7.2a). Similarly to actual molecules, the two dots can experience an effective attractive Coulomb interaction if electrons are localized to each dot but still capacitively coupled. This is essentially an ionic bond, and is characterized by weak inter-dot coupling. If the coupling is stronger, however, a covalent-like bond forms, in which the electron wavefunction spreads out over the dots and the wavefunctions of both dots are coupled. In either case, the energy of the bonded state must be lower than the sum of the two unbonded dots; the extra energy goes to the coupling strength, t, which will be the hopping term in the TQD Hamiltonian [244–246]. Producing a TQD requires the same process, except that the gate geometry is chosen to create three areas of spatial confinement.

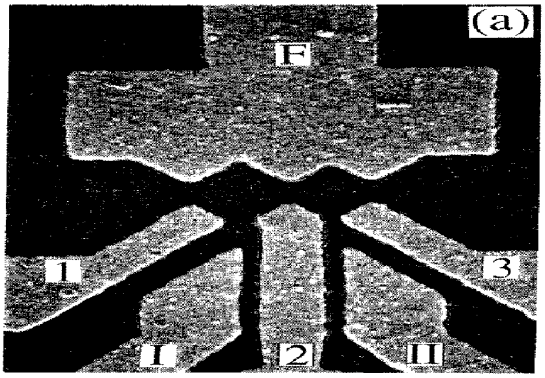

(a) STM micrograph of a double dot created via depletion of a 2DEG placed 100nm below the surface of a GaAs/AlGaAs heterostructure. The two dark squares framed by components F, 1, 2, and 3 are the two dots. Adapted with permission from Ref.[245], © 1995 American Physical Society.

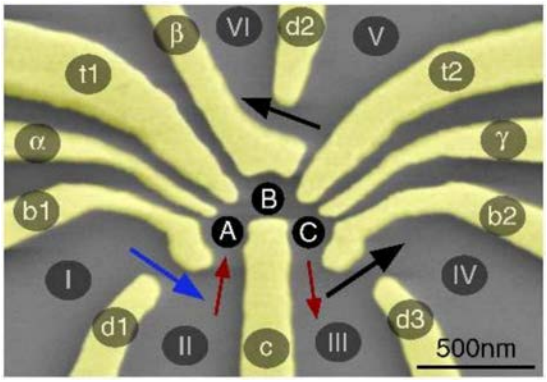

(b) STM micrograph of a triple quantum dot created via depletion of a 2DEG placed 120nm below the surface of a GaAs/AlGaAs heterostructure. The three dots are labelled A, B, and C, and form a series geometry as opposed to the ring configuration we consider. Reprinted with permission from Ref.[247], © 2007 American Physical Society.

Figure 7.2

Between coherently coupling DQDs and coherently coupling TQDs, several groups experimented with intermediate cases. Vidan *et al.* [248] and Stopa [249], for example, capacitively coupled two out of three QDs in an array so as to cause current rectification via a ratchet effect. In a further effort, they capacitively coupled all three QDs to again find charge rectification in the Coulomb blockade regime [250]. Soon after these experiments, Gaudreau *et al.* [251] created the first ever coherently coupled TQD by splitting the potential of one dot in a DQD array. Although they intended to create the TQD in a chain formation, which was eventually achieved by Schröer *et al.* [247], they accidentally created a ring formation instead, where two dots were coupled to the source and one to the drain; this is the configuration we have shown in Fig.(7.1a) and Fig.(7.1b). They were able to identify it as a TQD from the stability diagram [252] and were later able to create these ring TQDs on purpose, also observing Aharonov-Bohm interference effects and thus confirming that the transport was coherent [253, 254]. Rogge and Haug [255] also measured interference effects in a star-like TQD configuration; although, as two dots remained uncoupled, the interference was not due to Aharonov-Bohm oscillations, but rather to multiple pathways leading to different drains. Amaha *et al.* [256, 257] have produced lateral TQDs from a mesa configuration, which also allowed them to arrange the dots in parallel, rather than series, between the source and drain.

Beyond just experimental realization, however, TQDs offer great potential to fields like quantum computing. which requires a measurable quantity that can serve as the qubit. One proposal is to use the spin, $|\psi\rangle = a|\uparrow\rangle + b|\downarrow\rangle$, of an electron in a quantum dot [258]. While this qubit can be fully controlled via a time-dependent magnetic field, it is also vulnerable to decoherence due to magnetic noise from, for example, spins of surrounding nuclei. Qubits defined from the singlet, $\frac{1}{\sqrt{2}}(|\uparrow\downarrow\rangle - |\downarrow\uparrow\rangle)$, and triplet, $\frac{1}{\sqrt{2}}(|\uparrow\downarrow\rangle + |\downarrow\uparrow\rangle)$, states of two elec-

trons in a DQD, on the other hand, do not lose coherence due to magnetic noise [259]. To go one step further, encoding information in three electrons on a TQD, creating a 3-spin qubit, provides decoherence protection and also greater electrical control [260, 261]. Laird *et al.*, for example, were able to create, measure, and control a 3-spin qubit in a serial TQD system [262]. Gaudrea's group [263] were later able to provide more control over this system, maintaining coherence while controlling inter-dot spin-coupling strengths. Long-range spin transfer between the two outermost dots in a serial TQD has also been demonstrated [264]. Łuczack and Bułka, meanwhile, have presented theory detailing the coherent manipulation of a 3-spin qubit in a triangular TQD [265, 266].

These last theoretical results are symptomatic of TQD research; since coherent multi-dot synthesis is a relatively new development, the accompanying theory has in many cases far outstripped experiment. Due to the multiple geometries, large number of tunable parameters, and complex Fock space, TQDs admit a wide variety of novel phenomena, such as quantum phase transitions [267], charge frustration [268], and spin-entangled current [269]. One of the most interesting and well-explored such effects in the rich TQD literature is the appearance of Kondo physics, which also has a long history outside of molecular transport.

In 1964, Kondo famously demonstrated that magnetic impurities would produce anamolous behavior in the resistivity of metals at low temperatures [270]. Macroscopically, the scattering rate of conduction electrons decreases as temperature decreases. At low enough temperatures, however, when a conduction electron comes close enough to an impurity with opposite spin, they form a Kondo spin-singlet state; the scattering rate, and thus the resistivity, increases accordingly. Below the so-called Kondo temperature, then, impurity spins are essentially screened due to the formation of these Kondo states.

In molecular junctions, a QD can operate as the magnetic impurity, such as in the Anderson model, and for odd-occupancy Kondo scattering actually enhances the conductance [271, 272]. For the dot spin to interact with the conduction electrons and form a Kondo state, however, requires again low temperatures and also a strong molecule-electrode coupling. In TQDs, the Kondo regime was initially explored for serially coupled configurations [273, 274]. There has also been much interest in the Kondo regime for triangular TQDs [275, 276], where the inter-dot coupling symmetry becomes important [277–279] and Aharonov-Bohm interference affects the formation of the spin-singlet state [280].

Beyond affecting the Kondo physics, Aharonov-Bohm interference actually plays an important role in triangular TQDs in all transport regimes. Before discussing its role in more detail, we will briefly overview the effect. In 1959, Aharonov and Bohm proposed an experiment in which a coherent electron beam is split into two paths along a closed loop and then made to recombine, and thus interfere, at some later point [281]. Their proposal also contained a magnetic field $\mathbf{B}$ localized to some point interior to the loop and oriented perpendicular to the plane of the electron paths. The total magnetic flux is $\phi = \int_{\mathbf{S}} \mathbf{B} \cdot d\mathbf{S}$, which implies that

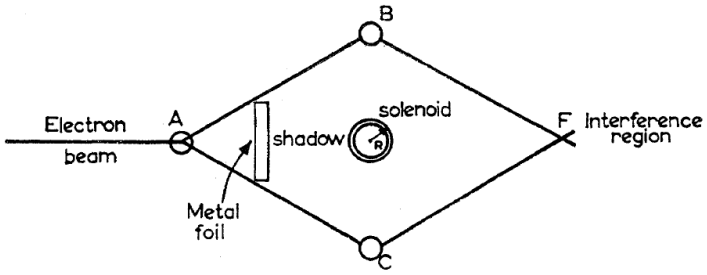

Figure 7.3: Original experimental schematic to measure the Aharonov-Bohm interference pattern due to a magnetic vector field acting on charged particles. A coherent electron beam is split at point A along paths B and C and recombine at point F to produce an interference pattern. Inside is a solenoid generating a magnetic field perpendicular to the loop, which is shielded from the incoming beam by a metal foil acting as a shadow; it acts only on the electrons in each path. Reprinted with permission from Ref.[281], © 1959 American Physical Society.

the magnetic vector potential, $\mathbf{A}$, defined by $\mathbf{B} = \boldsymbol{\nabla} \times \mathbf{A}$, is non-zero at points other than the magnetic field location, since by Stokes' theorem $\phi = \int_{\mathbf{S}} \mathbf{A} \cdot d\boldsymbol{\ell}$ [282].

The accompanying electron Hamiltonian is $H = \frac{1}{2m}(\mathbf{p} - e\mathbf{A})^2$ [283], and it can be solved by noting that the total wavefunction, $\psi = \psi_u + \psi_l$, contains a component from the upper, ψ_u, and lower, ψ_l, arms. Reintroducing e and $\hbar$ for a moment, the solution for each follows $\psi_{u/l} = \psi^0_{u/l} e^{-iV_{u/l}/\hbar}$, where $\psi^0_{u/l}$ is the solution when $\mathbf{A} = 0$ and $V_{u/l} = e\int_{u/l} \mathbf{A} \cdot d\boldsymbol{\ell}$. They naturally expected that the phase difference at recombination will be

$$\frac{V_u - V_l}{\hbar} = \frac{e}{\hbar}\int_{\mathbf{S}} \mathbf{A} \cdot d\boldsymbol{\ell} = \frac{e}{h} 2\pi\phi = 2\pi\frac{\phi}{\phi_0}, \tag{7.1}$$

where $\phi_0 = \frac{e}{h}$ is the quantum of magnetic flux. Aharonov and Bohm concluded, therefore, that the interference pattern would be altered by a magnetic flux ϕ through the loop. Experimental verification appeared rapid [284]; however, early results were doubted due to potential "leaks" in the localized magnetic field, and it was not until Tonomura *et al.* in the 1980s that the Aharonov-Bohm effect was fully accepted as a quantum mechanical phenomenon [285].

Considering the apparatus in Fig.(7.3), it is evident that a triangular TQD with coherent coupling between all dots and a perpendicular magnetic field serves as an Aharonov-Bohm interferometer on the nanoscale. Indeed, since its experimental verification for coherent electron beams, the Aharonov-Bohm effect has also appeared in nanoscale physics [286, 287], including quantum dot experiments [288, 289].

For triangular TQDs, the Aharonov-Bohm effect is often analyzed in conjunction with coherent population trapping. This occurs when the coupling parameters of the TQD are tuned so as to form a "dark" state [290, 291]: a coherent superposition of dot states that block the current. In the configuration depicted in Fig.(7.1a), and when the occupancy of the three dots is limited to one electron, Emary [242] demonstrated that there exists certain parameters for which the

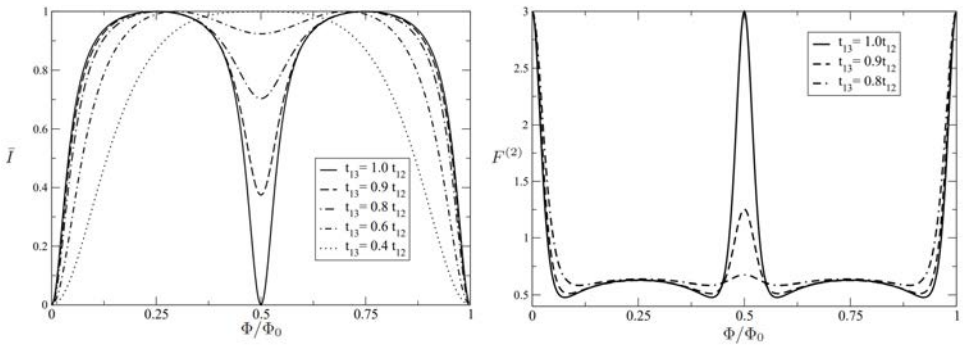

Figure 7.4: Example of a dark state formed in the single occupancy regime and tuned by the Aharonov-Bohm effect. The dark state appears in the complete suppression of the current at periods of $n\pi$ (left) and the corresponding super-Poissonian noise within the coherent blockade (right). The parameters t_{ij} demonstrate that the dark state lifts for increasing asymmetry of the inter-dot tunnel couplings. Adapted with permission from Ref.[242], © 2007 American Physical Society.

coherent state $|\psi_{\text{dark}}\rangle = a|A\rangle + c|C\rangle$ is an eigenstate of the Hamiltonian, decoupling the B dot, and thus the drain. He also showed that a magnetic flux lifts the coherent blockade and produces Aharonov-Bohm oscillations in the stationary current, and that, at the peak of destructive interference, the Fano factor is super-Poissonian, possibly due to avalanche tunneling. These features are displayed in Fig.(7.4), which contains a reprint from Ref.[242] of the dark state and corresponding noise.

The dark state is not just a feature of the single electron regime; Poltl *et al.* [292, 293] and Busl *et al.* [294] have shown that for double occupancy of the TQD, with each dot now modeled as an Anderson impurity, spin effects could produce coherent electron trapping if the inter-dot coupling $U_{\nu\nu'}$ equaled the intra-dot coupling $U_{\nu\nu}$. Dark states are evidently an interesting quantum phenomenon, but they can also produce current rectification and negative differential resistance [295], two promising technological applications. If not penetrated by a magnetic flux, a strong molecule-electrode coupling can lift the coherent blockade, as Weymann *et al.* [296] showed by including cotunneling processes in a triangular TQD, although Noiri *et al.* [297] has found that cotunneling can introduce an additional spin blockade in serially coupled TQDs. Coherent population trapping also occurs for higher occupancies [298]; for example, in the triple occupancy regime a coherent spin blockade forms for certain parameters under an applied electric field [299].

These investigations into dark states provide the inspiration for this chapter, as there are clearly interesting current fluctuations in a triangular TQD that bear analysis via fluctuating-time statistics. In particular, we investigate those systems considered by Emary [242] and Poltl *et al.* [292, 293] for correlations arising from quantum interference in the dark state and moderated by the Aharonov-Bohm effect. Although previous work on WTDs for TQDs did not calculate correlations [165], within only the last year Engelhardt and Cao [243] have shown that the WTD for a similar TQD configuration displays oscillatory behavior, which is corre-

lated with relevant occupations of the three dots. We find similar results for the geometries in Fig.(7.1a) and Fig.(7.1b), albeit for more complicated transport regimes.

7.3 Triple quantum dot model

We perform all theory on a TQD arranged in either of the triangular geometries in Fig.(7.1a) and Fig.(7.1b). The three dots, to which we give the index $\nu \in \{A, B, C\}$, each contain a single available orbital that is at most accessible to two electrons with opposite spin. The system Hamiltonian, for either geometry, is

$$H_Q = \sum_{\sigma}\sum_{\nu} \varepsilon_\nu a^\dagger_{\nu,\sigma} a_{\nu,\sigma} - \sum_{\nu\neq\nu'} t_{\nu\nu',\sigma} a^\dagger_{\nu,\sigma} a_{\nu',\sigma} + \sum_{\nu} U_{\nu\nu} n_{\nu,\uparrow} n_{\nu,\downarrow} + \sum_{\nu<\nu'}\sum_{\sigma\sigma'} U_{\nu\nu'} n_{\nu,\sigma} n_{\nu',\sigma'}. \tag{7.2}$$

where ε_ν is the energy of each dot, $U_{\nu\nu}$ and $U_{\nu\nu'}$ are the intra- and inter-dot Coulomb repulsions, respectively, and $t_{\nu\nu'} = t^*_{\nu'\nu}$ is the hopping parameter for tunneling from dot ν' to dot ν. As usual, the $a^\dagger_{\nu,\sigma}$ and $a_{\nu,\sigma}$ operators create and annihilate an electron on dot ν with energy ε_ν and spin σ, respectively, while $n_{\nu,\sigma} = a^\dagger_{\nu,\sigma} a_{\nu,\sigma}$ is the corresponding particle number operator. In all calculations, we choose a gauge where the phase difference between the two paths is factored entirely onto the coupling between dot A and dot C: $t_{AC} = |t_{AC}|e^{i\phi}$, with $t_{AB} = |t_{AB}|$ and $t_{BC} = |t_{BC}|$.

For the configuration in Fig.(7.1a), where both the A and C dots are coupled to the source and the B dot alone is coupled to the drain, the interaction Hamiltonian is

$$H_T = \sum_{\mathbf{k}_S}\sum_{\nu=\{A,C\}} t_{\mathbf{k}_S,\nu,\sigma}\left(a^\dagger_{\mathbf{k}_S} a_{\nu,\sigma} + a^\dagger_{\nu,\sigma} a_{\mathbf{k}_S}\right) + \sum_{\mathbf{k}_D} t_{\mathbf{k}_D,B,\sigma}\left(a^\dagger_{\mathbf{k}_D} a_{B,\sigma} + a^\dagger_{B,\sigma} a_{\mathbf{k}_D}\right). \tag{7.3}$$

Conversely, the interaction Hamiltonian for the configuration in Fig.(7.1b), where the B dot is coupled to the source and the A and C dots are coupled to the drain, is

$$H_T = \sum_{\mathbf{k}_D}\sum_{\nu=\{A,C\}} t_{\mathbf{k}_D,\nu,\sigma}\left(a^\dagger_{\mathbf{k}_D} a_{\nu,\sigma} + a^\dagger_{\nu,\sigma} a_{\mathbf{k}_D}\right) + \sum_{\mathbf{k}_S} t_{\mathbf{k}_S,B,\sigma}\left(a^\dagger_{\mathbf{k}_S} a_{B,\sigma} + a^\dagger_{B,\sigma} a_{\mathbf{k}_S}\right). \tag{7.4}$$

We are interested in the coherent transport through these two configurations, and so we will use the full master equation in Eq.(2.89). At this point in the theory, however, we cannot do so; it requires the system Hamiltonian to be diagonal and Eq.(7.2), since it is written in the basis of dot states, is not. As opposed to the Holstein model, for which we could apply the analytic Lang-Firsov transformation, we will instead numerically diagonalize H_Q with its molecular

eigenstates:

$$\begin{aligned}\tilde{H}_Q &= \sum_{kk'} |m_k\rangle\langle m_k|H_Q|m_{k'}\rangle\langle m_{k'}| \\ &= \sum_{k=1}^{N} E_k|m_k\rangle\langle m_k|, \end{aligned} \tag{7.5}$$

where E_k is the eigenenergy of eigenstate $|m_k\rangle$ and N is the total number of pure states. We are safe to make this transformation because the eigenstates, by definition, span the system space: $I = \sum_{k=1}^{N} |m_k\rangle\langle m_k|$. We can also write the dot states, $|d_i\rangle$, in the new basis,

$$|d_i\rangle = \sum_{k=1}^{N} |m_k\rangle\langle m_k|d_i\rangle, \tag{7.6}$$

and, since the dot states also span the system space, compute the inverse transformation:

$$|m_k\rangle = \sum_{i=1}^{N} |d_i\rangle\langle d_i|m_k\rangle. \tag{7.7}$$

With no parameter restrictions the full Fock space is quite large and numerical diagonalization is a formidable task. There can be a maximum of six electrons occupying the configuration, and $N = \sum_{k=0}^{6} \frac{6!}{k!(6-k)!} = 64$; the resulting density matrix has 4096 elements. To reduce the complexity and computational requirements, many theoretical investigations instead focus on limiting regimes where the dimensionality is much smaller; several of which we will consider here.

7.3.1 Spin-independent triple and single occupancy

In the first scenario, we assume that the intra-dot Coulomb repulsion is large: $U_{\nu\nu} \to \infty$. Under this limit, each dot in the configuration can be occupied by only one excess electron, which we label the *triple occupancy* regime. Spanning the system are ten dot states: the configuration can be empty, $|0\rangle$; a single electron may occupying any of the three dots, $|A\rangle$, $|B\rangle$, or $|C\rangle$; two electrons may be occupying any two of the dots, $|AB\rangle$, $|AC\rangle$, or $|BC\rangle$; or all three dots are occupied, $|ABC\rangle = |3\rangle$.

Although $|0\rangle$ and $|3\rangle$ are invariant under the diagonalization, we find that the transformed basis has three new single occupancy,

$$|1i\rangle = a_{1i,A}|A\rangle + a_{1i,B}|B\rangle + a_{1i,C}|C\rangle \tag{7.8}$$

and double occupancy,

$$|2i\rangle = a_{2i,AB}|AB\rangle + a_{2i,AC}|AC\rangle + a_{2i,BC}|BC\rangle, \tag{7.9}$$

states, where $i = 1, 2, 3$. From Eq.(7.7), we can see that the coefficients are $a_{1i,\nu} = \langle \nu|1i\rangle$ and $a_{2i,\nu\nu'} = \langle \nu\nu'|2i\rangle$. The density matrix, with all 64 elements, is shown in Appendix E.1. In addition to this large reduction in dimensionality, all eigenstates with different electron occupancy are orthogonal and thus decouple in the master equation; the remaining 20 elements unfold into the probability vector

$$\begin{aligned}\mathbf{P}(\chi,t) = [&P_0(\chi,t), P_{11}(\chi,t), P_{12}(\chi,t), P_{13}(\chi,t), P_{21}(\chi,t), P_{22}(\chi,t), P_{23}(\chi,t), P_3(\chi,t),\\ &\rho_{11,12}(\chi,t), \rho_{11,13}(\chi,t), \rho_{12,13}(\chi,t), \rho_{12,11}(\chi,t), \rho_{13,11}(\chi,t), \rho_{13,12}(\chi,t),\\ &\rho_{21,22}(\chi,t), \rho_{21,23}(\chi,t), \rho_{22,23}(\chi,t), \rho_{22,21}(\chi,t), \rho_{23,21}(\chi,t), \rho_{23,22}(\chi,t)]^T.\end{aligned} \tag{7.10}$$

All that is required now is to compute the 1st-order differential equation for each density matrix element from the full master equation. Using the Fourier transform of Eq.(2.89) for the configuration in Fig.(7.1a), we get

$$\begin{aligned}\dot{\rho}_{mn}(\chi,t) = -i\omega_{mn}\rho_{mn}(\chi,t) - \sum_{k\ell}\Big[\sum_{\nu=\{A,C\}}\Big(&\Sigma_S^<(\omega_{k\ell})^*\langle m|a_\nu|k\rangle\langle k|a_\nu^\dagger|\ell\rangle\rho_{\ell n} +\\ &\Sigma_S^>(\omega_{\ell k})\langle m|a_\nu^\dagger|k\rangle\langle k|a_\nu|\ell\rangle\rho_{\ell n} + \Sigma_S^<(\omega_{n\ell})\langle m|a_\nu^\dagger|k\rangle\rho_{k\ell}\langle\ell|a_\nu|n\rangle\\ &+\Sigma_S^>(\omega_{\ell n})^*\langle m|a_\nu|k\rangle\rho_{k\ell}\langle\ell|a_\nu^\dagger|n\rangle - \Sigma_S^<(\omega_{k\ell})\rho_{m\ell}\langle\ell|a_\nu|k\rangle\langle k|a_\nu^\dagger|n\rangle\\ &-\Sigma_S^>(\omega_{\ell k})^*\rho_{m\ell}\langle\ell|a_\nu^\dagger|k\rangle\langle k|a_\nu|n\rangle - \Sigma_S^<(\omega_{k\ell})^*\langle m|a_\nu^\dagger|\ell\rangle\rho_{\ell k}\langle k|a_\nu|n\rangle\\ &-\Sigma_S^>(\omega_{\ell m})\langle m|a_\nu|\ell\rangle\rho_{\ell k}\langle k|a_\nu^\dagger|n\rangle\Big) + \Sigma_D^<(\omega_{k\ell})^*\langle m|a_B|k\rangle\langle k|a_B^\dagger|\ell\rangle\rho_{\ell n}\\ &+\Sigma_D^>(\omega_{\ell k})e^{i\chi}\langle m|a_B^\dagger|k\rangle\langle k|a_B|\ell\rangle\rho_{\ell n} + \Sigma_D^<(\omega_{n\ell})e^{-i\chi}\langle m|a_B^\dagger|k\rangle\rho_{k\ell}\langle\ell|a_B|n\rangle\\ &+\Sigma_D^>(\omega_{\ell n})^*\langle m|a_B|k\rangle\rho_{k\ell}\langle\ell|a_B^\dagger|n\rangle - \Sigma_D^<(\omega_{k\ell})\rho_{m\ell}\langle\ell|a_B|k\rangle\langle k|a_B^\dagger|n\rangle\\ &-\Sigma_D^>(\omega_{\ell k})^*\rho_{m\ell}\langle\ell|a_B^\dagger|k\rangle\langle k|a_B|n\rangle - \Sigma_D^<(\omega_{k\ell})^*e^{-i\chi}\langle m|a_B^\dagger|\ell\rangle\rho_{\ell k}\langle k|a_B|n\rangle\\ &-\Sigma_D^>(\omega_{\ell m})e^{i\chi}\langle m|a_B|\ell\rangle\rho_{\ell k}\langle k|a_B^\dagger|n\rangle\Big)\Big].\end{aligned} \tag{7.11}$$

The corresponding master equation for the configuration in Fig.(7.1b) is similar, except that the drain self-energies now lie under the summation of A, C, and the source self-energies do not. For triple occupancy, there are four types of density matrix elements, $\dot{\rho}_{0,0}$, $\dot{\rho}_{1i,1j}$, $\dot{\rho}_{2i,2j}$, and $\dot{\rho}_{3,3}$, which we display in Appendix E.1.

If we also take the inter-dot repulsion as large, $U_{\nu\nu'} \to \infty$, then only one dot may be occupied at a time: the *single occupancy* regime. In this case, the probability vector is much smaller:

$$\begin{aligned}\mathbf{P}(\chi,t) = [&P_0(\chi,t), P_{11}(\chi,t), P_{12}(\chi,t), P_{13}(\chi,t), \rho_{11,12}(\chi,t),\\ &\rho_{11,13}(\chi,t), \rho_{12,13}(\chi,t), \rho_{12,11}(\chi,t), \rho_{13,11}(\chi,t), \rho_{13,12}(\chi,t)]^T\end{aligned} \tag{7.12}$$

7.3.2 Spin-dependent double occupancy

In the *double occupancy* regime, the intra-dot Coulomb repulsion is finite, but the inter-dot repulsion is large, $U_{\nu\nu'} \to \infty$; each dot can be occupied by two electrons of opposite spins, but only two electrons are allowed in the entire TQD configuration. There are now 6 single electron states and 15 double electron states, for a total of 22 pure states spanning the system and 262 coupled density matrix elements. To simplify, we also assume a large bias voltage, $V_{SD} \to \infty$, so that tunneling can only be from the source to the TQD or from the TQD to the drain. In this limit, we can write the master equation in Lindblad form, which for the configuration in Fig.(7.1a) is

$$\frac{d\rho}{dt} = -i\left[H_Q, \rho\right] + \sum_{\sigma} \sum_{\nu=\{A,C\}} \gamma^S \left(a^\dagger_{\nu,\sigma} \rho a_{\nu,\sigma} - \frac{1}{2} a_{\nu,\sigma} a^\dagger_{\nu,\sigma} \rho - \frac{1}{2} \rho a_{\nu,\sigma} a^\dagger_{\nu,\sigma} \right) + \sum_{\sigma} \gamma^D \left(a_{B,\sigma} \rho a^\dagger_{B,\sigma} e^{i\chi} - \frac{1}{2} a^\dagger_{B,\sigma} a_{B,\sigma} \rho - \frac{1}{2} \rho a^\dagger_{B,\sigma} a_{B,\sigma} \right), \tag{7.13}$$

and for the configuration in Fig.(7.1b) is

$$\frac{d\rho}{dt} = -i\left[H_Q, \rho\right] + \sum_{\sigma} \sum_{\nu=\{A,C\}} \gamma^D \left(a_{\nu,\sigma} \rho a^\dagger_{\nu,\sigma} - \frac{1}{2} a^\dagger_{\nu,\sigma} a_{\nu,\sigma} \rho - \frac{1}{2} \rho a^\dagger_{\nu,\sigma} a_{\nu,\sigma} \right) + \sum_{\sigma} \gamma^S \left(a^\dagger_{B,\sigma} \rho a_{B,\sigma} e^{i\chi} - \frac{1}{2} a_{B,\sigma} a^\dagger_{B,\sigma} \rho - \frac{1}{2} \rho a_{B,\sigma} a^\dagger_{B,\sigma} \right). \tag{7.14}$$

We are justified in making this final assumption because all results are calculated from the WTD, which requires unidirectional tunneling and, therefore, a large bias voltage.

7.4 Results

7.4.1 Spin-independent single occupancy

The single occupancy case, in which the TQD can only be occupied by one excess electron, has received great theoretical attention as there exist analytic solutions for certain parameter regimes. For example, Emary [242] showed that when $\varepsilon_B = 0$, $\varepsilon_A = \Delta$, and $\varepsilon_C = -\Delta$, where

$$\Delta = \frac{|t_{AC}|}{2|t_{AB}||t_{CB}|} \left(|t_{AB}|^2 - |t_{CB}|^2 \right), \tag{7.15}$$

one of the eigenvectors is

$$|\Psi\rangle = \frac{1}{\sqrt{t_{AC}^2 + t_{BC}^2}} \left(t_{BC}|A\rangle - t_{AB}|C\rangle \right). \tag{7.16}$$

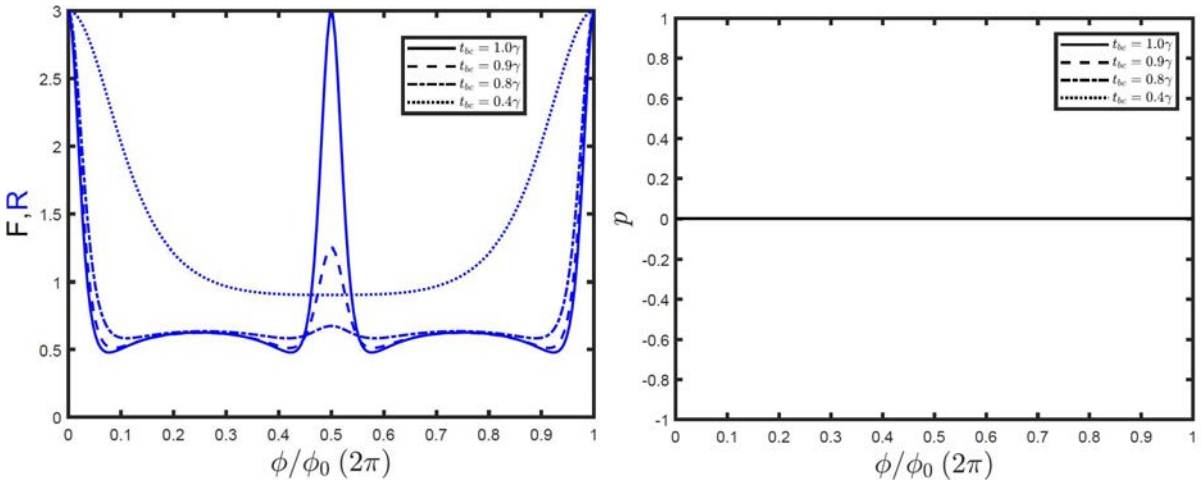

(a) (b)

Figure 7.5: (a) The Fano factor plotted alongside the randomness parameter for the same parameters as Fig.3 and Fig.4 in Ref.[242], shown in this chapter in Fig.(7.4). (b) Corresponding Pearson correlation coefficient between two waiting times, τ and τ'. Parameters are: $\varepsilon_B = 0$, $\varepsilon_A = \Delta$, $\varepsilon_C = -\Delta$, $t_{AC} = \gamma e^{i\phi}$, $t_{AB} = \gamma$, $T = 0.075$meV, $\gamma = 0.01$meV, and, to keep all levels within the bias window, $\mu_S = -\mu_D = 100\gamma$.

If the system starts in this state, then, dot B is completely decoupled and current is blocked; hence the name dark state.

In Fig.(7.5a) and Fig.(7.5b), we have plotted the second cumulants and Pearson correlation coefficient as a function of ϕ/ϕ_0 for the same system as in Fig.(7.4). Here, Aharonov-Bohm interference produces current oscillations with periods of π and a diminishing of the destructive interference for increasing asymmetry of the inter-dot coupling [242]. Additionally, Emary found that the Fano factor becomes super-Poissonian when the dark state appears, as it produces bunching phenomena. From Fig.(7.5a), it is evident that the transport is entirely renewal for all parameters; F is exactly reproduced by R and in Fig.(7.5b) the respective Pearson correlation coefficient is accordingly zero.

Upon thought, it is clear why this should be the case; why, even though quantum interference is obviously present, it does not reflect in a statistic that measures correlations. In Fig.(7.5a)-Fig.(7.5b) we are measuring the waiting time between successive tunnelings to the drain. Because we allow only one electron in the TQD at a time, this means that after a jump $\mathbf{J}_D^F$, another electron has to tunnel in from the source before the next $\mathbf{J}_D^F$. While each electron can interfere with itself, it cannot interfere with other electrons; hence, there are no correlations between successive waiting times. Apart from the correlation behavior, however, the WTD still provides useful information about the dynamics of this transport regime.

Because we allow only one electron in the configuration, the TQD is in this case a single-reset system; after a jump to the drain the system must be empty and $w(0) = 0$. For $t > 0$, the WTD calculated from the rate equation and from the full master equation display qualitatively and quantitatively different behavior; the most obvious being periodic oscillations present in the

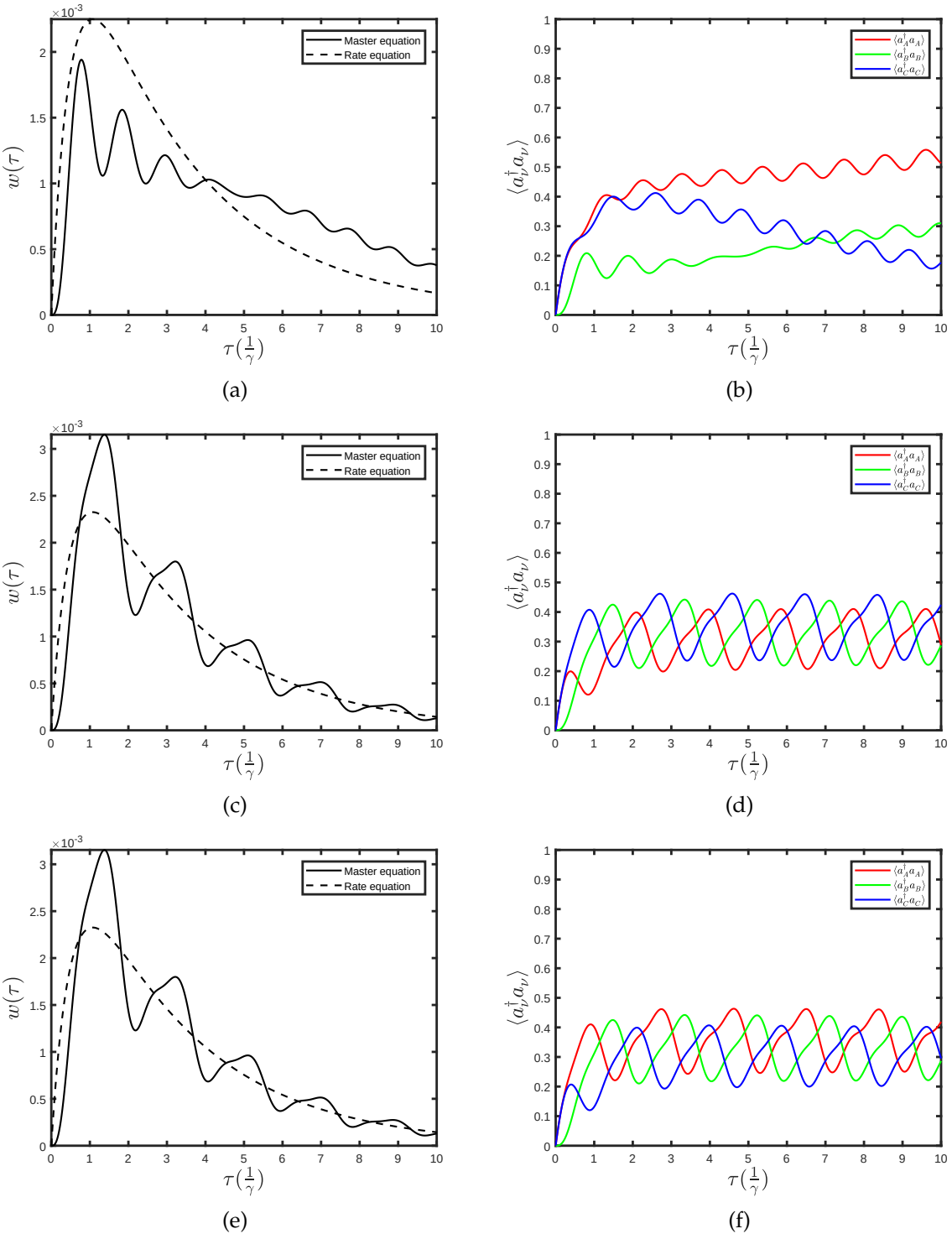

Figure 7.6: Left column: WTD between two jumps to the drain, $\mathbf{J}_D^F$, for the configuration in Fig.(7.1a) and different ϕ. Solid black line is the WTD calculated from the full master equation including coherences, while the dashed black line is the WTD calculated from the rate equation only. Right column: corresponding occupation probabilities for each dot: red is $\langle a_A^\dagger a_A \rangle$, green is $\langle a_B^\dagger a_B \rangle$, and blue is $\langle a_C^\dagger a_C \rangle$. (a) and (b) set $\phi = \pi$, while (c) and (d), and (e) and (f), set $\phi = \pm\frac{\pi}{2}$, respectively. Dot couplings are $|t_{AB}| = |t_{AC}| = 2\gamma$ and $t_{BC} = 0.9\gamma$; else, all other parameters are the same as those in Fig.(7.5a) - Fig.(7.5b). The master equation average waiting time in (a) is $\langle \tau \rangle_{ME} = 5.4\frac{1}{\gamma}$, while the rate equation average waiting time is $\langle \tau \rangle_{RE} = 3.8\frac{1}{\gamma}$. For (b) and (c) they are $\langle \tau \rangle_{ME} = 3.6\frac{1}{\gamma}$ and $\langle \tau \rangle_{RE} = 3.5\frac{1}{\gamma}$. Note that we have not displayed P_0, so the occupancy sum is not unity.

latter. As Engelhardt and Cao found, these WTD oscillations all correlate, and can thus be described by, the time-dependent occupation probabilities of each dot after the initial jump to the drain [243]. When the dot B occupation is at a peak, which is required to observe a quantum jump in this configuration, so is the corresponding WTD. Since the rate equation WTD and occupation probabilities do not display these oscillations, it is likely they originate from the phase factors introduced when coherences are included.

Of note in Fig.(7.6a) are the occupation probabilities of dots A and C; even though they evolve similarly, since a jump into the drain fills either dot with equal probability, they quickly become out of phase. It appears that, although the dark state is a linear combination of the two dot states, the wavefunction is not spread evenly between them and, as time goes on, becomes more localized on dot A. In Fig.(7.6d) and Fig.(7.6f), $\phi = \pi/2$ and Aharonov-Bohm interference lifts the dark state; the electron wavefunction is more evenly spread between the three dots, and dot B is out of phase with both dot A and C. This results in each peak of the WTD being itself double-peaked; the smaller one occurring when $\langle a_B^\dagger a_B \rangle > \langle a_A^\dagger a_A \rangle$ and the greater one when $\langle a_B^\dagger a_B \rangle$ is larger than both other occupancies. We can also see in Fig.(7.6d) and Fig.(7.6f) the effect of the magnetic flux direction. For $\phi = +\pi/2$, in Fig.(7.6d), the phase shift is positive and the electron moves anti-clockwise from dot C to B to A. Fig.(7.6f), in contrast, sets $\phi = -\pi/2$, and so the electron moves clockwise from A to B to C.

Fig.(7.6a) and Fig.(7.6b), where $\phi = pi$, correspond to value of the dashed line at $\phi/\phi_0 = 0.5$ in Fig.(7.4). At this point, destructive interference suppresses the current to about 40% of its maximum value. Accordingly, the average waiting time of Fig.(7.6a) is $\langle \tau \rangle_{ME} = 5.4\frac{1}{\gamma}$ while the average waiting time for $\phi = \pi/2$ is $\langle \tau \rangle_{ME} = 3.6\frac{1}{\gamma}$. Since the dark state is a result of coherent superposition between dots A and C, the WTD calculated from the rate equation has a much smaller tail and average waiting time: $\langle \tau \rangle_{RE} = 3.8\frac{1}{\gamma}$. Even at $\phi = \pi/2$, when the current is at a maximum, the average waiting time calculated from the master equation is longer than that calculated from the rate equation, indicating that destructive interference is the dominant coherent effect.

So far we have considered waiting times between two tunnelings to the drain, a natural choice when relating fluctuating-time statistics to fixed-time statistics. As an interesting case, Fig.(7.7a) and Fig.(7.7b) display the WTD and corresponding occupation probabilities between a tunneling into the system from the source and a tunneling from the system to the drain:

$$w_{SD}(\tau) = \frac{\left(\mathbf{I}, \mathbf{J}_D^F e^{(\mathbf{L}-\mathbf{J}_D^F-\mathbf{J}_S^F)\tau}\mathbf{J}_S^F\bar{\mathbf{P}}\right)}{\left(\mathbf{I}, \mathbf{J}_S^F\bar{\mathbf{P}}\right)}. \tag{7.17}$$

Since we use the same parameters as in Fig.(7.6a), the dark state is again observable by the long tail. Since the first jump is into the system, both dot A and C start with a 50% probability of being occupied. As the system evolves, it appears that eventually dot B becomes more likely to be occupied than dot C, regardless of the dark state. This is, perhaps, why the WTD

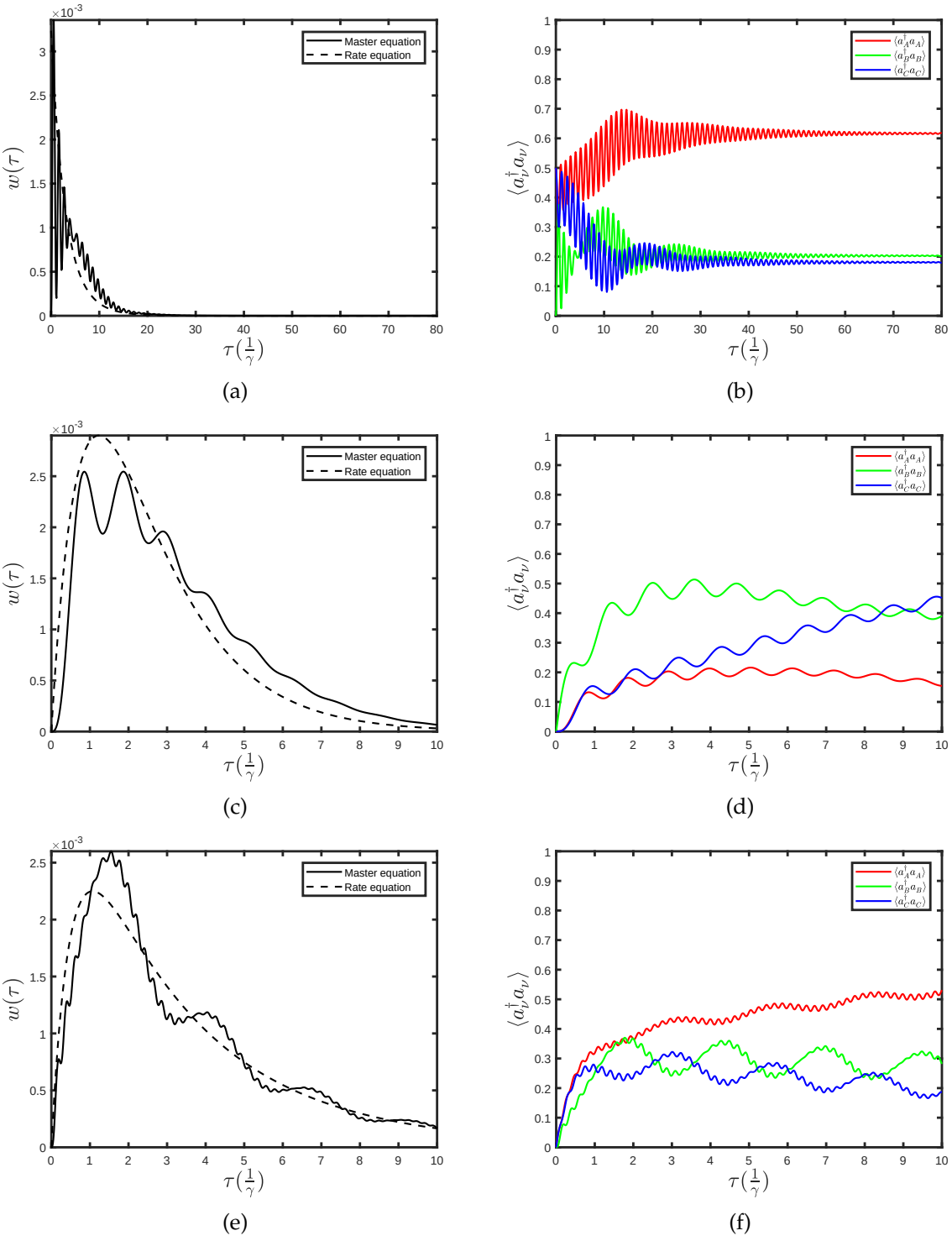

Figure 7.7: WTD, left column, and occupation probabilities, right column, for some interesting cases. In (a) and (b) we have used the same parameters as in Fig.(7.6a) and Fig.(7.6b), except now the waiting time is between a jump into the system from the source, $\mathbf{J}_S^F$, and a jump from the system to the drain, $\mathbf{J}_D^F$. In (c) and (d) we have used the same parameters again, but now the waiting time is between two jumps to the drain for the mirror configuration, shown in Fig.(7.1b). In (e) and (f) we return to the same configuration as in (a) and (e), calculating the waiting time between successive jumps to the drain, but now $|t_{AB}| = |t_{AC}| = 10\gamma$ and $|t_{BC}| = 9\gamma$.

decays with two different rates; the initial probability density decays quickly but at $\tau = 4\frac{1}{\gamma}$ transitions to a slower rate. We have plotted this WTD and set of occupation probabilities for much longer τ, from which the dephasing of coherent oscillations due to electrode interactions is visible.

In Fig.(7.7c) and Fig.(7.7d), we have shown the WTD and occupation probabilities for the mirror configuration, equivalent to reversing the current. Destructive interference still suppresses the current to some degree, but evidently the dark state is not present; accordingly, the average waiting times in this configuration are much smaller, $\langle\tau\rangle_{ME} = 3.2\frac{1}{\gamma}$ and $\langle\tau\rangle_{RE} = 2.6\frac{1}{\gamma}$. Since in this configuration a jump to the drain can occur from dot A or C, the first two WTD peaks have equal magnitude, each corresponding to a dip in the dot B occupancy.

The final single occupancy case we consider is that of large inter-dot coupling: $|t| \sim 10\gamma$ in Fig.(7.7e) and Fig.(7.7f). For such coupling, the electron is strongly hybridized across the three dots, and also undergoes many inter-dot transitions between tunnelings to the drain. This results in distinct global WTD oscillations, occurring with period $\sim 2.5\frac{1}{\gamma}$, supplemented by small local oscillations with period $\sim 0.2\frac{1}{\gamma}$. We theorize that, as the hybridized wavepacket moves slowly around the configuration, becoming more localized on each dot in turn, its shape rapidly changes to produce the smaller oscillations, or vice versa.

7.4.2 Spin-independent triple occupancy

In triple occupancy, the dot may be occupied by three excess electrons but each dot may be occupied by only one electron at a time. Correspondingly, the Fock space is now more complicated, as are the time-dependent occupation probabilities associated with each WTD. Despite the addition of 2 and 3 electron states, however, we can still correlate the WTD with the state corresponding to a single electron in the TQD occupying dot B, displayed in Fig.(7.8a)-Fig.(7.8d).

Since each dot can still be occupied by only one electron, and the initial jump empties dot B, *some* time must pass before another jump to the drain can occur; the system is still single-reset. Clearly, then, the WTD in Fig.(7.8a), which is calculated from the rate equation, displays an unphysical result as $w_{RE}(0) \neq 0$. The WTD from the master equation, on the other hand, satisfies $w_{ME}(0) = 0$. Turning to Fig.(7.8c), we see that the $P_B(0) = 0$: if the system was in state $|AB\rangle$ or $|BC\rangle$, then a tunneling to the drain will leave it in $|A\rangle$ or $|C\rangle$, respectively; if the system was in state $|3\rangle$, then a tunneling to the drain will leave it in $|AC\rangle$; and if the system was in state $|B\rangle$, then a tunneling to the drain will leave it empty, $|0\rangle$. By this logic, P_{AB} and P_{BC} should be zero too after the initial jump, but they are clearly not in Fig.(7.8c). All quantum jumps in this system detail transitions between the TQD and the electrodes, so this could be the result of an internal coherent transition that fills dot B at the same time a jump occurs.

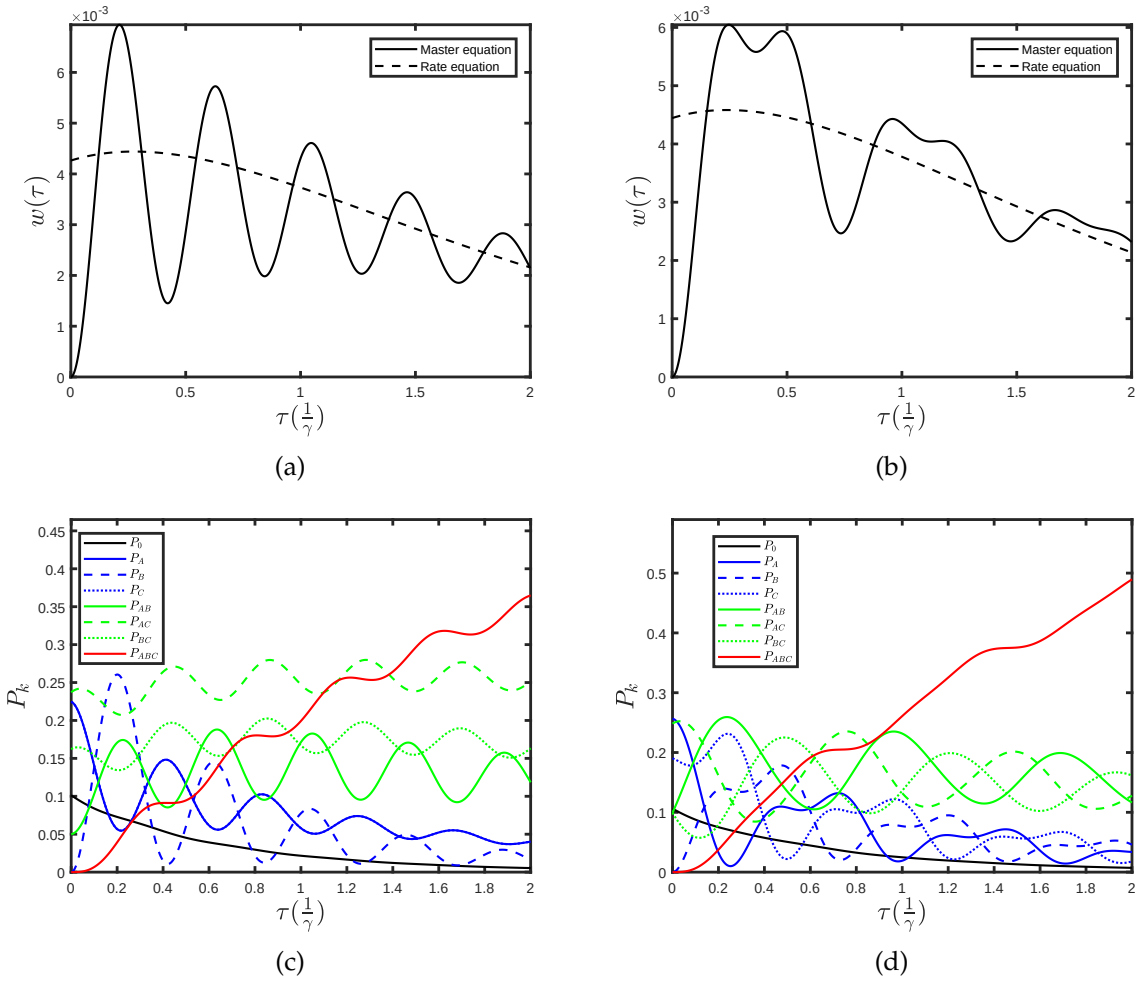

Figure 7.8: WTD (a)-(b) and occupation probabilities (c)-(d) for the triple occupancy regime. Both plots use the energies $\varepsilon_A = \Delta$, $\varepsilon_C = -\Delta$, and $\varepsilon_B = 0$, the inter-dot repulsion $U_{\nu\nu'} = U = \gamma$, and the dot couplings $|t_{AB}| = |t_{AC}| = |t_{BC}| = 5\gamma$. In (a) and (c) we set $\phi = 0$ and in (b) and (d) we set $\phi = \pi/2$.

If the initial quantum jump leaves the system with a single electron, then it will be on either dot A or C, as shown by the solid blue line in Fig.(7.8c). The system may evolve for some time without a jump from the source, in which case the charge number will remain 1. Since $P_A = P_C$, it appears that, for these parameters, there are two available single-electron states: $\frac{1}{\sqrt{2}}(|A\rangle + |C\rangle)$ and $|B\rangle$. As the excess electron moves around the TQD, peaks in the WTD correlate exactly to peaks in P_B, thus indicating that most second jumps occur when dot B empties to make the TQD empty. From $\bar{\mathbf{P}}$, the probability of all charge states in the steady state are

$$\begin{bmatrix} P_0 \\ P_1 \\ P_2 \\ P_3 \end{bmatrix} = \begin{bmatrix} 0.03 \\ 0.17 \\ 0.58 \\ 0.25 \end{bmatrix}; \tag{7.18}$$

so it is likely that the first quantum jump operates on a TQD occupied by 2 excess electrons. After this jump, the strong inter-dot couplings, which are $\sim 5\gamma$, are likely to bring a electron to dot B before another electron may enter the configuration from the source.

In calculating these results, we have used parameters that would result in a dark state in the single-electron regime. Therefore, despite the fact that allowing three electrons in the system lifts the dark state, there is still destructive interference. In fact, Fig.(7.9a) shows that, for $|t| = 5\gamma$, the current at $\phi = \pi$ is only 80% of the maximum at $\phi = \pi/2$. Indeed, in Fig.(7.8b), where we have set $\phi = \pi/2$, there is different behavior as each WTD peak is split in two. Examining Fig.(7.8d), the single-occupancy probabilities all display multi-peak oscillations, where each peak is roughly in phase with another peak from the occupation of another dot. This indicates that for a phase of $\pi/2$ the single conduction electron spreads over two dots and is best described by a coherent superposition of the two. The WTD is then double-peaked because the electron may form a superposition of B and either A or C. Contrary to intuition, for each period the larger WTD peak does not correspond to the larger peak in P_B, but rather to the peak for which the probability of the superposition is largest, which always occurs at smaller τ.

Unlike the single-occupancy regime, there are negative correlations between successive waiting times when three electrons occupy the dot. Coherent effects also clearly determine correlation behavior, as the correlations have local maximums in magnitude when $\phi = n\pi/2$, where destructive interference is weakest. Ultimately, this is a very interesting research avenue, as the potential for tuning correlations with interference could lead to novel information processing methods. At this point, however, the transport cannot necessarily be considered correlated as the Pearson coefficient is $|p| < 0.1$. In the mirror configuration, for which equivalent results are shown in Fig.(7.9b)-Fig.(7.9f), we might expect larger correlations; two dots are connected to the drain and so coherent electrons may be detected simultaneously. The

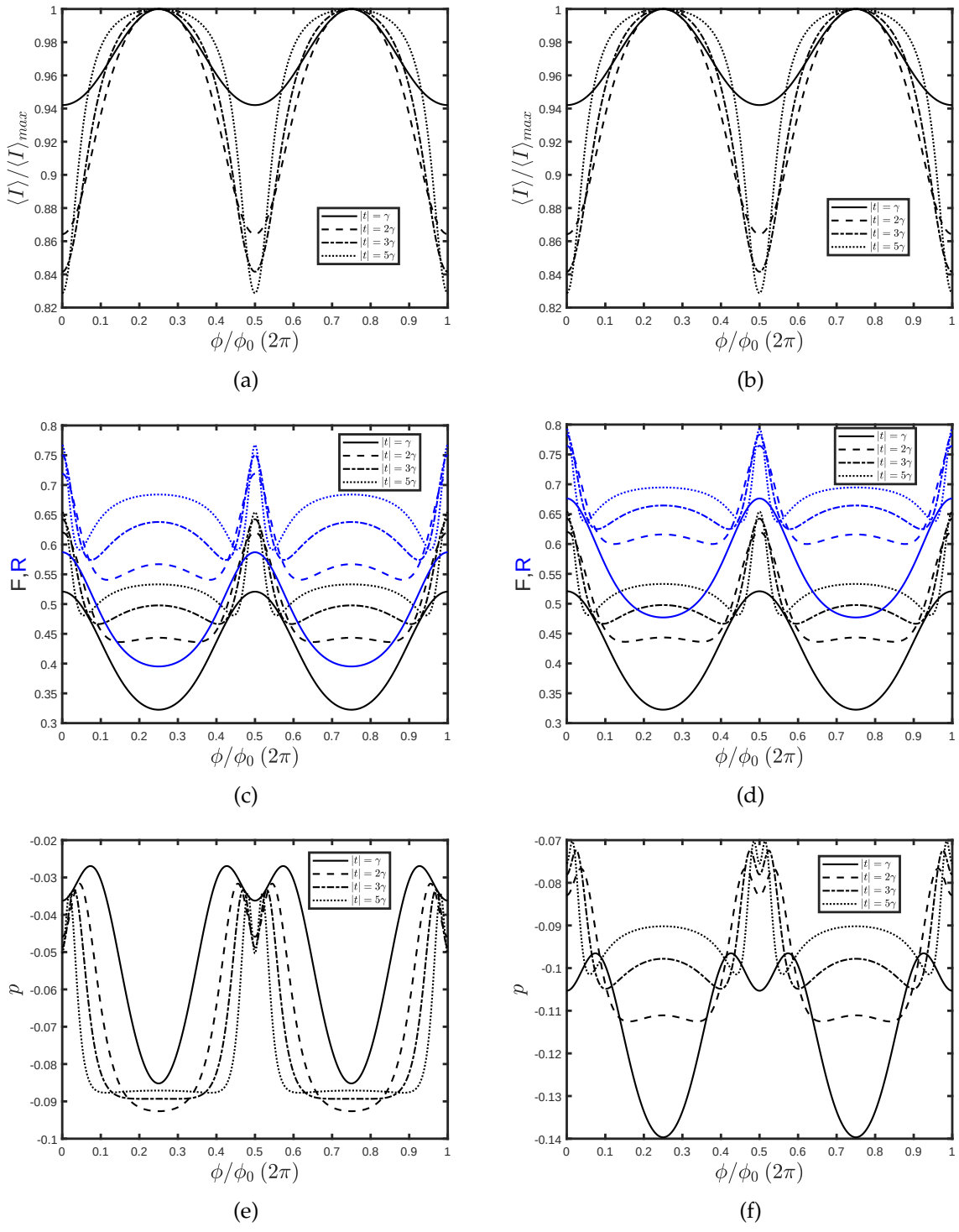

Figure 7.9: Current as a proportion of its maximum (a) and (b), corresponding Fano factor and randomness parameter (c) and (d), and Pearson correlation coefficient (e) and (f), all as a function of penetrating magnetic flux ϕ and in the triple occupancy regime. We use the same parameters as all previous plots. The left column is calculated for the configuration in Fig.(7.1a) and the right column for its mirror image in Fig.(7.1b).

Pearson coefficient does actually increase in magnitude for the mirror configuration, but it is still small: $|p| < 0.2$.

It is also important to note that in Fig.(7.9a)-Fig.(7.9f), while $\langle I \rangle$ and F are the same for both TQD configurations, R and p display qualitatively and quantiatively different behavior and so break this symmetry. From an experimental point of view, the WTD could therefore provide a way of determining the orientation of the TQD without a stability diagram.

Since the Aharonov-Bohm effect is an electron interfering with itself, it is not surprising that it does not have a great affect on the correlations. The better candidate for correlations, then, is coherent population blocking, as this can be a two-particle effect. In Fig.(7.9a) and Fig.(7.9b), we can see that in the triple occupancy regime destructive interference suppresses the current to, at most, about 80% of its maximum value: definitely not a dark state. Furthermore, the complicated Fock space of the triple occupancy regime prevents us from easily finding one. The spin-dependent double occupancy regime, however, has a dark state that has already been identified in previous work.

7.4.3 Spin-dependent double occupancy

For spin-dependent double occupancy, each dot may be occupied by one or two electrons, but the TQD as a whole may only be occupied by two electrons. In this regime, Poltl *et al.* [292] found that for certain parameters a two-particle dark state forms when the inter-dot repulsion between A and C is equal to the intra-dot repulsion within A: $\delta U = U_{AA} - U_{AC} = 0$. Their configuration did not allow tunneling between dot A and C, and we demonstrate in Fig.(7.10a) that a dark state exists for the same parameters even when dots A and C are coherently coupled. The dark state can be tuned by δU and, now that tunneling between A and C is allowed, the magnetic flux penetrating the ring. Fig.(7.10b) shows that, when $\phi = \pi/2$, the dark state is lifted at $\delta U = 0$. Interestingly, though, it suppresses the current more for $\delta U \geq 10\gamma$.

As with the single occupancy case, the dark state is accompanied by strong super-Poissonian noise, $F, R > 10$ when $\delta U = 0$; the double occupancy noise being noticeably larger than that for the single occupancy case. For $\phi = \pi/2$, in Fig.(7.10d), there is no super-Poissonian peak because the dark state does not form. At large δU, super-Poissonian noise persists regardless of the magnetic flux, indicating that it depends little on t_{AC}. From Fig.(7.10c) and Fig.(7.10d), it also appears that the transport is non-renewal at most values of δU; the Fano factor and randomness parameter rarely agree.

As expected, the correlation between successive waiting times reaches a peak in magnitude at the value of δU corresponding to the dark state. The result, however, is still underwhelming because $|p| < 0.1$; disproving the idea that a greater level of destructive interference will

yield stronger correlations. In Fig.(7.10f), it is apparent that a dark state is not necessary for correlations to occur; the Pearson coefficient peak is comparable in magnitude to that of the dark state, except that it forms when the current is at a maximum, when destructive interference is at minimum.

In the mirror configuration, Fig.(7.11a), and at $\delta U = 0$, the current is approximately 50% of its maximum; the dark state is mostly lifted, which we also saw for the single occupancy case. Accordingly, in Fig.(7.11c), the noise is limited to smaller values, although it is still super-Poissonian when the current is suppressed by any amount. For most values of δU, the correlation between successive waiting times is negligible, shown in Fig.(7.11c). At $\delta U \approx 5.5\gamma$, however, the current is at a maximum and the Pearson correlation coefficient is $p \approx -0.15$. In this case it appears that a lack of destructive interference causes correlations between successive waiting times. This peak in the correlation magnitude is actually accompanied by sub-Poissonian noise, which indicates electron anti-bunching.

If we take the value of δU at this point, for which $U_{AA} \approx 15.5\gamma$, and plot the same results as a function of ϕ now, we can see the usual Aharonov-Bohm oscillations in the current. Minimums occur at $(2n+1)\pi$, for $n = 0, 1, 2, \ldots$. Noticeably, the current for $\delta U = 15.5\gamma$ is actually a minimum for $\phi = \pi$; minimum destructive interference occurring at $\phi = (2n+1)\pi/2$. At these points, the noise is markedly sub-Poissonian, dropping below the level of even a single channel. The Pearson correlation coefficient also increases in magnitude around destructive interference minimums: $|p| > 0.2$.

7.5 Summary

The TQD is a rich experiment and theoretical system displaying quantum phenomena, such as Aharonov-Bohm oscillations and coherent population blocking. In this chapter, we have applied the WTD to a triangular TQD under two geometries and in three regimes: spin-independent single and triple occupancy and spin-dependent double occupancy. We found that coherent oscillations present in the WTD itself, which correlate to occupation probabilities of dots coupled to the drain. Coherent transport also produces correlations between successive waiting times, which are weakly dependent on Aharonov-Bohm oscillations, as this is an electron interfering with itself, and more strongly dependent on parameters influencing the formation of a dark state, which can be a two-particle effect.

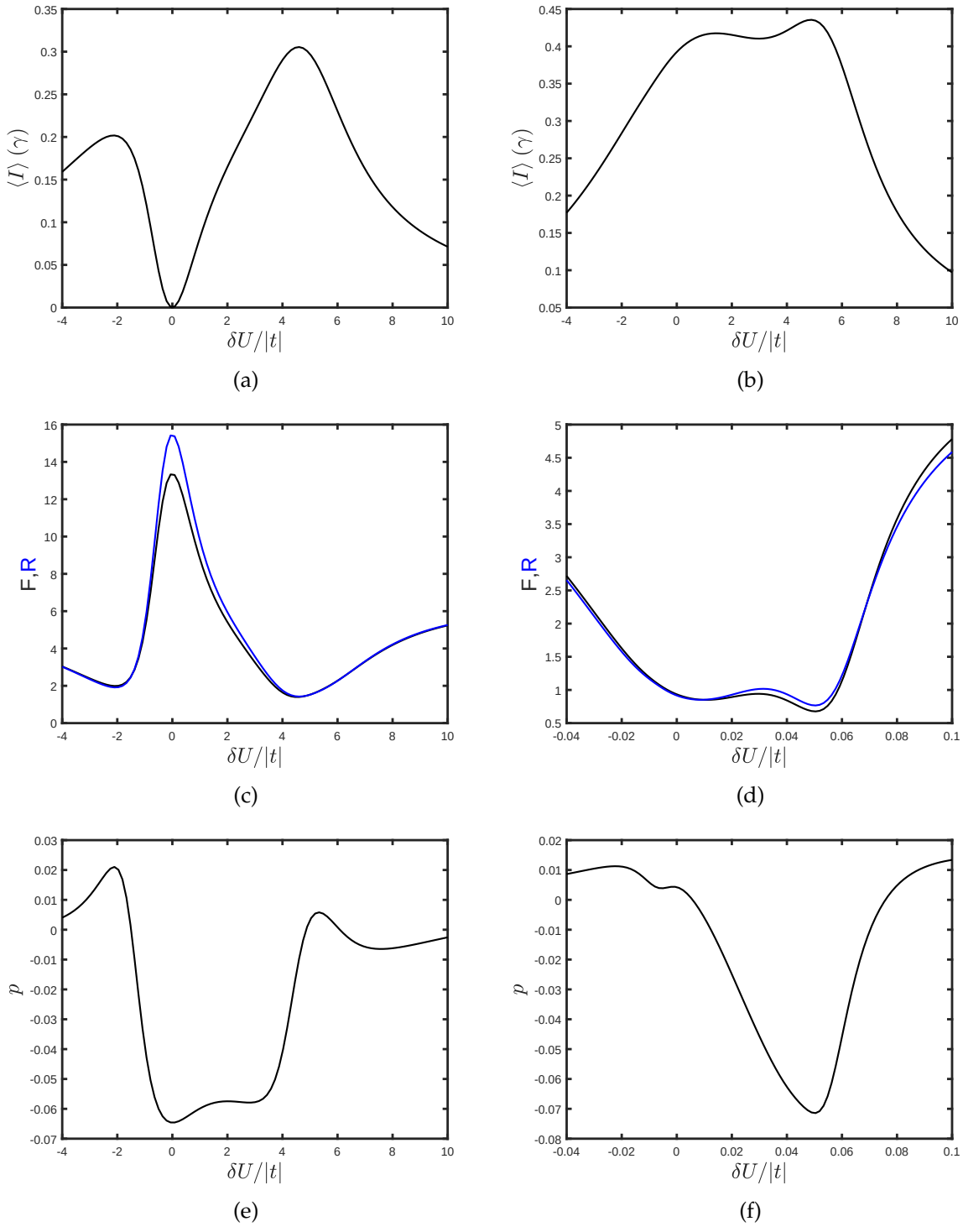

Figure 7.10: (a) and (b) Current, (c) and (d) Fano factor and randomness parameters, and (e) and (f) Pearson correlation coefficient as a function of δU, for the configuration in Fig.(7.1a). In the left column $\phi = \pi$, and in the right $\phi = +\pi/2$. The inter-dot couplings are $t_{AC} = |t|e^{i\phi}$ and $t_{AB} = t_{BC} = |t|$ where $|t| = \gamma$, while the intra-dot Coulomb repulsions are $U_{AA} = U_{CC}$ and $U_{BB} = 15\gamma$ and the inter-dot Coulomb repulsions are $U_{AC} = 10\gamma$ and $U_{AB} = U_{BC} = 11\gamma$.

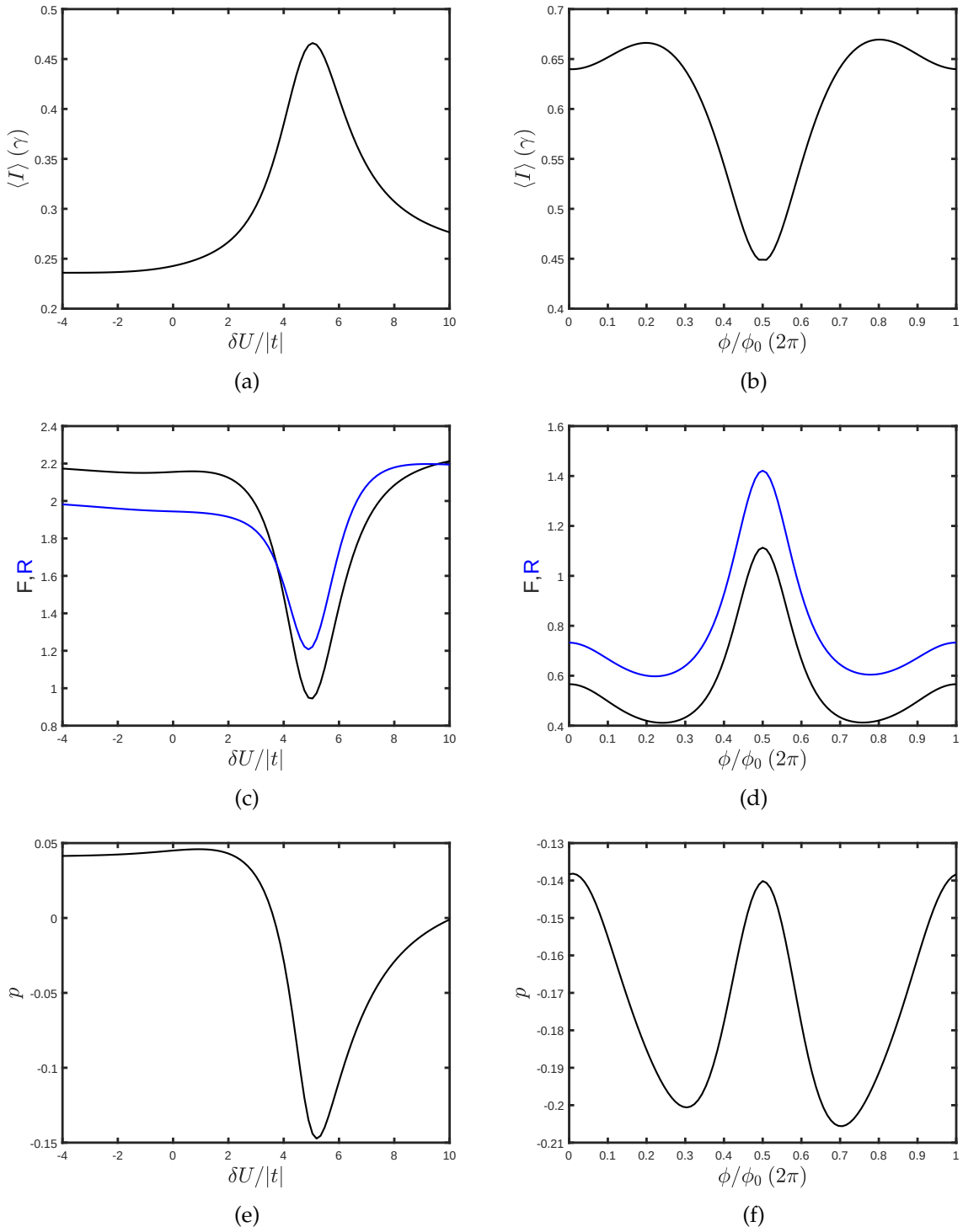

Figure 7.11: Current, (a) and (b), Fano factor and randomness parameter, (c) and (d), Pearson correlation coefficient, (e) and (f), as a function of δU in the left column and ϕ in the right column. In the left column, we fix $\phi = \pi$, and in the right column we fix $U_{AA} = 15.5\gamma$. All other parameters are the same as in Fig.(7.10a)-Fig.(7.10f).

Conclusion

In this thesis, we have analyzed a variety of nanoscale transport scenarios using the WTD and FPTD, two fluctuating-time statistics that are relatively new to nanoscale quantum transport. As opposed to more conventional measures like the FCS, the WTD and FPTD offer information on short timescales. Of particular interest was the concept of non-renewal transport, which occurs when successive waiting or first-passage times are correlated. We first reviewed the three fluctuation tools, including drawing a novel connection between two definitions of the WTD.

We extended the Markovian master equation technique for calculating WTDs in quantum electron transport to include cotunneling effects, and demonstrated the method for transport through an Anderson impurity. We primarily investigated how cotunneling processes affect the non-renewal statistics already present in the Anderson impurity, where electrons experience strong inelastic electron-electron interactions. We have shown that for large voltages, cotunneling increases the magnitude of the negative correlation between waiting times of subsequent electron tunnelings to the drain, which is caused by a strong electron-electron interaction. However, in the Coulomb blockade regime where cotunneling processes dominate, the correlation between subsequent waiting times is negligible and the system displays renewal behavior. We also applied the FPTD to the intermediate regime where the transport is bidirectional and the WTD fails. In this regime, inelastic cotunneling processes have previously been shown to induce super-Poissonian noise, which we show is accompanied by correlations between successive first-passage times, although they are relatively small and negative.

Sequential tunneling through the Holstein models further shows the greater applicability of the FPTD as opposed to the WTD. We first demonstrated that the WTD itself displays signatures of vibrationally assisted transport, like the Franck-Condon blockade. Next, we compared correlations calculated from the FPTD to those calculated from the WTD in a regime where it has previously been shown that an elastic shortcut channel opens for a strong electron-phonon coupling. The FPTD correlations are slightly smaller than those from the WTD, as expected since the first-passage time must always be as long or longer than the waiting time, and that the corresponding non-renewal behavior in the Fano factor and randomness parameter matches for the FPTD but not the WTD. This is further exacerbated when we apply a temper-

ature gradient but no bias voltage; bidirectional transitions are dominant in this regime and determining non-renewal behavior from the WTD is inaccurate.

The next chapter investigated telegraphic switching, which occurs in molecular junctions due to a variety of physical effects. If the rate of telegraphic switching, ν, is much less than the rate of electron transfer, γ, then the molecule spends a long time in each configuration before switching over. If the conductance difference between the two configurations, $|\langle I_a \rangle - \langle I_b \rangle|$, is large, and both $\langle I_a \rangle$ and $\langle I_b \rangle$ are non-negligible, then successive first-passage times are positively correlated. Experimentally, one of the most important sources of telegraphic switching could come from an interaction with two different vibrational modes. To test this behavior, we applied the telegraphic switching rate equation to the Holstein model. We found that, when the Franck-Condon physics induced large differences between $\langle I_a \rangle$ and $\langle I_b \rangle$, there are strong positive correlations between successive first-passage times. We also found that if the current through one configuration is completely suppressed and the other is non-negligible, then the transport is more aptly described by avalanche tunneling, which is not accompanied by strong non–renewal behavior. Via the Anderson model, we also analyzed telegraphic switching between a spin-split electronic level and a degenerate electronic level, corresponding to stochastically switching a magnetic field $\mathbf{B}$ on and off. We found positive correlations, with Pearson correlation coefficient $p \approx 0.5$ at voltages where the degenerate level is fully open, but only one spin-dependent level is partially open. As ν increases the correlations decrease, until they are negligible at $\nu \propto \gamma$. Finally, we constructed a rudimentary model of molecule-drain bonds stochastically forming and breaking, by switching between a transport scenario with $\gamma^D \propto \gamma$, and one in which $\gamma^D \ll \gamma$. Here, the Franck-Condon blockade plays a role in the non-renewal behavior at low voltages. At high voltages, however, the different γ^D produced strong positive correlations, which for were comparable for equilibrated and unequilibrated phonons.

Our final transport scenario was sequential tunneling through a triangular triple quantum dot, which required us to use the full master equation. The main goal of this chapter was to investigate how coherent effects like Aharonov-Bohm interference and population trapping affect correlations and non-renewal behavior. We find that the Aharonov-Bohm interference manifests as periodic oscillations in the correlations. Since this is from electrons interfering with themselves, however, this has little effect on interactions between electrons and the oscillations are small. Furthermore, the presence of coherent population trapping produces stronger correlations. Apart from the correlation behavior, however, there are coherent oscillations present in the WTD itself: directly relating to relevant dot occupations.

8.1 Future Work

Throughout all case studies we have presented in the thesis, it is clear that, while there are a variety of a mechanisms causing positive correlations between successive waiting times, negative correlations are either small or entirely absent. In an Anderson impurity, for example, negative correlations with $p \approx -0.1$ appear at high voltages when the electron can be doubly occupied, as two tunnelings separated by a waiting time τ must empty the impurity, forcing the second waiting time τ' to be long simply because the impurity must refill. While interesting, this is not due to any interaction; it is just an artifact of the allowed electron occupancy. In general, however, it is not currently clear what physical processes are necessary to observe negative correlations between successive waiting or first-passage times.

In Chapter 5, we saw that the electron-phonon interaction opens an elastic shortcut channel and causes positive correlations. If we could conceive of a similar scenario in which a phonon state is highly occupied after a short τ but the corresponding Franck-Condon matrix elements are small, then the next waiting time τ' will be long, potentially producing negative correlations. Part of future work, then, would be exploring more complex vibrational systems, either by introducing anharmonicity into the potential or adding a vibrational mode.

An important question also remains from the cotunneling section; what is the origin of the unphysical negative WTD probabilities for certain voltage regimes? We proposed that this was an indication that either neglecting coherences was not valid, or it was an area where higher-order tunneling contributions are present. Future work would investigate this question by taking the Redfield master equation one expansion further or including a 3$^{\text{rd}}$-order term from the T-matrix.

There are also many systems for which cotunneling processes have been included and the resulting FCS calculated. It would be interesting to compare the fluctuating-time statistics for many of these scenarios, including cotunneling through the Holstein model [196, 197], Coulomb drag in DQDs [300], and TQDs [296]. In our analysis, we also neglected the inelastic $\Gamma_{02}^{\alpha\alpha'}$ and $\Gamma_{20}^{\alpha\alpha'}$ cotunneling rates; the justification being that we considered positive U only. For systems in which the effective Coulomb interaction is $U < 0$, for example due to lattice vibrations, this is no longer a valid assumption [217], and this extension would be contained in future work.

There are many regimes we did not explore in the TQD section, and it is likely that fluctuating time statistics have many applications to quantum information processing in these systems. For example, Poltl *et al.* constructed a spin-entangled dark state between two coupled TQDs; investigating how spin-entanglement affects correlations between successive waiting times would be especially interesting.

Coherent effects, present in systems like a TQD, are strongest in the weak-coupling limit

where dephasing due to bath interactions are minimized. This is ideal for master equations, as we make a perturbation around γ anyway. In the strong-coupling limit, however, coherent effects may be reduced but bath correlations will affect the system dynamics; the transport becomes non-Markovian:

$$\dot{\mathbf{P}}(n,t) = \sum_{n'} \int_{t_{n'}}^{t} d\tau \mathcal{K}(n-n', t-\tau)\mathbf{P}(n', t_{n'}). \tag{8.1}$$

Here, the time-independent Liouvillian is replaced with the time-dependent kernel $\mathcal{K}(n - n', t - \tau)$ and the methods we presented in Chapter 2 no longer apply. Non-Markovian effects have previously been included in the FCS [120, 301, 302] and WTD [167, 303] of nanoscale systems via the addition of non-Markovian corrections. Potential future work would extend these results to more transport scenarios with a focus on waiting and first-passage time correlations. Another approach is the recently developed hierarchical equation of motion method for obtaining the n-resolved density matrix, which treats electron-phonon and electron-electron exactly [304, 305].

References

[1] A. Aviram and M. A. Ratner, *Molecular rectifiers*, Chem. Phys. Lett **29**, 277 –283 (1974).

[2] H. Choi and C. Mody, *The long history of molecular electronics: microelectronics origins of nanotechnology*, Soc. Stud. Sci. **39**, 11–50 (2009).

[3] G. Moore, *Cramming more components onto integrated circuits, reprinted from electronics, volume 38, number 8, april 19, 1965, pp.114 ff.*, IEEE Solid-State Circuits Society Newsletter **11**, 33–35 (2006).

[4] H. Bu, *5 nanometer transistors inching their way into chips*, 2017.

[5] M. A. Nielsen and I. L. Chuang, *Quantum Computation and Quantum Information* (Cambridge University Press, Cambridge, 2010).

[6] P. Shor, *Polynomial-time algorithms for prime factorization and discrete logarithms on a quantum computer*, SIAM Rev. **41**, 303–332 (1997).

[7] X. Guo, A. Whalley, J. E. Klare, L. Huang, S. O'Brien, M. Steigerwald, and C. Nuckolls, *Single-molecule devices as scaffolding for multicomponent nanostructure assembly*, Nano Lett. **7**, 1119–1122 (2007).

[8] J. Cuevas and E. Scheer, *Molecular Electronics: An Introduction to Theory and Experiment* (World Scientific, Singapore, 2010).

[9] D. Xiang, X. Wang, C. Jia, T. Lee, and X. Guo, *Molecular-Scale Electronics: From Concept to Function*, Chem. Rev. **116**, 4318 (2016).

[10] G. Binnig, H. Rohrer, C. Gerber, and E. Weibel, *Surface studies by scanning tunneling microscopy*, Phys. Rev. Lett. **49**, 57–61 (1982).

[11] D. A. Kislitsyn, J. D. Hackley, and G. V. Nazin, *Vibrational excitation in electron transport through carbon nanotube quantum dots*, J. Phys. Chem. Lett. **5**, 3138–3143 (2014).

[12] C. Muller, J. van Ruitenbeek, and L. de Jongh, *Experimental observation of the transition from weak link to tunnel junction*, Physica C **191**, 485 –504 (1992).

[13] J. Krans, C. Muller, I. Yanson, and J. van Ruitenbeek, *One atom point contacts*, Physica B **194-196**, 1033 –1034 (1994).

[14] C. Martin, D. Ding, H. van der Zant, and J. van Ruitenbeek, *Lithographic mechanical break junctions for single-molecule measurements in vacuum: possibilities and limitations*, New J. Phys. **10**, 065008 (2008).

[15] R. J. Nichols, W. Haiss, S. J. Higgins, E. Leary, S. Martin, and D. Bethell, *The experimental determination of the conductance of single molecules*, Phys. Chem. Chem. Phys. **12**, 2801–2815 (2010).

[16] R. J. Nichols and S. J. Higgins, *Single-molecule electronics: chemical and analytical perspectives*, Annu. Rev. Anal. Chem. **8**, 389–417 (2015).

[17] I. Díez-Pérez, J. Hihath, Y. Lee, L. Yu, L. Adamska, M. A. Kozhushner, I. I. Oleynik, and N. Tao, *Rectification and stability of a single molecular diode with controlled orientation*, Nat. Chem **1**, 635–641 (2009).

[18] N. Zhang, W.-Y. Lo, Z. Cai, L. Li, and L. Yu, *Molecular rectification tuned by through-space gating effect*, Nano Lett. **17**, 308–312 (2017).

[19] J. Trasobares, D. Vuillaume, D. Théron, and N. Clément, *A 17 GHz molecular rectifier*, Nat. Comm **7**, 12850 (2016).

[20] M. K. Ashraf, N. A. Bruque, J. L. Tan, G. J. O. Beran, and R. K. Lake, *Conductance switching in diarylethenes bridging carbon nanotubes*, J. Chem. Phys. **134**, 024524 (2011).

[21] S. J. van der Molen, J. Liao, T. Kudernac, J. S. Agustsson, L. Bernard, M. Calame, B. J. van Wees, B. L. Feringa, and C. Schönenberger, *Light-controlled conductance switching of ordered metal-molecule-metal devices*, Nano Lett. **9**, 76–80 (2009).

[22] M. Irie, *Diarylethenes for memories and switches*, Chem. Rev. **100**, 1685–1716 (2000).

[23] E. Braun, Y. Eichen, U. Sivan, and G. Ben-Yoseph, *DNA-templated assembly and electrode attachment of a conducting silver wire*, Nature **391**, 775–778 (1998).

[24] Y. Chen, G.-Y. Jung, D. A. A. Ohlberg, X. Li, D. R. Stewart, J. O. Jeppesen, K. A. Nielsen, J. F. Stoddart, and R. S. Williams, *Nanoscale molecular-switch crossbar circuits*, Nanotechnology **14**, 462–468 (2003).

[25] J. Chen, W. Wang, M. A. Reed, A. M. Rawlett, D. W. Price, and J. M. Tour, *Room-temperature negative differential resistance in nanoscale molecular junctions*, App. Phys. Lett. **77**, 1224–1226 (2000).

[26] K. Y. Tan, M. Partanen, R. E. Lake, J. Govenius, S. Masuda, and M. Möttönen, *Quantum-circuit refrigerator*, Nat. Commun. **8**, 15189 (2017).

[27] B. Warner, F. El Hallak, H. Prüser, J. Sharp, M. Persson, A. J. Fisher, and C. F. Hirjibehedin, *Tunable magnetoresistance in an asymmetrically coupled single-molecule junction*, Nat. Nanotechnol. **10**, 259 (2015).

[28] M. A. Reed, C. Zhou, C. J. Muller, T. P. Burgin, and J. M. Tour, *Conductance of a molecular junction*, Science **278**, 252–254 (1997).

[29] M. Tsutsui, M. Taniguchi, and T. Kawai, *Local heating in metal-molecule-metal junctions*, Nano Letters **8**, 3293–3297 (2008).

[30] Y. M. Blanter and M. B. Büttiker, *Shot noise in mesoscopic conductors*, Phys. Rep. **336**, 1 (2000).

[31] Y. V. Nazarov and Y. M. Blanter, *Quantum Transport: Introduction to Nanoscience* (Cambridge University Press, 2009).

[32] C. A. Martin, J. M. van Ruitenbeek, and H. S. J. van der Zant, *Sandwich-type gated mechanical break junctions*, Nanotechnology **21**, 265201 (2010).

[33] S. L. Rudge and D. S. Kosov, *Counting quantum jumps: a summary and comparison of fixed-time and fluctuating-time statistics in electron transport*, J. Chem. Phys. **151**, 034107 (2019).

[34] R. O. Jones, *Density functional theory: its origins, rise to prominence, and future*, Rev. Mod. Phys. **87**, 897–923 (2015).

[35] D. Bera, L. Qian, T.-K. Tseng, and P. H. Holloway, *Quantum dots and their multimodal applications: a review*, Materials **3**, 2260–2345 (2010).

[36] C. Bureau-Oxton, J. Camirand Lemyre, and M. Pioro-Ladrière, *Nanofabrication of gate-defined GaAs/AlGaAs lateral quantum dots*, J. Vis. Exp., e50581 (2013).

[37] J. B. Johnson, *Thermal agitation of electricity in conductors*, Phys. Rev. **32**, 97–109 (1928).

[38] H. Nyquist, *Thermal agitation of electric charge in conductors*, Phys. Rev. **32**, 110–113 (1928).

[39] W. Schottky, *Über spontane stromschwankungen in verschiedenen elektrizitätsleitern*, Ann. Phys. (Leipzeig) **362**, 541–567 (1918).

[40] W. Belzig, *Full counting statistics of super-Poissonian shot noise in multilevel quantum dots*, Phys. Rev. B **71**, 161301 (2005).

[41] A. Cottet, W. Belzig, and C. Bruder, *Positive cross-correlations due to dynamical channel blockade in a three-terminal quantum dot*, Phys. Rev. B **70**, 115315 (2004).

[42] A. Carmi and Y. Oreg, *Enhanced shot noise in asymmetric interacting two-level systems*, Phys. Rev. B **85**, 045325 (2012).

[43] J. Koch and F. von Oppen, *Franck-Condon blockade and giant Fano factors in transport through single molecules*, Phys. Rev. Lett. **94**, 206804 (2005).

[44] K. Ptaszyński, *Nonrenewal statistics in transport through quantum dots*, Phys. Rev. B **95**, 045306 (2017).

[45] K. Ptaszyński, *Waiting time distribution revealing the internal spin dynamics in a double quantum dot*, Phys. Rev. B **96**, 035409 (2017).

[46] A. Thielmann, M. H. Hettler, J. König, and G. Schön, *Cotunneling current and shot noise in quantum dots*, Phys. Rev. Lett. **95**, 146806 (2005).

[47] K. Kaasbjerg and W. Belzig, *Full counting statistics and shot noise of cotunneling in quantum dots and single-molecule transistors*, Phys. Rev. B **91**, 235413 (2015).

[48] A. Thielmann, M. H. Hettler, J. König, and G. Schön, *Super-Poissonian noise, negative differential conductance, and relaxation effects in transport through molecules, quantum dots, and nanotubes*, Phys. Rev. B **71**, 045341 (2005).

[49] Y. V. Nazarov and J. J. R. Struben, *Universal excess noise in resonant tunneling via strongly localized states*, Phys. Rev. B **53**, 15466–15468 (1996).

[50] L. Y. Chen and C. S. Ting, *Noise characteristics of sequential tunneling through double-barrier junctions*, Phys. Rev. B **46**, 4714–4717 (1992).

[51] B. J. van Wees, H. van Houten, C. W. J. Beenakker, J. G. Williamson, L. P. Kouwenhoven, D. van der Marel, and C. T. Foxon, *Quantized conductance of point contacts in a two-dimensional electron gas*, Phys. Rev. Lett. **60**, 848–850 (1988).

[52] S. Gustavsson, R. Leturcq, M. Studer, I. Shorubalko, T. Ihn, K. Ensslin, D. C. Driscoll, and A. C. Gossard, *Electron counting in quantum dots*, Surf. Sci. Rep. **64**, 191 (2009).

[53] Y. Kim, H. Song, D. Kim, T. Lee, and H. Jeong, *Noise characteristics of charge tunneling via localized states in metal-molecule-metal junctions*, ACS Nano **4**, 4426–4430 (2010).

[54] M. Bruderer, L. D. Contreras-Pulido, M. Thaller, L. Sironi, D. Obreschkow, and M. B. Plenio, *Inverse counting statistics for stochastic and open quantum systems: the characteristic polynomial approach*, New J. Phys. **16**, 033030 (2014).

[55] B. Reulet, J. Senzier, and D. E. Prober, *Environmental effects in the third moment of voltage fluctuations in a tunnel junction*, Phys. Rev. Lett. **91**, 196601 (2003).

[56] Y. Bomze, G. Gershon, D. Shovkun, L. S. Levitov, and M. Reznikov, *Measurement of counting statistics of electron transport in a tunnel junction*, Phys. Rev. Lett. **95**, 176601 (2005).

[57] W. Lu, Z. Ji, L. Pfeiffer, K. W. West, and A. J. Rimberg, *Real-time detection of electron tunnelling in a quantum dot*, Nature **423**, 422 (2003).

[58] T. Fujisawa, T. Hayashi, Y. Hirayama, H. Cheong, and Y. H. Jeong, *Electron counting of single-electron tunneling current*, Appl. Phys. Lett **84**, 2343–2345 (2004).

[59] S Gustavsson, R Leturcq, B Simovič, R Schleser, T Ihn, P Studerus, K Ensslin, D. C. Driscoll, and A. C. Gossard, *Counting statistics of single electron transport in a quantum dot*, Phys. Rev. Lett. **96**, 76605 (2006).

[60] S. Gustavsson, M. Studer, R. Leturcq, T. Ihn, K. Ensslin, D. C. Driscoll, and A. C. Gossard, *Frequency-selective single-photon detection using a double quantum dot*, Phys. Rev. Lett. **99**, 206804 (2007).

[61] T. Fujisawa, T. Hayashi, R. Tomita, and Y. Hirayama, *Bidirectional counting of single electrons*, Science **312**, 1634 (2006).

[62] C. Fricke, F. Hohls, W. Wegscheider, and R. J. Haug, *Bimodal counting statistics in single-electron tunneling through a quantum dot*, Phys. Rev. B **76**, 155307 (2007).

[63] S. Gustavsson, R. Leturcq, M. Studer, T. Ihn, K. Ensslin, D. C. Driscoll, and A. C. Gossard, *Time-resolved detection of single-electron interference*, Nano Lett. **8**, 2547–2550 (2008).

[64] S. Gustavsson, M. Studer, R. Leturcq, T. Ihn, K. Ensslin, D. C. Driscoll, and A. C. Gossard, *Detecting single-electron tunneling involving virtual processes in real time*, Phys. Rev. B **78**, 155309 (2008).

[65] V. F. Maisi, D. Kambly, C. Flindt, and J. P. Pekola, *Full counting statistics of Andreev tunneling*, Phys. Rev. Lett. **112**, 036801 (2014).

[66] C. Flindt, C. Fricke, F. Hohls, T. Novotný, K. Netočný, T. Brandes, and R. J. Haug, *Universal oscillations in counting statistics*, Proc. Natl. Acad. Sci. USA **106**, 10116 (2009).

[67] G. Gershon, Y. Bomze, E. V. Sukhorukov, and M. Reznikov, *Detection of non-Gaussian fluctuations in a quantum point contact*, Phys. Rev. Lett. **101**, 016803 (2008).

[68] N. Ubbelohde, C. Fricke, C. Flindt, F. Hohls, and R. J. Haug, *Measurement of finite-frequency current statistics in a single-electron transistor*, Nat. Commun. **3**, 612 (2012).

[69] E. V. Sukhorukov, A. N. Jordan, S. Gustavsson, R. Leturcq, T. Ihn, and K. Ensslin, *Conditional statistics of electron transport in interacting nanoscale conductors*, Nat. Phys. **3**, 243–247 (2007).

[70] E. Zbydniewska, A. Duzynska, M. Popoff, D. Hourlier, S. Lenfant, J. Judek, M. Zdrojek, and T. Mélin, *Charge blinking statistics of semiconductor nanocrystals revealed by carbon nanotube single charge sensors*, Nano Lett. **15**, 6349–6356 (2015).

[71] A. Kurzmann, P. Stegmann, J. Kerski, R. Schott, A. Ludwig, A. D. Wieck, J. König, A. Lorke, and M. Geller, *Optical detection of single-electron tunneling into a semiconductor quantum dot*, Phys. Rev. Lett. **122**, 247403 (2019).

[72] M. Jenei, E. Potanina, R. Zhao, K. Y. Tan, A. Rossi, T. Tanttu, K. W. Chan, V. Sevriuk, M. Möttönen, and A. Dzurak, *Waiting time distributions in a two-level fluctuator coupled to a superconducting charge detector*, Phys. Rev. Res. **1**, 033163 (2019).

[73] M. Albert, C. Flindt, and M. Büttiker, *Distributions of waiting times of dynamic single-electron emitters*, Phys. Rev. Lett. **107**, 086805 (2011).

[74] A. A. Budini, *Large deviations of ergodic counting processes: a statistical mechanics approach*, Phys. Rev. E **84**, 011141 (2011).

[75] S. K. Gorman, Y. He, M. G. House, J. G. Keizer, D. Keith, L. Fricke, S. J. Hile, M. A. Broome, and M. Y. Simmons, *Tunneling statistics for analysis of spin-readout fidelity*, Phys. Rev. Appl. **8**, 034019 (2017).

[76] S. Matsuo, K. Kuroyama, S. Yabunaka, S. R. Valentin, A. Ludwig, A. D. Wieck, and S. Tarucha, *Full counting statistics of spin-flip/conserving charge transitions in pauli-spin blockade*, arXiv.org (2019).

[77] S. Singh, P. Menczel, D. S. Golubev, I. M. Khaymovich, J. T. Peltonen, C. Flindt, K. Saito, E. Roldán, and J. P. Pekola, *Universal first-passage-time distribution of non-Gaussian currents*, Phys. Rev. Lett. **122**, 230602 (2019).

[78] D. S. Kosov, *Non-renewal statistics for electron transport in a molecular junction with electron-vibration interaction*, J. Chem. Phys. **147**, 104109 (2017).

[79] O. S. Lumbroso, L. Simine, A. Nitzan, D. Segal, and O. Tal, *Electronic noise due to temperature differences in atomic-scale junctions*, Nature **562**, 240 (2018).

[80] D. S. Kosov, *Telegraph noise in Markovian master equation for electron transport through molecular junctions*, J. Chem. Phys. **148**, 184108 (2018).

[81] S. Gurvitz, A. Aharony, and O. Entin-Wohlman, *Temporal evolution of resonant transmission under telegraph noise*, Phys. Rev. B **94**, 075437 (2016).

[82] M. Thoss and F. Evers, *Perspective: theory of quantum transport in molecular junctions*, J. Chem. Phys. **148**, 030901 (2018).

[83] E. Schrödinger, *An undulatory theory of the mechanics of atoms and molecules*, Phys. Rev. **28**, 1049–1070 (1926).

[84] H. Bruus and K. Flensberg, *Many-Body Quantum Theory in Condensed Matter Physics: An Introduction* (Oxford University Press, Oxford, 2002).

[85] J. von Neumann, *Probabilistic theory of quantum mechanics*, News from the Society of Sciences in Goettingen **1927**, 245–272 (1927).

[86] A. Redfield, "The theory of relaxation processes", in *Advances in magnetic resonance*, Vol. 1, edited by J. S. Waugh, Advances in Magnetic and Optical Resonance (Academic Press, Cambridge, 1965), pp. 1 –32.

[87] P. A. M. Dirac and N. H. D. Bohr, *The quantum theory of the emission and absorption of radiation*, Proc. R. Soc. Lond. A. **114**, 243–265 (1927).

[88] H.-P. Breuer and F. Petruccione, *The Theory of Open Quantum Systems* (Oxford University Press, London, 2002).

[89] J. H. Davies, S. Hershfield, P. Hyldgaard, and J. W. Wilkins, *Current and rate equation for resonant tunneling*, Phys. Rev. B **47**, 4603–4618 (1993).

[90] S. A. Gurvitz and Y. S. Prager, *Microscopic derivation of rate equations for quantum transport*, Phys. Rev. B **53**, 15932 (1996).

[91] S. A. Gurvitz, H. J. Lipkin, and Y. S. Prager, *Interference effects in resonant tunneling and the pauli principle*, Phys. Lett. A **212**, 91 (1996).

[92] S. A. Gurvitz, *Rate equations for quantum transport in multidot systems*, Phys. Rev. B **57**, 6602 (1998).

[93] C. Timm, *Tunneling through molecules and quantum dots: master-equation approaches*, Phys. Rev. B **77**, 195416 (2008).

[94] E. Merzbacher, *Quantum Mechanics* (Wiley, New Jersey, 1998).

[95] M. Leijnse and M. R. Wegewijs, *Kinetic equations for transport through single-molecule transistors*, Phys. Rev. B **78**, 235424 (2008).

[96] U. Harbola, M. Esposito, and S. Mukamel, *Quantum master equation for electron transport through quantum dots and single molecules*, Phys. Rev. B **74**, 235309 (2006).

[97] K. Ptaszyński, *First-passage times in renewal and nonrenewal systems*, Phys. Rev. E **97**, 012127 (2018).

[98] D. A. Bagrets and Y. V. Nazarov, *Full counting statistics of charge transfer in Coulomb blockade systems*, Phys. Rev. B **67**, 085316 (2003).

[99] Y. V. Nazarov, *Universalities of weak localization*, arXiv.org (1999).

[100] S. A. Gurvitz, L. Fedichkin, D. Mozyrsky, and G. P. Berman, *Relaxation and the zeno effect in qubit measurements*, Phys. Rev. Lett. **91**, 066801 (2003).

[101] X.-Q. Li, P. Cui, and Y. Yan, *Spontaneous relaxation of a charge qubit under electrical measurement*, Phys. Rev. Lett. **94**, 066803 (2005).

[102] X.-Q. Li, J. Luo, Y.-G. Yang, P. Cui, and Y.-J. Yan, *Quantum master-equation approach to quantum transport through mesoscopic systems*, Phys. Rev. B **71**, 205304 (2005).

[103] H.-S. Goan, G. J. Milburn, H. M. Wiseman, and H. Bi Sun, *Continuous quantum measurement of two coupled quantum dots using a point contact: a quantum trajectory approach*, Phys. Rev. B **63**, 125326 (2001).

[104] A. A. Budini, R. M. Turner, and J. P. Garrahan, *Fluctuating observation time ensembles in the thermodynamics of trajectories*, J. Stat. Mech. **2014**, P03012 (2014).

[105] M. Esposito, K. Lindenberg, and I. M. Sokolov, *On the relation between event-based and time-based current statistics*, EPL **89**, 10008 (2010).

[106] L. S. Levitov, H. Lee, and G. B. Lesovik, *Electron counting statistics and coherent states of electric current*, J. Math. Phys. **37**, 4845 (1996).

[107] Y. Nazarov, ed., *Quantum Noise in Mesoscopic Physics*, Nato Science Series (Kluwer, Dordrecht, 2003).

[108] G. B. Lesovik, F. Hassler, and G. Blatter, *Using qubits to measure fidelity in mesoscopic systems*, Phys. Rev. Lett. **96**, 106801 (2006).

[109] F. Hassler, M. V. Suslov, G. M. Graf, M. V. Lebedev, G. B. Lesovik, and G. Blatter, *Wave-packet formalism of full counting statistics*, Phys. Rev. B **78**, 165330 (2008).

[110] G. M. Tang and J. Wang, *Full-counting statistics of charge and spin transport in the transient regime: A nonequilibrium Green's function approach*, Phys. Rev. B **90**, 195422 (2014).

[111] Z. Yu, G.-M. Tang, and J. Wang, *Full-counting statistics of transient energy current in mesoscopic systems*, Phys. Rev. B **93**, 195419 (2016).

[112] T.-H. Park and M. Galperin, *Self-consistent full counting statistics of inelastic transport*, Phys. Rev. B **84**, 205450 (2011).

[113] B. K. Agarwalla, J.-H. Jiang, and D. Segal, *Full counting statistics of vibrationally assisted electronic conduction: transport and fluctuations of thermoelectric efficiency*, Phys. Rev. B **92**, 245418 (2015).

[114] J.-S. Wang, B. K. Agarwalla, and H. Li, *Transient behavior of full counting statistics in thermal transport*, Phys. Rev. B **84**, 153412 (2011).

[115] A. Ueda, Y. Utsumi, Y. Tokura, O. Entin-Wohlman, and A. Aharony, *AC transport and full-counting statistics of molecular junctions in the weak electron-vibration coupling regime*, J. Chem. Phys **146**, 092313 (2017).

[116] M. Ridley, V. N. Singh, E. Gull, and G. Cohen, *Numerically exact full counting statistics of the nonequilibrium Anderson impurity model*, Phys. Rev. B **97**, 115109 (2018).

[117] C. Emary, *Counting statistics of cotunneling electrons*, Phys. Rev. B **80**, 235306 (2009).

[118] Y. Utsumi, D. S. Golubev, and G. Schön, *Full counting statistics for a single-electron transistor: Nonequilibrium effects at intermediate conductance*, Phys. Rev. Lett. **96**, 086803 (2006).

[119] L. Simine and D. Segal, *Vibrational cooling, heating, and instability in molecular conducting junctions: full counting statistics analysis*, Phys. Chem. Chem. Phys. **14**, 13820–13834 (2012).

[120] A. Braggio, J. König, and R. Fazio, *Full counting statistics in strongly interacting systems: non-Markovian effects*, Phys. Rev. Lett. **96**, 026805 (2006).

[121] C. Flindt, T. Novotný, A. Braggio, M. Sassetti, and A.-P. Jauho, *Counting statistics of non-Markovian quantum stochastic processes*, Phys. Rev. Lett. **100**, 150601 (2008).

[122] C. Flindt, T. Novotný, A. Braggio, and A.-P. Jauho, *Counting statistics of transport through Coulomb blockade nanostructures: high-order cumulants and non-Markovian effects*, Phys. Rev. B **82**, 155407 (2010).

[123] M. Esposito, U. Harbola, and S. Mukamel, *Nonequilibrium fluctuations, fluctuation theorems, and counting statistics in quantum systems*, Rev. Mod. Phys. **81**, 1665 (2009).

[124] H. Touchette, *The large deviation approach to statistical mechanics*, Phys. Rep. **478**, 1–69 (2009).

[125] T. Karzig and F. von Oppen, *Signatures of critical full counting statistics in a quantum-dot chain*, Phys. Rev. B **81**, 045317 (2010).

[126] D. K. C. Macdonald, *Spontaneous fluctuations*, Rep. Prog. Phys **12**, 56–81 (1949).

[127] A. V. Galaktionov, D. S. Golubev, and A. D. Zaikin, *Statistics of current fluctuations in mesoscopic coherent conductors at nonzero frequencies*, Phys. Rev. B **68**, 235333 (2003).

[128] K. E. Nagaev, S. Pilgram, and M. Büttiker, *Frequency scales for current statistics of mesoscopic conductors*, Phys. Rev. Lett. **92**, 176804 (2004).

[129] S. Pilgram, K. E. Nagaev, and M. Büttiker, *Frequency-dependent third cumulant of current in diffusive conductors*, Phys. Rev. B **70**, 045304 (2004).

[130] A. V. Galaktionov and A. D. Zaikin, *Current fluctuations in composite conductors: beyond the second cumulant*, Phys. Rev. B **84**, 115418 (2011).

[131] D. Marcos, C. Emary, T. Brandes, and R. Aguado, *Finite-frequency counting statistics of electron transport: Markovian theory*, New J. Phys. **12**, 123009 (2010).

[132] J. Salo, F. W. J. Hekking, and J. P. Pekola, *Frequency-dependent current correlation functions from scattering theory*, Phys. Rev. B **74**, 125427 (2006).

[133] M. Benito, M. Niklas, and S. Kohler, *Full-counting statistics of time-dependent conductors*, Phys. Rev. B **94**, 195433 (2016).

[134] P. Stegmann and J. König, *Inverse counting statistics based on generalized factorial cumulants*, New J.Phys **19**, 023018 (2017).

[135] C. Emary, D. Marcos, R. Aguado, and T. Brandes, *Frequency-dependent counting statistics in interacting nanoscale conductors*, Phys. Rev. B **76**, 161404 (2007).

[136] P. Stegmann and J. König, *Short-time counting statistics of charge transfer in Coulomb-blockade systems*, Phys. Rev. B **94**, 125433 (2016).

[137] P. Stegmann, J. König, and S. Weiss, *Coherent dynamics in stochastic systems revealed by full counting statistics*, Phys. Rev. B **98**, 035409 (2018).

[138] D. Kambly, C. Flindt, and M. Büttiker, *Factorial cumulants reveal interactions in counting statistics*, Phys. Rev. B **83**, 075432 (2011).

[139] D. Kambly and C. Flindt, *Time-dependent factorial cumulants in interacting nano-scale systems*, J. Comput. Electron **12**, 331 (2013).

[140] P. Stegmann, B. Sothmann, A. Hucht, and J. König, *Detection of interactions via generalized factorial cumulants in systems in and out of equilibrium*, Phys. Rev. B **92**, 155413 (2015).

[141] C Flindt, T Novotný, and A.-P Jauho, *Full counting statistics of nano-electromechanical systems*, EPL **69**, 475 (2005).

[142] N. G. van Kampen, *Stochastic Processes in Physics and Chemistry* (Elsevier Science, Amsterdam, 1992).

[143] S. Chowdhury and S. P. Mukherjee, *Estimation of waiting time distribution in an M/M/1 Queue*, OPSEARCH **48**, 306–317 (2011).

[144] S. Saha, S. Ghose, R. Adhikari, and A. Dua, *Nonrenewal statistics in the catalytic activity of enzyme molecules at mesoscopic concentrations*, Phys. Rev. Lett. **107**, 218301 (2011).

[145] M. Srinivas and E. Davies, *Photon Counting Probabilities in Quantum Optics*, Opt. Acta **28**, 981 (2010).

[146] H. J. Carmichael, S. Singh, R. Vyas, and P. R. Rice, *Photoelectron waiting times and atomic state reduction in resonance fluorescence*, Phys. Rev. A **39**, 1200–1218 (1989).

[147] A. A. Budini, *Quantum jumps and photon statistics in fluorescent systems coupled to classically fluctuating reservoirs*, J. Phys. B **43**, 115501 (2010).

[148] J. Cao, *Correlations in single molecule photon statistics: a renewal indicator*, J. Phys. Chem. B **110**, 19040–19043 (2006).

[149] I. S. Osad'ko and V. V. Fedyanin, *Influence of conformational changes in complex molecules on photon statistics of single molecule fluorescence*, Phys. Rev. A **83**, 063841 (2011).

[150] T. Brandes, *Waiting Times and Noise in Single Particle Transport*, Ann. Phys. (Berlin) **17**, 477 (2008).

[151] M. Albert, D. Chevallier, and P. Devillard, *Waiting times of entangled electrons in normal–superconducting junctions*, Phys. E **76**, 209 –215 (2016).

[152] D. Chevallier, M. Albert, and P. Devillard, *Probing Majorana and Andreev bound states with waiting times*, EPL **116**, 27005 (2016).

[153] S. Mi, P. Burset, and C. Flindt, *Electron waiting times in hybrid junctions with topological superconductors*, Sci. Rep **8**, 16828 (2018).

[154] M. Albert and P. Devillard, *Waiting time distribution for trains of quantized electron pulses*, Phys. Rev. B **90**, 035431 (2014).

[155] D. Dasenbrook, P. P. Hofer, and C. Flindt, *Electron waiting times in coherent conductors are correlated*, Phys. Rev. B **91**, 195420 (2015).

[156] G. Haack, M. Albert, and C. Flindt, *Distributions of electron waiting times in quantum-coherent conductors*, Phys. Rev. B **90**, 205429 (2014).

[157] M. Albert, G. Haack, C. Flindt, and M. Büttiker, *Electron waiting times in mesoscopic conductors*, Phys. Rev. Lett. **108**, 186806 (2012).

[158] G. M. Tang, F. Xu, and J. Wang, *Waiting time distribution of quantum electronic transport in the transient regime*, Phys. Rev. B **89**, 205310 (2014).

[159] G. Tang, Z. Yu, and J. Wang, *Full-counting statistics of energy transport of molecular junctions in the polaronic regime*, New J. Phys. **19**, 083007 (2017).

[160] G. Tang, F. Xu, S. Mi, and J. Wang, *Spin-resolved electron waiting times in a quantum-dot spin valve*, Phys. Rev. B **97**, 165407 (2018).

[161] R. Seoane Souto, R. Avriller, R. C. Monreal, A. Martín-Rodero, and A. Levy Yeyati, *Transient dynamics and waiting time distribution of molecular junctions in the polaronic regime*, Phys. Rev. B **92**, 125435 (2015).

[162] N. Walldorf, C. Padurariu, A. P. Jauho, and C. Flindt, *Electron Waiting Times of a Cooper Pair Splitter*, Phys. Rev. Lett. **120**, 087701 (2018).

[163] L. Rajabi, C. Pöltl, and M. Governale, *Waiting time distributions for the transport through a quantum-dot tunnel coupled to one normal and one superconducting lead*, Phys. Rev. Lett. **111**, 067002 (2013).

[164] E. Potanina and C. Flindt, *Electron waiting times of a periodically driven single-electron turnstile*, Phys. Rev. B **96**, 045420 (2017).

[165] S. Welack, S. Mukamel, and Y. J. Yan, *Waiting time distributions of electron transfers through quantum dot Aharonov-Bohm interferometers*, EPL **85**, 57008 (2009).

[166] B. Sothmann, *Electronic waiting-time distribution of a quantum-dot spin valve*, Phys. Rev. B **90**, 155315 (2014).

[167] K. H. Thomas and C. Flindt, *Electron waiting times in non-Markovian quantum transport*, Phys. Rev. B **87**, 121405 (2013).

[168] S. L. Rudge and D. S. Kosov, *Distribution of tunnelling times for quantum electron transport*, J. Chem. Phys. **144**, 124105 (2016).

[169] S. L. Rudge and D. S. Kosov, *Distribution of residence times as a marker to distinguish different pathways for quantum transport*, Phys. Rev. E **94**, 042134 (2016).

[170] S. L. Rudge and D. S. Kosov, *Distribution of waiting times between electron cotunneling events*, Phys. Rev. B **98**, 245402 (2018).

[171] D. S. Kosov, *Waiting time distribution for electron transport in a molecular junction with electron-vibration interaction*, J. Chem. Phys. **146**, 074102 (2017).

[172] D. S. Kosov, *Waiting time between charging and discharging processes in molecular junctions*, J. Chem. Phys. **149**, 164105 (2018).

[173] J. Koch, F. von Oppen, and A. V. Andreev, *Theory of the Franck-Condon blockade regime*, Phys. Rev. B **74**, 205438 (2006).

[174] G. Haack, A. Steffens, J. Eisert, and R. Hübener, *Continuous matrix product state tomography of quantum transport experiments*, New J. Phys. **17**, 113024 (2015).

[175] S. L. Rudge and D. S. Kosov, *Nonrenewal statistics in quantum transport from the perspective of first-passage and waiting time distributions*, Phys. Rev. B **99**, 115426 (2019).

[176] S. L. Rudge and D. S. Kosov, *Fluctuating-time and full counting statistics for quantum transport in a system with internal telegraphic noise*, Phys. Rev. B **100**, 235430 (2019).

[177] M. Bauer and F. Cornu, *Affinity and Fluctuations in a Mesoscopic Noria*, J. Stat. Phys. **155**, 703 (2014).

[178] E. Roldán, I. Neri, M. Dörpinghaus, H. Meyr, and F. Jülicher, *Decision making in the arrow of time*, Phys. Rev. Lett. **115**, 250602 (2015).

[179] I. Neri, E. Roldán, and F. Jülicher, *Statistics of infima and stopping times of entropy production and applications to active molecular processes*, Phys. Rev. X **7**, 011019 (2017).

[180] J. P. Garrahan, *Simple bounds on fluctuations and uncertainty relations for first-passage times of counting observables*, Phys. Rev. E **95**, 032134 (2017).

[181] K. Saito and A. Dhar, *Waiting for rare entropic fluctuations*, EPL **114**, 50004 (2016).

[182] D. Dasenbrook and C. Flindt, *Quantum theory of an electron waiting time clock*, Phys. Rev. B **93**, 245409 (2016).

[183] J. B. Witkoskie and J. Cao, *Testing for renewal and detailed balance violations in single-molecule blinking processes*, J. Phys. Chem. B **110**, 19009–19017 (2006).

[184] J. Cao and R. J. Silbey, *Generic schemes for single-molecule kinetics. 1: self-consistent pathway solutions for renewal processes*, J. Phys. Chem. B **112**, 12867–12880 (2008).

[185] E. V. Sukhorukov, G. Burkard, and D. Loss, *Noise of a quantum dot system in the cotunneling regime*, Phys. Rev. B **63**, 125315 (2001).

[186] Y. Okazaki, S. Sasaki, and K. Muraki, *Shot noise spectroscopy on a semiconductor quantum dot in the elastic and inelastic cotunneling regimes*, Phys. Rev. B **87**, 041302 (2013).

[187] Y. Zhang, L. DiCarlo, D. T. McClure, M. Yamamoto, S. Tarucha, C. M. Marcus, M. P. Hanson, and A. C. Gossard, *Noise correlations in a Coulomb-blockaded quantum dot*, Phys. Rev. Lett. **99**, 036603 (2007).

[188] E. Onac, F. Balestro, B. Trauzettel, C. F. J. Lodewijk, and L. P. Kouwenhoven, *Shot-noise detection in a carbon nanotube quantum dot*, Phys. Rev. Lett. **96**, 026803 (2006).

[189] C. W. J. Beenakker, *Theory of Coulomb-blockade oscillations in the conductance of a quantum dot*, Phys. Rev. B **44**, 1646 (1991).

[190] A. Romito and Y. Gefen, *Weak measurement of cotunneling time*, Phys. Rev. B **90**, 085417 (2014).

[191] L. J. Geerligs, D. V. Averin, and J. E. Mooij, *Observation of macroscopic quantum tunneling through the Coulomb energy barrier*, Phys. Rev. Lett. **65**, 3037 (1990).

[192] D. V. Averin and A. A. Odintsov, *Macroscopic quantum tunneling of the electric charge in small tunnel junctions*, Phys. Lett. A **140**, 251 (1989).

[193] D. V. Averin and Y. V. Nazarov, *Virtual electron diffusion during quantum tunneling of the electric charge*, Phys. Rev. Lett. **65**, 2446 (1990).

[194] D. V. Averin, *Periodic conductance oscillations in the single-electron tunneling transistor*, Phys. B **194-196**, 979 (1994).

[195] S De Franceschi, S Sasaki, J. M. Elzerman, W. G. van der Wiel, S Tarucha, and L. P. Kouwenhoven, *Electron Cotunneling in a Semiconductor Quantum Dot*, Phys. Rev. Lett. **86**, 878 (2001).

[196] J. Koch, F. von Oppen, Y. Oreg, and E. Sela, *Thermopower of single-molecule devices*, Phys. Rev. B **70**, 195107 (2004).

[197] M. Turek and K. A. Matveev, *Cotunneling thermopower of single electron transistors*, Phys. Rev. B **65**, 115332 (2002).

[198] Y. Dinaii, A. Shnirman, and Y. Gefen, *Statistics of energy dissipation in a quantum dot operating in the cotunneling regime*, Phys. Rev. B **90**, 201404 (2014).

[199] N. M. Gergs, C. B. M. Hörig, M. R. Wegewijs, and D. Schuricht, *Charge fluctuations in nonlinear heat transport*, Phys. Rev. B **91**, 201107 (2015).

[200] V. N. Golovach and D. Loss, *Transport through a double quantum dot in the sequential tunneling and cotunneling regimes*, Phys. Rev. B **69**, 245327 (2004).

[201] J. N. Pedersen, B. Lassen, A. Wacker, and M. H. Hettler, *Coherent transport through an interacting double quantum dot: Beyond sequential tunneling*, Phys. Rev. B **75**, 235314 (2007).

[202] J.-F. Dayen, E. Devid, M. V. Kamalakar, D. Golubev, C. Guédon, V. Faramarzi, B. Doudin, and S. J. van der Molen, *Enhancing the molecular signature in molecule-nanoparticle networks via inelastic cotunneling*, Adv. Mater. **25**, 400 (2013).

[203] T. B. Tran, I. S. Beloborodov, J. Hu, X. M. Lin, T. F. Rosenbaum, and H. M. Jaeger, *Sequential tunneling and inelastic cotunneling in nanoparticle arrays*, Phys. Rev. B **78**, 75437 (2008).

[204] G. Begemann, S. Koller, M. Grifoni, and J. Paaske, *Inelastic cotunneling in quantum dots and molecules with weakly broken degeneracies*, Phys. Rev. B **82**, 045316 (2010).

[205] M. Leijnse, M. R. Wegewijs, and M. H. Hettler, *Pair tunneling resonance in the single-electron transport regime*, Phys. Rev. Lett. **103**, 156803 (2009).

[206] D. M. Zumbühl, C. M. Marcus, M. P. Hanson, and A. C. Gossard, *Cotunneling Spectroscopy in Few-Electron Quantum Dots*, Phys. Rev. Lett. **93**, 256801 (2004).

[207] N. Roch, R. Vincent, F. Elste, W. Harneit, W. Wernsdorfer, C. Timm, and F. Balestro, *Cotunneling through a magnetic single-molecule transistor based on N@C_{60}*, Phys. Rev. B **83**, 081407 (2011).

[208] I. Weymann, J. Barnaś, and S. Krompiewski, *Transport through single-wall metallic carbon nanotubes in the cotunneling regime*, Phys. Rev. B **78**, 035422 (2008).

[209] J. Aghassi, M. H. Hettler, and G. Schön, *Cotunneling assisted sequential tunneling in multilevel quantum dots*, Appl. Phys. Lett. **92**, 202101 (2008).

[210] O. Zilberberg, A. Carmi, and A. Romito, *Measuring cotunneling in its wake*, Phys. Rev. B **90**, 205413 (2014).

[211] H. Schoeller and G. Schön, *Mesoscopic quantum transport: Resonant tunneling in the presence of a strong Coulomb interaction*, Phys. Rev. B **50**, 18436 (1994).

[212] J. König, H. Schoeller, and G. Schön, *Cotunneling at resonance for the single-electron transistor*, Phys. Rev. Lett. **78**, 4482 (1997).

[213] P. W. Anderson, *Localized magnetic states in metals*, Phys. Rev. **124**, 41–53 (1961).

[214] J. Koch, M. E. Raikh, and F. von Oppen, *Pair tunneling through single molecules*, Phys. Rev. Lett. **96**, 056803 (2006).

[215] E. Kleinherbers, P. Stegmann, and J. König, *Revealing attractive electron-electron interaction in a quantum dot by full counting statistics*, New J. Phys. **20**, 073023 (2018).

[216] M.-J. Hwang, M.-S. Choi, and R. López, *Pair tunneling and shot noise through a single molecule in a strong electron-phonon coupling regime*, Phys. Rev. B **76**, 165312 (2007).

[217] T.-F. Fang, A.-M. Guo, H.-T. Lu, H.-G. Luo, and Q.-F. Sun, *Charge Kondo effect in negative-U quantum dots with superconducting electrodes*, Phys. Rev. B **96**, 085131 (2017).

[218] H. Park, J. Park, A. K. L. Lim, E. H. Fano, A. P. Alivisatos, and P. L. McEuen, *Nanomechanical oscillations in a single-C_{60} transistor*, Nature **407**, 10.1038/35024031 (2000).

[219] D. Fedorets, L. Y. Gorelik, R. I. Shekhter, and M. Jonson, *Vibrational instability due to coherent tunneling of electrons*, EPL **58**, 99–104 (2002).

[220] J. Koch, M. E. Raikh, and F. von Oppen, *Full counting statistics of strongly non-ohmic transport through single molecules*, Phys. Rev. Lett. **95**, 056801 (2005).

[221] B. De and B. Muralidharan, *Manipulation of non-linear heat currents in the dissipative Anderson-Holstein model*, J. Phys. Condens. Matter **32**, 035305 (2019).

[222] T. Holstein, *Studies of polaron motion : part i. the molecular-crystal model*, Ann. Phys. **8**, 325–342 (1959).

[223] I. G. Lang and Y. A. Firsov, *Kinetic Theory of Semiconductors With Low Mobility*, J. Exp. Theor. Phys **16**, 1301 (1963).

[224] A. Mitra, I. Aleiner, and A. J. Millis, *Phonon effects in molecular transistors: quantal and classical treatment*, Phys. Rev. B **69**, 245302 (2004).

[225] S. Boussaad, B. Xu, L. Nagahara, I. Amlani, W. Schmickler, R. Tsui, and N. Tao, *Discrete tunneling current fluctuations in metal–water–metal tunnel junctions*, J. Chem. Phys **118**, 8891–8897 (2003).

[226] M. Lastapis, M. Martin, D. Riedel, L. Hellner, G. Comtet, and G. Dujardin, *Picometer-scale electronic control of molecular dynamics inside a single molecule*, Science **308**, 1000–1003 (2005).

[227] D.-g. Cho, M. Yang, M. Lee, and S. Hong, *Nanoscale anomalous noise source switching with a trap-free current transition in a PEDOT:PSS film*, Nanotechnology **29**, 425704 (2018).

[228] Y. Song, H. Jeong, S. Chung, G. H. Ahn, T.-Y. Kim, J. Jang, D. Yoo, H. Jeong, A. Javey, and T. Lee, *Origin of multi-level switching and telegraphic noise in organic nanocomposite memory devices*, Sci. Rep. **29**, 425704 (2018).

[229] A. E. Baber, H. L. Tierney, and E. C. H. Sykes, *A quantitative single-molecule study of thioether molecular rotors*, ACS Nano **2**, 2385–2391 (2008).

[230] R. A. Wassel, R. R. Fuierer, N. Kim, and C. B. Gorman, *Stochastic variation in conductance on the nanometer scale: a general phenomenon*, Nano Lett. **3**, 1617–1620 (2003).

[231] A. M. Kuznetsov, I. G. Medvedev, and J. Ulstrup, *Electric double layer effect on observable characteristics of the tunnel current through a bridged electrochemical contact*, J. Chem. Phys **127**, 104708 (2007).

[232] Z. J. Donhauser, B. A. Mantooth, K. F. Kelly, L. A. Bumm, J. D. Monnell, J. J. Stapleton, D. W. Price, A. M. Rawlett, D. L. Allara, J. M. Tour, and P. S. Weiss, *Conductance switching in single molecules through conformational changes*, Science **292**, 2303–2307 (2001).

[233] W. Auwärter, K. Seufert, F. Bischoff, D. Ecija, S. Vijayaraghavan, S. Joshi, F. Klappenberger, N. Samudrala, and J. V. Barth, *A surface-anchored molecular four-level conductance switch based on single proton transfer*, Nat. Nanotechnol. **7**, 41–46 (2012).

[234] D. Cho, M. Yang, N. Shin, and S. Hong, *Mapping reversible photoswitching of molecular resistance fluctuations during the conformational transformation of azobenzene-terminated molecular switches*, Nanotechnology **29**, 365704 (2018).

[235] J. M. Artés, M. López-Martínez, I. Díez-Pérez, F. Sanz, and P. Gorostiza, *Conductance switching in single wired redox proteins*, Small **10**, 2537–2541 (2014).

[236] S. Singh, J. T. Peltonen, I. M. Khaymovich, J. V. Koski, C. Flindt, and J. P. Pekola, *Distribution of current fluctuations in a bistable conductor*, Phys. Rev. B **94**, 241407 (2016).

[237] C. S. Lau, H. Sadeghi, G. Rogers, S. Sangtarash, P. Dallas, K. Porfyrakis, J. Warner, C. J. Lambert, G. A. D. Briggs, and J. A. Mol, *Redox-dependent Franck-Condon blockade and avalanche transport in a graphene–fullerene single-molecule transistor*, Nano Lett. **16**, 170–176 (2016).

[238] A. N. Jordan and E. V. Sukhorukov, *Transport statistics of bistable systems*, Phys. Rev. Lett. **93**, 260604 (2004).

[239] Y. M. Galperin, N. Zou, and K. A. Chao, *Resonant tunneling in the presence of a two-level fluctuator: average transparency*, Phys. Rev. B **49**, 13728–13739 (1994).

[240] Y. M. Galperin and K. A. Chao, *Resonant tunneling in the presence of a two-level fluctuator: low-frequency noise*, Phys. Rev. B **52**, 12126–12134 (1995).

[241] O. Entin-Wohlman, D. Chowdhury, A. Aharony, and S. Dattagupta, *Heat currents in electronic junctions driven by telegraph noise*, Phys. Rev. B **96**, 195435 (2017).

[242] C. Emary, *Dark states in the magnetotransport through triple quantum dots*, Phys. Rev. B **76**, 245319 (2007).

[243] G. Engelhardt and J. Cao, *Tuning the Aharonov-Bohm effect with dephasing in nonequilibrium transport*, Phys. Rev. B **99**, 075436 (2019).

[244] W. G. van der Wiel, S. De Franceschi, J. M. Elzerman, T. Fujisawa, S. Tarucha, and L. P. Kouwenhoven, *Electron transport through double quantum dots*, Rev. Mod. Phys. **75**, 1–22 (2002).

[245] N. C. van der Vaart, S. F. Godijn, Y. V. Nazarov, C. J.P. M. Harmans, J. E. Mooij, L. W. Molenkamp, and C. T. Foxon, *Resonant tunneling through two discrete energy states*, Phys. Rev. Lett. **74**, 4702–4705 (1995).

[246] R. H. Blick, R. J. Haug, J. Weis, D. Pfannkuche, K. v. Klitzing, and K. Eberl, *Single-electron tunneling through a double quantum dot: the artificial molecule*, Phys. Rev. B **53**, 7899–7902 (1996).

[247] D. Schröer, A. D. Greentree, L. Gaudreau, K. Eberl, L. C. L. Hollenberg, J. P. Kotthaus, and S. Ludwig, *Electrostatically defined serial triple quantum dot charged with few electrons*, Phys. Rev. B **76**, 075306 (2007).

[248] A. Vidan, R. M. Westervelt, M. Stopa, M. Hanson, and A. C. Gossard, *Triple quantum dot charging rectifier*, Appl. Phys. Lett. **85**, 3602–3604 (2004).

[249] M. Stopa, *Rectifying behavior in Coulomb blockades: charging rectifiers*, Phys. Rev. Lett. **88**, 146802 (2002).

[250] A. Vidan, R. M. Westervelt, M. Stopa, M. Hanson, and A. C. Gossard, *Charging and spin effects in triple dot artificial molecules*, J. Supercond. **18**, 223–227 (2005).

[251] L. Gaudreau, S. A. Studenikin, A. S. Sachrajda, P. Zawadzki, A. Kam, J. Lapointe, M. Korkusinski, and P. Hawrylak, *Stability diagram of a few-electron triple dot*, Phys. Rev. Lett. **97**, 036807 (2006).

[252] M. Korkusinski, I. P. Gimenez, P. Hawrylak, L. Gaudreau, S. A. Studenikin, and A. S. Sachrajda, *Topological hunds rules and the electronic properties of a triple lateral quantum dot molecule*, Phys. Rev. B **75**, 115301 (2007).

[253] L. Gaudreau, A. S. Sachrajda, S. Studenikin, P. Zawadzki, A. Kam, and J. Lapointe, *Coherent transport through a quadruple point in a few electron triple dot*, AIP Conf. Proc. **893**, 857–858 (2007).

[254] L. Gaudreau, A. S. Sachrajda, S. Studenikin, A. Kam, F. Delgado, Y. P. Shim, M. Korkusinski, and P. Hawrylak, *Coherent transport through a ring of three quantum dots*, Phys. Rev. B **80**, 075415 (2009).

[255] M. C. Rogge and R. J. Haug, *Two-path transport measurements on a triple quantum dot*, Phys. Rev. B **77**, 193306 (2008).

[256] S. Amaha, T. Hatano, T. Kubo, Y. Tokura, D. G. Austing, and S. Tarucha, *Fabrication and characterization of a laterally coupled vertical triple quantum dot device*, Phys. E **40**, 1322–1324 (2008).

[257] S. Amaha, W. Izumida, T. Hatano, S. Teraoka, S. Tarucha, J. A. Gupta, and D. G. Austing, *Two- and three-electron pauli spin blockade in series-coupled triple quantum dots*, Phys. Rev. Lett. **110**, 016803 (2013).

[258] D. Loss and D. P. DiVincenzo, *Quantum computation with quantum dots*, Phys. Rev. A **57**, 120–126 (1998).

[259] M. Pioro-Ladrière, T. Obata, Y. Tokura, Y.-S. Shin, T. Kubo, K. Yoshida, T. Taniyama, and S. Tarucha, *Electrically driven single-electron spin resonance in a slanting Zeeman field*, Nat. Phys **4**, 776–779 (2008).

[260] T. Takakura, M. Pioro-Ladrière, T. Obata, Y.-S. Shin, R. Brunner, K. Yoshida, T. Taniyama, and S. Tarucha, *Triple quantum dot device designed for three spin qubits*, Appl. Phys. Lett. **97**, 212104 (2010).

[261] M. Russ and G. Burkard, *Three-electron spin qubits*, J. Phys. Condens. Matter **29**, 393001 (2017).

[262] E. A. Laird, J. M. Taylor, D. P. DiVincenzo, C. M. Marcus, M. P. Hanson, and A. C. Gossard, *Coherent spin manipulation in an exchange-only qubit*, Phys. Rev. B **82**, 075403 (2010).

[263] L. Gaudreau, G. Granger, A. Kam, G. C. Aers, S. A. Studenikin, P. Zawadzki, M. Pioro-Ladrière, Z. R. Wasilewski, and A. S. Sachrajda, *Coherent control of three-spin states in a triple quantum dot*, Nat. Phys. **8**, 54–58 (2012).

[264] R. Sánchez, G. Granger, L. Gaudreau, A. Kam, M. Pioro-Ladrière, S. A. Studenikin, P. Zawadzki, A. S. Sachrajda, and G. Platero, *Long-range spin transfer in triple quantum dots*, Phys. Rev. Lett. **112**, 176803 (2014).

[265] J. Łuczak and B. R. Bułka, *Readout and dynamics of a qubit built on three quantum dots*, Phys. Rev. B **90**, 165427 (2014).

[266] J. Łuczak and B. R. Bułka, *Landau-Zener transitions in spin qubit encoded in three quantum dots*, Quantum Inf. Process. **16**, 10 (2016).

[267] A. K. Mitchell, T. F. Jarrold, and D. E. Logan, *Quantum phase transition in quantum dot trimers*, Phys. Rev. B **79**, 085124 (2009).

[268] M. Seo, H. K. Choi, S.-Y. Lee, N. Kim, Y. Chung, H.-S. Sim, V. Umansky, and D. Mahalu, *Charge frustration in a triangular triple quantum dot*, Phys. Rev. Lett. **110**, 046803 (2013).

[269] D. S. Saraga and D. Loss, *Spin-entangled currents created by a triple quantum dot*, Phys. Rev. Lett. **90**, 166803 (2003).

[270] J. Kondo, *Resistance minimum in dilute magnetic alloys*, Progress of Theoretical Physics **32**, 37–49 (1964).

[271] T. K. Ng and P. A. Lee, *On-site Coulomb repulsion and resonant tunneling*, Phys. Rev. Lett. **61**, 1768–1771 (1988).

[272] W. G. van der Wiel, S. D. Franceschi, T. Fujisawa, J. M. Elzerman, S. Tarucha, and L. P. Kouwenhoven, *The Kondo effect in the unitary limit*, Science **289**, 2105–2108 (2000).

[273] Z.-t. Jiang, Q.-f. Sun, and Y. Wang, *Kondo transport through serially coupled triple quantum dots*, Phys. Rev. B **72**, 045332 (2005).

[274] R. Žitko, J. Bonča, A. Ramšak, and T. Rejec, *Kondo effect in triple quantum dots*, Phys. Rev. B **73**, 153307 (2006).

[275] T. Numata, Y. Nisikawa, A. Oguri, and A. C. Hewson, *Kondo effects in a triangular triple quantum dot: numerical renormalization group study in the whole region of the electron filling*, Phys. Rev. B **80**, 155330 (2009).

[276] Y. Cheng, Y. Wang, J. Wei, Z. Zhu, and Y. Yan, *Long-range exchange interaction in triple quantum dots in the Kondo regime*, Phys. Rev. B **95**, 155417 (2017).

[277] R. López, T. Rejec, J. Martinek, and R. Žitko, *SU(3) Kondo effect in spinless triple quantum dots*, Phys. Rev. B **87**, 035135 (2013).

[278] E. Vernek, C. A. Büsser, G. B. Martins, E. V. Anda, N. Sandler, and S. E. Ulloa, *Kondo regime in triangular arrangements of quantum dots: molecular orbitals, interference, and contact effects*, Phys. Rev. B **80**, 035119 (2009).

[279] A. Oguri, S. Amaha, Y. Nishikawa, T. Numata, M. Shimamoto, A. C. Hewson, and S. Tarucha, *Kondo effects in a triangular triple quantum dot with lower symmetries*, Phys. Rev. B **83**, 205304 (2011).

[280] T. Kuzmenko, K. Kikoin, and Y. Avishai, *Magnetically Tunable Kondo-Aharonov-Bohm Effect in a Triangular Quantum Dot*, Phys. Rev. Lett. **96**, 046601 (2006).

[281] Y. Aharonov and D. Bohm, *Significance of electromagnetic potentials in the quantum theory*, Phys. Rev. **115**, 485–491 (1959).

[282] G. B. Arfken and H. J. Weber, *Mathematical Methods for Physicists (Seventh Edition)*, Seventh Edition (Academic Press, Boston, 2013).

[283] A. G. Aronov and Y. V. Sharvin, *Magnetic flux effects in disordered conductors*, Rev. Mod. Phys. **59**, 755–779 (1987).

[284] R. G. Chambers, *Shift of an electron interference pattern by enclosed magnetic flux*, Phys. Rev. Lett. **5**, 3–5 (1960).

[285] A. Tonomura, T. Matsuda, R. Suzuki, A. Fukuhara, N. Osakabe, H. Umezaki, J. Endo, K. Shinagawa, Y. Sugita, and H. Fujiwara, *Observation of Aharonov-Bohm Effect by Electron Holography*, Phys. Rev. Lett. **48**, 1443–1446 (1982).

[286] Y. V. Nazarov, *Quantum interference, tunnel junctions and resonant tunneling interferometer*, Phys. B **189**, 57 (1993).

[287] Y. Ji, Y. Chung, D. Sprinzak, M. Heiblum, D. Mahalu, and H. Shtrikman, *An electronic Mach-Zehnder interferometer*, Nature **422**, 415–418 (2003).

[288] A. Yacoby, M. Heiblum, D. Mahalu, and H. Shtrikman, *Coherence and phase sensitive measurements in a quantum dot*, Phys. Rev. Lett. **74**, 4047–4050 (1995).

[289] R. Schuster, E. Buks, M. Heiblum, D. Mahalu, V. Umansky, and H. Shtrikman, *Phase measurement in a quantum dot via a double-slit interference experiment*, Nature **385**, 417–420 (1995).

[290] C. W. Groth, B. Michaelis, and C. W. J. Beenakker, *Counting statistics of coherent population trapping in quantum dots*, Phys. Rev. B **74**, 125315 (2006).

[291] B. Michaelis, C. Emary, and C. W. J. Beenakker, *All-electronic coherent population trapping in quantum dots*, EPL **73**, 677–683 (2006).

[292] C. Pöltl, C. Emary, and T. Brandes, *Two-particle dark state in the transport through a triple quantum dot*, Phys. Rev. B **80**, 115313 (2009).

[293] C. Pöltl, C. Emary, and T. Brandes, *Spin-entangled two-particle dark state in quantum transport through coupled quantum dots*, Phys. Rev. B **87**, 045416 (2013).

[294] M. Busl, R. Sánchez, and G. Platero, *Control of spin blockade by AC magnetic fields in triple quantum dots*, Phys. Rev. B **81**, 121306 (2010).

[295] T. Kostyrko and B. R. Bułka, *Symmetry-controlled negative differential resistance effect in a triangular molecule*, Phys. Rev. B **79**, 075310 (2009).

[296] I. Weymann, B. R. Bułka, and J. Barnaś, *Dark states in transport through triple quantum dots: the role of cotunneling*, Phys. Rev. B **83**, 195302 (2011).

[297] A. Noiri, T. Takakura, T. Obata, T. Otsuka, T. Nakajima, J. Yoneda, and S. Tarucha, *Cotunneling spin blockade observed in a three-terminal triple quantum dot*, Phys. Rev. B **96**, 155414 (2017).

[298] M. Niklas, A. Trottmann, A. Donarini, and M. Grifoni, *Fano stability diagram of a symmetric triple quantum dot*, Phys. Rev. B **95**, 115133 (2017).

[299] B. R. Bułka, T. Kostyrko, and J. Łuczak, *Linear and nonlinear stark effect in a triangular molecule*, Phys. Rev. B **83**, 035301 (2011).

[300] A. J. Keller, J. S. Lim, D. Sánchez, R. López, S. Amasha, J. A. Katine, H. Shtrikman, and D. Goldhaber-Gordon, *Cotunneling drag effect in Coulomb-coupled quantum dots*, Phys. Rev. Lett. **117**, 066602 (2016).

[301] C. Flindt, T. Novotný, A. Braggio, M. Sassetti, and A.-P. Jauho, *Counting statistics of non-Markovian quantum stochastic processes*, Phys. Rev. Lett. **100**, 150601 (2008).

[302] A. Braggio, C. Flindt, and T. Novotný, *Non-Markovian signatures in the current noise of a charge qubit*, Phys. E **40**, 1745 –1747 (2008).

[303] S. Welack and Y. Yan, *Non-Markovian theory for the waiting time distributions of single electron transfers*, J. Chem. Phys. **131**, 114111 (2009).

[304] A. Erpenbeck, L. Götzendörfer, C. Schinabeck, and M. Thoss, *Hierarchical quantum master equation approach to charge transport in molecular junctions with time-dependent molecule-lead coupling strengths*, Eur. Phys. J. - Spec. Top. **227**, 1981–1994 (2019).

[305] C. Schinabeck, R. Härtle, and M. Thoss, *Hierarchical quantum master equation approach to electronic-vibrational coupling in nonequilibrium transport through nanosystems: reservoir formulation and application to vibrational instabilities*, Phys. Rev. B **97**, 235429 (2018).

Appendices

Time-derivatives in the interaction picture

The wavefunction, written in the interaction picture, has the time-derivative

$$
\begin{aligned}
i\frac{\partial}{\partial t}|\Psi_I(t)\rangle &= i\frac{d}{dt}\left[e^{iH_0t}|\psi(t)\rangle\right] && \text{(A.1)}\\
&= -H_0 e^{iH_0t}|\psi(t)\rangle + e^{iH_0t}H|\psi(t)\rangle && \text{(A.2)}\\
&= e^{iH_0t}\left[-H_0+H\right]e^{-iH_0t}e^{iH_0t}|\psi(t)\rangle && \text{(A.3)}\\
&= H_{T,I}(t)|\psi_I(t)\rangle, && \text{(A.4)}
\end{aligned}
$$

while general operators follow

$$
\begin{aligned}
\frac{d}{dt}O_I(t) &= \frac{d}{dt}\left(e^{iH_0t}O(t)e^{-iH_0t}\right) && \text{(A.5)}\\
&= iH_0e^{iH_0t}O(t)e^{-iH_0t} + e^{iH_0t}\dot{O}(t)e^{-iH_0t} - ie^{iH_0t}O(t)H_0e^{-iH_0t} && \text{(A.6)}\\
&= e^{iH_0t}\left(\dot{O} + i\left[H_0,\rho(t)\right]\right)e^{-iH_0t}. && \text{(A.7)}
\end{aligned}
$$

Master equation derivations

B.1 Bath-correlation functions

For $t < 0$, the electrodes are held separate and at equilibrium, so that the density matrix of electrode α follows the grand canonical ensemble:

$$\rho_\alpha = \frac{e^{-(H_\alpha - \mu_\alpha N_\alpha)/T_\alpha}}{\mathrm{Tr}_{B_\alpha}\left[e^{-(H_\alpha - \mu_\alpha N_\alpha)/T_\alpha}\right]}, \tag{B.1}$$

where $N_\alpha = \sum_{\mathbf{k}_\alpha} a^\dagger_{\mathbf{k}_\alpha} a_{\mathbf{k}_\alpha}$ is the corresponding particle number operator. As an explicit example, consider the the lesser bath-correlation function

$$G^<(\tau) = \mathrm{Tr}_B\left[\rho_B d^\dagger_I(t) d_I(t-\tau)\right] \tag{B.2}$$

$$= \sum_{\alpha\alpha'} \sum_{\mathbf{k}_\alpha, \mathbf{k}'_\alpha} t_{\mathbf{k}_\alpha} t^*_{\mathbf{k}'_\alpha} \mathrm{Tr}_B\left[\rho_B e^{iH_\alpha t} a^\dagger_{\mathbf{k}_\alpha} e^{-iH_\alpha t} e^{iH_{\alpha'} t} a_{\mathbf{k}'_\alpha} e^{-iH_{\alpha'}(t-\tau)}\right] \delta_{\alpha\alpha'}\delta_{\mathbf{k}_\alpha \mathbf{k}'_\alpha}, \tag{B.3}$$

where the $\delta_{\alpha\alpha'}$ and $\delta_{\mathbf{k}_\alpha \mathbf{k}'_\alpha}$ are inserted because different eigenstates of H_α are orthogonal. Applying these delta functions, we get

$$G^<(\tau) = \sum_\alpha \sum_{\mathbf{k}_\alpha} |t_{\mathbf{k}_\alpha}|^2 e^{i\varepsilon_{\mathbf{k}_\alpha}\tau} \mathrm{Tr}_{B_\alpha}\left[\rho_\alpha a^\dagger_{\mathbf{k}_\alpha} a_{\mathbf{k}_\alpha}\right] \tag{B.4}$$

$$= \sum_\alpha \sum_{\mathbf{k}_\alpha} |t_{\mathbf{k}_\alpha}|^2 e^{i\varepsilon_{\mathbf{k}_\alpha}\tau} \sum_{i_\alpha} \frac{\langle i_\alpha | e^{-(H_\alpha - \mu_\alpha N_\alpha)/T_\alpha} a^\dagger_{\mathbf{k}_\alpha} a_{\mathbf{k}_\alpha} | i_\alpha\rangle}{\langle i_\alpha | e^{-(H_\alpha - \mu_\alpha N_\alpha)/T_\alpha} | i_\alpha |\rangle} \tag{B.5}$$

In taking the trace in Eq.(B.5), we can simplify on the next line because each $|\mathbf{k}_\alpha\rangle$ can only be empty or occupied by one electron:

$$\begin{aligned}
G^<(\tau) &= \sum_\alpha \sum_{\mathbf{k}_\alpha} |t_{\mathbf{k}_\alpha}|^2 e^{i\varepsilon_{\mathbf{k}_\alpha}\tau} \left[\frac{\langle \mathbf{k}_\alpha | e^{-(\varepsilon_{\mathbf{k}_\alpha} - \mu_\alpha)/T_\alpha} a^\dagger_{\mathbf{k}_\alpha} a_{\mathbf{k}_\alpha} | \mathbf{k}_\alpha\rangle + \langle 0 | a^\dagger_{\mathbf{k}_\alpha} a_{\mathbf{k}_\alpha} | 0\rangle}{e^{-(\varepsilon_{\mathbf{k}_\alpha} - \mu_\alpha)/T_\alpha} + 1}\right] \\
&= \sum_\alpha \sum_{\mathbf{k}_\alpha} |t_{\mathbf{k}_\alpha}|^2 e^{i\varepsilon_{\mathbf{k}_\alpha}\tau} \frac{e^{-(\varepsilon_{\mathbf{k}_\alpha} - \mu_\alpha)/T_\alpha}}{e^{-(\varepsilon_{\mathbf{k}_\alpha} - \mu_\alpha)/T_\alpha} + 1} \\
&= \sum_\alpha \sum_{\mathbf{k}_\alpha} |t_{\mathbf{k}_\alpha}|^2 e^{i\varepsilon_{\mathbf{k}_\alpha}\tau} \frac{1}{e^{(\varepsilon_{\mathbf{k}_\alpha} - \mu_\alpha)/T_\alpha} + 1} \\
&= \sum_\alpha \sum_{\mathbf{k}_\alpha} |t_{\mathbf{k}_\alpha}|^2 e^{i\varepsilon_{\mathbf{k}_\alpha}\tau} n_F(\varepsilon_{\mathbf{k}_\alpha} - \mu_\alpha) \\
&= -i\Sigma^>(-\tau).
\end{aligned} \tag{B.6}$$

Likewise, the greater bath-correlation function is

$$\begin{aligned} G^{>}(\tau) &= \mathrm{Tr}_B\left[\rho_B d_I(t) d_I^\dagger(t-\tau)\right] \\ &= \sum_\alpha \sum_{\mathbf{k}_\alpha} |t_{\mathbf{k}_\alpha}|^2 e^{i\varepsilon_{\mathbf{k}_\alpha}\tau} \mathrm{Tr}_B\left[\rho_B a_{\mathbf{k}_\alpha} a_{\mathbf{k}_\alpha}^\dagger\right] \\ &= \sum_\alpha \sum_{\mathbf{k}_\alpha} |t_{\mathbf{k}_\alpha}|^2 e^{i\varepsilon_{\mathbf{k}_\alpha}\tau} \left[\frac{0 + \langle 0| a_{\mathbf{k}_\alpha} a_{\mathbf{k}_\alpha}^\dagger |0\rangle}{e^{-(\varepsilon_{\mathbf{k}_\alpha} - \mu_\alpha)/T_\alpha} + 1}\right] \\ &= \sum_\alpha \sum_{\mathbf{k}_\alpha} |t_{\mathbf{k}_\alpha}|^2 e^{i\varepsilon_{\mathbf{k}_\alpha}\tau} \frac{1}{e^{-(\varepsilon_{\mathbf{k}_\alpha} - \mu_\alpha)/T_\alpha} + 1} \\ &= \sum_\alpha \sum_{\mathbf{k}_\alpha} |t_{\mathbf{k}_\alpha}|^2 e^{i\varepsilon_{\mathbf{k}_\alpha}\tau} \left[1 - n_F(\varepsilon_{\mathbf{k}_\alpha} - \mu_\alpha)\right] \\ &= i\Sigma^{>}(\tau) \end{aligned} \tag{B.7}$$

In the final line of each, we have introduced the self-energies:

$$\Sigma^{<}(\tau) = i \sum_\alpha \sum_{\mathbf{k}_\alpha} |t_{\mathbf{k}_\alpha}|^2 e^{-i\varepsilon_{\mathbf{k}_\alpha}\tau} n_F(\varepsilon_{\mathbf{k}_\alpha} - \mu_\alpha) \tag{B.8}$$

$$\Sigma^{>}(\tau) = -i \sum_\alpha \sum_{\mathbf{k}_\alpha} |t_{\mathbf{k}_\alpha}|^2 e^{i\varepsilon_{\mathbf{k}_\alpha}\tau} \left[1 - n_F(\varepsilon_{\mathbf{k}_\alpha} - \mu_\alpha)\right]. \tag{B.9}$$

B.2 Self-energy calculations

In performing the self-energy integrals, we will rely on a clever integration technique:

$$\begin{aligned} \int_0^\infty d\tau\, e^{i\omega\tau} = \lim_{\eta\to 0^+} \int_0^\infty d\tau\, e^{i(\omega + i\eta)\tau} &= \lim_{\eta\to 0^+} \frac{i}{\omega + i\eta} \\ &= \lim_{\eta\to 0^+} \frac{i(\omega - i\eta)}{\omega^2 + \eta^2} = \lim_{\eta\to 0^+} \frac{ix}{\omega^2 + \eta^2} + \pi\delta(\omega), \end{aligned} \tag{B.10}$$

which in turn relies on the definition of the delta function [282]

$$\delta(\omega) = \lim_{\eta\to 0^+} \frac{\eta}{\omega^2 + \eta^2}. \tag{B.11}$$

We now have to evaluate four different types of self-energies. The first form of the lesser

self-energy in Eq.(2.37) is

$$\begin{aligned}\int_0^\infty d\tau\, e^{-i\omega_{mn}\tau}\Sigma_\alpha^<(\tau) &= i\sum_{\mathbf{k}_\alpha}|t_{\mathbf{k}_\alpha}|^2 n_F(\varepsilon_{\mathbf{k}_\alpha}-\mu_\alpha)\int_0^\infty d\tau\, e^{-i(\omega_{mn}+\varepsilon_{\mathbf{k}_\alpha})\tau}\\ &= i\sum_{\mathbf{k}_\alpha}|t_{\mathbf{k}_\alpha}|^2 n_F(\varepsilon_{\mathbf{k}_\alpha}-\mu_\alpha)\int_0^\infty d\tau\, e^{-i(\varepsilon_{\mathbf{k}_\alpha}-\omega_{nm})\tau}\\ &= i\sum_{\mathbf{k}_\alpha}|t_{\mathbf{k}_\alpha}|^2 n_F(\varepsilon_{\mathbf{k}_\alpha}-\mu_\alpha)\left[-\lim_{\eta\to0^+}\frac{i(\varepsilon_{\mathbf{k}_\alpha}-\omega_{nm})}{(\varepsilon_{\mathbf{k}_\alpha}-\omega_{nm})^2+\eta^2}+\pi\delta(\varepsilon_{\mathbf{k}_\alpha}-\omega_{nm})\right]\\ &= \lim_{\eta\to0^+}\sum_{\mathbf{k}_\alpha}\frac{|t_{\mathbf{k}_\alpha}|^2(\varepsilon_{\mathbf{k}_\alpha}-\omega)n_F(\omega-\mu_\alpha)}{(\omega-\varepsilon_{\mathbf{k}_\alpha})^2+\eta^2}+i\pi|t_{\omega_{nm}}|^2 n_F(\omega_{nm}-\mu_\alpha). \qquad \text{(B.12)}\end{aligned}$$

At this point, we assume that the system-electrode coupling strength is proportional to the number of available microstates corresponding to energy $\varepsilon_{\mathbf{k}_\alpha}$:

$$|t_{\mathbf{k}_\alpha}|^2 \to |t_{\mathbf{k}_\alpha}|^2\rho(\varepsilon_{\mathbf{k}_\alpha})\Delta\varepsilon_{\mathbf{k}_\alpha}. \qquad \text{(B.13)}$$

This assumption results in the Lamb shift,

$$\Delta_\alpha^<(\omega) = \lim_{\eta\to0^+}\sum_{\mathbf{k}_\alpha}\frac{|t_{\mathbf{k}_\alpha}|^2\rho(\varepsilon_{\mathbf{k}_\alpha})(\varepsilon_{\mathbf{k}_\alpha}-\omega)n_F(\omega-\mu_\alpha)}{(\omega-\varepsilon_{\mathbf{k}_\alpha})^2+\eta^2}\Delta\varepsilon_{\mathbf{k}_\alpha}, \qquad \text{(B.14)}$$

and system-electrode coupling,

$$\gamma^\alpha(\omega) = 2\pi|t_\omega|^2\rho(\omega), \qquad \text{(B.15)}$$

which combine for the lesser self-energy

$$\Sigma_\alpha^<(\omega) = \Delta_\alpha^<(\omega)+\frac{i}{2}\gamma^\alpha(\omega)n_F(\omega-\mu_\alpha). \qquad \text{(B.16)}$$

The self-energy in Eq.(B.12) is thus

$$\int_0^\infty d\tau\, e^{-i\omega_{mn}\tau}\Sigma_\alpha^<(\tau) = \Sigma_\alpha^<(\omega_{nm}). \qquad \text{(B.17)}$$

Similarly, the second form of the lesser self-energy is

$$\begin{aligned}\int_0^\infty d\tau\, e^{-i\omega_{mn}\tau}\Sigma_\alpha^<(\tau) &= i\sum_{\mathbf{k}_\alpha}|t_{\mathbf{k}_\alpha}|^2 n_F(\varepsilon_{\mathbf{k}_\alpha}-\mu_\alpha)\int_0^\infty d\tau\, e^{i(\varepsilon_{\mathbf{k}_\alpha}-\omega_{mn})\tau}\\ &= i\sum_{\mathbf{k}_\alpha}|t_{\mathbf{k}_\alpha}|^2 n_F(\varepsilon_{\mathbf{k}_\alpha}-\mu_\alpha)\left[\lim_{\eta\to0^+}\frac{i(\varepsilon_{\mathbf{k}_\alpha}-\omega_{nm})}{((\varepsilon_{\mathbf{k}_\alpha}-\omega_{nm})^2+\eta^2}+\pi\delta(\varepsilon_{\mathbf{k}_\alpha}-\omega_{nm})\right]\\ &= -\Delta_\alpha^<(\omega_{mn})+\frac{i}{2}\gamma^\alpha(\omega_{mn})n_F(\omega_{mn}-\mu_\alpha)\\ &= -\Sigma_\alpha^<(\omega_{mn})^*. \qquad \text{(B.18)}\end{aligned}$$

We turn now to the greater self-energies, which rely on the greater Lamb shift,

$$\Delta_\alpha^>(\omega) = \lim_{\eta\to 0^+} \sum_{\mathbf{k}_\alpha} \frac{|t_{\mathbf{k}_\alpha}|^2 \rho(\varepsilon_{\mathbf{k}_\alpha})(\varepsilon_{\mathbf{k}_\alpha} - \omega)[1 - n_F(\omega - \mu_\alpha)]}{(\omega - \varepsilon_{\mathbf{k}_\alpha})^2 + \eta^2} \Delta\varepsilon_{\mathbf{k}_\alpha}, \tag{B.19}$$

to create

$$\Sigma_\alpha^>(\omega) = -\Delta_\alpha^>(\omega) - \frac{i}{2}\gamma^\alpha(\omega)[1 - n_F(\omega - \mu_\alpha)]. \tag{B.20}$$

The first form is

$$\begin{aligned}
&\int_0^\infty d\tau\, e^{-i\omega_{mn}\tau}\Sigma_\alpha^>(-\tau) = -i\sum_{\mathbf{k}_\alpha} |t_{\mathbf{k}_\alpha}|^2[1 - n_F(\varepsilon_{\mathbf{k}_\alpha} - \mu_\alpha)] \int_0^\infty d\tau\, e^{-i(\omega_{mn} - \varepsilon_{\mathbf{k}_\alpha})\tau} \\
&= -i\sum_{\mathbf{k}_\alpha} |t_{\mathbf{k}_\alpha}|^2[1 - n_F(\varepsilon_{\mathbf{k}_\alpha} - \mu_\alpha)] \left[\lim_{\eta\to 0^+} \frac{i(\varepsilon_{\mathbf{k}_\alpha} - \omega_{mn})}{(\varepsilon_{\mathbf{k}_\alpha} - \omega_{mn})^2 + \eta^2} + \pi\delta(\varepsilon_{\mathbf{k}_\alpha} - \omega_{mn})\right] \\
&= \Delta_\alpha^>(\omega_{mn}) - \frac{i}{2}\gamma^\alpha(\omega_{mn})[1 - n_F(\omega_{mn} - \mu_\alpha)] \\
&= -\Sigma_\alpha^>(\omega_{mn})^*,
\end{aligned} \tag{B.21}$$

while the second is

$$\int_0^\infty d\tau\, e^{-i\omega_{mn}\tau}\Sigma_\alpha^>(-\tau) = \Sigma_\alpha^>(\omega_{nm}). \tag{B.22}$$

B.3 Calculating the Lamb shift

If the density of states in electrode α is constant, then we can transform the Lamb shifts to integrals. In the limit $\Delta\varepsilon_{\mathbf{k}_\alpha} \to 0$, the lesser Lamb shift, for example, is

$$\Delta_\alpha^<(\omega) = \frac{\gamma^\alpha}{2\pi} \lim_{\eta\to 0^+} \int_{\omega_{\min}}^{\omega_{\max}} d\varepsilon\, \frac{(\varepsilon - \omega)n_F(\omega - \mu_\alpha)}{(\omega - \varepsilon)^2 + \eta^2}, \tag{B.23}$$

while the greater Lamb shift is

$$\Delta_\alpha^>(\omega) = \frac{\gamma^\alpha}{2\pi} \lim_{\eta\to 0^+} \int_{\omega_{\min}}^{\omega_{\max}} d\varepsilon\, \frac{(\varepsilon - \omega)[1 - n_F(\omega - \mu_\alpha)]}{(\omega - \varepsilon)^2 + \eta^2}. \tag{B.24}$$

Here, the limits $\omega_{\max}$ and $\omega_{\min}$ are the energies of the band within which the density of states is constant. Although the limit in Eq.(B.23) and Eq.(B.24) implies that they diverge, they can in fact be evaluated numerically using Cauchy's principal value:

$$\int_b^a f(x)dx = \lim_{\eta\to 0^+} \left[\int_b^{0-\eta} f(x)dx + \int_{0+\eta}^a f(x)dx\right], \tag{B.25}$$

defined here for a general function that diverges $f(x) \to \pm\infty$ at $x = 0$, as it does for the Lamb shifts.

If we operate under the wide-band approximation, furthermore, $\omega_{textmax,min} \to \pm\infty$ and the Lamb shifts can be evaluated analytically:

$$\Delta_\alpha^<(\omega) = \frac{\gamma^\alpha}{2\pi} \lim_{\eta\to 0^+} \int_{-\infty}^{\infty} d\varepsilon \, \frac{(\varepsilon-\omega) n_F(\omega-\mu_\alpha)}{(\omega-\varepsilon)^2+\eta^2}, \tag{B.26}$$

$$\Delta_\alpha^>(\omega) = \frac{\gamma^\alpha}{2\pi} \lim_{\eta\to 0^+} \int_{-\infty}^{\infty} d\varepsilon \, \frac{(\varepsilon-\omega)[1-n_F(\omega-\mu_\alpha)]}{(\omega-\varepsilon)^2+\eta^2}, \tag{B.27}$$

Applying residue theory, the definition of the digamma function $\psi(x)$, defined in Eq.(C.43) and the limit $\eta \to 0^+$, these integrals reduce to

$$\Delta_\alpha^<(\omega) = \Re\left\{ \frac{\gamma^\alpha}{2\pi} \psi\left(n + \frac{1}{2} + \frac{i}{2\pi T_\alpha}(\omega-\mu_\alpha) \right) \right\}, \tag{B.28}$$

$$\Delta_\alpha^>(\omega) = -\Re\left\{ \frac{\gamma^\alpha}{2\pi} \psi\left(n + \frac{1}{2} + \frac{i}{2\pi T_\alpha}(\omega-\mu_\alpha) \right) \right\}. \tag{B.29}$$

We have skipped many steps in this derivation because evaluating these integrals is essentially the same process required for cotunneling rates, which we cover in extensive detail in Appendix C.2.

Transition rates - Anderson impurity

C.1 Sequential tunneling rates for an Anderson impurity

To demonstrate the calculation of the sequential rates, in this section we will explicitly calculate $\Gamma^{\alpha}_{\sigma 0}$ from the starting point of Eq.(2.63). For the contribution from electrode α, and to 1^{st}-order in H_T, we get

$$\Gamma^{\alpha}_{\sigma 0} = 2\pi \sum_{f_\alpha, i_\alpha} |\langle f_\alpha | \langle \sigma | H^{\alpha}_T | 0 \rangle | i_\alpha \rangle|^2 \, W^{\alpha}_{i_0} \delta(\varepsilon_{i_\alpha} - \varepsilon_\sigma). \tag{C.1}$$

The initial state is $|i_0\rangle = |i_\alpha\rangle|0\rangle$ and the final state is $|f_\sigma\rangle = |f_\alpha\rangle|\sigma\rangle = a^\dagger_\sigma a_{\mathbf{k}_\alpha}|i_0\rangle$. Since an electron may tunnel from any state in the electrode, the sum over final states is over $\mathbf{k}_\alpha$. Applying these two changes, and introducing the exact form of H^{α}_T, leaves us with

$$\Gamma^{\alpha}_{\sigma 0} = 2\pi \sum_{\mathbf{k}_\alpha} \sum_{i_\alpha} \sum_{\mathbf{k}'_\alpha} |t_{\mathbf{k}_\alpha}|^2 \left| \langle \mathbf{k}_\alpha | \langle 0 | a^\dagger_{\mathbf{k}_\alpha} a_\sigma a_{\mathbf{k}'_\alpha} a^\dagger_\sigma | 0 \rangle | i_\alpha \rangle \right|^2 W^{\alpha}_{i_0} \delta(\varepsilon_{\mathbf{k}_\alpha} - \varepsilon_\sigma) \tag{C.2}$$

$$= 2\pi \sum_{\mathbf{k}_\alpha} \sum_{i_\alpha} |t_{\mathbf{k}_\alpha}|^2 \left| \langle i_\alpha | \langle 0 | a^\dagger_{\mathbf{k}_\alpha} a_\sigma a_{\mathbf{k}_\alpha} a^\dagger_\sigma | 0 \rangle | i_\alpha \rangle \right|^2 W^{\alpha}_{i_0} \delta(\varepsilon_{\mathbf{k}_\alpha} - \varepsilon_\sigma) \tag{C.3}$$

$$= 2\pi \sum_{\mathbf{k}_\alpha} \sum_{i_\alpha} |t_{\mathbf{k}_\alpha}|^2 \left| \langle 0 | a_\sigma a^\dagger_\sigma | 0 \rangle \langle i_\alpha | a^\dagger_{\mathbf{k}_\alpha} a_{\mathbf{k}_\alpha} | i_\alpha \rangle \right|^2 W^{\alpha}_{i_0} \delta(\varepsilon_{\mathbf{k}_\alpha} - \varepsilon_\sigma) \tag{C.4}$$

Within the summation on the third line, $\langle 0 | a_\sigma a^\dagger_\sigma | 0 \rangle = 1$ and the remaining $|\langle \mathbf{k}_\alpha | a^\dagger_{\mathbf{k}_\alpha} a_{\mathbf{k}_\alpha} | \mathbf{k}_\alpha \rangle|^2 = 0$ or 1, since electrons obey the Pauli exclusion principle. Because we are treating the baths as energy and particle reservoirs, the thermal distribution is that of a grand canonical ensemble and we can perform the same simplification as we did in Eq.(B.6):

$$\sum_{i_\alpha} |\langle \mathbf{k}_\alpha | a^\dagger_{\mathbf{k}_\alpha} a_{\mathbf{k}_\alpha} | \mathbf{k}_\alpha \rangle|^2 W^{\alpha}_{i_0} = n_F(\varepsilon_{\mathbf{k}_\alpha} - \mu_\alpha). \tag{C.5}$$

The final step is to again make the same assumption about the tunnel coupling $|t_{\mathbf{k}_\alpha}|^2 \rightarrow$

$|t_{\mathbf{k}_\alpha}|^2\rho(\varepsilon_{\mathbf{k}_\alpha})\Delta\varepsilon_{\mathbf{k}_\alpha}$:

$$\Gamma^{\alpha}_{\sigma 0} = 2\pi \sum_{\mathbf{k}_\alpha} \Delta\varepsilon_{\mathbf{k}_\alpha} |t_{\mathbf{k}_\alpha}|^2 \rho(\varepsilon_{\mathbf{k}_\alpha}) n_F(\varepsilon_{\mathbf{k}_\alpha} - \mu_\alpha)\, \delta(\varepsilon_{\mathbf{k}_\alpha} - \varepsilon_\sigma) \tag{C.6}$$

$$= \gamma^\alpha \int_{-\infty}^{\infty} d\varepsilon\, n_F(\varepsilon - \mu_\alpha)\delta(\varepsilon - \varepsilon_\sigma) \tag{C.7}$$

$$= \gamma^\alpha n_F(\varepsilon_\sigma - \mu_\alpha), \tag{C.8}$$

where we are able to simplify by our standard assumption that the density of states in electrode α is constant within the conduction band and we have also taken the wideband limit. We keep these series of assumptions for all rates calculated from Fermi's generalized golden rule. To calculate $\Gamma^{\alpha}_{0\sigma}$, $\Gamma^{\alpha}_{2\sigma}$, and $\Gamma^{\alpha}_{\sigma 2}$, we apply the same process, with results already displayed in the main text in Eq.(4.3).

C.2 Cotunneling rates for an Anderson impurity

In this subsection we will demonstrate will demonstrate the elastic cotunneling rates with $\Gamma^{\alpha\alpha'}_{00}$, which denotes the transition rate of moving an electron from electrode α to electrode α' through an initially empty orbital. The initial many-body state is $|i_0\rangle = |0\rangle|i_\alpha\rangle|i_{\alpha'}\rangle$, with energy $E_{i_0} = \varepsilon_{\mathbf{k}_\alpha}$, and the final many-body state is $|f_0\rangle = |0\rangle|f_\alpha\rangle|f_{\alpha'}\rangle = a^\dagger_{\mathbf{k}'_\alpha} a_\sigma a^\dagger_\sigma a_{\mathbf{k}_\alpha}|i_0\rangle$ with energy $E_{f_0} = \varepsilon_{\mathbf{k}'_\alpha}$. Inserting the second term of the T-matrix expansion into Eq.(2.63), we get

$$\Gamma^{\alpha\alpha'}_{00} = 2\pi \lim_{\eta\to 0^+} \sum_{f_0, i_0} \left| \langle f_{\alpha'}|\langle f_\alpha|\langle 0|H_T^{\alpha'} \frac{1}{E_{i_0} - H_0 + i\eta} H_T^{\alpha}|0\rangle|i_\alpha\rangle|i_{\alpha'}\rangle \right|^2 W^{\alpha}_{i_0} W^{\alpha'}_{i_0}\, \delta(\varepsilon_{\mathbf{k}_\alpha} - \varepsilon_{\mathbf{k}'_\alpha}) \tag{C.9}$$

$$= 2\pi \lim_{\eta\to 0^+} \sum_{\mathbf{k}_\alpha, \mathbf{k}'_\alpha} \sum_{i_0} |t_{\mathbf{k}_\alpha}|^2 \left|t_{\mathbf{k}'_\alpha}\right|^2 W^{\alpha}_{i_0} W^{\alpha'}_{i_0}\, \delta(\varepsilon_{\mathbf{k}_\alpha} - \varepsilon_{\mathbf{k}'_\alpha}) \times$$

$$\left| \langle i_{\alpha'}|\langle i_\alpha|\langle 0|a^\dagger_{\mathbf{k}_\alpha} a_\sigma a^\dagger_\sigma a_{\mathbf{k}'_\alpha} a^\dagger_{\mathbf{k}'_\alpha} (a_\uparrow + a_\downarrow) \frac{1}{\varepsilon_{\mathbf{k}_\alpha} - H_0 + i\eta} (a^\dagger_\uparrow + a^\dagger_\downarrow) a_{\mathbf{k}_\alpha}|0\rangle|i_\alpha\rangle|i_{\alpha'}\rangle \right|^2. \tag{C.10}$$

In Eq.(C.10), we have explicitly written the interaction Hamiltonian to demonstrate that there are two tunneling pathways for this cotunneling process; a spin-$\uparrow$ or a spin-$\downarrow$ electron may tunnel into and out of the system. We have excluded, however, the summations from the interaction Hamiltonian, instead performing the sums over the two delta terms, $\delta_{\mathbf{k}_\alpha \mathbf{k}'_\alpha}$ and $\delta_{\mathbf{k}'_\alpha k'_{\alpha'}}$, implicitly.

In expanding the brackets, we can ignore the cross terms as the two spin states are orthogonal. To simplify, we apply the unperturbed Hamiltonian in the denominator:

$$H_0 a^\dagger_\sigma a_{\mathbf{k}_\alpha}|0\rangle|i_\alpha\rangle|i_{\alpha'}\rangle = \varepsilon_\sigma a^\dagger_\sigma a_{\mathbf{k}_\alpha}|0\rangle|i_\alpha\rangle|i_{\alpha'}\rangle, \tag{C.11}$$

and we can now separate all scalars and operators within the $|\ldots|^2$ part. Of the remaining

	E_1	E_2	$\pm$
$\Gamma_{00}^{\alpha\alpha'}$	$\varepsilon_\uparrow$	$\varepsilon_\downarrow$	$+$
$\Gamma_{\sigma\sigma}^{\alpha\alpha'}$	ε_σ	$\varepsilon_{\bar{\sigma}}+U$	$-$
$\Gamma_{22}^{\alpha\alpha'}$	$\varepsilon_\uparrow+U$	$\varepsilon_\downarrow+U$	$+$

Table C.1: Table of energies for elastic cotunneling rates of an Anderson impurity.

operators, we will now get two Fermi-Dirac functions, since

$$\sum_{i_0} W_{i_0}^{\alpha} \left|\langle i_\alpha | a_{\mathbf{k}_\alpha}^\dagger a_{\mathbf{k}_\alpha} | i_\alpha\rangle\right|^2 = n_F(\varepsilon_{\mathbf{k}_\alpha}-\mu_\alpha) \tag{C.12}$$

$$\sum_{i_0} W_{i_0}^{\alpha'} \left|\langle i_\alpha | a_{\mathbf{k}'_\alpha} a_{\mathbf{k}'_\alpha}^\dagger | i_\alpha\rangle\right|^2 = 1-n_F(\varepsilon_{\mathbf{k}'_\alpha}-\mu_{\alpha'}). \tag{C.13}$$

The resulting expression is much tidier,

$$\Gamma_{00}^{\alpha\alpha'} = 2\pi \lim_{\eta\to 0^+} \sum_{\mathbf{k}_\alpha,\mathbf{k}'_\alpha} |t_{\mathbf{k}_\alpha}|^2 |t_{\mathbf{k}'_\alpha}|^2 \left|\frac{1}{\varepsilon_{\mathbf{k}_\alpha}-\varepsilon_\uparrow+i\eta}+\frac{1}{\varepsilon_{\mathbf{k}_\alpha}-\varepsilon_\downarrow+i\eta}\right|^2 \times$$
$$n_F(\varepsilon_{\mathbf{k}_\alpha}-\mu_\alpha)[1-n_F(\varepsilon_{\mathbf{k}'_\alpha}-\mu_{\alpha'})]\,\delta(\varepsilon_{\mathbf{k}_\alpha}-\varepsilon_{\mathbf{k}'_\alpha}), \tag{C.14}$$

and after the same assumption about a constant density of states, the double summation becomes a double integral, which then reduces to one after the delta function is applied:

$$\Gamma_{00}^{\alpha\alpha'} = \frac{\gamma^\alpha\gamma^{\alpha'}}{2\pi}\lim_{\eta\to 0^+}\int_{-\infty}^{\infty}d\varepsilon_{\alpha'}\int_{-\infty}^{\infty}d\varepsilon_\alpha \left|\frac{1}{\varepsilon_\alpha-\varepsilon_\uparrow+i\eta}+\frac{1}{\varepsilon_\alpha-\varepsilon_\downarrow+i\eta}\right|^2 \times$$
$$n_F(\varepsilon_\alpha-\mu_\alpha)\left[1-n_F(\varepsilon_{\alpha'}-\mu_{\alpha'})\right]\,\delta(\varepsilon_\alpha-\varepsilon_{\alpha'}) \tag{C.15}$$
$$= \frac{\gamma^\alpha\gamma^{\alpha'}}{2\pi}\lim_{\eta\to 0^+}\int_{-\infty}^{\infty}d\varepsilon \left|\frac{1}{\varepsilon-\varepsilon_\uparrow+i\eta}+\frac{1}{\varepsilon-\varepsilon_\downarrow+i\eta}\right|^2 n_F(\varepsilon-\mu_\alpha)\left[1-n_F(\varepsilon-\mu_{\alpha'})\right]. \tag{C.16}$$

The other elastic cotunneling rates are similarly derived; they have the general formula

$$\Gamma_{mm}^{\alpha\alpha'} = \frac{\gamma^\alpha\gamma^{\alpha'}}{2\pi}\lim_{\eta\to 0^+}\int_{-\infty}^{\infty}d\varepsilon \left|\frac{1}{\varepsilon-E_1+i\eta}\pm\frac{1}{\varepsilon-E_2\pm i\eta}\right|^2 n_F(\varepsilon-\mu_\alpha)\left[1-n_F(\varepsilon-\mu_{\alpha'})\right], \tag{C.17}$$

where the E_1 and E_2 arise from the two different cotunneling pathways available to each rate. Elastic cotunneling through an initially doubly-occupied orbital, for example, can occur by a spin-$\uparrow$ electron tunneling out and then another spin-$\uparrow$ electron tunneling back in, resulting in $E_1=\varepsilon_\uparrow+U$, or a spin-$\downarrow$ electron tunneling out and then another spin-$\downarrow$ electron tunneling back in, resulting in $E_2=\varepsilon_\downarrow+U$. Elastic cotunneling through an orbital initially occupied by a spin-σ electron, on the other hand, has two distinct types of pathways. First, a spin-σ electron may tunnel out and then back in, resulting in $E_1=\varepsilon_\sigma$, or a spin-$\bar{\sigma}$ electron may tunnel in and then out, resulting in an extra negative and $E_2=\varepsilon_{\bar{\sigma}}+U$. These different results are displayed in Table (C.1).

We will next demonstrate the same calculation for the inelastic cotunneling rates, which are of the form $\Gamma^{\alpha\alpha'}_{\bar{\sigma}\sigma}$. For this cotunneling transition, the initial many-body state is $|i_\sigma\rangle = |\sigma\rangle|i_\alpha\rangle|i_{\alpha'}\rangle$ with energy $E_{i_\sigma} = \varepsilon_\sigma + \varepsilon_{\mathbf{k}_\alpha}$, and the final many-body state is $|f_{\bar{\sigma}}\rangle = |\bar{\sigma}\rangle|f_\alpha\rangle|f_{\alpha'}\rangle = a^\dagger_{\mathbf{k}'_\alpha} a_\sigma a^\dagger_{\bar{\sigma}} a_{\mathbf{k}_\alpha}|i_\sigma\rangle$, with energy $E_{f_{\bar{\sigma}}} = \varepsilon_{\bar{\sigma}} + \varepsilon_{\mathbf{k}'_\alpha}$. As with elastic cotunneling through an initially singly-occupied orbital, there are two pathways via which the cotunneling process can occur. First, a spin-σ electron can tunnel to electrode α' and then a spin-$\bar{\sigma}$ can tunnel from electrode α to replace it in the orbital, essentially applying $H_T^{\alpha'}$ then H_T^{α}, or a spin-$\bar{\sigma}$ electron can tunnel from electrode α to the orbital and then a spin-σ can tunnel from the orbital to electrode α', essentially applying H_T^{α} then $H_T^{\alpha'}$. With these two pathways in mind, the transition rate is

$$\Gamma^{\alpha\alpha'}_{\bar{\sigma}\sigma} = 2\pi \lim_{\eta\to 0^+} \sum_{\mathbf{k}_\alpha,\mathbf{k}'_\alpha} \sum_{i_\sigma} |t_{\mathbf{k}_\alpha}|^2 |t_{\mathbf{k}'_\alpha}|^2 W^\alpha_{i_\sigma} W^{\alpha'}_{i_\sigma} \delta(\varepsilon_{\mathbf{k}_\alpha} + \varepsilon_\sigma - \varepsilon_{\mathbf{k}'_\alpha} - \varepsilon_{\bar{\sigma}}) \times \left| \langle i_{\alpha'}|\langle i_\alpha|\langle\sigma| a^\dagger_{\mathbf{k}_\alpha} a^\dagger_\sigma a_{\bar{\sigma}} a_{\mathbf{k}'_\alpha} \left(a^\dagger_{\bar{\sigma}} a_{\mathbf{k}_\alpha} + a^\dagger_{\mathbf{k}'_\alpha} a_\sigma\right) \frac{1}{\varepsilon_{\mathbf{k}_\alpha} + \varepsilon_\sigma - H_0 + i\eta} \left(a^\dagger_{\bar{\sigma}} a_{\mathbf{k}_\alpha} + a^\dagger_{\mathbf{k}'_\alpha} a_\sigma\right) |\sigma\rangle|i_\alpha\rangle|i_{\alpha'}\rangle \right|^2 \tag{C.18}$$

$$= 2\pi \lim_{\eta\to 0^+} \sum_{\mathbf{k}_\alpha,\mathbf{k}'_\alpha} \sum_{i_\sigma} \|t_{\mathbf{k}_\alpha}|^2 |t_{\mathbf{k}'_\alpha}|^2 W^\alpha_{i_\sigma} W^{\alpha'}_{i_\sigma} \delta\left(\varepsilon_{\mathbf{k}'_\alpha} - (\varepsilon_{\mathbf{k}_\alpha} - \varepsilon_{\bar{\sigma}} + \varepsilon_\sigma)\right) \times \left| \langle i_{\alpha'}|\langle i_\alpha|\langle\sigma| a^\dagger_{\mathbf{k}_\alpha} a^\dagger_\sigma a_{\bar{\sigma}} a_{\mathbf{k}'_\alpha} \left[a^\dagger_{\bar{\sigma}} a_{\mathbf{k}_\alpha} \frac{1}{\varepsilon_{\mathbf{k}_\alpha} + \varepsilon_\sigma - (\varepsilon_{\mathbf{k}_\alpha} + \varepsilon_{\mathbf{k}'_\alpha}) + i\eta} a^\dagger_{\mathbf{k}'_\alpha} a_\sigma + a^\dagger_{\mathbf{k}'_\alpha} a_\sigma \frac{1}{\varepsilon_{\mathbf{k}_\alpha} + \varepsilon_\sigma - (\varepsilon_\sigma + \varepsilon_{\bar{\sigma}} + U) + i\eta} a^\dagger_{\bar{\sigma}} a_{\mathbf{k}_\alpha} \right] |\sigma\rangle|i_\alpha\rangle|i_{\alpha'}\rangle \right|^2 . \tag{C.19}$$

Following the same steps as in Eq.(C.10)-Eq.(C.14), we get

$$\Gamma^{\alpha\alpha'}_{\bar{\sigma}\sigma} = \frac{\gamma^\alpha \gamma^{\alpha'}}{2\pi} \lim_{\eta\to 0^+} \int_{-\infty}^{\infty} d\varepsilon \left| \frac{1}{\varepsilon - (\varepsilon_{\bar{\sigma}} + U) + i\eta} - \frac{1}{\varepsilon - \varepsilon_{\bar{\sigma}} - i\eta} \right|^2 n_F(\varepsilon - \mu_\alpha)\left[1 - n_F(\varepsilon - \mu_{\alpha'} + \varepsilon_\sigma - \varepsilon_{\bar{\sigma}})\right] \tag{C.20}$$

C.2.1 Regularizating the cotunneling rates

Although we now have computable expressions for the sequential tunneling rates in Eq.(C.8), the cotunneling rates in Eq.(C.17) and Eq.(C.20) are still in the form of an integral and a limit: unusable in practical calculations. If, furthermore, we were to naively perform the limit $\eta \to 0^+$ and then do the integrals, then the rates would clearly diverge due to poles at E_1 and E_2. To overcome this we follow the approach first developed by Averin [194], and extended to the T-matrix method by Turek and Matveev [197] and Koch and von Oppen [173, 196].

Inspecting the limit $\eta \to 0^+$, we see that it plays an important role in preventing the cotunneling integrals from diverging, as it shifts the pole away from the real axis and thus the contour of integration. From the theory of Fermi's generalized golden rule, this limit is due to

the interaction being turned on adiabatically, with rate η. The interaction time, and therefore the lifetime of the virtual level in cotunneling processes, is consequently $\mathcal{O}(\eta^{-1})$. Koch and von Oppen saw that, by including the finite lifetime, they could use residue theory to obtain analytic expressions for cotunneling rates, and it is their approach that we closely follow here [173, 196].

Before starting, we note that, because the interaction time should be proportional to the coupling strength $\eta \sim \gamma$, any terms in the cotunneling rate that are $\mathcal{O}(\eta^{-1})$ will combine with the $\gamma^{\alpha}\gamma^{\alpha'}$ prefactor to be $\mathcal{O}(\gamma)$ overall: the same order as sequential tunneling terms. These appear because every cotunneling process can be replicated by two sequential tunneling processes and the total rate overcounts these terms. The regularization procedure, as a result, is actually twofold; the second step is to identify and remove the overcounted sequential terms.

Once expanded, the general elastic cotunneling rate in Eq.(C.14) is

$$\begin{aligned}\Gamma^{\alpha\alpha'}_{mm} =& \frac{\gamma^{\alpha}\gamma^{\alpha'}}{2\pi}\lim_{\eta\to 0^+}\Bigg[\int_{-\infty}^{\infty} d\varepsilon \frac{1}{(\varepsilon - E_1)^2+\eta^2} n_F(\varepsilon-\mu_\alpha)[1-n_F(\varepsilon-\mu_{\alpha'})] \\ &+ \int_{-\infty}^{\infty} d\varepsilon \frac{1}{(\varepsilon - E_2)^2+\eta^2} n_F(\varepsilon-\mu_\alpha)[1-n_F(\varepsilon-\mu_{\alpha'})] \\ &\pm 2\Re\int_{-\infty}^{\infty} d\varepsilon \frac{1}{\varepsilon - E_1 + i\eta}\frac{1}{\varepsilon - E_2 - i\eta} n_F(\varepsilon-\mu_\alpha)[1-n_F(\varepsilon-\mu_{\alpha'})]\Bigg],\end{aligned} \tag{C.21}$$

which means we actually need to perform two different types of integrals. We will start with the squared terms, which are generally

$$\lim_{\eta\to 0^+}\lim_{R\to\infty}\int_{-R}^{R} dz G(z) = \lim_{\eta\to 0^+}\lim_{R\to\infty}\int_{-R}^{R} dz \frac{1}{z-E+i\eta}\frac{1}{z-E-i\eta} n_F(z-\mu_\alpha)[1-n_F(z-\mu_{\alpha'})], \tag{C.22}$$

once we replace $\varepsilon \to z$ to conform with residue theory notation and introduce the function $G(z)$ for the integrand. The contour of integration is along the real axis, but if we can add integration along a semicircle contour C_1, as shown in Fig.(C.1), then the total contour C is closed and we are able to use Cauchy's residue theorem to solve the integral:

$$\begin{aligned}\lim_{\eta\to 0^+}\lim_{R\to\infty}\int_{-R}^{R} G(z)\, dz &= \lim_{\eta\to 0^+}\lim_{R\to\infty}\left[\int_{-R}^{R} G(z)dz + \int_{C_1} G(z)dz\right] \\ &= \lim_{\eta\to 0^+}\int_{C} G(z)\, dz.\end{aligned} \tag{C.23}$$

This, of course, is only true if the contribution from C_1 disappears as $R \to \infty$; that is, if

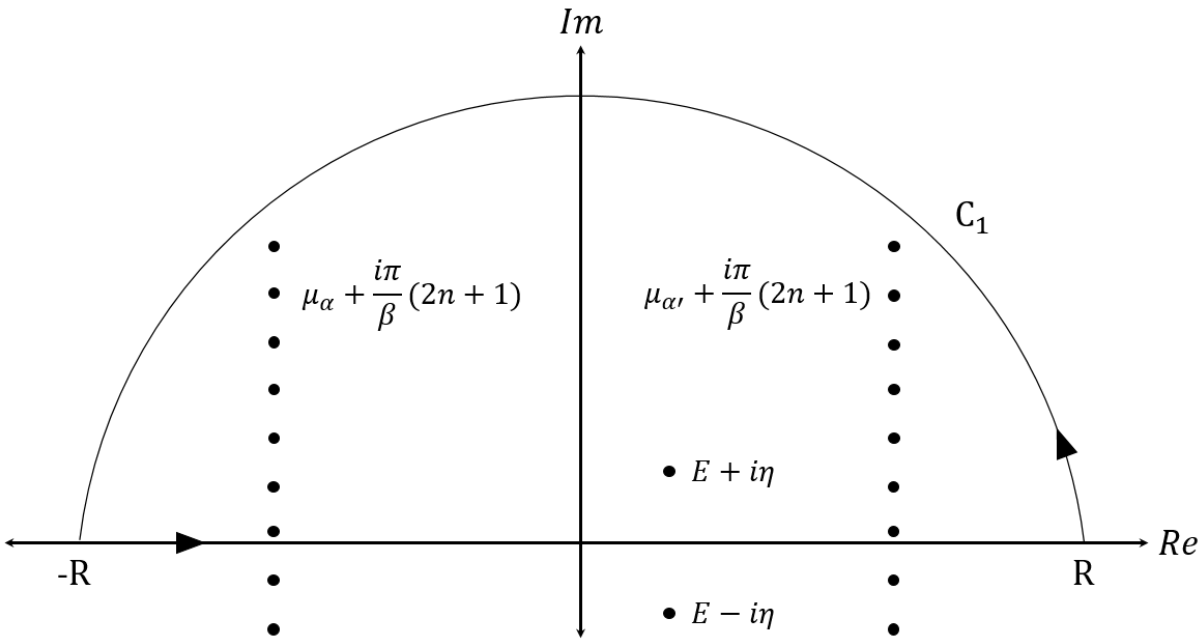

Figure C.1: Contour used for the integration in Eq.(C.22) with Matsubara poles included.

$\lim_{|z|\to\infty} zG(z) = 0$. In polar coordinates, where $z = Re^{i\theta}$, the limit is

$$\lim_{|z|\to\infty} z\,G(z) = \lim_{R\to\infty} \frac{Re^{i\theta}}{(Re^{i\theta}-E)^2+\eta^2} \frac{e^{\beta(Re^{i\theta}-\mu_{\alpha'})}}{(1+e^{\beta(Re^{i\theta}-\mu_\alpha)})(1+e^{\beta(Re^{i\theta}-\mu_{\alpha'})})} \tag{C.24}$$

$$\propto \lim_{R\to\infty} \frac{1}{Re^{R}} \tag{C.25}$$

$$= 0; \tag{C.26}$$

the condition is satisfied, and we are safe to use Cauchy's residue theorem. This states that, if integrating around a closed contour that is analytic everywhere inside except for a number of poles, the integral is

$$\int_C G(z)\,dz = 2\pi i \sum_{z^*} \mathrm{Res}(G(z), z^*), \tag{C.27}$$

where, for our contour, z^* are singularities in the upper half of the complex plane, and $\mathrm{Res}(G(z), z^*)$ is the residue of $G(z)$ at z^* [282].

The integrand in Eq.(C.22) has three sets of singularities, which we will discuss individually below.

1. The component $\frac{1}{(z-E)+i\eta}\frac{1}{(z-E)-i\eta}$ has simple poles at $z = E \pm i\eta$; however, only $z^* =$

$E + i\eta$ is in the upper half of the complex plane. The residue at $z^* = E + i\eta$ is

$$\begin{aligned}\mathrm{Res}(G(z), E+i\eta) &= \lim_{z\to E+i\eta} \frac{z-E-i\eta}{(z-E)-i\eta}\frac{1}{(z-E)+i\eta} n_F(z-\mu_\alpha)[1-n_F(z-\mu_{\alpha'})] \\ &= \frac{1}{2i\eta} n_F(E-\mu_\alpha+i\eta)[1-n_F(E-\mu_{\alpha'}+i\eta)]. \end{aligned} \tag{C.28}$$

2. The component $n_F(z-\mu_\alpha) = \frac{1}{e^{\beta(z-\mu_\alpha)}+1}$ has simple poles in the upper half of the complex plane when z solves the equation $\beta(z-\mu_\alpha) = i\pi(2n+1)$, where $n = 0, 1, 2, 3, \ldots$. These are the Matsubara frequencies, shown in Fig.(C.1):

$$z^*_{\alpha,n} = \frac{i\pi}{\beta}(2n+1) + \mu_\alpha. \tag{C.29}$$

The corresponding residue at $z^*_{\alpha,n}$ is

$$\mathrm{Res}(G(z), z^*_{\alpha,n}) = \lim_{z\to z^*_{\alpha,n}} \frac{z-\mu_\alpha-\frac{i\pi}{\beta}(2n+1)}{(z-E)^2+\eta^2} n_F(z-\mu_\alpha)[1-n_F(z-\mu_{\alpha'})] \tag{C.30}$$

$$= \frac{1}{(\frac{i\pi}{\beta}(2n+1)+\mu_\alpha-E)^2+\eta^2}[1-n_F(\frac{i\pi}{\beta}(2n+1)+\mu_\alpha-\mu_{\alpha'})]$$

$$\times \lim_{z\to z^*_{\alpha,n}} \frac{z-\mu_\alpha-\frac{i\pi}{\beta}(2n+1)}{e^{(z-\mu_\alpha)\beta}+1} \tag{C.31}$$

$$= \frac{1}{(\frac{i\pi}{\beta}(2n+1)+\mu_\alpha-E)^2+\eta^2}[1-\frac{1}{e^{i\pi(2n+1)}e^{\mu_\alpha-\mu_{\alpha'}}+1}] \lim_{z\to z^*_{\alpha,n}} \frac{1}{\beta e^{(z-\mu_\alpha)\beta}} \tag{C.32}$$

$$= -\frac{1}{\beta}\frac{1}{(\frac{i\pi}{\beta}(2n+1)+\mu_\alpha-E)^2+\eta^2}[1+n_B(\mu_\alpha-\mu_{\alpha'})] \tag{C.33}$$

$$= \frac{1}{\beta}\frac{1}{(\frac{i\pi}{\beta}(2n+1)+\mu_\alpha-E)^2+\eta^2} n_B(\mu_{\alpha'}-\mu_\alpha), \tag{C.34}$$

where we have applied L'Hôpital's rule [282] to simplify the limit; introduced the Bose-Einstein distribution,

$$n_B(\mu_\alpha-\mu_{\alpha'}) = \frac{1}{e^{(\mu_\alpha-\mu_{\alpha'})}-1}; \tag{C.35}$$

and then used the self-evident relation $1 + n_B(\mu_\alpha - \mu_{\alpha'}) = -n_B(\mu_\alpha - \mu_{\alpha'})$.

3. Similarly, the component $1 - n_F(z-\mu_{\alpha'})$ has simple poles in the upper half plane at

$$z^*_{\alpha',n} = \frac{i\pi}{\beta}(2n+1) + \mu_{\alpha'}, \tag{C.36}$$

and the corresponding residues are

$$\begin{aligned}\mathrm{Res}(G(z), z^*_{\alpha',n}) &= \frac{1}{\beta}\frac{1}{(\frac{i\pi}{\beta}(2n+1)+\mu_{\alpha'}-E)^2+\eta^2}[n_F(\frac{i\pi}{\beta}(2n+1)+\mu_{\alpha'}-\mu_\alpha)] \\ &= -\frac{1}{\beta}\frac{1}{(\frac{i\pi}{\beta}(2n+1)+\mu_{\alpha'}-E)^2+\eta^2}n_B(\mu_{\alpha'}-\mu_\alpha). \end{aligned} \tag{C.37}$$

Now that we have the residues at all singularities within the contour, the integral is

$$\begin{aligned}\lim_{\eta\to 0^+}\int_C G(z)\,dz &= \lim_{\eta\to 0^+} 2\pi i\Bigg[\mathrm{Res}(G(z), E+i\eta) + \sum_{n=0}^{\infty}\mathrm{Res}(G(z), \frac{i\pi}{\beta}(2n+1)+\mu_\alpha) \\ &\quad + \sum_{n=0}^{\infty}\mathrm{Res}(G(z), \frac{i\pi}{\beta}(2n+1)+\mu_{\alpha'})\Bigg] \end{aligned} \tag{C.38}$$

$$\begin{aligned} &= \Bigg[\frac{\pi}{\eta}n_F(E-\mu_\alpha+i\eta)[1-n_F(E-\mu_{\alpha'}+i\eta)] + \frac{2\pi i}{\beta}n_B(\mu_{\alpha'}-\mu_\alpha)\times \\ &\left(\sum_{n=0}^{\infty}\frac{1}{(\frac{i\pi}{\beta}(2n+1)+\mu_\alpha-E)^2+\eta^2} - \frac{1}{(\frac{i\pi}{\beta}(2n+1)+\mu_{\alpha'}-E)^2+\eta^2}\right)\Bigg]. \end{aligned} \tag{C.39}$$

In the first term, the imaginary $i\eta$ will contribute an oscillatory part to the Fermi-Dirac functions in the limit $\eta \to 0^+$. The overall order of this term, then, is $\mathcal{O}(\eta^{-1})$: exactly the sequential overcounting that we must remove to complete the regularization. The integral from Eq.(C.22) thus reduces to

$$\lim_{\eta\to 0^+}\lim_{R\to\infty}\int_{-R}^{R} dz G(z) = \frac{2\pi i}{\beta}n_B(\mu_{\alpha'}-\mu_\alpha)\sum_{n=0}^{\infty}\frac{1}{(\frac{i\pi}{\beta}(2n+1)+\mu_\alpha-E)^2} - \frac{1}{(\frac{i\pi}{\beta}(2n+1)+\mu_{\alpha'}-E)^2} \tag{C.40}$$

$$= -\frac{i\beta}{2\pi}n_B(\mu_{\alpha'}-\mu_\alpha)\sum_{n=0}^{\infty}\frac{1}{\left(n+\frac{1}{2}+\frac{i\beta}{2\pi}(E-\mu_\alpha)\right)^2} - \frac{1}{\left(n+\frac{1}{2}+\frac{i\beta}{2\pi}(E-\mu_{\alpha'})\right)^2}. \tag{C.41}$$

Although the series in Eq.(C.41) converges, and we could thus evaluate it numerically, we will introduce the polygamma functions so as to obtain a more compact form:

$$\psi^{(n)}(z) = \frac{d^{n+1}}{dz^{n+1}}\ln\Gamma(z), \tag{C.42}$$

where $\Gamma(z)$ is the standard gamma function. We will specifically use the digamma function,

$$\psi(z) = \frac{d}{dz}\ln\Gamma(z) = -\sum_{n=0}^{\infty}\frac{1}{n+z}, \tag{C.43}$$

and trigamma function,

$$\psi^{(1)}(z) = \frac{d^2}{dz^2}\ln\Gamma(z) = \sum_{n=0}^{\infty}\frac{1}{(n+z)^2}. \tag{C.44}$$

The result in Eq.(C.41) now simplifies to

$$\lim_{\eta\to 0^+}\lim_{R\to\infty}\int_{-R}^{R} dz \frac{1}{z-E+i\eta}\frac{1}{z-E-i\eta} n_F(z-\mu_\alpha)[1-n_F(z-\mu_{\alpha'})] = \frac{\beta}{2\pi} n_B(\mu_{\alpha'}-\mu_\alpha)\Im\left\{\psi^{(1)}\left(\frac{1}{2}+\frac{i\beta}{2\pi}(E-\mu_\alpha)\right)-\psi^{(1)}\left(\frac{1}{2}+\frac{i\beta}{2\pi}(E-\mu_{\alpha'})\right)\right\}. \tag{C.45}$$

In treating the second type of integral in Eq.(C.21), which has the integrand

$$P(z) = \frac{1}{z-E_1+i\eta}\frac{1}{z-E_2-i\eta} n_F(z-\mu_\alpha)[1-n_F(z-\mu_{\alpha'})], \tag{C.46}$$

we will use a similar approach. Applying the same contour as in Fig.(C.1), the integral becomes

$$\pm 2\Re\lim_{\eta\to 0^+}\lim_{R\to\infty}\int_{-R}^{R} dz\, P(z) = \pm 2\Re\lim_{\eta\to 0^+}\int_C dz\, P(z). \tag{C.47}$$

Within the contour, there are, again, a set of singularities arising from the Matsubara frequencies, Eq.(C.29) and Eq.(C.36), and also one at $z^* = E_2 + i\eta$. Using the same theory as before, we get

$$\pm 2\Re\left\{\lim_{\eta\to 0^+}\int_C dz\, P(z) = \pm 2\Re\lim_{\eta\to 0^+} 2\pi i\left[\mathrm{Res}(P(z), E_2+i\eta) + \sum_{n=0}^{\infty}\mathrm{Res}(P(z), \frac{i\pi}{\beta}(2n+1)+\mu_\alpha) + \sum_{n=0}^{\infty}\mathrm{Res}(P(z), \frac{i\pi}{\beta}(2n+1)+\mu_{\alpha'})\right]\right\} \tag{C.48}$$

$$= \pm 2\Re\left\{\lim_{\eta\to 0^+} 2\pi i\left[n_F(E_2-\mu_\alpha+i\eta)[1-n_F(E_2-\mu_{\alpha'}+i\eta)\frac{1}{E_2-E_1+2i\eta} + \frac{1}{\beta} n_B(\mu_{\alpha'}-\mu_\alpha)\sum_{n=0}^{\infty}\frac{1}{\mu_\alpha-E_1+\frac{i\pi}{\beta}(2n+1)+i\eta}\frac{1}{\mu_\alpha-E_2+\frac{i\pi}{\beta}(2n+1)+i\eta} - \frac{1}{\mu_{\alpha'}-E_1+\frac{i\pi}{\beta}(2n+1)+i\eta}\frac{1}{\mu_{\alpha'}-E_2+\frac{i\pi}{\beta}(2n+1)+i\eta}\right]\right\}. \tag{C.49}$$

After applying the limit $\eta \to 0^+$ we can ignore any imaginary components and also write the

summation terms using partial fractions:

$$\pm 2\Re\left\{\lim_{\eta\to 0^+}\lim_{R\to\infty}\int_{-R}^{R} dz\, P(z)\right\} = \pm\frac{1}{E_1-E_2}n_B(\mu_{\alpha'}-\mu_\alpha)\Re\left\{\sum_{n=0}^{\infty}\left[\frac{1}{n+\frac{1}{2}+\frac{i\beta}{2\pi}(E_1-\mu_\alpha)}-\right.\right.$$
$$\left.\left.\frac{1}{n+\frac{1}{2}+\frac{i\beta}{2\pi}(E_2-\mu_\alpha)}-\frac{1}{n+\frac{1}{2}+\frac{i\beta}{2\pi}(E_1-\mu_{\alpha'})}+\frac{1}{n+\frac{1}{2}+\frac{i\beta}{2\pi}(E_2-\mu_{\alpha'})}\right]\right\}$$
$$= \pm\frac{1}{E_1-E_2}n_B(\mu_{\alpha'}-\mu_\alpha)\Re\left\{\psi\left(\frac{1}{2}+\frac{i\beta}{2\pi}(E_2-\mu_\alpha)\right)-\right.$$
$$\left.\psi\left(\frac{1}{2}+\frac{i\beta}{2\pi}(E_1-\mu_\alpha)\right)-\psi\left(\frac{1}{2}+\frac{i\beta}{2\pi}(E_2-\mu_{\alpha'})\right)+\psi\left(\frac{1}{2}+\frac{i\beta}{2\pi}(E_1-\mu_{\alpha'})\right)\right\}. \quad \text{(C.50)}$$

With the regularized expressions for the two integral types in Eq.(C.45) and Eq.(C.50), we can construct transition rates for all cotunneling processes. Combining these expressions with the overall rate in Eq.(C.21), for example, gives us the expression for a general elastic cotunneling rate,

$$\Gamma^{\alpha\alpha'}_{mm} = \gamma^\alpha\gamma^{\alpha'}n_B(\mu_{\alpha'}-\mu_\alpha)\left[\frac{\beta}{4\pi^2}\Im\left\{\psi^{(1)}\left(\frac{1}{2}+\frac{i\beta}{2\pi}(E_1-\mu_\alpha)\right)-\psi^{(1)}\left(\frac{1}{2}+\frac{i\beta}{2\pi}(E_1-\mu_{\alpha'})\right)\right.\right.$$
$$\left.+\psi^{(1)}\left(\frac{1}{2}+\frac{i\beta}{2\pi}(E_2-\mu_\alpha)\right)-\psi^{(1)}\left(\frac{1}{2}+\frac{i\beta}{2\pi}(E_2-\mu_{\alpha'})\right)\right\}$$
$$\pm\frac{1}{\pi(E_1-E_2)}\Re\left\{\psi\left(\frac{1}{2}+\frac{i\beta}{2\pi}(E_2-\mu_\alpha)\right)-\psi\left(\frac{1}{2}+\frac{i\beta}{2\pi}(E_1-\mu_\alpha)\right)\right.$$
$$\left.\left.-\psi\left(\frac{1}{2}+\frac{i\beta}{2\pi}(E_2-\mu_{\alpha'})\right)+\psi\left(\frac{1}{2}+\frac{i\beta}{2\pi}(E_1-\mu_{\alpha'})\right)\right\}\right], \quad \text{(C.51)}$$

and the general inelastic cotunneling rate:

$$\Gamma^{\alpha\alpha'}_{\bar\sigma\sigma} = \gamma^\alpha\gamma^{\alpha'}n_B(\mu_{\alpha'}-\mu_\alpha-\varepsilon_\sigma+\varepsilon_{\bar\sigma})\left[\frac{\beta}{4\pi^2}\Im\left\{\psi^{(1)}\left(\frac{1}{2}+\frac{i\beta}{2\pi}(\varepsilon_{\bar\sigma}+U-\mu_\alpha)\right)\right.\right.$$
$$\left.-\psi^{(1)}\left(\frac{1}{2}+\frac{i\beta}{2\pi}(\varepsilon_\sigma+U-\mu_{\alpha'})\right)+\psi^{(1)}\left(\frac{1}{2}+\frac{i\beta}{2\pi}(\varepsilon_{\bar\sigma}-\mu_\alpha)\right)-\psi^{(1)}\left(\frac{1}{2}+\frac{i\beta}{2\pi}(\varepsilon_\sigma-\mu_{\alpha'})\right)\right\}$$
$$\pm\frac{1}{\pi U}\Re\left\{\psi\left(\frac{1}{2}+\frac{i\beta}{2\pi}(\varepsilon_{\bar\sigma}-\mu_\alpha)\right)-\psi\left(\frac{1}{2}+\frac{i\beta}{2\pi}(\varepsilon_{\bar\sigma}+U-\mu_\alpha)\right)-\psi\left(\frac{1}{2}+\frac{i\beta}{2\pi}(\varepsilon_\sigma-\mu_{\alpha'})\right)\right.$$
$$\left.\left.+\psi\left(\frac{1}{2}+\frac{i\beta}{2\pi}(\varepsilon_\sigma+U-\mu_{\alpha'})\right)\right\}\right]. \quad \text{(C.52)}$$

C.2.2 Cotunneling through a SRL

We can derive elastic cotunneling rates through a SRL similarly, albeit more easily, to those from the Anderson impurity:

$$\Gamma^{\alpha\alpha'}_{mm} = \beta\frac{\gamma^{\alpha}\gamma^{\alpha'}}{4\pi^2}n_B(\mu_{\alpha'}-\mu_{\alpha})\Im\left\{\psi^{(1)}\left(\frac{1}{2}+\frac{i\beta}{2\pi}(\varepsilon-\mu_{\alpha})\right)-\psi^{(1)}\left(\frac{1}{2}+\frac{i\beta}{2\pi}(\varepsilon-\mu_{\alpha'})\right)\right\}. \quad \text{(C.53)}$$

Because a SRL has no excited states, it has no inelastic transitions and the corresponding rate equation is equally trivial:

$$\mathbf{L}(\chi) = \begin{bmatrix} -\Gamma_{10}+\Gamma^{SD}_{00}(e^{i\chi}-1) & \Gamma^{S}_{01}+\Gamma^{D}_{01}e^{i\chi} \\ +\Gamma^{DS}_{00}(e^{-i\chi}-1) & \\ \Gamma^{S}_{10}+\Gamma^{D}_{10}e^{-i\chi} & -\Gamma_{01}+\Gamma^{SD}_{11}(e^{i\chi}-1) \\ & +\Gamma^{DS}_{11}(e^{-i\chi}-1) \end{bmatrix}. \quad \text{(C.54)}$$

Transition rates - Holstein model

This appendix is devoted to deriving the sequential tunneling transition rates for the Holstein model. We first diagonalize the Holstein Hamiltonian using the Lang-Firsov transformation, and then explicitly demonstrate how to calculate the transition rates, including the Franck-Condon factor.

D.1 Lang-Firsov transformation

We first define the operator

$$S = -\frac{\lambda}{\omega}(b^\dagger - b)a^\dagger a, \tag{D.1}$$

and then use it to transform all operators:

$$\tilde{O} = e^S O e^{-S}. \tag{D.2}$$

At this point, we need to use one of the Baker-Campbell-Hausdorf formulae [282]:

$$e^A B e^{-A} = B + [A,B] + \frac{1}{2!}[A,[A,B]] + \frac{1}{3!}[A,[A,[A,B]]] + \ldots \tag{D.3}$$

$$= \sum_{m=0}^{\infty} \frac{1}{m!}[A,B]_m\,, \tag{D.4}$$

which we will now quickly prove. To start, we will use the function

$$G(x) = e^{xA} B e^{-xA} \tag{D.5}$$

$$= \left[1 + xA + \frac{1}{2!}(xA)^2 + \ldots\right] B \left[1 - xA + \frac{1}{2!}(xA)^2 + \ldots\right] \tag{D.6}$$

$$= \sum_{n=0}^{\infty} \frac{G_m}{m!} x^m. \tag{D.7}$$

To prove Eq.(D.3), we obviously need $G(1)$. First, we differentiate Eq.(D.5) and Eq.(D.7),

$$[A, G(x)] = \sum_{m=1}^{\infty} \frac{G_m}{(m-1)!} x^{n-1} \tag{D.8}$$

$$\sum_{m=0}^{\infty} \frac{1}{m!} [A, G_m] x^m = \sum_{m=1}^{\infty} \frac{G_m}{(m-1)!} x^{m-1} \tag{D.9}$$

$$\sum_{m=1}^{\infty} \frac{1}{(m-1)!} [A, G_{m-1}] x^{m-1} = \sum_{m=1}^{\infty} \frac{G_m}{(m-1)!} x^{m-1}, \tag{D.10}$$

and equate coefficients to obtain the recursion relation $G_n = [A, G_{n-1}]$. Examining Eq.(D.6), we see that the first term of the expansion is B and, setting $x = 1$ in $G(x)$, the Taylor expansion in Eq.(D.7) becomes Eq.(D.3).

With the Baker-Campbell-Hausdorf formula, we can start applying the canonical transformation in Eq.(D.2) to operators. First, the fermionic annihilation and creation operators become

$$\begin{aligned}
\tilde{a} &= e^S a e^{-S} & \tilde{a}^\dagger &= e^S a^\dagger e^{-S} \\
&= \sum_{m=0}^{\infty} \frac{\left(-\frac{\lambda}{\omega}\right)^m (b^\dagger - b)^m}{m!} \left[a^\dagger a, a\right]_m & &= \sum_{m=0}^{\infty} \frac{\left(-\frac{\lambda}{\omega}\right)^m (b^\dagger - b)^m}{m!} \left[a^\dagger a, a^\dagger\right]_m \\
&= \sum_{m=0}^{\infty} \frac{\left(-\frac{\lambda}{\omega}\right)^m (b^\dagger - b)^m}{m!} (-1)^m a & &= \sum_{m=0}^{\infty} \frac{\left(-\frac{\lambda}{\omega}\right)^m (b^\dagger - b)^m}{m!} a^\dagger \\
&= a e^{-\frac{\lambda}{\omega}(b - b^\dagger)} & &= a^\dagger e^{\frac{\lambda}{\omega}(b - b^\dagger)},
\end{aligned} \tag{D.11}$$

from which we can see that the particle number operator remains unchanged: $\tilde{a}^\dagger \tilde{a} = a^\dagger a$.

The bosonic annihilation and creation operators, meanwhile, become

$$\begin{aligned}
\tilde{b} &= e^S b e^{-S} \\
&= \sum_{m=0}^{\infty} \frac{\left(-\frac{\lambda}{\omega}\right)^m (a^\dagger a)^m}{m!} \left[b^\dagger - b, b\right]_m \\
&= b - a^\dagger a \frac{\lambda}{\omega} \left[b^\dagger - b, b\right] + \frac{(a^\dagger a)^2}{2} \left(\frac{\lambda}{\omega}\right)^2 \left[b^\dagger - b, \left[b^\dagger - b, b\right]\right] + \dots \\
&= b + \frac{\lambda}{\omega} a^\dagger a
\end{aligned} \tag{D.12}$$

and

$$\begin{aligned}\tilde{b}^\dagger &= e^S b^\dagger e^{-S} \\ &= \sum_{m=0}^{\infty} \frac{\left(-\frac{\lambda}{\omega}\right)^m (a^\dagger a)^m}{m!} \left[b^\dagger - b, b^\dagger\right]_m \\ &= b^\dagger - a^\dagger a \frac{\lambda}{\omega}\left[b^\dagger - b, b^\dagger\right] + \frac{(a^\dagger a)^2}{2}\left(\frac{\lambda}{\omega}\right)^2 \left[b^\dagger - b, \left[b^\dagger - b, b^\dagger\right]\right] + \dots \\ &= b^\dagger + \frac{\lambda}{\omega} a^\dagger a, \end{aligned} \tag{D.13}$$

where we have used the canonical commutation relations of bosonic operators. Applying the transformed operators, the Holstein Hamiltonian becomes

$$\begin{aligned}\tilde{H}_Q &= \varepsilon_0 \tilde{a}^\dagger \tilde{a} + \lambda\left(\tilde{b}^\dagger + \tilde{b} - 2\frac{\lambda}{\omega}\tilde{a}^\dagger\tilde{a}\right)\tilde{a}^\dagger\tilde{a} + \omega\left(\tilde{b}^\dagger - \frac{\lambda}{\omega}\tilde{a}^\dagger\tilde{a}\right)\left(\tilde{b} - \frac{\lambda}{\omega}\tilde{a}^\dagger\tilde{a}\right) \\ &= \varepsilon \tilde{a}^\dagger\tilde{a} + \omega \tilde{b}^\dagger \tilde{b}, \end{aligned} \tag{D.14}$$

where the polaron shifted energy is $\varepsilon = \varepsilon_0 - \frac{\lambda^2}{\omega}$.

Likewise, under the transformation, the interaction Hamiltonian becomes

$$\tilde{H}_T = \sum_{\alpha=\{S,D\}} \sum_{\mathbf{k}_\alpha} t_{\mathbf{k}_\alpha} \left(\tilde{a}^\dagger_{\mathbf{k}_\alpha} \tilde{a}\, e^{-\frac{\lambda}{\omega}(\tilde{b}^\dagger - \tilde{b})} + \tilde{a}^\dagger \tilde{a}_{\mathbf{k}_\alpha} e^{\frac{\lambda}{\omega}(\tilde{b}^\dagger - \tilde{b})}\right). \tag{D.15}$$

Evidently, bath operators remain unchanged under the Lang-Firsov transformation, so that $\tilde{H}_\alpha = H_\alpha$.

D.2 Sequential tunneling rates for the Holstein model

With the diagonalized Hamiltonians in Eq.(D.14) and Eq.(D.15), we can now compute, using Fermi's generalized golden rule, the sequential tunneling transition rates between eigenstates of the Holstein Hamiltonian. For $\Gamma^\alpha_{1q';0q}$, the initial state is $|i_0\rangle = |0\rangle|q\rangle|i_\alpha\rangle$ with energy $E_i = \omega q + \varepsilon_{\mathbf{k}_\alpha}$, while the final state is $|f_1\rangle = \tilde{a}_{\mathbf{k}_\alpha}|1\rangle|q'\rangle|i_\alpha\rangle$ with energy $E_f = \varepsilon + \omega q'$. The rate, from the starting point of Eq.(2.63), is then

$$\begin{aligned}\Gamma^\alpha_{\sigma 0} &= 2\pi \sum_{\mathbf{k}_\alpha}\sum_{i_\alpha} |t_{\mathbf{k}_\alpha}|^2 \left|\langle i_\alpha|\langle q'|\langle 1|\tilde{a}^\dagger_{\mathbf{k}_\alpha}\tilde{a}_{\mathbf{k}_\alpha}\tilde{a}^\dagger e^{\frac{\lambda}{\omega}(\tilde{b}^\dagger - \tilde{b})}|0\rangle|q\rangle|i_\alpha\rangle\right|^2 W^\alpha_{i_0}\delta\left(\varepsilon_{\mathbf{k}_\alpha} - (\varepsilon - \omega(q-q'))\right) \\ &= 2\pi \sum_{\mathbf{k}_\alpha}\sum_{i_\alpha} |t_{\mathbf{k}_\alpha}|^2 \left|\langle i_\alpha|\tilde{a}^\dagger_{\mathbf{k}_\alpha}\tilde{a}_{\mathbf{k}_\alpha}|i_\alpha\rangle\right|^2 W^\alpha_{i_0} |\langle q'|e^{\frac{\lambda}{\omega}(\tilde{b}^\dagger - \tilde{b})}|q\rangle|^2 \delta\left(\varepsilon_{\mathbf{k}_\alpha} - (\varepsilon - \omega(q-q'))\right) \\ &= \gamma^\alpha |\mathbf{X}_{qq'}|^2 n_F\left(\varepsilon - \omega(q-q') - \mu_\alpha\right), \end{aligned} \tag{D.16}$$

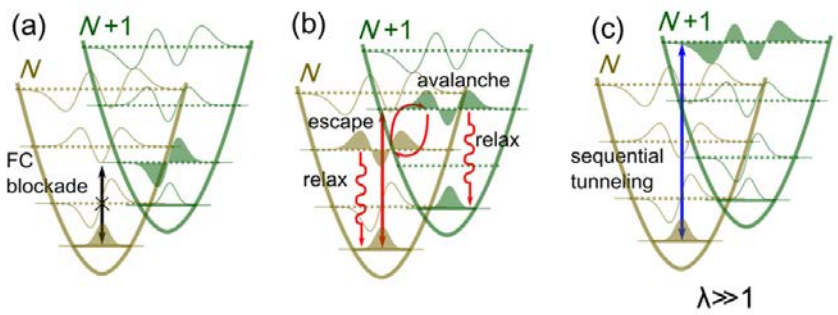

Figure D.1: Schematic of transitons between surface potentials. Adapted with permission from Ref.[237], © 2016 American Chemical Society.

which greatly resembles sequential rates for the Anderson impurity except for the Franck-Condon matrix elements $\left|\mathbf{X}_{qq'}\right|^2 = |\langle q'|\mathbf{X}|q\rangle|^2$, defined by the renormalization matrix

$$\mathbf{X} = e^{-\frac{\lambda}{\omega}(\tilde{b}^\dagger - \tilde{b})}. \tag{D.17}$$

We can apply a similar procedure for $\Gamma^{\alpha}_{0q';1q}$, where now the initial state is $|i_1\rangle = |1\rangle|q\rangle|0\rangle$ with energy $E_i = \varepsilon + \omega q$, and the final state is $|f_0\rangle = a^\dagger_{\mathbf{k}_\alpha}|0\rangle|q'\rangle|i_\alpha\rangle$ with energy $E_f = \varepsilon_{\mathbf{k}_\alpha} + \omega q'$. The rate is

$$\begin{aligned}
\Gamma^{\alpha}_{0q';1q} &= 2\pi \sum_{\mathbf{k}_\alpha}\sum_{i_\alpha} |t_{\mathbf{k}_\alpha}|^2 \left|\langle i_\alpha|\langle q'|\langle 0|\tilde{a}_{\mathbf{k}_\alpha}\tilde{a}^\dagger_{\mathbf{k}_\alpha}\tilde{e}^{-\frac{\lambda}{\omega}(\tilde{b}^\dagger-\tilde{b})}|1\rangle|q\rangle|i_\alpha\rangle\right|^2 W^{\alpha}_{i_0}\delta\left(\varepsilon - \omega(q-q') - \varepsilon_{\mathbf{k}_\alpha}\right) \\
&= 2\pi \sum_{\mathbf{k}_\alpha}\sum_{i_\alpha} |t_{\mathbf{k}_\alpha}|^2 \left|\langle i_\alpha|\tilde{a}_{\mathbf{k}_\alpha}\tilde{a}^\dagger_{\mathbf{k}_\alpha}|i_\alpha\rangle\right|^2 W^{\alpha}_{i_1}\left|\langle q'|e^{-\frac{\lambda}{\omega}(\tilde{b}^\dagger-\tilde{b})}|q\rangle\right|^2 \delta\left(\varepsilon - \omega(q-q') - \varepsilon_{\mathbf{k}_\alpha}\right) \\
&= \gamma^\alpha |\mathbf{X}_{qq'}|^2 \left[1 - n_F\left(\varepsilon - \omega(q-q') - \mu_\alpha\right)\right],
\end{aligned} \tag{D.18}$$

where we obtain the same Franck-Condon factor as the matrix elements are symmetric under $q \leftrightarrow q'$.

Note that we have applied the wide-band approximation in calculating Eq.(D.16) and Eq.(D.18).

D.2.1 Franck-Condon matrix elements

The matrix elements in Eq.(D.16) and Eq.(D.18) arise due to the quantum mechanical interpretation of the Franck-Condon effect. The phonon part of the Holstin Hamiltonian implies that the molecular surface potentials are harmonic, and so tunneling of electrons through the orbital results in transitions between vibrational states that are schematically similar to Fig.(D.1).

The Franck-Condon effect assumes that, since the timescale of electronic transitions are much

smaller than that of nuclei movement, we can treat tunneling processes as instantaneous. Quantum mechanically, this means that the probability of a vibrational transition depends upon the square of the overlap of vibrational states involved in the transition: $|\langle q'|\mathbf{X}|q\rangle|^2$. The renormalization matrix $\mathbf{X}$ is simply a representation, in second quantization, of the spatial distance between the overlapping surface potentials, with λ a measure of that distance.

In this picture of vibrational transitions, we could approach the Franck-Condon matrix elements from first quantization:

$$\left|\langle q'|\mathbf{X}|q\rangle\right|^2 = \int_{-\infty}^{\infty} dx \psi_q(x) e^{\frac{\lambda}{\sqrt{2m\omega}} i\frac{\partial}{\partial x}} \psi^*_{q'}(x), \tag{D.19}$$

Here, the bosonic annihilation and creation operators are

$$b = \sqrt{\frac{m\omega}{2}}\left(x + \frac{i}{m\omega}\frac{\partial}{\partial x}\right), \tag{D.20}$$

$$b^\dagger = \sqrt{\frac{m\omega}{2}}\left(x - \frac{i}{m\omega}\frac{\partial}{\partial x}\right). \tag{D.21}$$

The wavefunction of each vibrational state is given by the solution to the Schrödinger equation for the quantum harmonic oscillator,

$$-\frac{1}{2m}\frac{\partial^2\psi}{\partial x^2} + \frac{1}{2}m\omega^2 x^2 \psi(x) = E\psi(x), \tag{D.22}$$

for which the q^{th} solution is

$$\psi_q(x) = \frac{1}{\sqrt{2^q q!}}\left(\frac{m\omega}{\pi}\right)^{\frac{1}{4}} e^{-\frac{m\omega x^2}{2}} H_q\left(\sqrt{m\omega}x\right), \tag{D.23}$$

and the Hermite polynomials are $H_q(x) = (-1)^q e^{x^2}\frac{d^q}{dx^q}\left(e^{-x^2}\right)$.

Since we are already in second quantization, however, we will approach the problem using the operator relation $e^{A+B} = e^A e^B e^{-[A,B]/2}$. For simplicity, we will also use the variable $\zeta = \frac{\lambda}{\omega}$:

$$\left|\langle q'|\mathbf{X}|q\rangle\right|^2 = \left|e^{-\zeta\tilde{b}^\dagger} e^{\zeta\tilde{b}} e^{\zeta^2[\tilde{b}^\dagger,\tilde{b}]/2}\right|^2 \tag{D.24}$$

$$= \left|e^{-\zeta^2/2}\sum_{l=0}^{\infty}\sum_{m=0}^{\infty}\frac{(-\zeta)^m}{m!}\frac{(\zeta)^l}{l!}\langle q'|(\tilde{b}^\dagger)^m(\tilde{b}^l)|q\rangle\right|^2 \tag{D.25}$$

Bosonic ladder operators are applied to an q particle state as

$$\tilde{b}^\dagger|q\rangle = \sqrt{q+1}|q\rangle \tag{D.26}$$

$$\tilde{b}|q\rangle = \sqrt{q}|q-1\rangle, \tag{D.27}$$

so that Eq.(D.25) becomes

$$\left|\langle q'|\mathbf{X}|q\rangle\right|^2 = \left|e^{-\zeta^2/2}\sum_{l=0}^{\infty}\sum_{m=0}^{\infty}\frac{(-\zeta)^m(\zeta)^l}{m!l!}\sqrt{\frac{q!q'!}{(q-l)!(q'-m)!}}\langle q'-m|q-l)\rangle\right|^2 \tag{D.28}$$

$$= \left|e^{-\zeta^2/2}\sum_{l=0}^{q}\sum_{m=0}^{q'}\frac{(-\zeta)^m(\zeta)^l}{m!l!}\sqrt{\frac{q!q'!}{(q-l)!(q'-m)!}}\delta\left((q-l)-(q'+m)\right)\right|^2. \tag{D.29}$$

Swapping q and q' clearly does not change anything, so the matrix elements are symmetric under $q \leftrightarrow q'$. There are, however, three distinct cases for q and q', each with their own result.

For $q < q'$, the delta function is satisfied when $q - l = q' - m \Rightarrow m = q' - q + l$:

$$\left|\langle q'|\mathbf{X}|q\rangle\right|^2 = \left|\sum_{l=0}^{q}\frac{(-\zeta^2)^l\sqrt{q!q'!}\zeta^{|q'-q|}e^{-\zeta^2/2}}{l!(q-l)!(q'-q+l)!}\right|^2. \tag{D.30}$$

By contrast, for $q > q'$, the delta function is satisfied when $l = q' - q + m$:

$$\left|\langle q'|\mathbf{X}|q\rangle\right|^2 = \left|\sum_{m=0}^{q'}\frac{(-\zeta^2)^m\sqrt{q!q'!}\zeta^{|q'-q|}e^{-\zeta^2/2}}{m!(q'-m)!(q-q'+m)!}\right|^2. \tag{D.31}$$

In the case when $q = q'$, $l = m$ and

$$\left|\langle q'|\mathbf{X}|q\rangle\right|^2 = \left|\sum_{m=0}^{q}\frac{(-\zeta^2)^m q!e^{-\zeta^2/2}}{(m!)^2(q-m)!}\right|^2. \tag{D.32}$$

D.2.2 Jump operators for the Holstein model

The electronic current jump operators defined from the master equation in Eq.(5.4) and Eq.(5.5) are

$$\mathbf{J}_F = \begin{bmatrix} 0 & \Gamma^D_{00;10} & 0 & \Gamma^D_{00;11} & 0 & \cdots & \cdots & \cdots & \Gamma^D_{00;1N} \\ 0 & 0 & 0 & 0 & 0 & & & & 0 \\ 0 & \Gamma^D_{01;10} & 0 & \Gamma^D_{01;11} & 0 & & & & \Gamma^D_{01;1N} \\ \vdots & & & \ddots & & & & & \vdots \\ \vdots & & & & \ddots & & & & \vdots \\ \vdots & & & & & \ddots & & & \vdots \\ 0 & & & & & 0 & 0 & 0 & 0 \\ 0 & & & & & 0 & \Gamma^D_{0N;1(N-1)} & 0 & \Gamma^D_{0N;1N} \\ 0 & \cdots & \cdots & \cdots & \cdots & 0 & 0 & 0 & 0 \end{bmatrix}, \tag{D.33}$$

and

$$\mathbf{J}_B = \begin{bmatrix} 0 & 0 & 0 & 0 & \cdots & \cdots & \cdots & 0 & 0 \\ \Gamma^D_{10;00} & 0 & \Gamma^D_{10;01} & 0 & & & & \Gamma^D_{10;0N} & 0 \\ 0 & 0 & 0 & 0 & & & & 0 & 0 \\ \Gamma^D_{11;00} & 0 & \Gamma^D_{11;01} & 0 & & & & \Gamma^D_{11;0N} & 0 \\ \vdots & & & & \ddots & & & & \vdots \\ \vdots & & & & & \ddots & & & \vdots \\ \vdots & & & & & & \ddots & & \vdots \\ 0 & & & & & 0 & 0 & 0 & 0 \\ \Gamma^D_{1N;00} & \cdots & \cdots & \cdots & \cdots & \Gamma^D_{1N;0(N-1)} & 0 & \Gamma^D_{1N;0N} & 0 \end{bmatrix}. \tag{D.34}$$

Triple quantum dot calculations

E.1 Spin-independent triple and single occupancy

In the triple occupancy regime, the Hamiltonian is small enough to be written exactly:

$$H_Q = \begin{bmatrix} 0 & 0 & 0 & 0 & 0 & 0 & 0 & 0 \\ 0 & \varepsilon_A & t_{AB} & t_{AC} & 0 & 0 & 0 & 0 \\ 0 & t_{BA} & \varepsilon_B & t_{BC} & 0 & 0 & 0 & 0 \\ 0 & t_{CA} & t_{CB} & \varepsilon_C & 0 & 0 & 0 & 0 \\ 0 & 0 & 0 & 0 & \varepsilon_{AB} & t_{BC} & t_{AC} & 0 \\ 0 & 0 & 0 & 0 & t_{CB} & \varepsilon_{AC} & t_{AB} & 0 \\ 0 & 0 & 0 & 0 & t_{CA} & t_{BA} & \varepsilon_{BC} & 0 \\ 0 & 0 & 0 & 0 & 0 & 0 & 0 & \varepsilon_3 \end{bmatrix}, \tag{E.1}$$

where we have introduced the notation $\varepsilon_{\nu\nu'} = \varepsilon_\nu + \varepsilon_\nu + U_{\nu\nu'}$ and $\varepsilon_3 = \sum_\nu \varepsilon_\nu + \sum_{\nu\nu'} U_{\nu\nu'}$.

E.1.1 Elements of the master equation

In the basis of molecular eigenstates, the full triple occupancy density matrix is

$$\rho = \begin{bmatrix} \rho_{0,0} & \rho_{0,11} & \rho_{0,12} & \rho_{0,13} & \rho_{0,21} & \rho_{0,22} & \rho_{0,23} & \rho_{0,3} \\ \rho_{11,0} & \rho_{11,11} & \rho_{11,12} & \rho_{11,13} & \rho_{11,21} & \rho_{11,22} & \rho_{11,23} & \rho_{11,3} \\ \rho_{12,0} & \rho_{12,11} & \rho_{12,12} & \rho_{12,13} & \rho_{12,21} & \rho_{12,22} & \rho_{12,23} & \rho_{12,3} \\ \rho_{13,0} & \rho_{13,11} & \rho_{13,12} & \rho_{13,13} & \rho_{13,21} & \rho_{13,22} & \rho_{13,23} & \rho_{13,3} \\ \rho_{21,0} & \rho_{21,11} & \rho_{21,12} & \rho_{21,13} & \rho_{21,21} & \rho_{21,22} & \rho_{21,23} & \rho_{21,3} \\ \rho_{22,0} & \rho_{22,11} & \rho_{22,12} & \rho_{22,13} & \rho_{22,21} & \rho_{22,22} & \rho_{22,23} & \rho_{22,3} \\ \rho_{23,0} & \rho_{23,11} & \rho_{23,12} & \rho_{23,13} & \rho_{23,21} & \rho_{23,22} & \rho_{23,23} & \rho_{23,3} \\ \rho_{3,0} & \rho_{3,11} & \rho_{3,12} & \rho_{3,13} & \rho_{3,21} & \rho_{3,22} & \rho_{3,23} & \rho_{3,3} \end{bmatrix}, \tag{E.2}$$

which is still a large number of matrix elements. Because the eigenstates corresponding to different occupancy numbers are orthogonal, however, $\rho_{mi,nj} = 0$ when $m \neq n$. The individual equations of motion for each matrix element will rely on several general coefficients, which we define below:

$$D_{1i,1j} = \sum_{\nu=\{A,C\}} \langle 0|a_\nu|1i\rangle\langle 1j|a_\nu^\dagger|0\rangle = a_{1i,A}a_{1j,A}^* + a_{1i,C}a_{1j,C}^* \tag{E.3}$$

$$E_{2r,2s,1i,1j} = \sum_{\nu=\{A,C\}} \langle 1i|a_\nu|2r\rangle\langle 2s|a_\nu^\dagger|1j\rangle = \left(a_{2r,AB}a_{1i,B}^* + a_{2r,AC}a_{1i,C}^*\right)\left(a_{2s,AB}^* a_{1j,B} + a_{2s,AC}^* a_{1j,C}\right) \tag{E.4}$$

$$F_{2r,2s,1i,1j} = \langle 1i|a_B|2r\rangle\langle 2s|a_B^\dagger|1j\rangle = \left(a_{2r,AB}a_{1i,A}^* + a_{2r,BC}a_{1i,C}^*\right)\left(a_{2s,AB}^* a_{1j,A} + a_{2s,BC}^* a_{1j,C}\right) \tag{E.5}$$

$$G_{2r,2s} = \sum_{\nu=\{A,C\}} \langle 3|a_\nu^\dagger|2r\rangle\langle 2s|a_\nu|3\rangle = a_{2r,BC}a_{2s,BC}^* + a_{2r,AB}a_{2s,AB}^*. \tag{E.6}$$

The 1st-order differential equation for $\rho_{0,0}(\chi,t)$ is

$$\dot{\rho}_{0,0} = -\rho_{0,0}\left(\sum_{1i} D_{1i,1i}\, n_F(\varepsilon_{1i}-\mu_S) + |a_{1i,B}|^2 n_F(\varepsilon_{1i}-\mu_D)\right) - i\sum_{1j}\sum_{1i}\rho_{1i,1j}\left[D_{1i,1j}\left(\Sigma_S^>(\omega_{1j,0})^* - \Sigma_S^>(\omega_{1i,0})\right) + e^{i\chi}a_{1i,B}a_{1j,B}^*\left(\Sigma_D^>(\omega_{1j,0})^* - \Sigma_D^>(\omega_{1i,0})\right)\right]. \tag{E.7}$$

The 1st-order differential equation $\rho_{1i,1j}(\chi,t)$ is

$$\begin{aligned}\dot{\rho}_{1i,1j} = {}& \rho_{0,0}\left[D_{1j,1i}\left(\Sigma_S^<(\omega_{1j,0}) - \Sigma_S^<(\omega_{1i,0})^*\right) + e^{-i\chi}a_{1j,B}a_{1i,B}^*\left(\Sigma_D^<(\omega_{1j,0}) - \Sigma_D^<(\omega_{1i,0})^*\right)\right] \\ & - i\Bigg[\sum_{1k}\Big(\rho_{1k,1j}\Big[D_{1k,1i}\Sigma_S^>(\omega_{1k,0}) + a_{1k,B}a_{1i,B}^*\Sigma_D^>(\omega_{1k,0}) + \sum_{2r}\big(E_{2r,2r,1i,1k}\Sigma_S^<(\omega_{2j,1k})^* \\ & + F_{2r,2r,1i,1k}\Sigma_D^<(\omega_{2j,1k})^*\big)\Big] - \rho_{1i,1k}\Big[D_{1j,1k}\Sigma_S^>(\omega_{1k,0})^* + a_{1j,B}a_{1k,B}^*\Sigma_D^>(\omega_{1k,0})^* \\ & + \sum_{2r}\left(E_{2r,2r,1k,1j}\Sigma_S^<(\omega_{2j,1k}) + F_{2r,2r,1k,1j}\Sigma_D^<(\omega_{2j,1k})\right)\Big]\Big) + \sum_{2s}\sum_{2r}\rho_{2r,2s}\Big[E_{2r,2s,1i,1j}\left(\Sigma_S^>(\omega_{2s,1j})^*\right. \\ & \left. - \Sigma_S^>(\omega_{2r,1i})\right) + e^{i\chi}F_{2r,2s,1i,1j}\left(\Sigma_D^>(\omega_{2s,1j})^* - \Sigma_D^>(\omega_{2r,1i})\right)\Big]\Bigg].\end{aligned} \tag{E.8}$$

The 1st-order differential equation for $\rho_{3,3}(\chi,t)$ is

$$\dot{\rho}_{3,3} = -\rho_{3,3}\left(\sum_{2r} G_{2r,2r}\left[1 - n_F(\varepsilon_3 - \varepsilon_{2r} - \mu_S)\right] + |a_{2r,AC}|^2[1 - n_F(\varepsilon_3 - \varepsilon_{2r} - \mu_D)\right) - i\sum_{2s}\sum_{2r}\rho_{2r,2s}\left[G_{2r,2s}\left(\Sigma_S^<(\omega_{3,2s}) - \Sigma_S^<(\omega_{3,2r})^*\right) + e^{i\chi}a_{1i,B}a_{1j,B}^*\left(\Sigma_D^<(\omega_{3,2s}) - \Sigma_D^<(\omega_{3,2r})^*\right)\right]. \tag{E.9}$$

The 1st-order differential equation $\rho_{1i,1j}(\chi,t)$ is

$$\begin{aligned}\dot{\rho}_{1i,1j} = \rho_{0,0}\Big[D_{1j,1i}\left(\Sigma_S^<(\omega_{1j,0}) - \Sigma_S^<(\omega_{1i,0})^*\right) + e^{-i\chi}a_{1j,B}a_{1i,B}^*\left(\Sigma_D^<(\omega_{1j,0}) - \Sigma_D^<(\omega_{1i,0})^*\right)\Big] \\ - i\Bigg[\sum_{1k}\Big(\rho_{1k,1j}\Big[D_{1k,1i}\Sigma_S^>(\omega_{1k,0}) + a_{1k,B}a_{1i,B}^*\Sigma_D^>(\omega_{1k,0}) + \sum_{2r}\big(E_{2r,2r,1i,1k}\Sigma_S^<(\omega_{2j,1k})^* \\ + F_{2r,2r,1i,1k}\Sigma_D^<(\omega_{2j,1k})^*\big)\Big] - \rho_{1i,1k}\Big[D_{1j,1k}\Sigma_S^>(\omega_{1k,0})^* + a_{1j,B}a_{1k,B}^*\Sigma_D^>(\omega_{1k,0})^* \\ + \sum_{2r}\big(E_{2r,2r,1k,1j}\Sigma_S^<(\omega_{2j,1k}) + F_{2r,2r,1k,1j}\Sigma_D^<(\omega_{2j,1k})\big)\Big]\Big) + \sum_{2s}\sum_{2r}\rho_{2r,2s}\big[E_{2r,2s,1i,1j}\left(\Sigma_S^>(\omega_{2s,1j})^*\right. \\ \left.-\Sigma_S^>(\omega_{2r,1i})\right) + e^{i\chi}F_{2r,2s,1i,1j}\left(\Sigma_D^>(\omega_{2s,1j})^* - \Sigma_D^>(\omega_{2r,1i})\right)\big]\Bigg]. \qquad \text{(E.10)}\end{aligned}$$

The 1st-order differential equation $\rho_{2r,2s}(\chi,t)$ is

$$\begin{aligned}\dot{\rho}_{2r,2s} = \rho_{3,3}\Big[G_{2s,2r}\left(\Sigma_S^>(\omega_{3,2s})^* - \Sigma_S^>(\omega_{3,2r})\right) + e^{-i\chi}a_{2r,AC}a_{2s,AC}^*\left(\Sigma_D^>(\omega_{3,2s})^* - \Sigma_D^>(\omega_{3,2r})\right)\Big] \\ - i\Bigg[\sum_{2t}\Big(\rho_{2t,2s}\Big[G_{2t,2r}\Sigma_S^<(\omega_{3,2t})^* + a_{2t,AC}a_{2r,AC}^*\Sigma_D^<(\omega_{3,2t})^* + \sum_{1i}\big(E_{2t,2r,1i,1i}\Sigma_S^>(\omega_{2t,1i}) \\ + F_{2t,2r,1i,1i}\Sigma_D^>(\omega_{2t,1i})\big)\Big] - \rho_{2r,2t}\Big[G_{2s,2t}\Sigma_S^<(\omega_{3,2t})^* + a_{2s,AC}a_{2s,AC}^*\Sigma_D^<(\omega_{3,2t})^* \\ + \sum_{1i}\big(E_{2s,2t,1i,1i}\Sigma_S^>(\omega_{2t,1i})^* + F_{2s,2t,1i,1i}\Sigma_D^>(\omega_{2t,1i})^*\big)\Big]\Big) + \sum_{1j}\sum_{1i}\rho_{1i,1j}\big[E_{2s,2r,1j,1i}\left(\Sigma_S^<(\omega_{2s,1j})\right. \\ \left.-\Sigma_S^<(\omega_{2r,1i}^*)\right) + e^{i\chi}F_{2s,2r,1j,1i}\left(\Sigma_D^<(\omega_{2s,1j}) - \Sigma_D^<(\omega_{2r,1i}^*)\right)\big]\Bigg]. \qquad \text{(E.11)}\end{aligned}$$

For the reverse configuration in Fig.(7.1b), $\Sigma_S(\omega) \leftrightarrow \Sigma_D(\omega)$.